

IMPROVED PREDICTION OF THE EFFECTS OF ANTHROPOGENIC STRESSORS  
IN THE GULF OF MEXICO THROUGH REGIONAL-SCALE NUMERICAL  
MODELING AND DATA ASSIMILATION

by

Liuqian Yu

Submitted in partial fulfilment of the requirements  
for the degree of Doctor of Philosophy

at

Dalhousie University  
Halifax, Nova Scotia  
November 2018

© Copyright by Liuqian Yu, 2018

*To my better half, Nanju, and my twin sister tingting.*

# TABLE OF CONTENTS

<b>List of Tables</b> .....	vii
<b>List of Figures</b> .....	viii
<b>Abstract</b> .....	xiii
<b>List of Abbreviations and Symbols Used</b> .....	xiv
<b>Acknowledgements</b> .....	xviii
<b>Chapter 1 Introduction</b> .....	1
1.1 Background .....	1
1.2 Objectives .....	3
1.3 Outline .....	6
<b>Chapter 2 Primary Processes Controlling Oxygen Dynamics in the Northern Gulf of Mexico</b> .....	8
2.1 Introduction .....	8
2.2 Model Description .....	11
2.3 Results .....	18
2.3.1 Simulated Oxygen Dynamics and Model Validation .....	18
2.3.2 Validation of the Model+CCR Simulation .....	24
2.3.3 Oxygen Balance .....	25
2.3.4 Role of Sub-pycnocline Primary Production in Hypoxia Generation .....	31
2.4 Discussion .....	33
2.4.1 Simulated Oxygen Dynamics and Model Validation .....	33
2.4.2 Primary Processes Controlling Oxygen Dynamics .....	34
2.4.3 Role of Sub-pycnocline Primary Production in Hypoxia Generation .....	37
2.5 Summary .....	37
<b>Chapter 3 Physical controls on hypoxia generation in the Northern Gulf of Mexico</b> .....	39

3.1	Introduction .....	39
3.2	Methods .....	41
3.2.1	Model Description .....	41
3.2.2	Model Experiments .....	44
3.3	Results.....	48
3.3.1	Model Validation .....	54
3.3.2	Response of Hypoxia and Stratification to River Discharge and Wind forcing .....	54
3.3.2.1	River Discharge .....	54
3.3.2.2	Wind Forcing .....	64
3.4	Discussion .....	65
3.4.1	Model Validation and Roles of Water Column versus Sediment Processes .....	65
3.4.2	Model Response to River Discharge and Wind forcing: from Stratification to Hypoxia .....	67
3.4.2.1	River Discharge .....	67
3.4.2.2	Wind Forcing .....	69
3.4.3	Consistency with Observations of Hypoxia.....	70
3.5	Summary.....	72
<b>Chapter 4</b>	<b>Insights on Multivariate Updates of Physical and Biogeochemical Ocean Variables using an Ensemble Kalman Filter and an Idealized Model of Upwelling .....</b>	<b>74</b>
4.1	Introduction .....	74
4.2	Model Description and Experimental Setup .....	76
4.2.1	The Coupled Physical-Biogeochemical Model.....	76
4.2.2	Experimental Framework .....	79
4.2.2.1	DEnKF Algorithm .....	81
4.2.2.2	Assimilation Settings .....	82
4.2.2.3	Data Assimilation Experiments .....	83
4.3	Results .....	86
4.3.1	Comparison between Truth and Free Run .....	86



4.3.2	Impact of Assimilation on Physical and Biogeochemical States .....	91
4.3.2.1	Method 1 “Isolated Updates” .....	91
4.3.2.2	Method 2 “Multivariate Updates   Single Data Type” .....	93
4.3.2.3	Method 3 “Joint Updates   Both Data Types”.....	94
4.3.2.4	Nitrate and temperature correlation.....	96
4.3.3	Impact of assimilation on the forecast skill .....	98
4.3.4	Sensitivity of the Assimilation Methods to Twin Experimental Design .....	99
4.4	Discussion .....	101
4.5	Summary .....	104
<b>Chapter 5</b>	<b>Ensemble data assimilation for improving the simulation of circulation and movement of a deep-water hydrocarbon plume in the Gulf of Mexico .....</b>	<b>106</b>
5.1	Introduction .....	106
5.2	Model Description and Experimental Setup.....	110
5.2.1	The Coupled Physical-Hydrocarbon Model .....	110
5.2.2	Experimental Framework .....	114
5.2.2.1	Fraternal Twin Experiments .....	115
5.2.2.2	Data Assimilation Experiment Assimilating Real Observations .....	118
5.2.2.3	Identical Twin Experiments .....	118
5.3	Results .....	119
5.3.1	Impact of Assimilation on Physical Variables: Fraternal Twin Experiments .....	119
5.3.2	Impact of Assimilation on Physical Variables: Assimilating Real Observations .....	130
5.3.3	Impact of Assimilation on Physical Variables and Hydrocarbon Fields: Identical Twin Experiments .....	137
5.3.3.1	Physical Variables .....	137
5.3.3.2	Hydrocarbon Fields .....	140

5.4 Discussion.....	141
5.5 Summary .....	145
<b>Chapter 6 Conclusions .....</b>	<b>146</b>
6.1 Major Findings .....	147
6.2 Implications for Model Development and Assimilation Method Implementation and Assessment .....	149
6.3 Future Work .....	152
<b>Appendix A Copyright Permission .....</b>	<b>155</b>
<b>Appendix B.....</b>	<b>158</b>
<b>Appendix C.....</b>	<b>165</b>
<b>Appendix D.....</b>	<b>168</b>
<b>Bibliography .....</b>	<b>170</b>

# LIST OF TABLES

2.1	RMSE and bias between simulated and observed bottom DO concentrations. .....	20
2.2	RMSE and bias between simulated and observed primary production (PP) or water column respiration (WR). .....	23
2.3	RMSE and bias between simulated median of sediment oxygen consumption (SOC) and observed SOC. .....	24
2.4	Shelf-wide average observed and simulated percentage of primary production below the pycnocline. .....	30
3.1	Overview of models. .....	44
3.2	Overview of model experiments. .....	45
3.3	Integrated hypoxic areas simulated by different model runs in 2007. .....	56
3.4	Shelf area where hypoxic duration exceeds 50 and 250 days/year, average area of the surface river plume (area of surface salinity $\leq 24$ ) and average stratification (maximum $N^2$ ) over specific periods for all model runs. .....	58
4.1	Overview of assimilation experiments. .....	85
4.2	Overview of assimilation effect on physical and biogeochemical model state variables in Scenario 1. .....	95
5.1	Overview of data assimilation twin experiments. .....	118
5.2	Mean Absolute Deviations (MAD) from the “truth” of physical variables for free and data assimilation runs in fraternal twin and identical experiments. .....	120
5.3	Mean Absolute Deviations (MAD) from the observations of physical variables for free and data assimilation runs in the assimilation system using real data. .....	133

# LIST OF FIGURES

2.1	Model grid and bathymetry.	12
2.2	Mississippi and Atchafalaya River freshwater discharge and nutrient loads in 2004-2007.	14
2.3	Schematic of the biological model.	15
2.4	Time series of simulated and observed dissolved oxygen concentration in bottom water in the 4 subregions.	19
2.5	Vertical profiles of model bias in dissolved oxygen calculated from 2004 to 2007 for June to August in the 4 subregions.	21
2.6	Vertically integrated rates of observed and simulated primary production and water column respiration in the 4 subregions.	22
2.7	Model simulated sediment oxygen consumption versus bottom dissolved oxygen for the period 2004 to 2007.	24
2.8	Simulated net community production (PP-TR) versus air-sea flux of oxygen for the 4 subregions.	27
2.9	Simulated 4-year (2004-2007) mean oxygen balance in summer for the 4 subregions.	29
2.10	Time series of simulated hypoxic extent for the full model and the model without biological processes in the water column.	32
3.1	Model grid and bathymetry.	42
3.2	Fitted net water column respiration rate (NWR) based on observations of <i>Murrell et al.</i> [2013b].	43
3.3	Mississippi and Atchafalaya River freshwater discharge.	46

3.4	NARR W-E wind and NARR N-S wind averaged over the shelf. .....	47
3.5	Time series of simulated hypoxic extent for the full biogeochemical model, the NWR+SOC model, the SOC only model and the NWR only model. .....	49
3.6	Simulated and observed hypoxic conditions from the full biogeochemical model, the NWR+SOC model and the SOC only model for the years 2004 to 2007. .....	50
3.7	Vertical profiles of model bias in dissolved oxygen from June to August in 2004-2007 in the 4 subareas. .....	51
3.8	Comparison between the simulated and observed dissolved oxygen concentrations at station C6 for full biogeochemical model and the simple NWR+SOC model. .....	53
3.9	Comparison between the simulated and observed seasonal average dissolved oxygen concentrations along the C transect for the full biogeochemical model and simple NWR+SOC model. .....	54
3.10	Comparison of the simulated hypoxic area for the different model runs. .....	55
3.11	Simulated number of hypoxic days for each model run. .....	57
3.12	Averaged stratification over the shelf for different model runs. .....	59
3.13	The deviation in summer averaged stratification from the baseline model run. .....	60
3.14	Averaged surface salinity for all model runs. .....	62
3.15	Averaged salinity on a cross-shore transect for all model runs. .....	63
4.1	(a) Wind stress for the high-wind and low-wind model runs. (b) Model bathymetry and (c) vertical grid of cross-channel transect. .....	78
4.2	Time series of the surface domain-averaged water temperature, concentrations of nitrate, and phytoplankton for truth, free run and different assimilation runs. .....	87

4.3	Surface layer on day 140 (assimilation step 17) for different state variables from the truth, free run and different assimilation runs.	88
4.4	Cross-channel transect on day 140 (assimilation step 17) for different state variables from the truth, free run and different assimilation runs.	89
4.5	Averaged temperature and nitrate profiles over stations along the along-channel section on day 140 (assimilation step 17) for the truth, free run and different assimilation runs.	90
4.6	The domain- and time-averaged $\text{bias}_{\text{surf}}$ , $\text{MAD}_{\text{surf}}$ and $\text{MAD}_{\text{all}}$ for different state variables from the free run and different assimilation runs.	91
4.7	Scatterplots of nitrate and temperature for the free run and different assimilation runs.	97
4.8	Difference of domain-averaged $\text{MAD}_{\text{surf}}$ and $\text{MAD}_{\text{all}}$ between the free run and forecast runs initialized from the ensemble analysis on day 140 (assimilation step 17).	99
4.9	Same as Figure 4.2 but for the “overestimating upwelling and productivity” Scenario 2 twin experiments.	100
5.1	Model domain and bathymetry.	112
5.2	Sea surface height, and transects of temperature and salinity on 28 May 2010.	116
5.3	Time series of MAD averaged over the open Gulf (excluding shelf regions shallower than 300 m) for SSH, temperature, salinity, u, and v from the free run and fraternal twin runs.	121
5.4	The difference of physical variables’ time-averaged (daily snapshots from 1 April to 1 October) MAD between fraternal twin F1 and the free run.	123
5.5	Same as Figure 5.4 but for salinity comparing the fraternal twins F1 and F3.	123
5.6	Profiles of MAD averaged over the open Gulf (excluding shelf regions shallower than 300 m) and daily snapshots from 1 April to 1 October 2010 for temperature, salinity, u, and v from the free run and the fraternal twin runs.	124

5.7	Point-by-point comparison of temperature and salinity from the “truth” versus those from free, F1 and F3 runs.	125
5.8	August-mean temperature and salinity at 400 m from the “truth”, free, F1 and F3 run in fraternal twin experiments.	127
5.9	Time series of subregion- and water column-averaged MAD for velocity components u and v from the free and fraternal twin runs.	128
5.10	August-mean velocity at 400 m in the “truth”, free and F1 runs in fraternal twin experiments.	129
5.11	Time series of MAD averaged over the open Gulf (excluding shelf regions shallower than 300 m) for SSH and SST from the free run and data assimilation run with real observations.	130
5.12	Temporally averaged (daily snapshots from 1 April to 1 October) difference in MAD between the DA run and the free run for SSH and SST.	131
5.13	Time-evolving Loop Current front depicted by the 10 cm SSH isoline from altimeter observations, free run and DA run.	132
5.14	Point-by-point comparison of temperature and salinity from Argo observations versus those from free and DA run.	134
5.15	Profiles of averaged MAD and bias for temperature and salinity from the free and the DA run in relative to Argo observations.	135
5.16	Argo observations of temperature and salinity at 200 m and difference between simulated and observed temperature and salinity at 200 m in the free run and DA run.	136
5.17	Time series of subregion- and water column-averaged MAD for velocity components u and v from the free run and I1.	137
5.18	Overlay of time-evolving 0.1 g/m <sup>2</sup> HydroC contours with the time-averaged velocity at 1000 m during selected time interval in the “truth”, free and DA1 runs in identical twin experiment.	139

5.19 Time series of domain-averaged MAD for water column integrated HydroC  
from free run and I1 run in the identical twin experiments.  
.....141



# ABSTRACT

The Gulf of Mexico (GOM) is of great ecological and socio-economic importance; however, its ecosystems are increasingly stressed by anthropogenic pressures. Two of the most serious are excessive nutrient inputs from land that affect the shelf in the northern GOM and lead to reoccurring extensive hypoxia, and oil exploration and extraction activities that have become more risky by increasingly extending into the deep sea leading to pollution there. Realistic physical-biogeochemical models are invaluable tools for understanding and predicting the resulting effects on the marine system, but a model's predictive capabilities are limited by various sources of error resulting from imperfect descriptions of physical and biological processes, inaccurate forcing, uncertain initial and boundary conditions, and imprecise parameter values. Data assimilation methods that merge the information contained in observations and dynamical models are crucial for providing the most accurate views of ocean processes. This thesis aims to improve our understanding and our predictive capabilities of shelf hypoxia and movement of deep-water pollutants in the GOM through regional-scale numerical modeling and data assimilation. First, two numerical models of dissolved oxygen with different ecological complexity are applied to investigate the mechanisms controlling the development of seasonal bottom-water hypoxia on the continental shelf in the northern GOM. Next, a multivariate sequential data assimilation method, the deterministic Ensemble Kalman Filter (DEnKF), is tested in an idealized upwelling model to explore the effects of multivariate updates of physical and biogeochemical model states. Finally, the DEnKF technique is implemented in a realistic physical-hydrocarbon model of the GOM to assess the effects of data assimilation on the mesoscale circulation and the movement of a deep-water hydrocarbon plume.

# LIST OF ABBREVIATIONS AND SYMBOLS USED

---

<b>Abbreviation</b>	<b>Description</b>
3D	Three-dimensional
4D	Four-dimensional
AVISO	Archiving, Validation and Interpretation of Satellite Oceanographic Data
AVHRR	Advanced Very High Resolution Radiometer
BGC	Biogeochemical
DA	Data Assimilation
DEnKF	Deterministic Ensemble Kalman Filter
DF	Downwelling-favorable
DO	Dissolved Oxygen
DON	Dissolved Organic Nitrogen
DwH	Deepwater Horizon
ECMWF	European Centre for Medium-Range Weather Forecasts
EOF	Empirical Orthogonal Function
EnKF	Ensemble Kalman Filter
EnOI	Ensemble Optimal Interpolation
GOM	Gulf of Mexico
HSIMT	High-order Spatial Interpolation at the Middle Temporal level
HYCOM	Hybrid Coordinate Ocean Model
KF	Kalman Filter
LA	Louisiana
LC	Loop Current
LCEs	Loop Current Eddies
MAD	Mean Absolute Deviations
MCH	Mechanisms Controlling Hypoxia
MDT	Mean Dynamic Topography
NARR	North American Regional Reanalysis
NCEP	National Centers for Environmental Prediction
NODC	National Oceanographic Data Center

---

---

NWR	Net Water Column Respiration
OI	Optimal Interpolation
PDF	Probability density function (PDF)
PI	Photosynthesis-irradiance
PON	Particulate Organic Nitrogen
PP	Primary Production
RD	River Discharge
RDOM	River-born dissolved organic matter
RMS	Root Mean Square
RMSE	Root Mean Square Error
ROMS	Regional Ocean Modeling System
SLA	Sea Level Anomaly
SOC	Sediment Oxygen Consumption
SSH	Sea Surface Height
SST	Sea Surface Temperature
TKN	Total Kjeldahl Nitrogen
UF	Upwelling-favorable
US	United States
USGS	United States Geological Survey
WR	Water Column Respiration

---

<b>Symbol</b>	<b>Description (Unit)</b>
$\text{bias}_{\text{surf}}$	bias averaged over the surface layer only
Chl	Chlorophyll
$DO_{\text{sat}}$	Oxygen concentration at saturation ( $\text{mmol } O_2 \text{ m}^{-3}$ )
$F_{\text{air-sea}}$	Air-sea flux of oxygen ( $\text{mmol } O_2 \text{ m}^{-2} \text{ d}^{-1}$ )
$F_{\text{bf}}$	Boundary oxygen fluxes ( $\text{mmol } O_2 \text{ m}^{-2} \text{ d}^{-1}$ )
H	Measurement operator mapping the model state onto the observations
HydroC	Hydrocarbon
HydroC1	Insoluble fraction of Hydrocarbon
HydroC2	Soluble fraction of Hydrocarbon
K	Kalman gain matrix
$K_H$	Horizontal diffusivity ( $\text{m}^2 \text{ s}^{-1}$ )
$K_v$	Vertical diffusivity ( $\text{m}^2 \text{ s}^{-1}$ )
LDet	Large detritus
$\text{MAD}_{\text{surf}}$	MAD averaged over the surface layer only
$\text{MAD}_{\text{all}}$	MAD averaged over the entire water column
N	Nitrogen
$N^2$	Maximum Brunt-Vaisala Frequency
NH4	Ammonium
NO3	Nitrate
$O_2$	Oxygen
$Ox$	Oxygen concentration ( $\text{mmol } O_2 \text{ m}^{-3}$ )
$Ox_{\text{sat}}$	Oxygen concentration at saturation ( $\text{mmol } O_2 \text{ m}^{-3}$ )
Phy	Phytoplankton
PO4	Phosphate
$Q_{10}$	Rate of change as a result of increasing the temperature by 10 °C
$R^2$	Coefficient of determination
S	Salinity
$Sc_{Ox}$	Schmidt number
SDet	Small detritus
T	Temperature (°C)
u	Horizontal component of velocity in east-west direction ( $\text{m s}^{-1}$ )

---

$u_{10}$	wind speed at 10 m above the sea surface ( $\text{m s}^{-1}$ )
$v$	Horizontal component of velocity in north-south direction ( $\text{m s}^{-1}$ )
$vk_{O_2}$	gas exchange coefficient for oxygen
$w$	Vertical component of velocity ( $\text{m s}^{-1}$ )
Zoo	Zooplankton
$\Delta z$	Thickness of the respective grid box
$\nabla$	gradient operator

---

# ACKNOWLEDGEMENTS

I would like to thank my supervisor Katja Fennel for her endless support, help, guidance, inspiration and encouragement. Having her as my supervisor is the best thing I could ever have in this PhD journey. I would also like to thank the members of my committee Keith Thompson, Wendy Gentleman and Jinyu Sheng for their continuous support, constructive comments, and helpful discussions. Special thank goes to Keith for his unlimited patience, inspiration and encouragement in strengthening my knowledge in statistics and improving the thesis. My thank also extends to Arnaud Laurent, my collaborator and honorable Adjunct Ex Officio in the committee, for his tremendous help and insightful discussions.

Many thanks to Laurent Bertino and Mohamad Gharamti, my collaborators in Nansen Environmental and Remote Sensing Center, for making my exchange study in Bergen a very fruitful and pleasant journey. I am very grateful to the expertise and time they devoted to strengthening my knowledge in data assimilation. A special thank also goes to Annette Samuelsen for her help and insightful discussions during my stay in Nansen.

I would also like to thank the great colleagues and friends I have met in Marine Environmental Modelling group and Oceanography Department. Specially I would like to thank Paul Mattern and Jiatang Hu for their legacy in data assimilation, Arnaud Laurent, Wenxia Zhang and Haiyan Zhang for sharing the ideas and discussions in ROMS models and hypoxia projects, Bin Wang for the help in improving Gulf of Mexico model, Angela Kuhn, Krysten Rutherford, Rui Zhang, Catherine Brennan and Laura Bianucci for all the helpful discussions, encouragement, and sharing ups and downs. I must also thank my many dearest fellow Chinese friends in Halifax for years of constantly providing support, food and company during the journey, especially Wenxia Zhang, Haiyan Zhang, Chen Hu, Qiang Shi, Jing Tao, Lanli Guo and Bin Wang.

Last but not least, I would like to thank my loving family: my parents, grandma, and my siblings especially Tingting, for the endless love and support throughout my PhD journey despite the long distance between us.

Finally, I want to thank my better half, Nanju Zhang, to whom I utterly count on for love and support, and without whom I could never complete this marathon.

Financial Support for this thesis work was provided by the NOAA CSCOR grant, the US IOOS Coastal Ocean Modeling Testbed, The Gulf of Mexico Research Initiative, Nova Scotia Graduate Fellowship program, and the POME (Prediction and Observation of the Marine Environment) mobility grant.

# CHAPTER 1

## INTRODUCTION

### 1.1 Background

The Gulf of Mexico (GOM) is a semi-enclosed marginal sea, characterized by a complex set of physical and biogeochemical processes, and a vast and productive body of water with tremendous ecological, economic and social value. However, this valuable ecosystem, along with the goods and services it provides, is threatened by intensifying anthropogenic pressures. Two of the most serious are: 1) excessive inputs of agriculturally derived nutrients by the Mississippi and Atchafalaya Rivers which lead to widespread seasonal hypoxia (oxygen concentrations  $< 2 \text{ mg l}^{-1}$  or  $62.5 \text{ mmol m}^{-3}$ ) on the shelf of northern GOM, and 2) pollution associated with intensive oil exploration and extraction activities that increasingly occur in the deep sea. Developing effective mitigation and management strategies for these environmental threats demands improved understanding and prediction capabilities for the fundamental physical and biogeochemical processes in the GOM.

Numerical models are invaluable tools for understanding the dynamics of marine systems, predicting their responses to natural and anthropogenic perturbations, and providing useful information for marine management and decision-making. In recent decades, a surge in computing power has greatly advanced the development of numerical ocean models with improved predictive capabilities and increased value as scientific tools (e.g., Allen et al. 2010; Peña et al., 2010; Gehlen et al. 2015; Bianucci et al., 2015). Nevertheless, models offer an imperfect representation of the true ocean, involving only a limited number of complex processes, simplifying their characterization as well as being prone to errors arising from numerical approximations, choice of mathematical functions and parameter values, and specification of model forcing, initial and boundary conditions.

Observations are an essential source of information for understanding the ocean and for validating and calibrating models. In the past decades a revolution in global



ocean-observing capabilities has occurred, providing an unprecedented view of marine ecosystems from the ocean surface to the ocean interior (Johnson et al., 2009, 2013; Schofield et al., 2013). Of course, these observations also contain errors arising from various sources, such as the measuring device, and instrumental and environmental noise (Robinson and Lermusiaux, 2002). Moreover, in utilizing observations for model validation or assimilation into models, the observations additionally have representation (or representativeness) errors. The representation error often arises from a mismatch between the scales and processes represented in the observations and model fields, from the approximations involved in the observation operators mapping the model fields to the observation equivalent, and from quality-control or pre-processing procedures of observations (e.g., Lorenc, 1986; Daley, 1991; and a recent review by Janjić et al., 2017). Last but not least, despite substantially improved data coverage, the ocean is still severely undersampled with respect to its complexity and temporal and spatial scales of variability.

In this context, using data assimilation (DA) methods to optimally merge the heterogeneous and potentially erroneous information in observations and dynamical models is crucial for providing the most accurate representation of marine physical and biogeochemical processes. The foundations of DA methods are rooted in Bayes' theorem, which fuses observational data with prior knowledge (e.g., mathematical models approximating physical laws) to obtain an estimate of the distribution of the true state of a process (Wikle and Berliner 2007). Ocean DA methods generally fall into two categories: the variational approach, which seeks the model trajectory that best fits available observations by minimizing a cost function measuring the model-data misfit (e.g., Le Dimet and Talagrand, 1986; Thacker and Long, 1988), and the sequential approach, which seeks a best state vector that maximizes the posterior distribution at each instant observations become available (e.g., Kitagawa, 1996; Doucet et al., 2000). Dependent on whether future observations are included to constrain the current model state estimates, the DA methods could also be loosely divided into filtering and smoothing approaches, where the former does not include future observations for current assimilation step (e.g., Kalman Filter) while the latter includes all previous and future observations within an assimilation time window to determine the analysis state (e.g., Kalman Smoother, 4D-Var

approach). In the case of linear dynamics and Gaussian error distributions, the cost function in the variational approach is proportional to the negative of the logarithm of the posterior distribution in the sequential approach such that minimizing the cost function becomes equivalent to maximizing the posterior distribution (Lorenc, 1986; Wikle and Berliner, 2007).

One state-of-art DA method following the sequential assimilation approach is the Ensemble Kalman Filter (EnKF), which applies the Monte Carlo method to propagate model uncertainties with the full nonlinear model before sequentially updating the model state based on the Bayesian inference (Evensen, 1994). The EnKF and its variants have gained popularity in geophysical applications because they are relatively easy to implement, computationally tractable and robust, have a flow-dependent background error covariance, and their multivariate nature allows updates to state variables not directly observed. The covariance-based EnKF method by nature is not best suited for correcting model bias. However, through state augmentation the EnKF can also be used to jointly estimate the bias and the model state variables (e.g., Dee, 2005; Houtekamer and Zhang, 2016). Nevertheless, this thesis will not explore EnKF's potential of simultaneous bias correction but focus on its application in improving physical and/or biogeochemical ocean state estimation.

## **1.2 Objectives**

This thesis focuses on the two major anthropogenic stressors in the Gulf of Mexico—shelf water hypoxia and deep-sea oil spill pollution—with the overall goal to improve predictive capabilities of the effects of these anthropogenic stressors in the GOM. Steps taken toward this goal are: i) regional-scale numerical ecosystem modeling to investigate recurring bottom-water hypoxia on the shelf in the northern GOM, ii) implementation of the EnKF, which is first examined in an idealized upwelling model to explore the potential benefits of multivariate model updates, and iii) the application of this method to a realistic physical-hydrocarbon model for the GOM to assess if the characterization of mesoscale circulation features and the movement of a simulated deep-water oil plume are improved through DA.

The specific objectives of this thesis work, which are organized into the four following chapters, are as follows:

*1. Identify the primary processes controlling oxygen dynamics and hypoxia in the northern GOM. (Chapter 2)*

The shelf in the northern GOM receives large amounts of freshwater and nutrients from the Mississippi and Atchafalaya Rivers. These river inputs contribute to widespread bottom-water hypoxia on the shelf every summer. Understanding the causes of the seasonal hypoxia and designing effective nutrient management strategy requires quantitative knowledge of the mechanisms controlling dissolved oxygen (DO) dynamics. Generally, the distribution of DO is determined by physical processes (air-sea flux, horizontal advection, vertical mixing across the pycnocline) and biogeochemical processes (photosynthetic production, respiration in the water column and sediments, and oxidation of reduced substances). To constrain the magnitudes and spatial and temporal dynamics of these processes I conducted a comprehensive model-data comparison between a realistic three-dimensional (3D) physical-biogeochemical model that explicitly simulates oxygen sources and sinks on the shelf, and then used the validated model to identify the key mechanisms controlling oxygen dynamics and hypoxia development.

*2. Develop a relatively simple oxygen model to examine the physical controls on hypoxia generation in the northern GOM. (Chapter 3)*

Models with different complexities, ranging from statistical to fully coupled physical-biogeochemical models, have been developed to understand mechanisms controlling hypoxia formation on the northern GOM shelf. While statistical models are simple and instructive, they can only demonstrate correlation not causation. Fully coupled physical-biogeochemical models like the one used in Chapter 2 can mechanistically elucidate the complex interactions of physical and biological processes, but they can be difficult to calibrate and their results are sometimes difficult to interpret. The objective of this chapter is to assess whether an intermediate approach, coupling a simple oxygen model (which parameterizes biological oxygen terms using empirical relationships

derived from observations) with the realistic circulation model used in Chapter 2, can skillfully simulate hypoxic conditions on the LA shelf. After demonstrating that the model reproduces the observed variability of dissolved oxygen and hypoxia on the shelf, I use it to evaluate the role of physical forcing factors (river discharge, wind speed, and the seasonal shift in wind direction) in hypoxia formation.

*3. Investigate the potential benefits of multivariate EnKF updates of physical and biogeochemical ocean state variables. (Chapter 4)*

Effective data assimilation methods for incorporating observations into marine biogeochemical models are required to improve hindcasts, nowcasts and forecasts of the ocean's biogeochemical state. Recent assimilation efforts have shown that updating model physics alone can degrade biogeochemical fields while only updating biogeochemical variables may not improve a model's predictive skill when the physical fields are inaccurate. This chapter aims to systematically investigate whether multivariate EnKF updates of physical and biogeochemical model states, taking advantage of the inherently multivariate nature of the EnKF, can outperform isolated updates of either physical or biogeochemical variables. Towards that aim, a series of twin experiments is conducted in an idealized model of upwelling to test the performance of different strategies for assimilating different combinations of synthetic physical and biogeochemical observations.

*4. Apply EnKF to improve the simulation of circulation and movement of a deep-water hydrocarbon plume in the Gulf of Mexico. (Chapter 5)*

Accurate estimates of ocean circulation are essential for predicting transport of ocean biogeochemical constituents and pollutants, assessing environmental impacts, and managing accident response efforts. For example, the explosion and sinking of the offshore drilling rig Deepwater Horizon (DwH) in April 2010 resulted in the delivery of an unprecedented quantity of crude oil (4.9 million barrels) into the GOM. The frenzied response that followed clearly demonstrates the need for reliable circulation forecasts to aid in response and mitigation actions after such incidents. In this chapter, the EnKF implementation developed in Chapter 4 is applied to a 3D physical-

hydrocarbon model for the GOM. The skill of the data-assimilative system is rigorously assessed through fraternal and identical twin experiments as well as a realistic assimilation experiment for satellite and *in situ* profile observations. Through the twin experiments, the following three questions are addressed: i) what are the relative benefits of assimilating temperature and salinity profiles versus satellite data in improving the skill of different physical variables in the model? ii) does the assimilation system's skill in reproducing the satellite-observed dynamics of the LC and associated eddies in the GOM translate into skill in simulating the subsurface circulation? iii) does an improvement in circulation of the deep GOM lead to improved circulation near the DwH spill site and hence improved distribution of the deep-water hydrocarbon plume?

### 1.3 Outline

This thesis is organized into manuscripts where Chapters 2 to 4 contain the individual manuscripts published in peer-reviewed journals and Chapter 5 is to be submitted in the fall/winter of 2018.

In Chapter 2, a 3D physical-biogeochemical model that can explicitly simulate oxygen sources and sinks on the shelf in the northern GOM is presented and validated against available observations. The validated model is then used to analyze the summer dissolved oxygen balance for different regions to quantify the relative importance of the key controlling processes and examine how they vary in space.

In Chapter 3, a simple oxygen model, which parameterizes biological oxygen terms using empirical relationships derived from observations, is coupled to the same physical model used in Chapter 2. The coupled model is validated against available observations and outputs from the full biogeochemical model of Chapter 2, and then used to investigate the role of different physical forcing factors in hypoxia formation.

In Chapter 4, an idealized ocean model of upwelling for conducting twin experiments is described. The principles, implementation and configuration of the EnKF technique are detailed. The impacts of updating physical and biogeochemical model fields

individually versus simultaneously via different assimilation strategies on ocean ecosystem estimation and prediction are assessed through a series of twin experiments.

In Chapter 5, the EnKF-based data assimilative model for the GOM is described, validated through fraternal and identical twin experiments, and tested in a realistic configuration for assimilating satellite and profile observations.

The main conclusions of this thesis are given in Chapter 6.

## CHAPTER 2

# PRIMARY PROCESSES CONTROLLING OXYGEN DYNAMICS IN THE NORTHERN GULF OF MEXICO<sup>1</sup>

### 2.1 Introduction

The Louisiana shelf (LA shelf) in the northern Gulf of Mexico receives large inputs of freshwater, nutrients and organic matter from the Mississippi/Atchafalaya River system and experiences widespread hypoxia (oxygen concentrations  $< 2 \text{ mg l}^{-1}$  or  $62.5 \text{ mmol m}^{-3}$ ) in bottom waters every summer (Rabalais et al. 2007; Bianchi et al. 2010). Hypoxia stresses and can even lead to death of marine animals. The classic paradigm for explaining the recurring hypoxic conditions on the LA shelf is that high nutrient inputs from the river stimulate high rates of primary production in coastal waters; as this organic matter sinks below the pycnocline and is respired, dissolved oxygen (DO) becomes depleted due to a combination of high microbial respiration and low re-oxygenation of the bottom waters because of strong stratification (Rabalais et al. 2002).

While the statistical linkage between spring nutrient loads and the spatial extent of summer hypoxic area is well documented (Turner et al., 2005; Greene et al., 2009; Forrest et al., 2011), the distribution of hypoxia on the LA shelf is known to be the integrated result of various physical and biogeochemical processes that interact non-linearly (Bianchi et al. 2010; Fennel et al. 2011). Rowe and Chapman (2002) suggested that as the distance from the river mouth increases, the primary driver of hypoxia changes from deposition of riverine organic matter to biological production and respiration and finally to physical stratification. Model simulations (Bierman et al., 1994; Breed et al., 2004; Eldridge and Roelke 2010) also show that the dominant processes contributing to hypoxia change in the westward direction, namely allochthonous organic matter accounts for most of DO consumption near the Mississippi river mouth and autochthonous organic

---

<sup>1</sup>Based on: Yu, L., Fennel, K., Laurent, A., Murrell, M. C., and Lehrter, J. C. (2015) Numerical analysis of the primary processes controlling oxygen dynamics on the Louisiana shelf, *Biogeosciences*, 12, 2063-2076.

matter dominates DO consumption farther west. Hetland and DiMarco (2008) suggested that the differences in vertical stratification within the Mississippi and Atchafalaya River plumes lead to differences in the dominant type of respiration responsible for hypoxia with water column respiration driving hypoxia near the Mississippi River plume and benthic respiration controlling hypoxia near Atchafalaya Bay and further west. Recent work suggests that the main axis of variability in hydrography and metabolism is inshore to offshore on the shelf (Lehrter et al. 2012; Murrell et al., 2013a; Lehrter et al., 2013; Fry et al., 2014).

Understanding the causes of hypoxia on the LA shelf requires quantitative knowledge of the mechanisms controlling DO dynamics. Generally, the distribution of DO is determined by physical processes (air-sea flux, horizontal advection, vertical mixing across the pycnocline) and biogeochemical processes (photosynthetic production, respiration in the water column and sediments, and oxidation of reduced substances) (Testa and Kemp, 2011). The magnitudes and spatial and temporal dynamics of these processes on the LA shelf are as of now poorly constrained.

Circulation over the LA shelf displays two distinct modes (Cochrane and Kelly, 1986; Cho et al., 1998): an upcoast circulation mode during the dominantly upwelling-favorable (westerly) winds in summer (June to August) versus westward flow during the dominantly downwelling-favorable (easterly) winds for the rest of the year. Previous statistical studies (Forrest et al., 2011; Feng et al., 2012) have shown that the observed hypoxic extent is correlated to the duration of upwelling-favorable wind. Feng et al. (2014) further showed that the wind influences the distribution of low salinity, high chlorophyll water on the shelf and thereby the bottom water DO concentrations and hypoxic area.

A substantial fraction of phytoplankton production is observed below the pycnocline (Lehrter et al., 2009) and even at the sediment-water interface when light is available (Lehrter et al., 2014), but the effect of sub-pycnocline production on bottom water hypoxia is not well known. Eldridge and Morse (2008) highlighted the importance of benthic respiration as a DO sink at the beginning and end of hypoxic events, and suggested water column respiration in bottom water near the pycnocline as primary O<sub>2</sub>



sink once hypoxia has developed. Quinones-Rivera et al. (2007, 2010) estimated benthic respiration to account for ~73% of the total DO loss within 1 m of the bottom sediments during summer based on  $\delta^{18}O$  measurements and an isotope fractionation model, whereas Murrell and Lehrter (2011) found that benthic respiration only contributes on average  $20\pm 4\%$  of total respiration below the pycnocline. The relative contributions of benthic and water column respiration are strongly affected by the assumed depth of the bottom layer.

In order to better understand the relative importance of these processes, considerable efforts have been invested in modeling the DO dynamics and hypoxia within the system. These models range from relatively simple regression models (Turner et al., 2005, 2006; Greene et al., 2009; Forrest et al., 2011; Feng et al. 2012) to more complex process simulations that emphasize either biogeochemical processes in simplified physical frameworks (Justić et al. 1996, 2002; Eldridge and Morse, 2008; Green et al. 2008) or physical circulation using detailed hydrographic models with simple parameterizations of biogeochemical process (Hetland and DiMarco 2008; Lehrter et al., 2013). More recently a number of fully coupled physical-biogeochemical models have become available (Fennel et al. 2013; Laurent and Fennel 2014; Feng et al. 2014; Justić and Wang 2014).

Coupled models of DO dynamics and circulation have been used successfully in other coastal systems with seasonal hypoxia including Chesapeake Bay (i.e., Cerco and Cole, 1993; Cerco, 1995). More recently, Li et al. (2015) coupled an empirical DO model derived from observations with a high-resolution hydrodynamic model to derive a DO budget for Chesapeake Bay. An even simpler empirical DO parameterization was used by Scully (2013) to illustrate the important role of physical forcing in the formation of seasonal hypoxia. Both, Li et al. (2015) and Scully (2013) obtained a realistic simulation of the seasonal cycle of DO and spatial distributions of hypoxic water.

Here I use a coupled physical-biogeochemical model for the LA shelf described in Fennel et al. (2011, 2013) that was recently extended to include phosphate by Laurent et al. (2012) and Laurent and Fennel (2014). The biogeochemical model explicitly simulates

DO and is coupled to the realistic 3-dimensional circulation model of Hetland and DiMarco (Hetland and DiMarco 2008, Hetland et al. 2012). Here I build upon the earlier work to identify the key processes controlling DO dynamics.

The chapter is organized as follows. First I describe the coupled physical-biogeochemical model and its DO source and sink terms. Then I validate model-simulated DO and oxygen production and consumption rates against available observations. I explore spatial and temporal patterns of water column metabolism across the shelf and its interaction with air-sea fluxes. I also analyze the summer DO balance for different regions which allows me to identify the key controlling processes and how they vary in space. Finally, I examine the role that sub-pycnocline primary production plays in hypoxia generation.

## **2.2 Model Description**

The physical model is the Regional Ocean Modelling System (Haidvogel et al. 2008, ROMS, <http://myroms.org>) configured for the Mississippi/Atchafalaya outflow region as described in Hetland and DiMarco (2008, 2012). The model grid covers the Louisiana continental shelf with a horizontal resolution ranging from ~20 km in the southwestern corner to 1 km near the Mississippi Delta, and has 20 terrain-following vertical layers with increased resolution near the surface and bottom (Fig. 2.1). The model uses a fourth-order horizontal advection scheme for tracers and a third-order upwind scheme for the advection term in the momentum equation. Vertical gradients are calculated with conservative parabolic splines, and vertical mixing is parameterized using the Mellor and Yamada (1982) turbulent closure scheme. An average profile of temperature and salinity, based on historical hydrographic data (Boyer et al., 2006) and assumed to be horizontally uniform, is used as physical boundary condition. At the three open boundaries, gradient conditions are used for the free surface, radiation conditions for the three-dimensional velocities, and a Flather (1976) condition with no mean barotropic background flow for the two-dimensional velocities. The model is forced with 3-hourly winds from the NCEP North American Regional Reanalysis (NARR) and climatological surface heat and freshwater fluxes from da Silva et al. (1994a, b). Freshwater inputs from

the Mississippi and Atchafalaya rivers are based on daily measurements of transport by the US Army Corps of Engineers at Tarbert Landing and Simmesport, respectively.

The physical model realistically captures the two distinct modes of circulation over the LA shelf: an upcoast circulation mode during the dominantly upwelling-favorable (westerly) winds in summer (June to August) versus westward flow during the dominantly downwelling-favorable (easterly) winds for the rest of the year (Hetland and DiMarco, 2008). The skill assessment by Hetland and DiMarco (2012) shows that the physical model is able to faithfully reproduce the observed broad-scale features and seasonal patterns of the Mississippi/Atchafalaya River plume system and hence can be considered a reasonable hydrodynamic foundation for regional biogeochemical models.

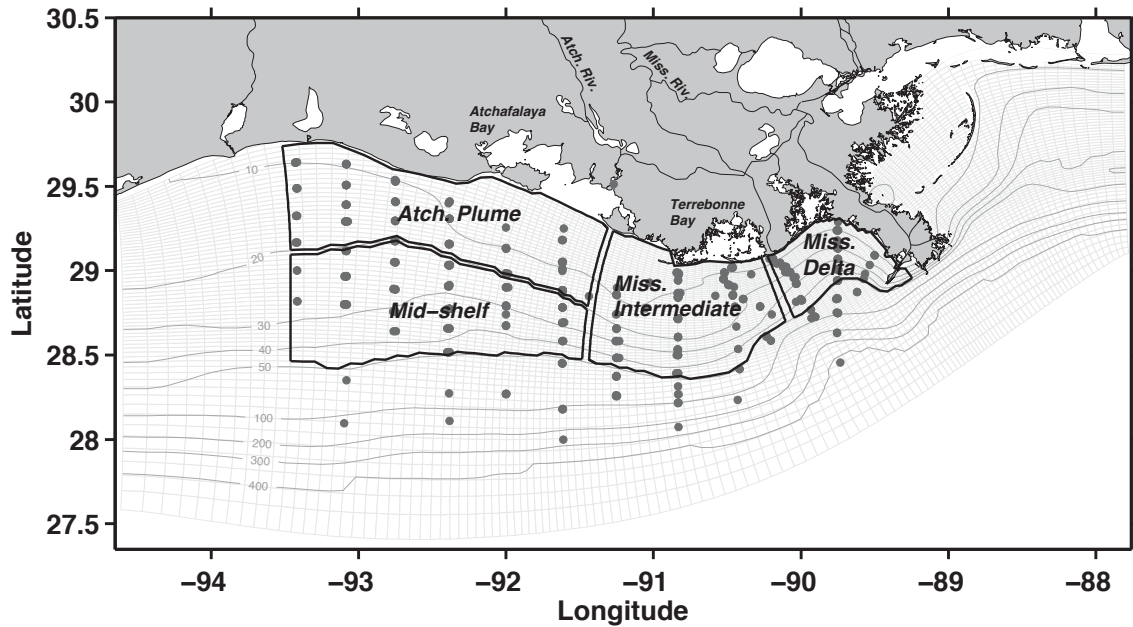


**Fig. 2.1.** Model grid (light grey lines) and bathymetry (in meters). The black lines delineate areas used during model analysis and are referred to as Mississippi Delta, Mississippi Intermediate, Atchafalaya Plume and Mid-shelf region in the text. The black dots are stations where primary production (Lehrter et al. 2009) and respiration rates (Murrell et al. 2013) were collected.

The biological component of the model uses the nitrogen cycle model of Fennel et al. (2011, 2013) but was extended to include phosphate (Laurent et al., 2012) and river dissolved organic matter as additional state variables. The model is a relatively simple representation of the pelagic nitrogen (N) cycle, including two species of dissolved inorganic N, nitrate ( $\text{NO}_3$ ) and ammonium ( $\text{NH}_4$ ), phosphorus ( $\text{PO}_4$ ), one phytoplankton group (Phy), chlorophyll (Chl) as a separate state variable to allow for photoacclimation, one zooplankton group (Zoo), two pools of detritus representing large, fast-sinking particles (LDet), and suspended, small particles (SDet), and river-born dissolved organic matter (RDOM). Combined with the freshwater discharge described above, the model receives river nutrients ( $\text{NO}_3$  and  $\text{NH}_4$ ) and organic matter based on the US Geological Survey (USGS) estimates (<http://toxics.usgs.gov/>). More specifically, river dissolved organic nitrogen (DON) was determined as the difference between filtered Total Kjeldahl Nitrogen (TKN) and  $\text{NH}_4$ ; and particulate organic nitrogen (PON) was defined as the difference between unfiltered and filtered TKN (Fig. 2.2). Different from the previously published simulations of this coupled model where river organic nitrogen enters the pool of SDet in the model without distinguishing between dissolved and particulate fractions, here river DON and PON enter the pools of RDOM and SDet, respectively. The only biological term in the equation for RDOM is remineralization to  $\text{NH}_4$  in the water column. I chose a remineralization rate of  $0.03 \text{ d}^{-1}$  for RDOM, an order of magnitude lower than that of small detritus ( $0.3 \text{ d}^{-1}$ ) to reflect the observation that riverine dissolved organic matter is less labile than phytoplankton-derived organic matter (Shen et al., 2012).

A schematic of the extended N cycle model is shown in Figure 2.3. Also shown are the biological sources and sinks of DO, including photosynthetic production, nitrification, respiration in water column and sediment, and the air-sea flux of oxygen across the air-sea interface. At the open boundaries  $\text{NO}_3$ ,  $\text{PO}_4$  and oxygen were prescribed using the NODC World Ocean Atlas. All other biological state variables at the boundary were set to small positive values. Model parameterization and previous validations were described in Fennel et al. (2006, 2011, 2013), Laurent et al. (2012), Laurent and Fennel (2014). For completeness' sake, all parameter values are given in Table B1 of the Appendix B.

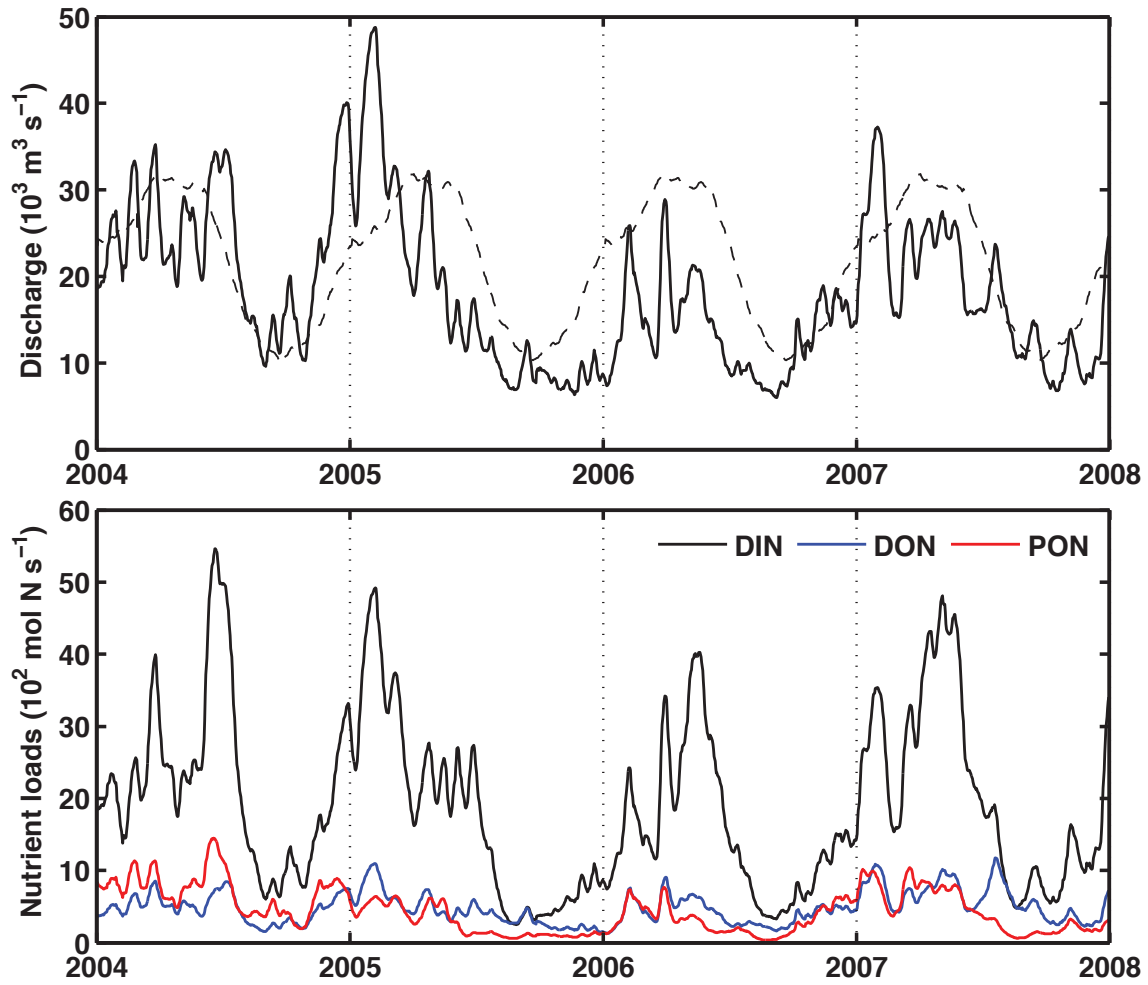


**Fig. 2.2.** Mississippi and Atchafalaya River freshwater discharge (upper panel) and nutrient loads (lower panel) in 2004-2007. The dash line indicates the long-term climatology (1983-2010).

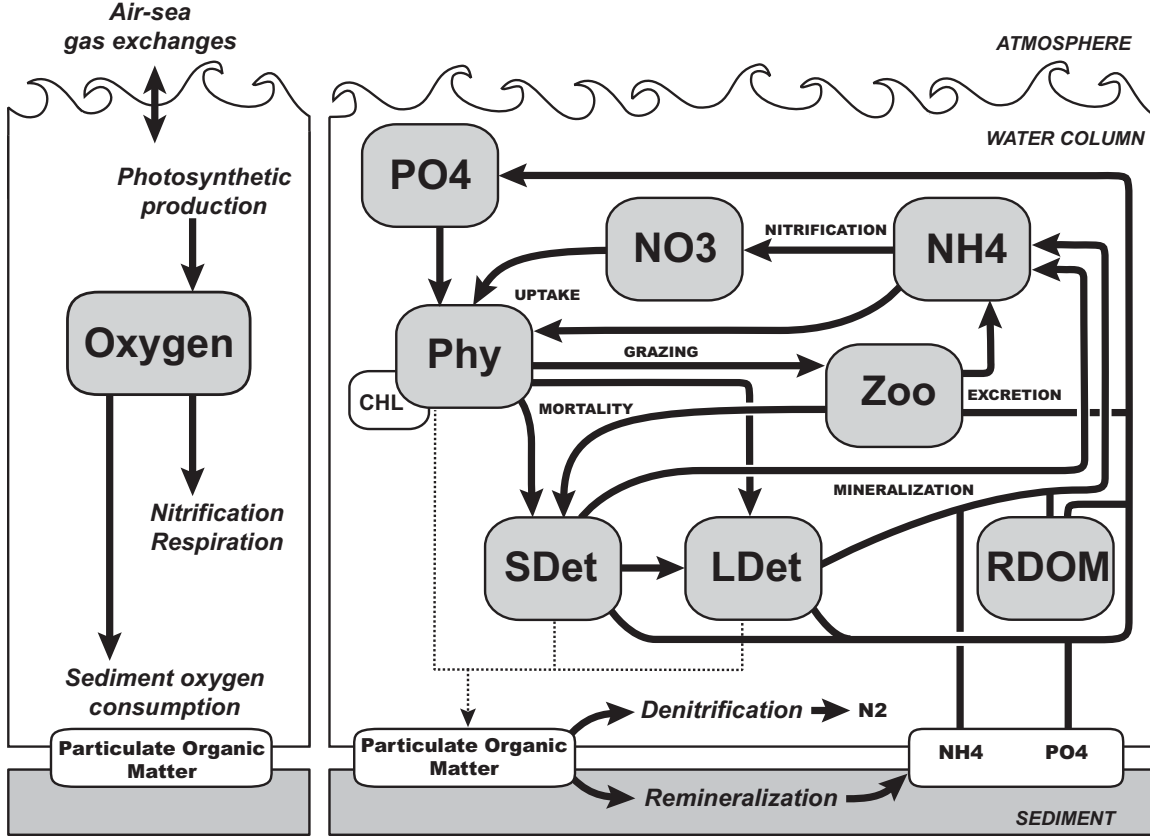


**Fig. 2.3.** Schematic of the biological model.

The equation for the evolution of  $DO$  is given by

$$\frac{\partial DO}{\partial t} = -\left(u \frac{\partial DO}{\partial x} + v \frac{\partial DO}{\partial y} + w \frac{\partial DO}{\partial z}\right) + \frac{\partial}{\partial z} \left(K_v \frac{\partial DO}{\partial z}\right) + PP + WR + F_{bf} \quad (2.1)$$

where  $x$  and  $y$  represent the two horizontal coordinates and  $z$  the vertical coordinate,  $u$ ,  $v$ , and  $w$  ( $\text{m s}^{-1}$ ) represent velocity components in  $x$ -,  $y$ -, and  $z$ -coordinates, respectively, and  $K_v$  is the vertical diffusivity ( $\text{m s}^{-2}$ ). On the right-hand side of the Eq. (2.1), the first term represents horizontal and vertical advection of  $DO$ , and the second term is the vertical diffusion of  $DO$  (horizontal diffusivity  $K_H$  is set 0 in the model and hence I neglected horizontal diffusion terms in equation 2.1). Here the advection and diffusion terms are computed using the advanced numerical schemes built into the ROMS hydrodynamic model. The term  $PP$  is the primary production and  $WR$  represents the sum of water column respiration and nitrification. Although not strictly accurate, the use of the terminology  $WR$  is consistent with the use of  $WR$  in the observational literature where

measurements of water column oxygen consumption include the contribution of nitrification. The term  $F_{bf}$  represents the boundary oxygen fluxes, namely the air-sea flux of oxygen at the top layer and the sediment oxygen consumption at the bottom layer, the parameterizations of which are detailed below.

Following Fennel et al. (2013), an air-sea flux of oxygen ( $F_{air-sea}$ , in units of  $\text{mmol O}_2 \text{ m}^{-2} \text{ d}^{-1}$ ) is prescribed in the top layer of the model as:

$$F_{air-sea} = \frac{vk_{O_2}}{\Delta z} (DO_{sat} - DO), \quad (2.2)$$

where  $DO$  and  $DO_{sat}$  are the oxygen concentration and concentration at saturation, respectively,  $\Delta z$  is the thickness of the respective surface grid box, and  $vk_{O_2}$  is the gas exchange coefficient for oxygen based on Wanninkhof (1992), such that:

$$vk_{O_2} = 0.31 u_{10}^2 \sqrt{\frac{660}{Sc_{Ox}}}, \quad (2.3)$$

where  $u_{10}$  is the wind speed at 10 m above the sea surface, and  $Sc_{Ox}$  is the Schmidt number, calculated as in Wanninkhof (1992).

The parameterization for Sediment Oxygen Consumption (SOC) used in this chapter was developed by Hetland and DiMarco (2008) and based on observed sediment oxygen fluxes from Rowe et al. (2002). In this parameterization, SOC ( $\text{mmol O}_2 \text{ m}^{-2} \text{ d}^{-1}$ ) linearly increases with increasing bottom water oxygen ( $DO$ ,  $\text{mmol O}_2 \text{ m}^{-3}$ ) for concentrations lower than about  $50 \text{ mmol O}_2 \text{ m}^{-3}$  and saturates when concentrations are higher than  $100 \text{ mmol O}_2 \text{ m}^{-3}$ . Also, SOC is dependent on temperature ( $T$ ,  $^{\circ}\text{C}$ ) such that it doubles for every  $10^{\circ}\text{C}$  temperature increase above  $0^{\circ}\text{C}$  (i.e.,  $Q_{10} = 2$ ). The equation is given as follows:

$$SOC = 6 [\text{mmol O}_2 \text{ m}^{-2} \text{ d}^{-1}] * 2^{T/10^{\circ}\text{C}} * (1 - \exp\left(-\frac{DO}{30[\text{mmol O}_2 \text{ m}^{-3}]}\right)). \quad (2.4)$$

In Fennel et al. (2013) this parameterization was extended to include an  $\text{NH}_4$  flux into the bottom water proportional to oxygen uptake by the sediments. Therefore, organic matter sinking out of the water column essentially leaves the system while empirically

determined fluxes of oxygen into the sediments and ammonium out of the sediments are prescribed.

Motivated by the model-data comparisons, described below, I conducted a sensitivity experiment where a spatially and temporally constant oxygen consumption rate ( $1.5 \text{ mmol O}_2 \text{ m}^{-3} \text{ d}^{-1}$ ) was added to the water column oxygen pool (simulation denoted as ‘Model+CCR’). In order to distinguish between the role of biological processes in the water column (primary production and water column respiration, denoted as PP and WR, respectively) and the combination of physical transport and sediment respiration, I conducted two further sensitivity experiments where all biological processes in the water column were turned off (denoted as ‘Model w/o PP and WR’ and ‘Model+CCR w/o PP and WR’ in comparison to the full model simulation and Model+CCR, respectively).

All simulations were run from 1 January 2004 to 31 December 2007. For model analysis I defined four geographical zones across the Louisiana continental shelf: three subregions associated with the Mississippi River plume (Mississippi Delta, Mississippi Intermediate, Mid-shelf), and another subregion associated with the Atchafalaya River plume (Atchafalaya Plume) (Fig. 2.1). These four subregions cover most stations that comprise the observational data sets used for model validation: (1) DO concentrations from Rabalais et al. (2007), Nunally et al. (2013), Murrell et al. (2013b), and the Mechanisms Controlling Hypoxia (MCH) program; (2) in situ measurements of water column respiration rates from 10 cruises during spring, summer and fall from 2003 to 2007 (Murrell et al., 2013a); (3) the concurrent measurements of phytoplankton production from Lehrter et al. (2009); (4) benthic flux measurements from Rowe et al. (2002), Murrell and Lehrter (2011), Lehrter et al. (2012), and McCarthy et al. (2013). Locations for the observed primary production and water column respiration rates are shown as black dots in Figure 2.1.



## 2.3 Results

### 2.3.1 Simulated oxygen dynamics and model validation

Time series of simulated and observed bottom DO both show a seasonal cycle reaching a maximum between December and February and minimum between July and August (Fig. 2.4). In summer the median of simulated bottom DO is consistently larger than observations in the Mississippi Intermediate region, but otherwise observations and simulation agree well. Simulated bottom DO falls within the observed range of variability for all 4 regions.

I report model bias and root mean square error (RMSE) as statistical measures of agreement between simulated and observed bottom DO in Table 2.1. Bias was calculated as model minus observations; thus a positive bias indicates that the model overestimates the observations. Table 2.1 indicates that the model overestimates the observed bottom DO in all regions with an average bias of 33.7 mmol O<sub>2</sub> m<sup>-3</sup>. Based on this comparison, the model performs best in the Mid-shelf region (bias of 15.6 mmol O<sub>2</sub> m<sup>-3</sup>) and worst in the Mississippi Delta region (bias of 43.3 mmol O<sub>2</sub> m<sup>-3</sup>).

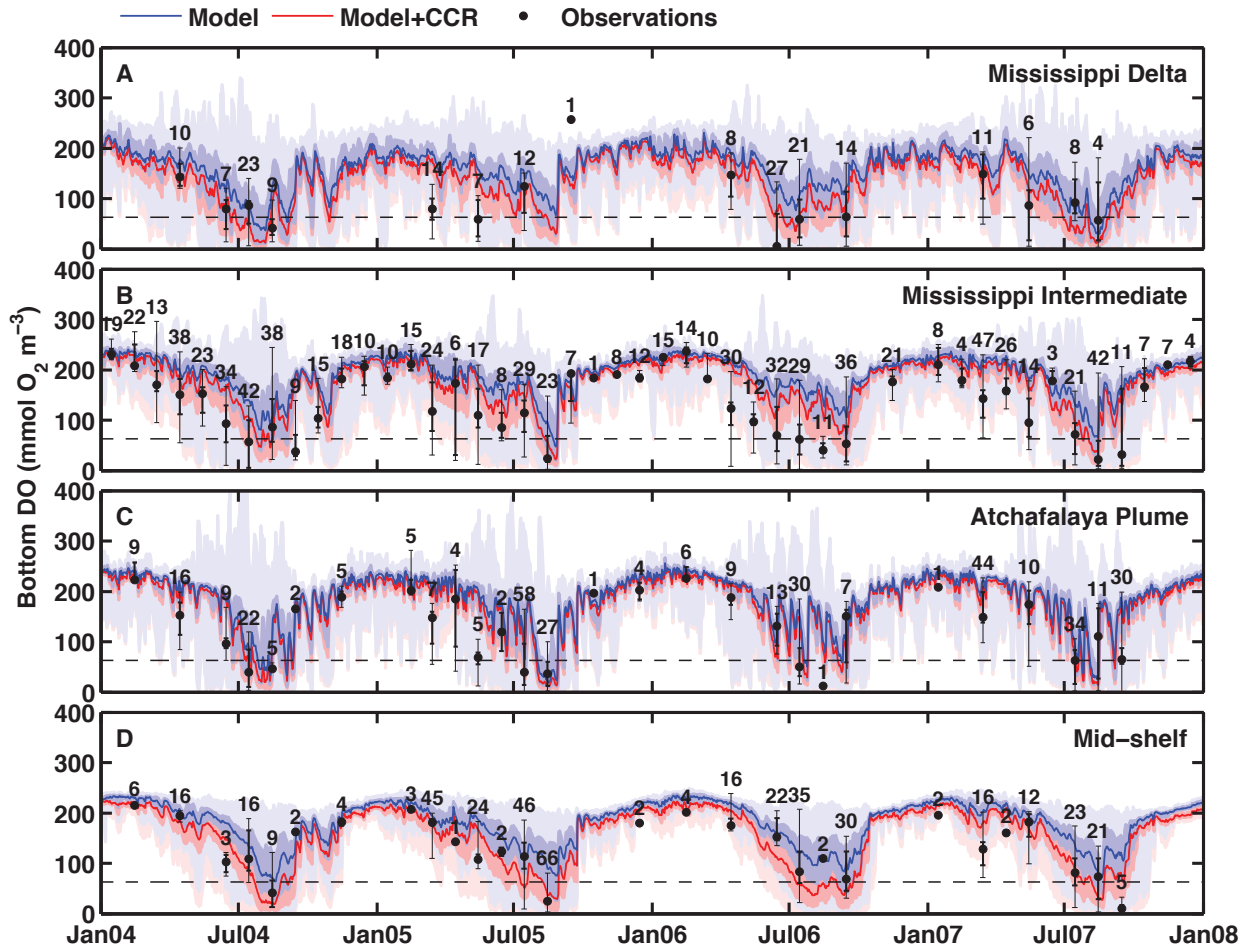


**Fig. 2.4.** Time series of simulated and observed dissolved oxygen concentration (DO) in bottom water in the Mississippi Delta, Mississippi Intermediate, Atchafalaya Plume and Mid-shelf regions. For the simulations, the medians are shown as solid lines (Model: blue line, Model+CCR: red line), the range between the 25th and 75th percentiles as dark blue/red area and the range between the minimum and maximum value as light blue/red area. For the observations, the medians of monthly binned observations are shown as black dots, the range between the 25th and 75th percentiles as thick vertical lines and the range between minimum and maximum values as thin vertical lines. The number of observations in each monthly bin is given above each maximum value. The dashed line indicates the hypoxia criterion of  $62.5 \text{ mmol O}_2 \text{ m}^{-3}$ . Observations are from Rabalais et al. (2007), Lehrter et al. (2009, 2012), Nunnally et al. (2012), Murrell et al. (2013b), and the MCH program.

**Table 2.1.** RMSE and bias (both in units of  $\text{mmol O}_2 \text{ m}^{-3}$ ) between simulated and observed bottom DO concentrations. Comparisons were conducted over the simulation period from 2004 to 2007 using all available observations. Bias was calculated as model minus observation. N is the number of observations available for each category.

	Model		Model+CCR		N
	RMSE	Bias	RMSE	Bias	
Mississippi Delta	74.6	43.3	61.6	15.6	182
Mississippi Intermediate	72.2	40.3	61.5	18.7	845
Atchafalaya Plume	66.3	35.0	58.7	16.6	377
Mid-shelf	48.9	15.6	54.0	-18.8	435
All data	66.4	33.7	59.3	9.1	1839

Profiles of bias between simulated and observed DO profiles are shown in Figure 2.5 for the summer months. Simulated DO often overestimates observed DO, but remains typically within one standard deviation of the observations except for the bottom layer (e.g. in June).

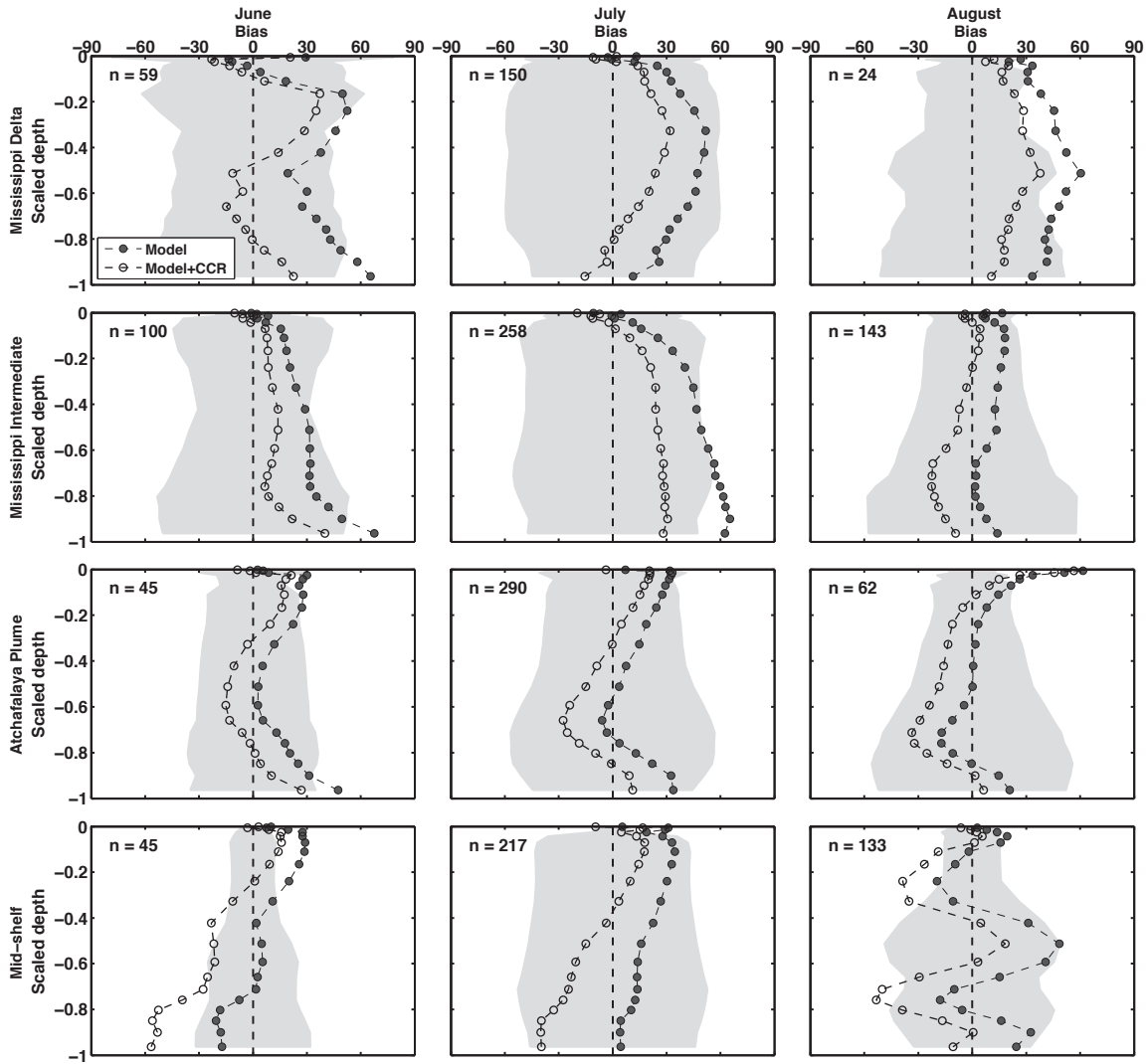


**Fig. 2.5.** Vertical profiles of model bias (model minus observations,  $\text{mmol O}_2 \text{ m}^{-3}$ ) in dissolved oxygen (DO) calculated from 2004 to 2007 for June to August in the 4 subregions. The vertical axis is the scaled depth, where 0 corresponds to the surface and -1 to the bottom. The light grey areas represent the standard deviation in the observations. Observations are from Rabalais et al. (2007), Lehrter et al. (2009, 2012), Murrell et al. (2013b), and the MCH program.

Observed and simulated rates of primary production (PP) and water column respiration (WR) are shown in Figure 2.6, and statistical measures of model-data agreement are given in Table 2.2. The model simulates the observed PP reasonably well, but underestimates the WR observations, although the model is within one standard deviation of the observations (Fig. 2.6 and Table 2.2).

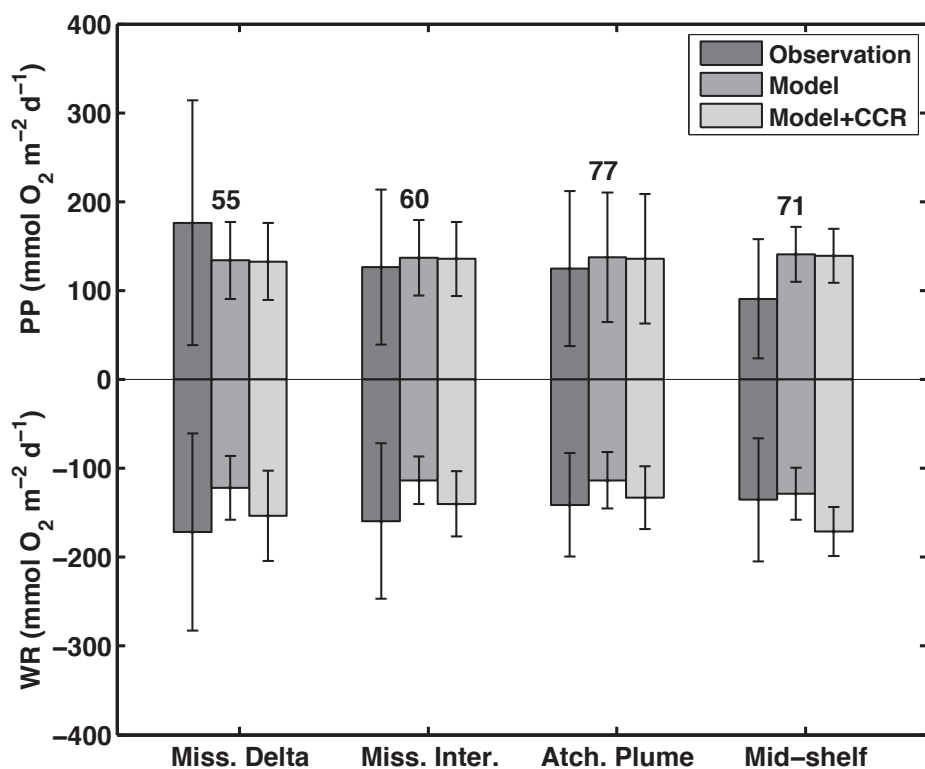


**Fig. 2.6.** Vertically integrated rates of observed and simulated primary production (upper panel) and water column respiration (lower panel) in the 4 subregions. The error bars indicate the standard deviation. The number of observations in each subregion is given above the error bars.

**Table 2.2.** RMSE and bias (both in units of  $\text{mmol O}_2 \text{ m}^{-2} \text{ d}^{-1}$ ) between simulated and observed primary production (PP) or water column respiration (WR). Comparisons were conducted over the simulation period from 2004 to 2007 using all available observations. Bias was calculated as model minus observations. N is the number of observations for each category.

	PP				WR				N
	Model		Model+CCR		Model		Model+CCR		
	RMSE	Bias	RMSE	Bias	RMSE	Bias	RMSE	Bias	
Miss. Delta	145.2	-42.3	145.5	-43.6	115.8	-49.4	104.4	-17.9	55
Miss. Inter.	94.7	10.5	95.0	9.2	93.3	-45.9	84.5	-19.4	60
Atch. Plume	114.1	12.5	114.0	11.2	62.6	-27.6	58.4	-8.2	77
Mid-shelf	91.8	50.2	91.1	48.4	75.8	-7.0	81.7	35.6	71
All data	112.0	10.8	112.0	9.3	86.5	-30.8	81.9	-1.0	263

Simulated SOC within all 4 regions is plotted against bottom DO and compared with available observations in Figure 2.7. Simulated SOC increases with increasing bottom DO for oxygen concentrations below  $\sim 80 \text{ mmol O}_2 \text{ m}^{-3}$  and declines thereafter because of the temperature effect (SOC halves for each temperature decrease of  $10^\circ\text{C}$ ). SOC observations from different sources vary over a large range from 0 to  $40 \text{ mmol O}_2 \text{ m}^{-2} \text{ d}^{-1}$  (Fig. 2.7). Simulated SOC is at the upper range of the available observations. Model bias in Table 2.3 indicates that the median of simulated SOC overestimates the observed SOC when combining all sources (average bias  $18.2 \text{ mmol O}_2 \text{ m}^{-2} \text{ d}^{-1}$ ).

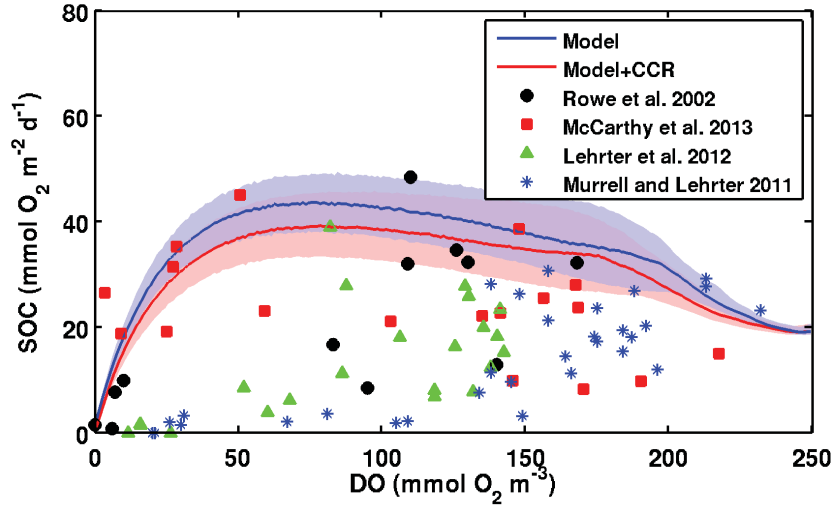


**Fig. 2.7.** Model simulated sediment oxygen consumption (SOC) versus bottom dissolved oxygen (DO) for the period 2004 to 2007, including the median (solid line) and the range between 25th and 75th percentiles (shaded area). Also shown for comparison are observations from Rowe et al. (2002), McCarthy (2013), Lehrter et al. (2012) and Murrell and Lehrter (2011).

**Table 2.3.** RMSE and bias (both in units of  $\text{mmol O}_2 \text{ m}^{-2} \text{ d}^{-1}$ ) between simulated median of sediment oxygen consumption (SOC) and observed SOC. The simulation period ranged from 2004 to 2007 while observations from different sources were collected during longer period from 1991 to 2011. Bias was calculated as model median minus observation with same bottom dissolved oxygen (DO) concentration. N is the number of observations available for each category.

	Model		Model+CCR		N
	RMSE	Bias	RMSE	Bias	
Rowe et al. 2012	15.9	11.1	13.6	8.0	12
McCarthy et al. 2013	15.8	10.2	13.9	7.0	18
Lehrter et al. 2012	26.1	24.6	22.4	20.7	22
Murrell and Lehrter 2011	24.7	21.2	21.7	18.1	31
All data	22.3	18.2	19.5	14.9	83

### 2.3.2 Validation of the Model+CCR simulation

The model biases described in previous section (i.e. the underestimation of WR and overestimation of SOC) motivated us to carry out an additional simulation

(Model+CCR) with increased WR. The additional, constant oxygen consumption rate ( $1.5 \text{ mmol O}_2 \text{ m}^{-3} \text{ d}^{-1}$ ) was determined from Table 2.2 (average bias of  $30.8 \text{ mmol O}_2 \text{ m}^{-2} \text{ d}^{-1}$  divided by the average water column depth of 20.4 m) and should compensate for the bias in model-simulated WR.

Compared with the previous model simulation, Model+CCR reduces the overall model data discrepancy in WR (average bias of  $-1.0 \text{ mmol O}_2 \text{ m}^{-2} \text{ d}^{-1}$ ) but overestimates the observed WR in the Mid-shelf region (bias of  $35.6 \text{ mmol O}_2 \text{ m}^{-2} \text{ d}^{-1}$ ) (Fig. 2.6 and Table 2.2). The increased WR draws down the simulated DO concentrations, improving agreement between the observed and simulated bottom DO in all regions (average bias of  $9.1 \text{ mmol O}_2 \text{ m}^{-3}$ ) except in the Mid-shelf region where the observed bottom DO is significantly underestimated (bias of  $-18.8 \text{ mmol O}_2 \text{ m}^{-3}$ ) (Fig. 2.4 and Table 2.1). Compared to the previous simulation, the reduced DO concentrations throughout the water column in Model+CCR generally improve the model performance with lower biases, except for the Mid-shelf region in June and July (Fig. 2.5). The reduced bottom DO concentrations in Model+CCR also lead to a reduction in the simulated SOC (as SOC is dependent on bottom DO) and thereby slightly improve the agreement between simulated and observed SOC with lower RMSE and bias (average bias of  $14.9 \text{ mmol O}_2 \text{ m}^{-2} \text{ d}^{-1}$ ) (Fig. 2.7 and Table 2.3).

### **2.3.3 Oxygen balance**

In this section, I evaluate the DO balance for the summer period (June to August) for different regions of the LA shelf to identify the key processes controlling hypoxia. I focus the detailed analysis on the model simulation without additional WR; results from Model+CCR will be discussed at the end of the section. For simplicity, I am considering that oxygen consumption due to nitrification to be included in the respiration term, and not as a separate process for deriving the oxygen balance. Though I am referring to the sum of respiration and nitrification as WR, I recognize that nitrification is a chemoautotrophic process. While not strictly accurate, this is consistent with the use of WR in the observational literature where measurements of water column oxygen consumption include the contribution of nitrification.



I first explore the simulated seasonal and spatial patterns in water column metabolism across the shelf and its interaction with the air-sea flux of oxygen (Fig. 2.8). The Mississippi Delta and Atchafalaya Plume regions, which are directly impacted by the river, transit from autotrophy in June and July to heterotrophy for the rest of the year. The Mississippi Intermediate and Mid-shelf regions, however, are heterotrophic throughout the year. In terms of air-sea exchange, oxygen is outgassing during summer and taken up during the rest of the year in all subregions, corresponding to the seasonal pattern in water column metabolism (more heterotrophic in winter and less heterotrophic or autotrophic in summer) and the seasonal cycle of surface water temperatures, which affect oxygen solubility contributing to outgassing in summer and uptake in winter. The oxygen flux into the ocean increases with the degree of heterotrophy, demonstrating the important role of air-sea gas exchange in replenishing DO in the water column.

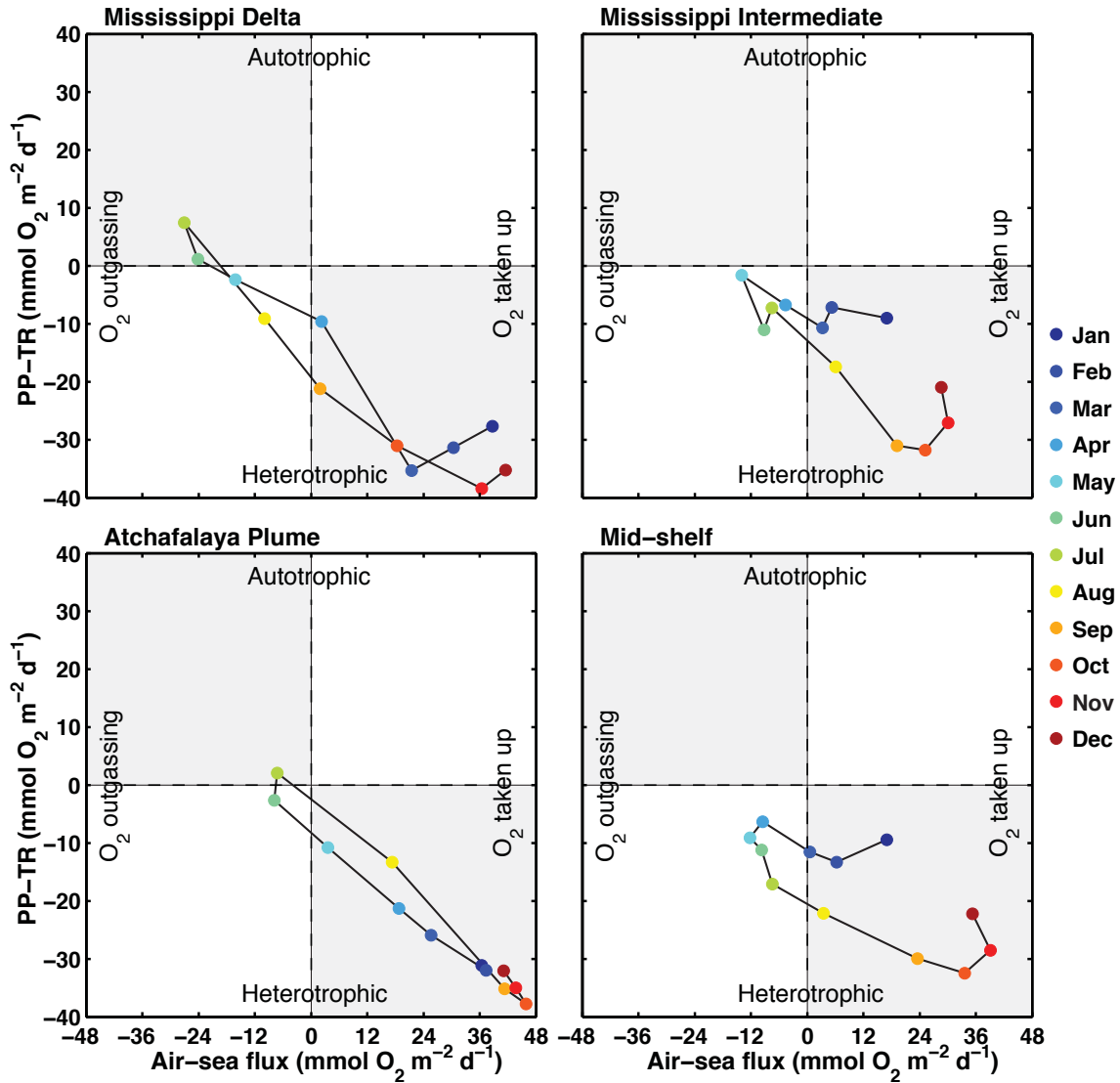


**Fig. 2.8.** Simulated net community production (PP-TR) versus air-sea flux of oxygen for the 4 subregions. The colored dots represent monthly means averaged over 2004 to 2007. Positive air-sea flux indicates oxygen is taken by water whereas negative air-sea flux indicates oxygen outgasses. Positive (PP-TR) suggests autotrophic whereas negative (PP-TR) suggests heterotrophic. Standard deviations of the air-sea flux in different months and subregions range widely from 13 to 58  $\text{mmol O}_2 \text{ m}^{-2} \text{ d}^{-1}$  and standard deviation of (PP-TR) range from 12 to 63  $\text{mmol O}_2 \text{ m}^{-2} \text{ d}^{-1}$ , both of which are higher in Mississippi Delta and Atchafalaya Plume and lower in the other two regions.

When considering an oxygen balance for the water column it is useful to distinguish distinct vertical layers. I considered the following three layers in my analysis of the summer oxygen balance: a surface layer above the main pycnocline, a mid-layer

extending from the main pycnocline to 5 m above the sediment and a 5-m thick bottom layer above the sediment (i.e., the layer where hypoxia occurs most frequently, as demonstrated in Figure 6 in Fennel et al., 2013). I defined the pycnocline as the depth of maximum Brunt-Vaisala Frequency (Pond and Pickard, 1983) and restricted my analysis to horizontal grid cells where all three layers existed (i.e. a main pycnocline was present and was more than 5 m above the bottom). I then integrated the terms in Eq. (2.1) vertically over each layer at each desired grid cell on each desired day. The advection and diffusion terms were evaluated as divergences, namely fluxes of DO into or out of the given volume through advection or diffusion. Finally I averaged the integrated results over all grid cells within a selected subregion and over June to August in order to obtain the summer oxygen balance for the subregion.

Figure 2.9 shows the summer oxygen balance in the three layers and four subregions (numbers are provided in Table B2 of the Appendix B). The surface layers in all four subregions are autotrophic while the bottom layers are heterotrophic (Fig. 2.9). In the surface layer, biochemical processes (PP and WR) far exceed physical transport of oxygen. The positive net community production and decreasing oxygen solubility associated with the increasing water temperature in summer lead to oxygen outgassing to the atmosphere and net transport of oxygen downward to deeper waters.

The mid-layer is autotrophic in all four subregions as well, with an average PP of 48% occurring below the pycnocline and 38% in the mid-layer. About 10% of PP occurs within the 5-m bottom layer where hypoxia occurs most frequently (Fig. 2.9). I compared the simulation results with observations from Lehrter et al. (2009), as percentage of production below the pycnocline for each cruise (Table 4). Considering the rather large observed standard deviations, the percentages of sub-pycnocline PP in the simulations (18.6 - 40.9%) agree well with observations (23.3 - 38.7%).

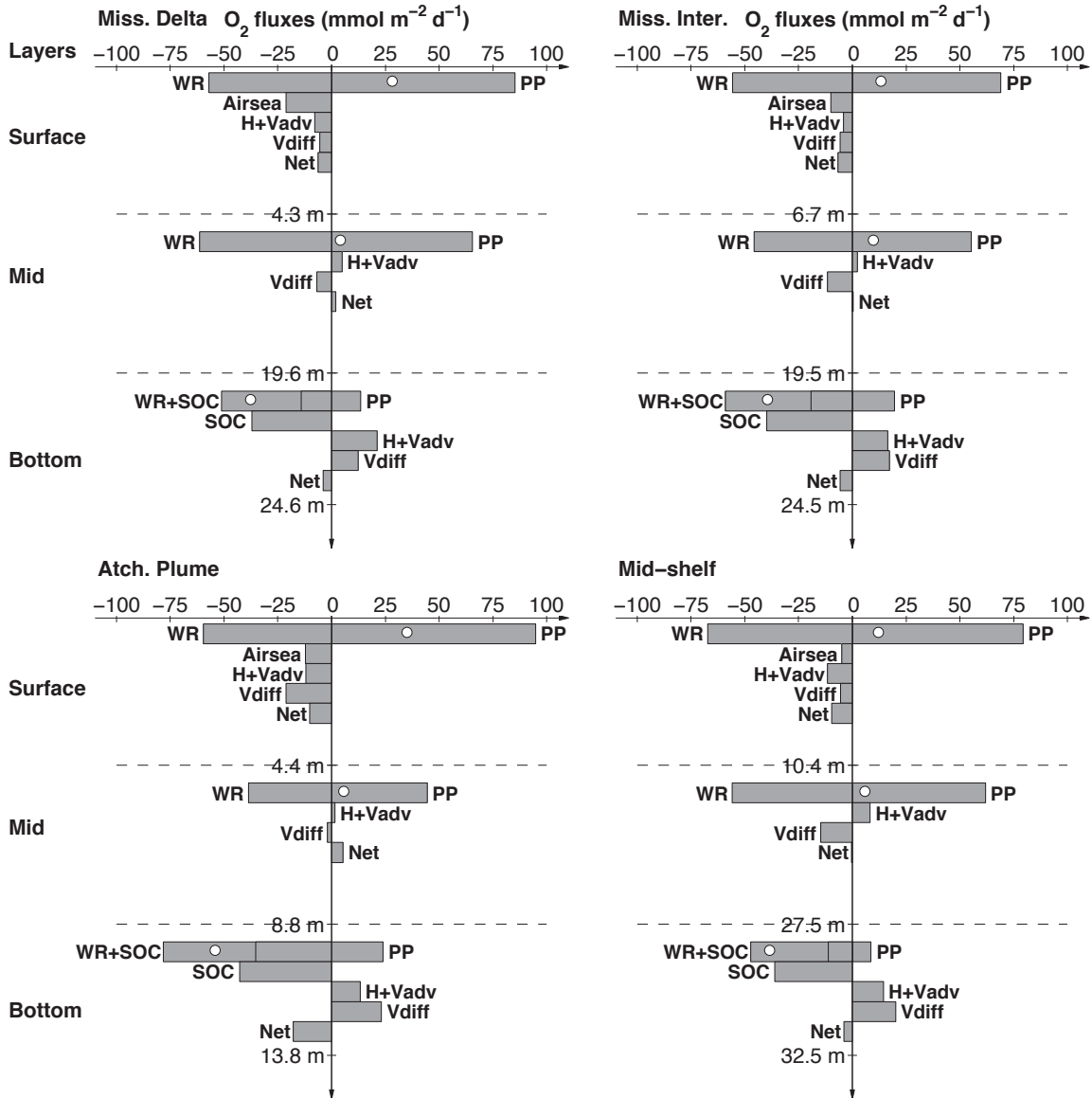


**Fig. 2.9.** Simulated 4-year (2004-2007) mean oxygen balance in summer for the 4 subregions. Oxygen source and sink terms are given for the surface layer above the pycnocline, for the mid layer and for the 5-m thick bottom layer. The average depth of the pycnocline, depth at 5 m above bottom and the average water column depth are indicated for each subregion. The open circles indicate the balance of primary production (PP) and respiration+nitrification (WR) in each layer. For the bottom layer, the bars for respiration+nitrification (WR) and sediment oxygen consumption (SOC) are shown stacked and SOC is repeated separately. The net rate of oxygen change in each layer (i.e. the sum of all oxygen source and sink terms) is given and denoted as Net.

**Table 2.4.** Shelf-wide average observed and simulated percentage of primary production below the pycnocline (mean±standard deviation). N is the number of observations.

Cruise	N	Percentage of PP below pycnocline (%)	
		Observation	Simulation
Mar 2005	24	23.3±29.4	27.8±26.9
Apr 2006	31	35.3±30.0	23.4±25.2
Jun 2006	54	29.3±25.7	18.6±19.2
Sep 2006	71	38.7±25.7	39.4±28.2
May 2007	64	25.8±25.0	36.2±29.6
Aug 2007	60	24.7±23.3	40.9±30.9
RMSE			42.5
Bias			2.8
N			304

On average the sub-pycnocline PP offsets 68% of total respiration below the pycnocline and 27% of total respiration within the 5-m bottom layer (Fig. 2.9). The percentages are higher in 2006 (a drought year) where PP offsets 72% of total respiration below pycnocline and 31% of total respiration within the bottom 5 m.

The 5-m bottom layer is heterotrophic in all subregions with SOC representing the single largest oxygen flux (Fig. 2.9). The SOC accounts for 36% of total respiratory oxygen demand below the pycnocline when averaged over the shelf and summer months. The fraction of SOC rises to 68% when limited to the bottom 5 m (Fig. 2.9). Driven by the strong vertical DO gradient in the water column, vertical diffusion is the primary mode of DO replenishment for the bottom layer offsetting on average 32% of total respiration over the shelf. Advection, driven by the typical summer upwelling circulation on the LA shelf, is another important DO source for bottom waters offsetting on average 29% of total respiration shelf-wide.

Adding WR in the Model+CCR simulation impacted the summer oxygen balance by making the water column more heterotrophic and decreasing the relative contributions

of SOC and WR to total respiration (Table B3 and Fig. B3). In Model+CCR the mid layers in all subregions and all three layers in Mid-shelf region become heterotrophic in summer months. Also, the simulated fraction of SOC to total respiration averaged over the 4 subregions during summer decreases from 36% to 26% within below-pycnocline water layer and from 68% to 57% within the bottom 5-m layer.

#### **2.3.4 Role of sub-pycnocline PP in hypoxia generation**

Time series of simulated hypoxic area from the sensitivity run without biological processes in the water column (Model w/o PP and WR) are shown in comparison to the full model and the observed hypoxic extent in Figure 2.10. The temporal evolution of hypoxic area is almost identical in both simulations, with ‘Model w/o PP and WR’ simulating an only slightly larger hypoxic area in summer. A similar pattern is observed for simulated hypoxic volume (Fig. B1) and for the simulations with the additional oxygen sink (Fig. B4).

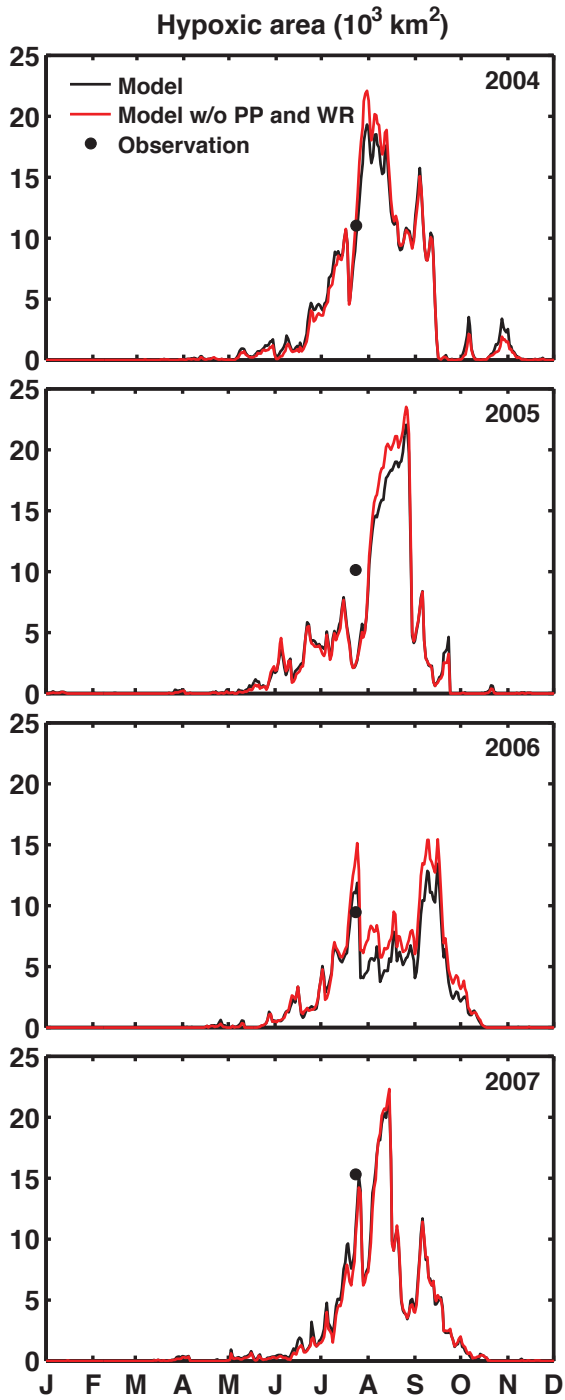


**Fig. 2.10.** Time series of simulated hypoxic extent for the full model (black line) and the model without biological processes in the water column (red line). Also shown is the observed hypoxic extent in late July (black dots). The observed hypoxic extent was estimated by linearly interpolating the observed oxygen concentrations onto the model grid and then calculating the area with oxygen concentrations below the hypoxic threshold (Fennel et al., 2013).

## 2.4 Discussion

### 2.4.1 Simulated oxygen dynamics and model validation

Overall, the model simulates the evolution of oxygen and the magnitudes and spatial distribution of PP well, but tends to overestimate bottom DO and underestimate WR (within one standard deviation of observations). One possible explanation is that the model does not receive any dissolved or particulate organic matter inputs from estuarine sources other than the Mississippi and Atchafalaya rivers. Several recent studies (Bianchi et al. 2010, Murrell et al. 2013a, and Fry et al. 2014) suggested that the inshore coastal waters represent a source of oxygen-consuming organic matter that may be episodically transported onto the LA shelf.

The model also overestimates the observed SOC from all sources, especially those observed by Lehrter et al. (2012) and Murrell and Lehrter (2011) (Fig. 2.7, Table 2.3). Using the same model as in this chapter, Fennel et al. (2013) have shown that generation of hypoxia on the LA shelf is very sensitive to the parameterization of SOC, primarily because the hypoxic conditions on the shelf are restricted to a relatively thin layer above the sediment. Fennel et al. (2013) have further shown that the SOC parameterization based on observations from Rowe et al. (2002), which is used in this chapter, performed best in simulating the observed hypoxic extent whereas parameterization based on lower SOC values from Murrell and Lehrter (2011) led to almost no hypoxia in this model. The apparent discrepancy between SOC observations and parameterizations used in mechanistic models remains to be reconciled. One explanation could be that empirical SOC measurements underestimate the true oxygen demand, because they do not account for accumulation of reduced metabolites of anaerobic metabolism (e.g.,  $\text{NH}_4^+$ ,  $\text{HS}^-$ ,  $\text{Fe}^{2+}$ ). Accumulation of anaerobic metabolites can be episodically important in scavenging oxygen, thus acting to maintain hypoxic conditions during periods when traditional SOC measurements suggest a small DO sink. This interpretation is supported by Lehrter et al. (2012) who found that DIC fluxes (a better measure of total oxygen demand) were relatively constant and insensitive to overlying DO concentration. Another explanation could be that the thickness of the simulated bottom boundary layer is overestimated. If



this is the case, SOC would have to be larger than in reality in order to produce hypoxic bottom water. Future work on validating the expression and dynamics of the bottom boundary layer and its effect on hypoxia dynamics will address this question.

The SOC parameterization has the inherent limitation that it does not account for spatial variability in the supply of particulate organic matter reaching the sediment. An alternative model, where SOC varies responsive to the amount of organic matter sinking to the sediment (Fennel et al. 2011, 2013), simulated essentially identical results as presented here. While the SOC parameterization used here is simple, it does include two key parameters known to modulate SOC: temperature and dissolved oxygen.

In order to assess the effects of the model biases in WR I conducted a sensitivity experiment where an additional, constant oxygen consumption rate was applied to the water column DO based on observed WR rates from Murrell et al. (2013a). This generally improves the comparisons among measured and simulated WR, bottom water DO and SOC except in the Mid-shelf region where WR is overestimated and bottom DO is underestimated. The increased WR and slightly decreased SOC in the Model+CCR simulation also reduce the SOC fraction of total respiratory oxygen demand.

#### **2.4.2 Primary processes controlling oxygen dynamics**

The simulated seasonal transition from autotrophy to heterotrophy in the Mississippi Delta and Atchafalaya Plume regions has previously been reported in mesohaline waters (salinity: 15-29) in the Mississippi River plume (Breed et al., 2004). The Mississippi Intermediate and Mid-shelf regions were heterotrophic throughout the year, implying a net import of organic carbon. This result is consistent with the observations of Murrell et al. (2013a) who found net heterotrophy on the western shelf and in deeper waters of the LA shelf. A more recent study by Fry et al. (2014) also suggested that the autotrophic near-river and nearshore areas could be net source regions of carbon fueling hypoxia in adjacent mid-shelf waters.

Despite the heterotrophy, the main sink for oxygen is outgassing in the Mississippi Intermediate and Mid-shelf regions during the summer hypoxic season. This result is

consistent with frequent observations of supersaturated DO concentrations in surface plume waters, particularly in the Louisiana Bight region (Murrell et al. 2013b). The simultaneous occurrence of heterotrophy and outgassing of oxygen is primarily due to density stratification of the water column, which isolates the autotrophic upper waters that actively exchange oxygen with the atmosphere from the heterotrophic waters below. As shown in the summer DO balance (Fig. 2.9), the surface layers above the pycnocline were autotrophic in all subregions, driving outgassing of oxygen to the atmosphere despite the whole water column being heterotrophic. The decreased oxygen solubility of warmer waters typical of summer conditions also promotes outgassing, but the effect is relatively small compared to the autotrophy in surface waters (oxygen gas-exchange is fast and the summer change in water temperature is relatively small on the LA shelf). I have carried out sensitivity experiments where I doubled and halved the air-sea gas exchange coefficient (results not presented in the manuscript) and found that the model results are insensitive to the air-sea gas exchange rates, likely because the air-sea oxygen flux is fast.

It has previously been demonstrated, based on observations, that a strong near-surface pycnocline is a prerequisite for hypoxia on the LA shelf, while a weaker, near-bottom pycnocline determines the hypoxic layer that actually forms (Wiseman et al., 1997). This was confirmed by model simulations (Fennel et al., 2013), which show that hypoxia is constrained to a thin layer above the sediment over large parts of the shelf. A more recent retrospective analysis of data collected during shelf-wide sampling cruises reported that the 27-year (1985-2011) average thickness of the bottom hypoxic layer is 3.9 m and that there was an increasing trend in hypoxic layer thickness from 1985 to 2011 (Obenour et al., 2013).

Consistent with observations by Lehrter et al. (2009), the model demonstrated that a large fraction of PP occurred below the pycnocline and even within bottom 5-m water (Fig. 2.9, Table 2.4). This is presumably because the euphotic zone extends well below the pycnocline and sometimes to the bottom on the LA shelf (Chen et al., 2000; Lehrter et al., 2009). Lehrter et al. (2009) also observed that the euphotic zone in non-plume areas (salinity > 31) is deeper than in plume areas, and that the average shelf-wide light attenuation strongly correlates with freshwater discharge from the Mississippi and

Atchafalaya rivers. In agreement with these observations, the simulated percentage of sub-pycnocline PP is higher in the Mississippi Intermediate region (52% below the pycnocline and 13.6% in the 5-m bottom layer) than in the Delta region (48% and 8.3%, respectively), and higher throughout the shelf in 2006 (a drought year with low freshwater discharge) than in average over the 4 years simulated (52% compared to 48%).

The importance of physical transport in replenishing bottom-water DO pools has been found in other coastal systems with seasonal hypoxia including Chesapeake Bay, where Kemp et al. (1992) estimated that in summer the vertical oxygen flux across the pycnocline and the net longitudinal oxygen exchange offset ~55% and ~38% of total respiration below the pycnocline, respectively. More recent modeling work by Li et al. (2015) estimated that vertical diffusion and net advective fluxes respectively offset ~27% and ~64% of total respiration in the bottom 10 m during summer. Kemp et al. (1992) also showed that increased biological consumption of DO in bottom waters of Chesapeake Bay increases horizontal and vertical DO gradients and thereby increases physical transport of DO to the bottom waters during March to July. On the LA shelf the occasional occurrence of tropical storms and hurricanes can rapidly erode stratification and replenish bottom waters with DO. The lateral advection of oxygenated water from adjacent deep basins during upwelling-favorable wind conditions can also increase bottom-water DO on the LA shelf (Rabalais et al, 2007).

The result that SOC is the dominant oxygen sink in waters directly overlying the sediments (within 5 m above the bottom) is consistent with previous observational estimates for the LA shelf. Quinones-Rivera et al. (2007) estimated that SOC accounts for ~73% of the total DO loss within 1 m of the sediments during summer based on  $\delta^{18}\text{O}$  measurements and an isotope fractionation model. Since the isotope approach only provides relative fractions of sediment and water column respiration, I cannot directly compare SOC and WR from Quinones-Rivera et al. (2007) to my simulations. However, the simulated proportions of sediment respiration to total respiration (on average 36% below pycnocline and 68% in the 5-m bottom layer) are consistent with the estimates of Quinones-Rivera et al. (2007). Adding the additional DO sink decreased the proportions of SOC to total respiration (26% below the pycnocline and 57% in the 5-m bottom layer)

but did not change the model result that SOC is the dominant DO sink in the bottom 5 m, demonstrating the relative sensitivity of the model to the SOC parameterization used.

### **2.4.3 Role of sub-pycnocline PP in hypoxia generation**

The summer oxygen balance presented in the previous section suggests that physical transport processes and sediment respiration are major drivers of oxygen dynamics on the LA shelf, and that PP below the pycnocline may mitigate hypoxic conditions. However, in a sensitivity experiment where I disabled all biological processes in the water column the spatial extent of hypoxic bottom waters is only slightly reduced, suggesting that PP below the pycnocline has only a minor effect on hypoxia.

## **2.5 Summary**

In this chapter I used a physical-biogeochemical model to investigate the dynamics of dissolved oxygen and hypoxia on the LA shelf and to identify the key controlling processes. Comparisons with observations demonstrate that the model simulates the evolution of oxygen well but tends to overestimate bottom DO and SOC, and underestimates WR. When adding a constant oxygen consumption rate in the water column to correct the bias in WR rates, the model-simulated oxygen dynamics agree better with observations in all subregions except the Mid-shelf. This result suggests that organic matter from inshore waters may need to be included in future versions of the model.

Consistent with observations of Murrell et al. (2013a), the model simulation demonstrated that the LA shelf is essentially heterotrophic throughout the year except for the areas directly impacted by rivers during June and July. This implies a net import of organic carbon on the LA shelf. Air-sea gas exchange was the primary mode of replenishing the very heterotrophic waters in non-summer months with relatively strong mixing. However, in summer, stratification isolates the autotrophic surface from the heterotrophic lower waters. In the Mississippi Intermediate and Mid-shelf regions this isolation results in significant outgassing of oxygen across the air-sea interface despite a heterotrophic water column, exacerbating the risk of hypoxia in these regions.

In summer, the model indicates that a substantial fraction of primary production (~48%) occurs below the pycnocline and about 10% of primary production occurs within 5 m of the bottom where hypoxia forms most frequently. In a sensitivity experiment where biological processes in the water column (i.e. PP and WR) were turned off I demonstrate that the below-pycnocline PP mitigates hypoxia only slightly, and that physical processes and sediment oxygen consumption together largely determine the spatial extent and dynamics of hypoxia on the LA shelf.

## CHAPTER 3

# PHYSICAL CONTROLS ON HYPOXIA GENERATION IN THE NORTHERN GULF OF MEXICO<sup>2</sup>

### 3.1 Introduction

The Louisiana shelf (LA shelf) in the northern Gulf of Mexico receives large amounts of freshwater and nutrients from the Mississippi/Atchafalaya River System. The freshwater discharge enhances the vertical water column stratification in summer, limiting the oxygen supply to near-bottom waters from above (Wiseman et al., 1997). The nutrient inputs stimulate primary production, leading to high sedimentation fluxes of organic matter and significant microbial consumption of oxygen below the pycnocline. The combined effects of water column stratification and nutrient-enhanced primary production lead to the recurring development of near-bottom hypoxia (oxygen concentrations  $< 2 \text{ mg l}^{-1}$  or  $62.5 \text{ mmol m}^{-3}$ ) on the LA shelf every summer (Rabalais et al., 2007; Bianchi et al., 2010).

Retrospective analysis (Obenour et al., 2013) and statistical regression models (Forrest et al., 2011) show an increasing trend in the areal extent of hypoxia over the LA shelf from 1985 to 2011. It is generally accepted that this increase in hypoxic extent is mainly driven by rising anthropogenic nutrient inputs from the watershed. However, statistical regressions using nutrient load as the only independent variable do not explain the majority of inter-annual variability in hypoxia; when physical factors are included a much larger fraction of the variability can be explained (Forrest et al., 2011; Feng et al., 2012). Forrest et al. (2011) found that nitrogen load alone explains only 24% of the variability in observed hypoxic area (from 1985 to 2014) whereas including the east-west wind in addition to the nitrogen load explains 47% of the variability. Feng et al. (2012)

---

<sup>2</sup> Based on: Yu, L., Fennel, K. and Laurent, A. (2015) A modeling study of physical controls on hypoxia generation in the Northern Gulf of Mexico. *Journal of Geophysical Research-Oceans*, 120, 5019-5039.

demonstrated that for the 1985-2010 and 1993-2010 hurricane-exclusive periods, May-June nitrate load correlates with the observed hypoxic area at  $r^2 = 0.36$  and  $r^2 = 0.24$ , respectively. Including May-June nitrate load and the duration of upwelling favorable (eastward) wind improves the statistical relationships for both periods to  $r^2 = 0.69$  and  $r^2 = 0.74$ , respectively. A geostatistical modeling study by Obenour et al. (2012) suggests that both river nutrient concentration and stratification play substantial and comparable roles in the year-to-year variability of hypoxia in the northern Gulf of Mexico. A more recent mechanistic modeling study by Obenour et al. (2015) found that, while seasonal nutrient loading remains an important driver of hypoxia, stratification (presented as a function of river discharge, summer east-west wind velocity, and wind stress) contributes to a larger extent to the interannual variability in hypoxia than indicated in their previous empirical modeling study (Obenour et al., 2012), especially on the western LA shelf.

While the statistical modeling studies are instructive, they can only demonstrate correlation not causation. Coupled physical-biogeochemical models are important complements that help build mechanistic understanding of the processes underlying hypoxia development and variability (Fennel et al., 2011, 2013; Feng et al., 2013; Laurent and Fennel, 2014; Justić and Wang, 2014; Yu et al., 2015a). While the fully coupled physical-biogeochemical models can mechanistically elucidate the complex interactions of physical and biological processes, they can be difficult to calibrate and their results are sometimes difficult to interpret. An intermediate approach is to couple a detailed hydrodynamic model with a simple parameterization of biogeochemical processes. This approach has been used successfully in Chesapeake Bay where physical forces play an important role in the development of seasonal hypoxia. For example, Scully (2013) implemented a very simple empirical dissolved oxygen parameterization (assuming a constant oxygen consumption rate in the water column) in a three-dimensional circulation model to examine the role of physical forcing on hypoxia in Chesapeake Bay. Despite its simplicity, the model skillfully reproduces the observed variability of dissolved oxygen and hypoxic volume in the Bay.

Motivated by these previous studies, I assess whether very simple oxygen parameterizations coupled with the hydrodynamic model I have used in Chapter 2 can

simulate hypoxic conditions in the northern Gulf of Mexico. I find this to be the case and then use the simplified model to evaluate the role of different physical forcing factors in hypoxia formation, including river discharge, wind speed, and the seasonal shift in wind direction from upwelling-favorable in summer to downwelling-favorable during the rest of the year.

The chapter is organized as follows. In section 3.2 I describe the models used in this chapter including a validation of the simple oxygen models against available observations and outputs from the fully coupled physical-biogeochemical model. In section 3.3 I examine how variations in river discharge, wind speed and wind direction change the distribution of river plume, stratification and thereby the extent and geographic distribution of hypoxia. The main conclusions, given in section 3.5, are that the simple oxygen parameterization coupled with a realistic hydrodynamic model realistically simulates hypoxic conditions on the LA shelf, and that river discharge, wind speed and wind direction can all significantly influence the distribution of the river plume and stratification, and thereby the bottom oxygen concentrations and hypoxia development on the LA shelf. The ability of the simple oxygen model to closely reproduce the hypoxia evolution of the full biogeochemical model, and the determining role of physical processes in hypoxia generation suggest that a full biogeochemical model may not be necessary for short-term hypoxia forecasting on the LA shelf.

## **3.2 Methods**

### **3.2.1 Model description**

The physical model described in Chapter 2 is used here (Fig. 3.1). I implemented three relatively simple oxygen models with different prescriptions of oxygen sinks in the water column and sediment within the three-dimensional circulation model. All models use the same parameterization of air-sea gas exchange ( $F_{\text{air-sea}}$ , in units of  $\text{mmol O}_2 \text{ m}^{-2} \text{ d}^{-1}$ ) following Fennel et al. (2013) which acts on the top layer of the model:

$$F_{\text{air-sea}} = \frac{vk_{\text{O}_2}}{\Delta z} (DO_{\text{sat}} - DO). \quad (3.1)$$



Here  $DO$  and  $DO_{sat}$  are the oxygen concentration and concentration at saturation, respectively,  $\Delta z$  is the thickness of the respective surface grid box, and  $vk_{O_2}$  is the gas exchange coefficient for oxygen based on Wanninkhof (1992), given as

$$vk_{O_2} = 0.31 u_{10}^2 \sqrt{\frac{660}{Sc_{Ox}}}, \quad (3.2)$$

where  $u_{10}$  is the wind speed at 10 m above the sea surface, and  $Sc_{Ox}$  is the Schmidt number, calculated as in Wanninkhof (1992).

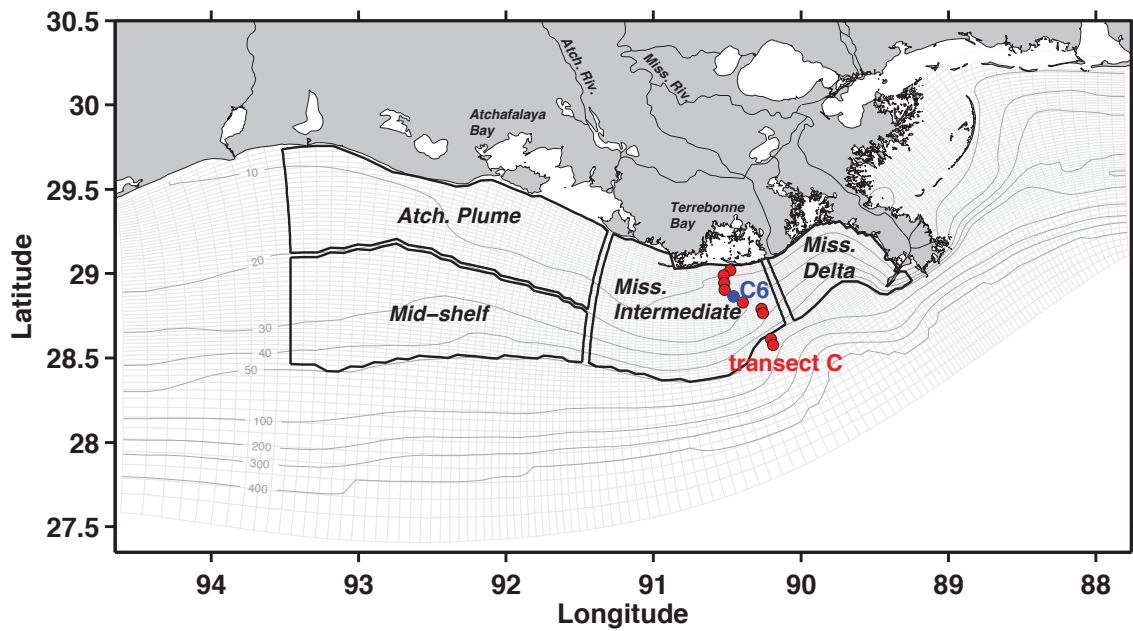


**Fig. 3.1.** Model grid (light gray lines) and bathymetry (dark gray lines). The black boxes indicate selected subregions for averaging: Mississippi delta, Mississippi Intermediate, Atchafalaya Plume and Mid-shelf region. Also shown are the stations on transect C (dots) from nearshore to offshore which represent stations C2, C3, C4, C5, C6 (blue dot), C7, C8, C9, C10 and C11.

The first simple oxygen model has sinks in both the water column and the sediment. A net water respiration rate (NWR, in units of  $\text{mmol O}_2 \text{ m}^{-3} \text{ d}^{-1}$ ) is prescribed in the water column that is constant in time and spatially varying with bathymetry ( $h$ , in units of m, with a minimum at 5m in the model). The functional form, shown in Figure 3.2, is a fit to the mean NWR observations for different isobath bins. Observations are

calculated from data in Murrell et al. (2013) by converting the net metabolism values in their Figure 5b (solid circles) to volumetric units. The NWR data set includes 341 measurements collected in spring, summer and fall from 2003 to 2007 at multiple sites across the LA shelf. The observations didn't show seasonal or along-shelf variability, but there is a cross-shelf gradient with negative NWR (indicating that primary production exceeds biological oxygen consumption in the water column) in shelf regions shallower than 20 m and positive NWR (indicating that biological consumption of oxygen exceeds primary production) deeper than 20 m (as shown by the gray bars in Figure 3.2). The functional form of NWR captures this cross-shelf variability and is given as:

$$\text{NWR} = 30 [\text{mmol O}_2 \text{ m}^{-3} \text{ d}^{-1}] * \sin \left( -15.29 + \frac{-h^{1.043}}{48.32[\text{m}]} \right) * \exp \left( -\frac{h^{1.587}}{99.95[\text{m}]} \right), \quad (3.3)$$

where  $h \geq 5\text{m}$ .

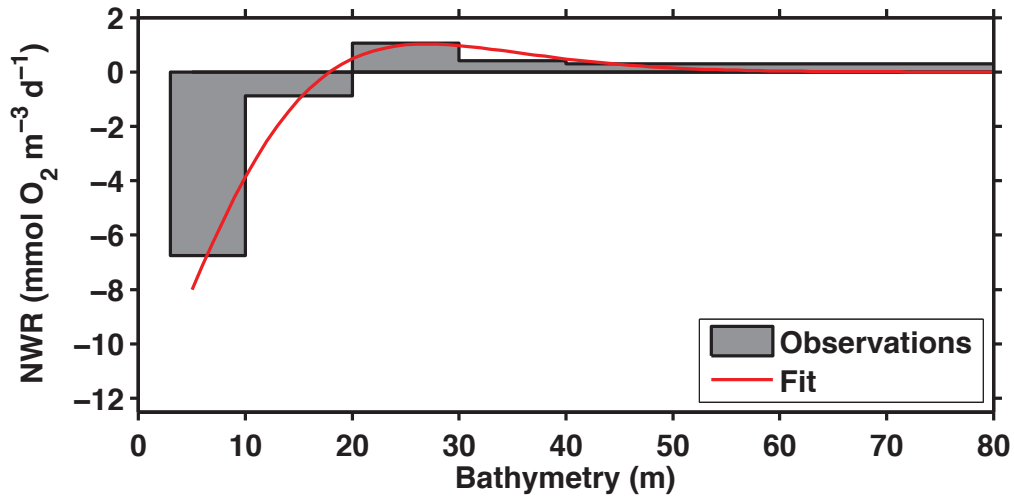


**Fig. 3.2.** Fitted net water column respiration rate (NWR) based on observations of Murrell et al. (2013b).

In addition, similar to Chapter 2, a temperature- and oxygen-dependent sediment oxygen consumption (SOC) rate is implemented in the model, drawing down oxygen in the bottom-most grid cell (Hetland and DiMarco, 2008) according to:

$$\text{SOC} = 6 [\text{mmol O}_2 \text{ m}^{-2} \text{ d}^{-1}] * 2^{T/10^\circ\text{C}} * \left( 1 - \exp \left( -\frac{\text{O}_x}{30[\text{mmol O}_2 \text{ m}^{-3}]} \right) \right), \quad (3.4)$$

where  $T$  ( $^{\circ}\text{C}$ ) and  $\text{Ox}$  ( $\text{mmol O}_2 \text{ m}^{-3}$ ) are the temperature and oxygen concentrations in the bottom water, respectively. I will refer to this model as NWR+SOC.

To examine the sensitivity of hypoxia to different prescriptions of oxygen sinks in water column and sediment, I ran two additional simple oxygen models in which either water column respiration or the sediment oxygen sink is turned off. These two models are denoted as ‘SOC only’ (without NWR) and ‘NWR only’ (without SOC), respectively. An overview of all models is given in Table 3.1.

I evaluate the performance of the three simple oxygen models, which were ran from 1 January 2004 to 31 December 2007, by comparing the simulated hypoxic extent and oxygen concentrations with available observations from Rabalais et al. (2007), Murrell et al. (2013a), Nunnally et al. (2013) and the Mechanisms Controlling Hypoxia (MCH) program. Considering that observations are spatially and temporally limited, I extended the validation by comparing output from the simple oxygen models to that of the full physical-biogeochemical model used in Chapter 2, which has been shown to realistically reproduce the observed oxygen dynamics on the LA shelf.

**Table 3.1.** Overview of models

<b>Model</b>	<b>Description</b>
Full bio-geochemical model (Full)	Realistic hydrodynamic model coupled with N-cycle model.
NWR+SOC model	Realistic hydrodynamic model coupled with simple DO parameterization where oxygen utilization rate in the water column is constant and sediment oxygen consumption rate is a function of bottom water oxygen and temperature.
SOC only model	Turn off the water column oxygen sink in the NWR+SOC model.
NWR only model	Turn off the sediment oxygen sink in the NWR+SOC model.

### 3.2.2 Model experiments

Based on the validation of the simple oxygen models against available observations and output from the full physical-biogeochemical model (see Results

section), I choose the NWR+SOC model to conduct sensitivity experiments that examine the effects of river discharge, wind speed and wind direction on the extent and geographic distribution of hypoxia.

The NWR+SOC model was first run with realistic river discharge and wind forcing (denoted as ‘Baseline’ simulation). Sensitivity experiments with varying river or wind forcing were then conducted and are compared with the baseline model experiment to evaluate the role of river discharge and wind forcing on the seasonal cycle of hypoxia (Table 3.2). I focus the detailed analysis of model experiments on the year 2007, which is an average year in terms of the hypoxic extent, freshwater discharge and duration of upwelling-favorable (westerly) wind in summer.

**Table 3.2.** Overview of model experiments.

<b>Experiment</b>	<b>Description</b>
Baseline	Baseline run with realistic river discharge and wind forcing in year 2007.
River discharge runs	
Const RD	River discharge is set to annual average value.
High RD	Double the river discharge.
Low RD	Halve the river discharge.
Wind runs	
UF	Winds from mid July to mid August (upwelling-favorable wind) were repeated each month of the year.
DF	Winds from January (downwelling-favorable wind) were repeated each month of the year.
High UF	The repeated upwelling-favorable wind magnitude was increased to be comparable to January upwelling favorable wind.
Low DF	The repeated downwelling-favorable wind magnitude was decreased to be comparable to summer upwelling favorable wind.

The freshwater discharge from the Mississippi River varies considerably on both seasonal and inter-annual time scales (Fig. 3.3). The discharge magnitude typically increases from winter to spring and then decreases to a minimum in summer. To evaluate the role of the seasonal variation in river discharge (RD) on the hypoxic area, I conducted a sensitivity experiment (denoted as ‘Const RD’) where river discharge was set to the annual average value throughout the year. To examine the role of the magnitude of river

discharge, I conducted High RD and low RD experiments where the event-scale variability in river discharge is preserved but the magnitude was doubled or halved, respectively. These changes in river discharge are mostly within the long-term (1983-2007) range of annual river discharge data, except in winter months and July when the increased river discharge exceeds the high end, and in spring, October and December when the decreased river discharge is below the low end of the range (Fig. 3.3).

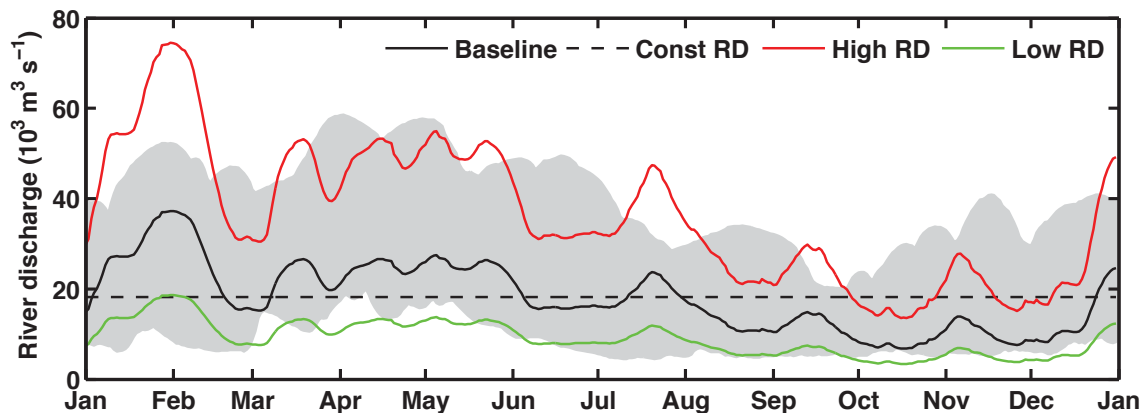


**Fig. 3.3.** Mississippi and Atchafalaya River freshwater discharge. The shaded area indicates the range of annual river discharge from 1983 to 2010.

Wind speed and wind direction over the LA shelf also have pronounced seasonal variability, namely low magnitude and dominantly upwelling-favorable direction (westerly) in summer (June to August) and relatively high magnitude and downwelling-favorable direction (easterly) during the rest of the year (Fig. 3.4). To evaluate the role of this seasonal change in wind forcing, I conducted an upwelling-favorable wind run (denoted as ‘UF’) where the mid-July to mid-August upwelling-favorable wind was repeated each month of the year, and a downwelling-favorable wind run (denoted as ‘DF’) where the downwelling-favorable wind from January was repeated each month of the year. To further examine the respective effects of wind speed and wind direction, I conducted a ‘High UF’ wind run where the wind speed from the UF run was increased (by  $\sim 2.2$  times) to be comparable in terms of strength to the downwelling-favorable wind in the DF run, and a ‘Low DF’ wind run where the wind speed from the DF run was decreased (by  $\sim 46\%$ ) to be comparable in strength to the upwelling-favorable wind from the UF run. Hence one

can assess the effects of wind speed by comparing UF and High UF or DF and Low DF runs, and evaluate the effects of wind direction by comparing the UF and Low DF, or High UF and DF. Although not realistic, these simulations provide insight into the impacts of wind speed and direction on the seasonal cycle of hypoxic area.

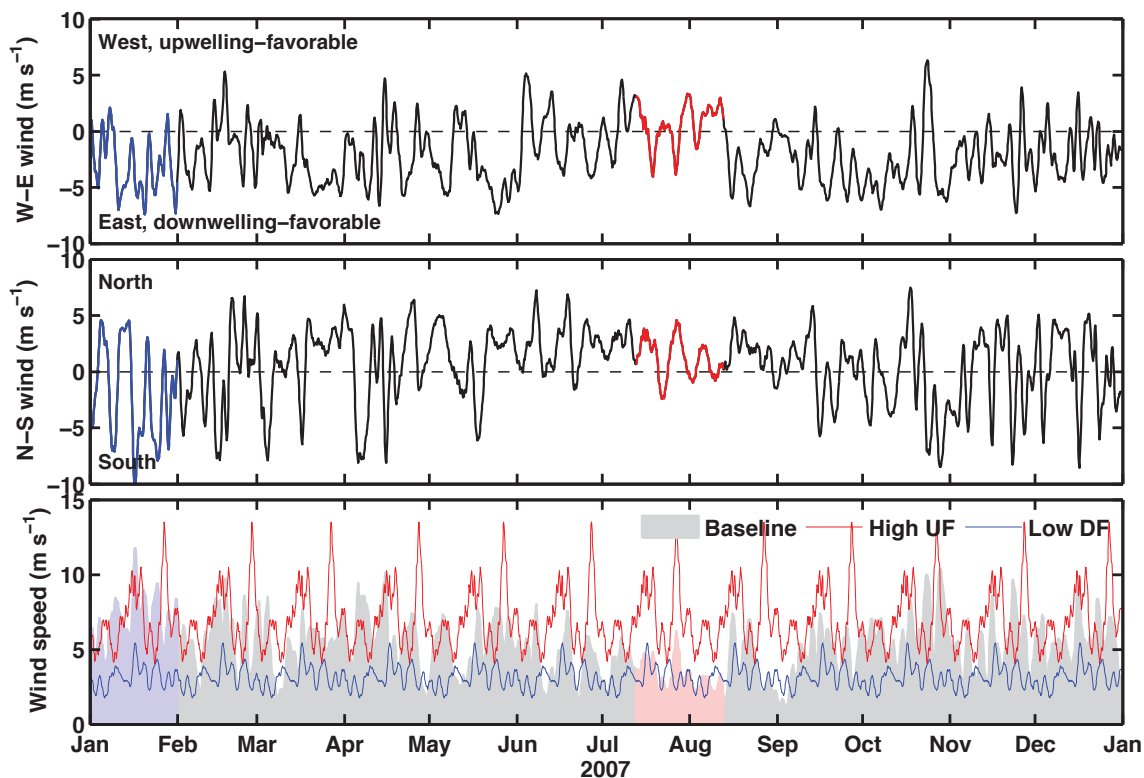


**Fig. 3.4.** a) NARR W-E wind and b) NARR N-S wind averaged over the shelf (shaded area in Figure 1). The blue and red lines indicate the January wind and Jul 13<sup>rd</sup>-Aug 12<sup>th</sup> wind repeated throughout the year for DF and UF scenarios, respectively. c) NARR wind speed in baseline run (gray shadow) and wind speed used in High UF (thin red line) and Low DF (thin blue line) scenarios. Values are averaged over the shelf (shaded area in Figure 1). The blue and red shaded area indicates the indicate the January wind speed and Jul 13<sup>rd</sup>-Aug 12<sup>th</sup> wind speed repeated throughout the year for DF and UF scenarios, respectively.

I quantify the hypoxic extent by calculating the total area of water that has bottom dissolved oxygen concentrations below a threshold value. To represent different degrees of hypoxia, four different threshold values are used: 0.5 mg l<sup>-1</sup> (anoxic), 1 mg l<sup>-1</sup> (strongly hypoxic), 2 mg l<sup>-1</sup> (hypoxic) and 3 mg l<sup>-1</sup>. In addition, I calculated the duration of hypoxia for each simulation by counting the number of days when bottom oxygen was less than a

threshold value at each grid box. I also calculated the shelf area where hypoxic duration exceeds 50 and 250 days/year by summing the area of grid cells where hypoxic conditions ( $\text{DO} < 2 \text{ mg l}^{-1}$ ) last for more than 50 days and 250 days in year 2007, respectively. I calculated the value of the maximum Brunt-Vaisala Frequency ( $N^2$ ) as a measure of the stratification strength (Pond and Pickard, 1983) for each grid box. I further calculated averaged stratification (maximum  $N^2$  value) by first spatially averaging the  $N^2$  value over the shelf and then averaging over the entire summer (Jun-Aug) and the whole year, respectively. I also quantified the extent of the surface river plume by calculating the daily shelf area with surface water salinity less than 24 and then averaging these values over the entire summer (Jun-Aug) and the whole year, respectively, for comparison with other metrics.

### **3.3 Results**

#### **3.3.1 Model validation**

Simulated temporal variations and spatial distributions of hypoxia from the different model variants are shown in comparison to the observed hypoxic extent in July in Figures 3.5 and 3.6, respectively. Despite their simplicity, both NWR+SOC and SOC models simulate temporal variations (Fig. 3.5) and spatial distributions of hypoxia (Fig. 3.6) that are very similar to those of the full biogeochemical model, with the two simple oxygen models producing only a slightly larger hypoxic area in summer. Comparison of the NWR+SOC and the SOC models illustrates the effect of turning off the oxygen term in the water column. The difference is small indicating that the net water column respiration rate (NWR) only slightly increases the simulated hypoxic area. The NWR simulation shows that without sediment oxygen consumption the model does not produce any hypoxia at all (Fig. 3.5). Therefore I do not present any further results from the NWR simulation.

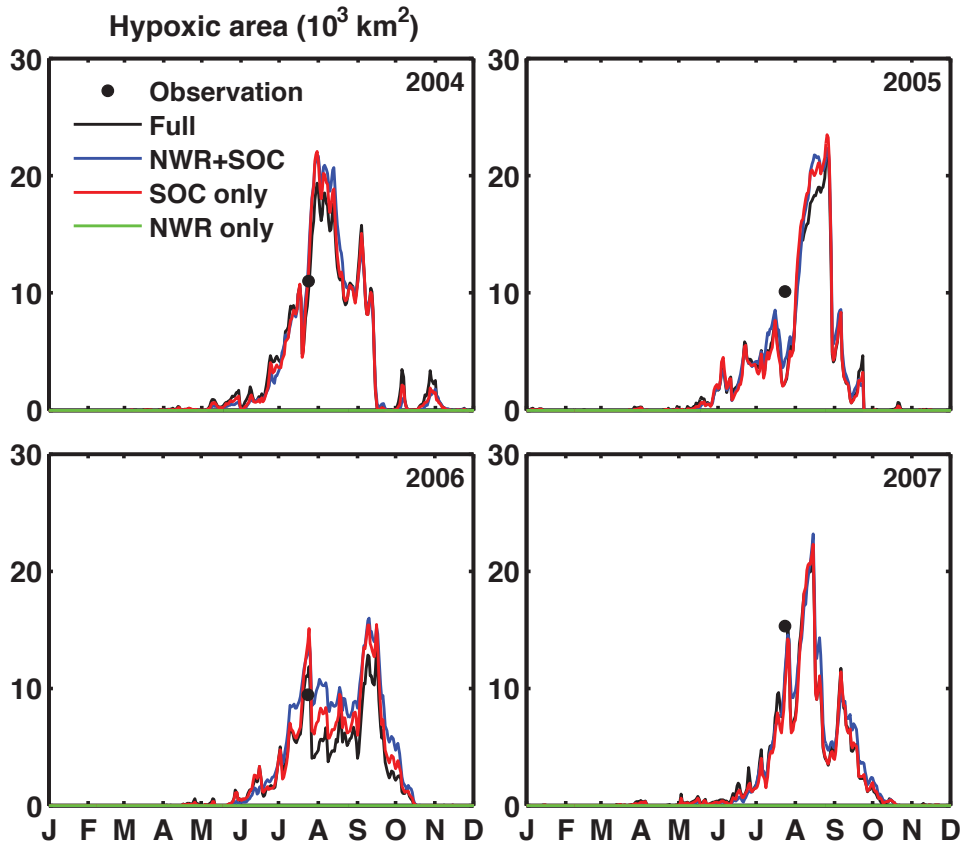


**Fig. 3.5.** Time series of simulated hypoxic extent (i.e. the area with oxygen concentrations below  $2 \text{ mg l}^{-1}$  or  $62.5 \text{ mmol m}^{-3}$ ) for the full biogeochemical model (black line), the NWR+SOC model (blue line), the SOC only model (red line) and the NWR only model (green line). Also shown is the observed hypoxic extent in late July (black dots). The observed hypoxic extent was estimated by linearly interpolating the observed oxygen concentrations onto the model grid and then calculating the area with oxygen concentrations below the hypoxic threshold (Fennel et al., 2013).



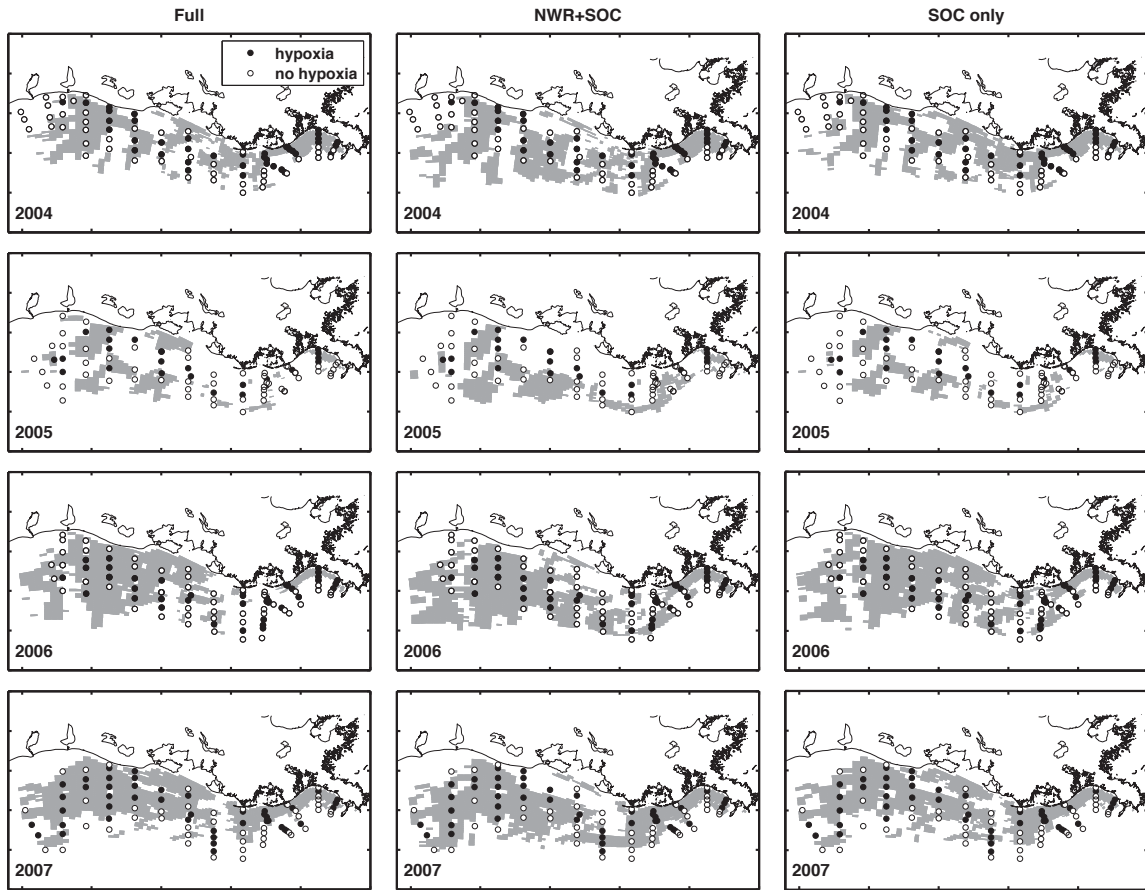


**Fig. 3.6.** Simulated (gray areas) and observed (dots) hypoxic conditions from the full biogeochemical model (left column), the NWR+SOC model (middle column) and the SOC only model (right column) for the years 2004 to 2007. The simulated hypoxic area includes all bottom grid boxes where dissolved oxygen  $< 2 \text{ mg l}^{-1}$  during the July monitoring cruise. The stations where hypoxia was observed are shown as filled black dots, while stations without hypoxia are shown as open dots.

Figure 3.7 shows profiles of bias between simulated and observed oxygen profiles in summer months. Overall, the model-data biases are often within one standard deviation of the observations. The full biogeochemical model generally overestimates the observed oxygen throughout the water column, whereas the two simple oxygen models mostly underestimate the observations in the upper layers but overestimate them in the lower layers (except in the Mississippi Intermediate region in August and Mid-shelf region in June and July). Of the three model simulations, NWR+SOC simulates the lowest oxygen values and agrees best with observed oxygen in bottom layers except in the Atchafalaya plume and Mid-shelf region in June and July. Since I am most interested in the oxygen

concentrations in bottom layers where hypoxia develops, I will focus on comparisons between NWR+SOC and the full biogeochemical models for the remainder of the manuscript.

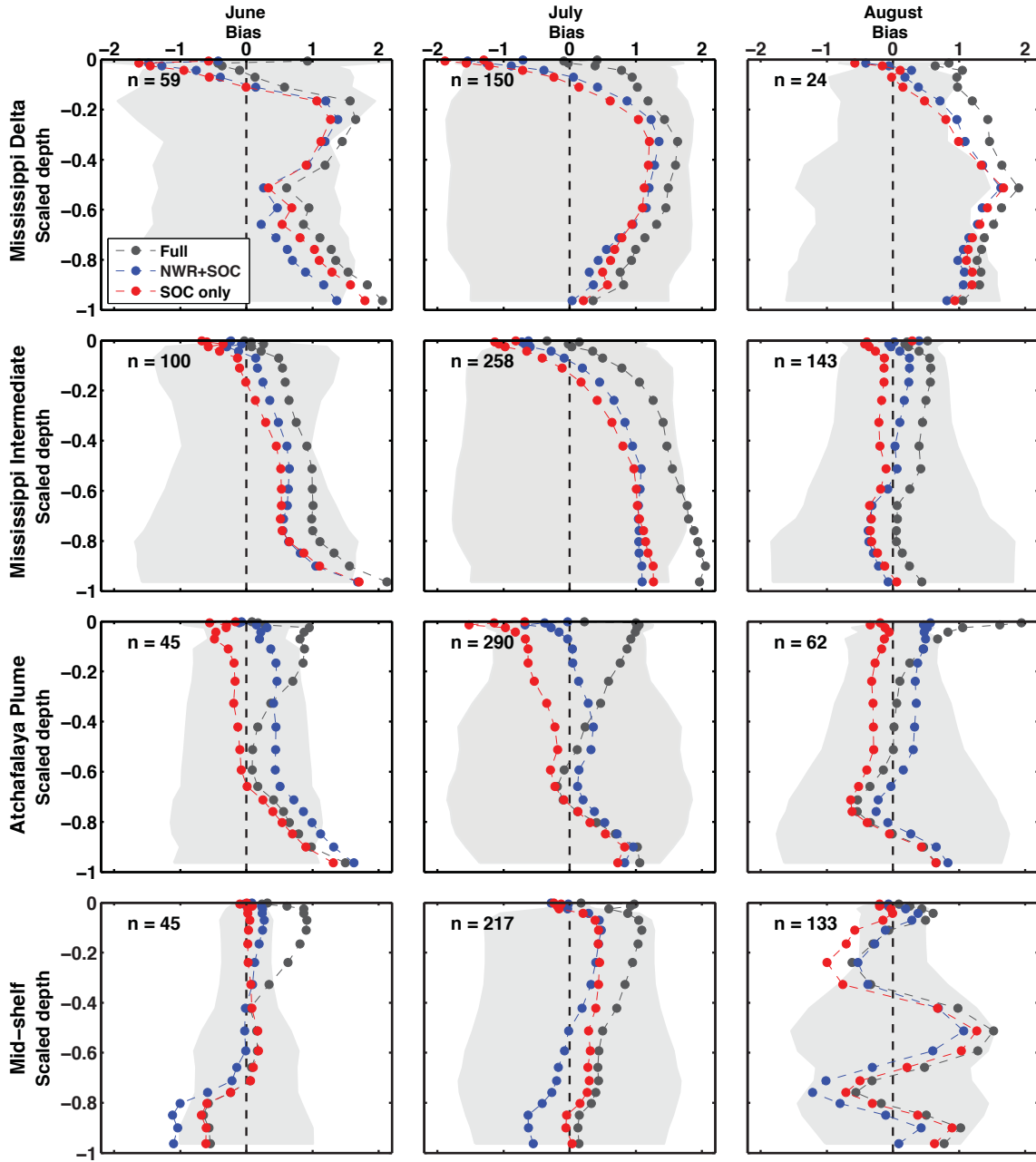


**Fig. 3.7.** Vertical profiles of model bias (model minus observations,  $\text{mg O}_2 \text{ l}^{-1}$ ) in dissolved oxygen (DO) from June to August in 2004-2007 in the 4 subareas. The vertical axis is the scaled depth, where 0 and -1 represent surface and bottom, respectively. The light shadows represent the one standard deviation in the observations. Observations are from LUMCON (Rabalais et al., 2007), EPA (Lehrter et al., 2009, 2012), Murrell et al. (2013b), and MCH.

Figure 3.8 shows a comparison between the simulated and observed oxygen concentrations at station C6. Both the full biogeochemical model and the NWR+SOC model reproduce the observed vertical distribution in oxygen concentrations and seasonal drawdown of oxygen in summer and the subsequent ventilation in the fall. The surface and bottom oxygen concentrations are similar in winter when the water column is well mixed, but they greatly diverge from each other in summer when strong stratification isolates the oxygen-rich surface waters from the oxygen-poor bottom waters (Fig. 3.8 lowest panel). The simulated oxygen distribution of the NWR+SOC model is almost identical to that of the full model, except that the former produces slightly lower oxygen concentrations throughout the water column and does not capture the observed supersaturation of surface oxygen during spring and summer. Profiles of bias between simulated and observed oxygen at station C6 (Figure C1, see Appendix C) show that both models underestimate observations in the upper half of the water column and overestimate observations in the lower half of water column; however, compared with the full model, the NWR+SOC model underestimates the observed oxygen more in the upper layers (i.e., surface layer biases are  $-0.65$  and  $-0.72$   $\text{mg l}^{-1}$  for the full and the NWR+SOC models, respectively) but overestimates the observed oxygen less in the lower water layers (bottom layer biases are  $1.19$  and  $0.84$   $\text{mg l}^{-1}$ , respectively).

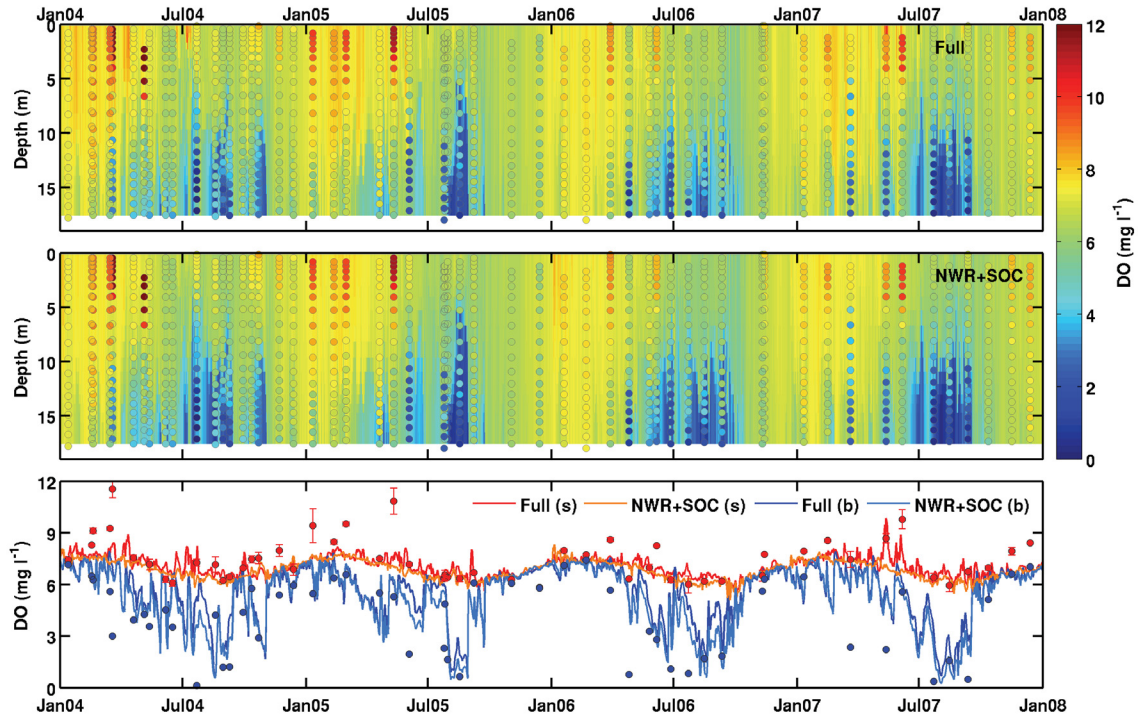


**Fig. 3.8.** Top panels: Comparison between the simulated (color map) and observed (colored dots) DO concentrations at station **C6** for full biogeochemical model (top panel) and the simple NWR+SOC model (middle panel). Bottom panel: Comparison between the simulated surface (thick lines) and bottom (thin lines) DO concentrations at station C6 for the full biogeochemical model (black) and the simple NWR+SOC model (gray). Also shown are observations of surface DO averaged over top 5-m layer (red spots with error bars indicating standard deviations) and bottom DO concentrations (blue spots).

A comparison between the simulated and observed summer and non-summer average oxygen concentrations along the C transect is shown in Figure 3.9. Both the full biogeochemical model and the NWR+SOC model capture the observed vertical differences in average oxygen for all stations along the C transect and cross-shore variations in the oxygen distribution. The models also capture the seasonality of those differences but generally underestimate the observations in the upper water column in non-summer months (see Figure C2, biases in the top 5 m range from  $-1.54$  to  $-0.03$  mg l<sup>-1</sup> and  $-2.15$  to  $-0.06$  mg l<sup>-1</sup> for the full and NWR+SOC models, respectively) while overestimating observations in the lower water column in summer (biases in the bottom layer range from  $0.63$  to  $3.15$  mg l<sup>-1</sup> and  $0.57$  to  $1.72$  mg l<sup>-1</sup> for the full and NWR+SOC

models, respectively). Compared to the full model, the NWR+SOC model simulates slightly lower oxygen concentrations in summer months within the whole water column and hence has relatively larger underestimation of the observed oxygen within the upper 5 m of the water column but smaller overestimation of the observed oxygen in the water column below 5 m.

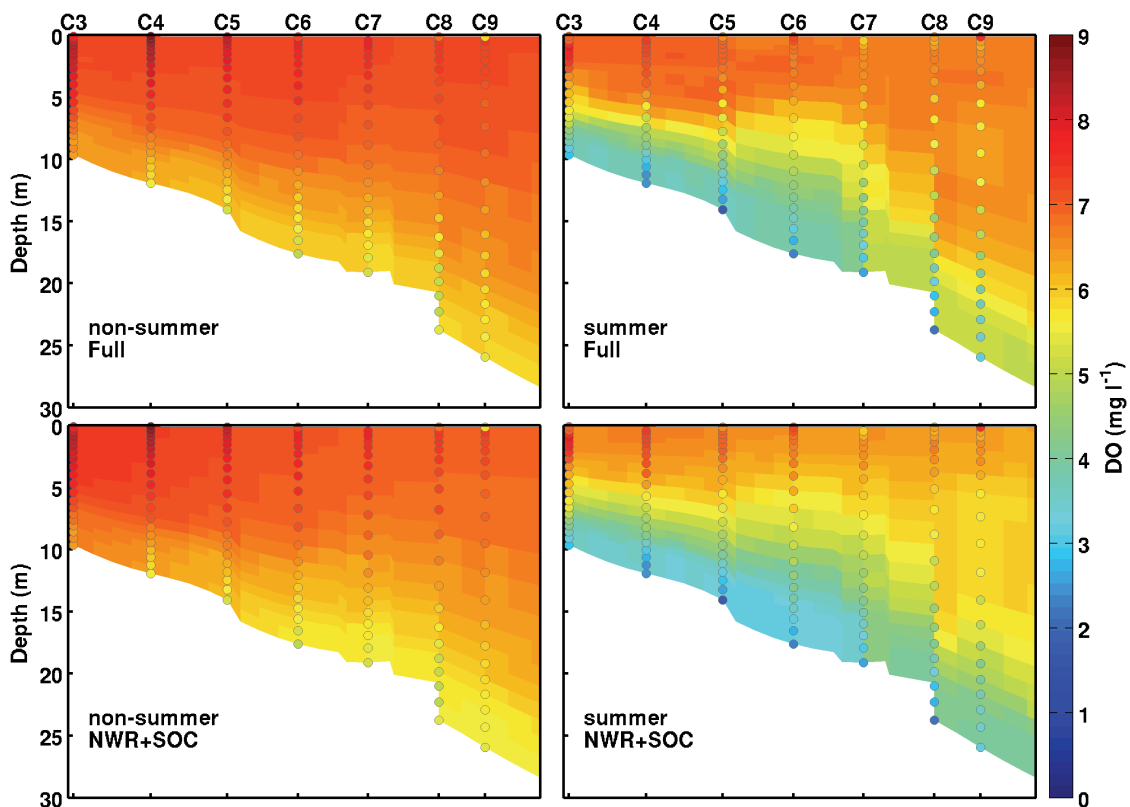


**Fig. 3.9.** Comparison between the simulated (color map) and observed (dots) seasonal average DO concentrations along the C transect for the full biogeochemical model (top) and simple NWR+SOC model (bottom).

### 3.3.2 Response of hypoxia and stratification to river discharge and wind forcing

#### 3.3.2.1 River discharge

The simulated temporal variations in hypoxic area in the Const RD run are almost identical to those of the baseline run (Fig. 3.10a), with the former simulating lower

hypoxic areas (a 15 to 36% decrease in integrated hypoxic area for different hypoxia thresholds, see Table 3.3). Doubling the river discharge increases the total integrated hypoxic area by up to 145% for the lowest hypoxia threshold. Halving the river discharge reduces the total integrated hypoxic area by up to 64%. Also noticeable in Table 3.3 is that the proportional changes of integrated hypoxic area are more pronounced for the more stringent threshold values of hypoxia.

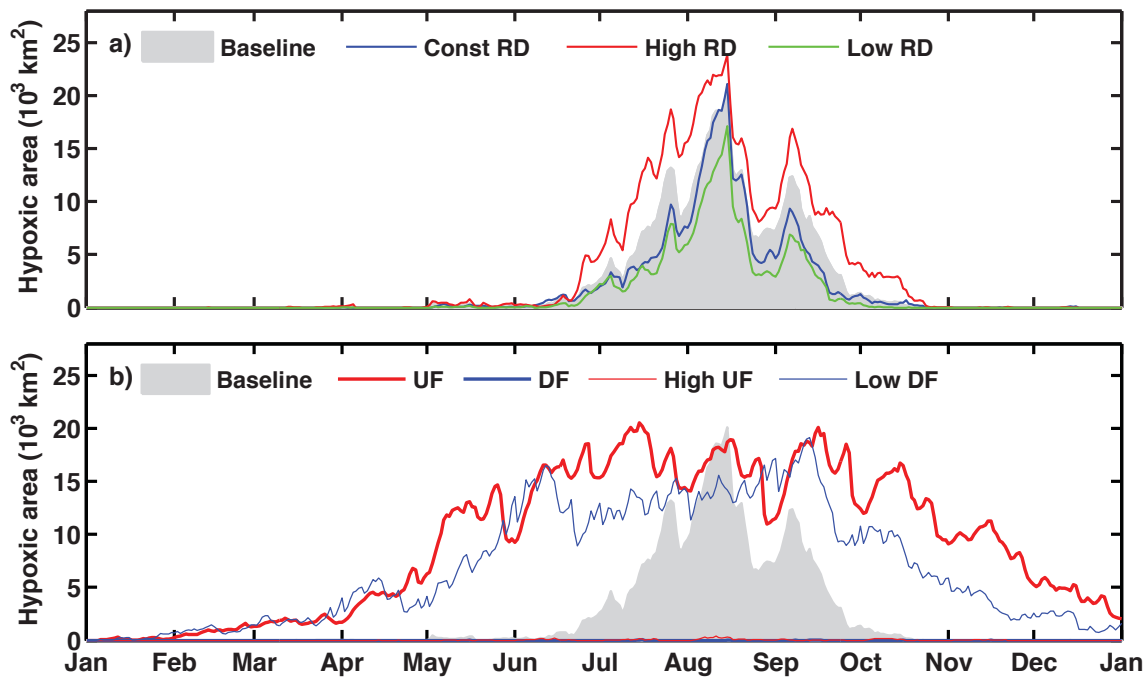


**Fig. 3.10.** Comparison of the simulated hypoxic area for the baseline run (shaded gray area) with **a)** river discharge runs (Const RD: blue line; High RD: red line; Low RD: green line) and **b)** wind runs (UF: thick red line; DF: thick blue line; High UF: thin red line; Low DF: thin blue line).

**Table 3.3** Integrated hypoxic areas simulated by different model runs in 2007. For each model run, the total area of water with dissolved oxygen concentration below 0.5 mg l<sup>-1</sup> (anoxic), 1 mg l<sup>-1</sup> (strongly hypoxic), 2 mg l<sup>-1</sup> (hypoxic) and 3 mg l<sup>-1</sup> was calculated at each day and integrated over all days in 2007. The percentage change relative to the Baseline model run is calculated for each model run ( $(\text{model}-\text{Baseline})/\text{Baseline}$ ) and presented in parenthesis. For clarity, changes relative to the Baseline model run are highlighted in blue if there was a decrease and in red if there was an increase in the respective metric.

Model run	Integrated hypoxic area (10 <sup>3</sup> km <sup>2</sup> days)			
	< 0.5 mg l <sup>-1</sup>	<1 mg l <sup>-1</sup>	< 2 mg l <sup>-1</sup>	< 3mg l <sup>-1</sup>
Baseline	140.1	364.0	820.7	1390.2
Const RD	89.8 (-36%)	261.2 (-28%)	656.1 (-20%)	1181.1 (-15%)
High RD	343.3 (+145%)	666.3 (+83%)	1254.5 (+53%)	1927.5 (+39%)
Low RD	50.7 (-64%)	161.6 (-56%)	479.5 (-42%)	955.6 (-31%)
UF	946.9 (+576%)	1861.8 (+411%)	3383.4 (+312%)	4934.3 (+255%)
DF	0.0 (-100%)	0.0 (-100%)	0.3 (-100%)	3.1 (-100%)
High UF	0.1 (-100%)	0.8 (-99%)	10.0 (-98%)	51.9 (-96%)
Low DF	403.5 (+188%)	1045.1 (+187%)	2517.4 (207%)	4255.9 (+206%)

The duration of hypoxia (bottom oxygen < 2 mg l<sup>-1</sup>) for each simulation is shown in Figure 3.11. Compared with the baseline run, holding river discharge constant reduces the duration of hypoxia on the western shelf (Fig. 3.11d). Doubling river discharge leads to a westward extension of persistent hypoxia (hypoxia lasting more than 50 days a year) (Fig. 3.11e) and increases the area experiencing persistent hypoxia by 215% above the baseline run, whereas halving river discharge restricts persistent hypoxic condition to the eastern shelf (Fig. 3.11f) and decreases the area experiencing persistent hypoxia by 46% relative to the baseline run (Table 3.4).



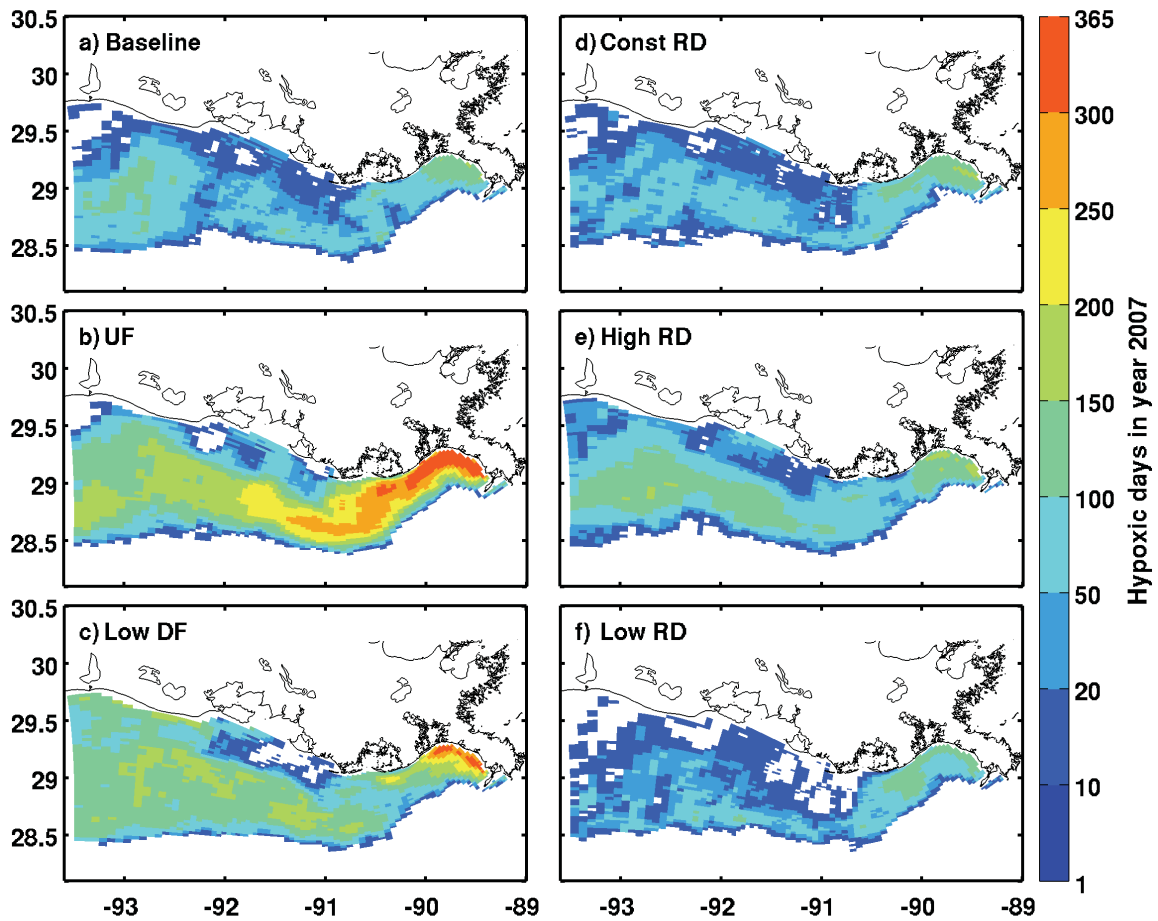


**Fig. 3.11.** Simulated number of hypoxic days for each model run. The value is calculated at each model grid by counting the number of days when bottom DO < 2 mg l<sup>-1</sup> (or 62.5 mmol m<sup>-3</sup>) in year 2007.



**Table 3.4.** Shelf area where hypoxic duration exceeds 50 and 250 days/year, average area of the surface river plume (area of surface salinity  $\leq 24$ ) and average stratification (maximum  $N^2$ ) over specific periods for all model runs. The percentage change relative to the Baseline model run ( $[\text{model}-\text{Baseline}]/\text{Baseline}$ ) is given in parentheses. Changes relative to the Baseline model run are highlighted in blue if there was a decrease and in red if there was an increase in the respective metric.

Model Run	Area of $\text{DO} < 2 \text{ mg l}^{-1}$ ( $10^3 \text{ km}^2$ )		Average area of surface river plume ( $10^6 \text{ km}^2$ )		Average $N^2$ ( $10^{-3} \text{ s}^{-2}$ )	
	duration > 50 days/year	duration > 250 days/year	summer average	yearly average	summer average	yearly average
Baseline	3.2	0.0	0.9	2.3	15.9	9.2
Const RD	2.0 (-36%)	0.0	0.8 (-13%)	2.2 (-7%)	15.3 (-4%)	9.0 (-2%)
High RD	10.0 (+215%)	0.0	2.1 (+116%)	4.8 (+107%)	22.0 (+39%)	13.3 (+45%)
Low RD	1.7 (-46%)	0.0	0.4 (-62%)	1.0 (-56%)	9.5 (-40%)	5.4 (-41%)
UF	23.7 (+647%)	1.3	1.1 (+11%)	4.2 (+78%)	18.0 (+13%)	17.9 (+95%)
DF	0.0 (-100%)	0.0	0.3 (-67%)	1.3 (-46%)	4.5 (-72%)	4.4 (-52%)
High UF	0.0 (-100%)	0.0	0.4 (-57%)	1.6 (-31%)	5.3 (-67%)	5.2 (-43%)
Low DF	24.3 (+667%)	0.2	1.0 (+4%)	3.8 (+64%)	13.7 (-13%)	13.0 (+42%)

The shelf-averaged stratification changes markedly with the changes in river discharge (Fig. 3.12). Doubling or halving the river discharge leads to a significant increase or decrease in the shelf-averaged stratification throughout the year (Fig. 3.12a). The deviation in stratification for the Const RD run relative to the Baseline run (Fig. 3.12d) demonstrates a strong negative correlation ( $r=-0.74$ ) with river discharge (Fig. 3.3) when lagged by 9 days.

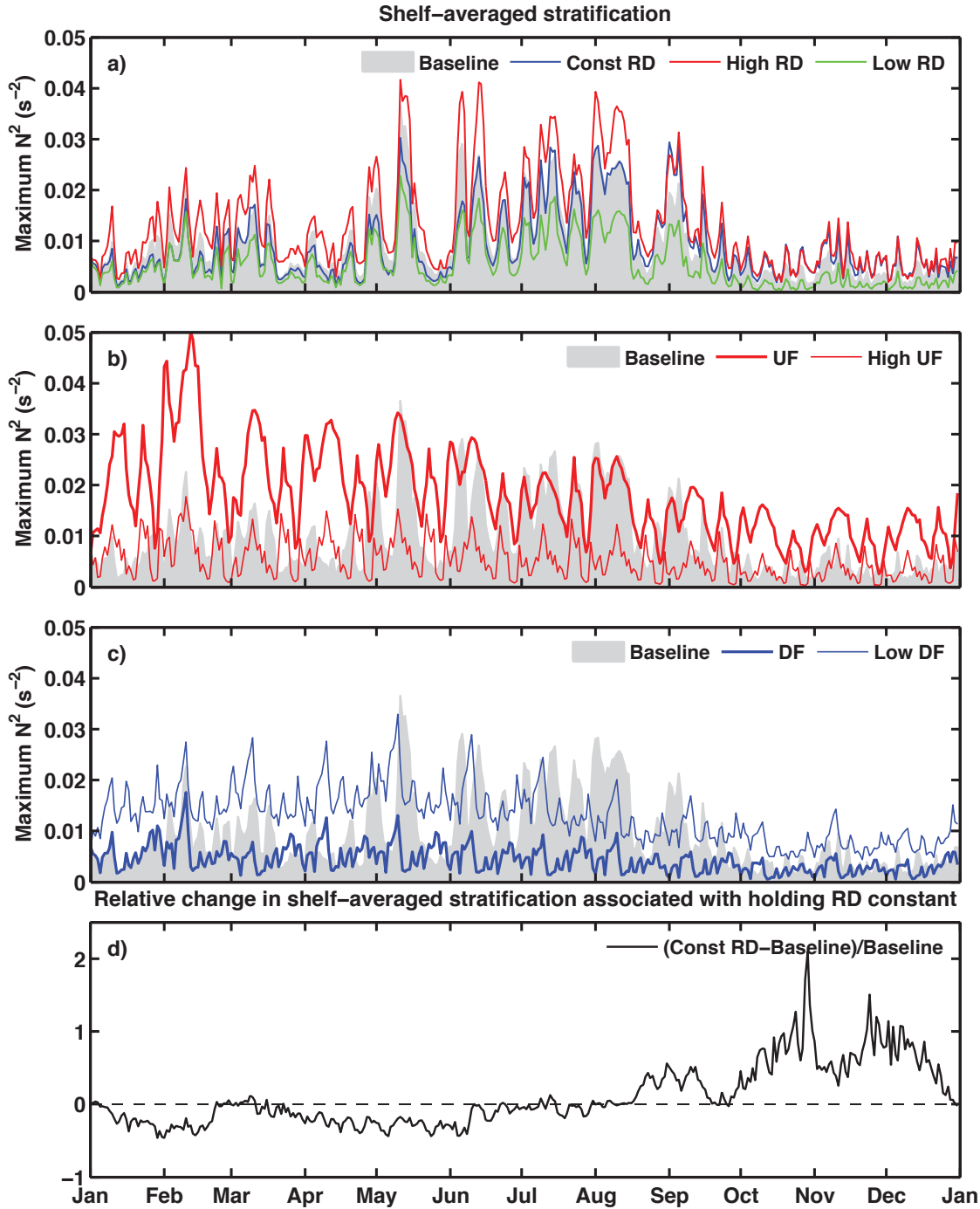


**Fig. 3.12.** Averaged stratification over the shelf (shaded area in Figure 1) for **a)** baseline run (gray shadow) and river discharge runs (Const RD: blue line; High RD: red line; Low RD: green line); **b)** baseline run (gray shadow) and upwelling-favorable wind runs (UF: thick red line; High UF: thin red line); **c)** baseline run (gray shadow) and downwelling-favorable wind runs (DF: thick blue line; Low DF: thin blue line); **d)** Relative change in shelf-averaged stratification associated with holding river discharge constant  $[(\text{Const RD} - \text{Baseline}) / \text{Baseline}]$ . Positive values indicate higher stratification for Const RD run than baseline run.

Figure 3.13 further shows that doubling or halving the river discharge respectively enhances or reduces stratification over the majority of the shelf in summer months, except in the regions adjacent to the river mouths where stratification goes down with increasing river discharge.

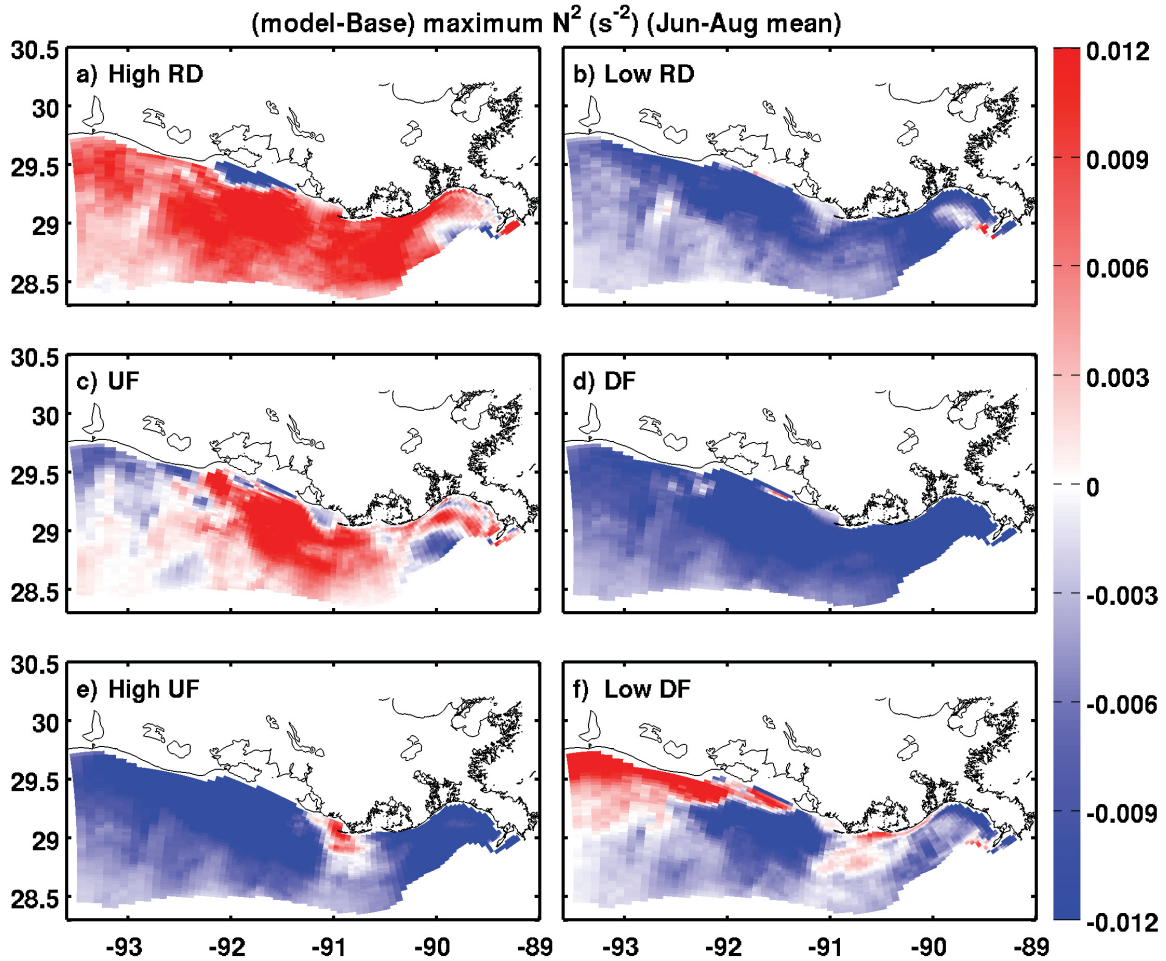


**Fig. 3.13.** The deviation in summer averaged stratification from the baseline model run (model - Baseline). Stratification is quantified by maximum  $N^2$  value and averaged for the period June-August. Red (positive value) represents higher and blue (negative value) represents lower stratification than the baseline run.

The horizontal and vertical distributions of the river plume under the different river scenarios are shown in Figures 3.14 and 3.15, respectively. Increasing the river discharge leads to a large westward and offshore extension of the lighter, fresher plume

water, where the isohalines are almost parallel to the coast (Fig. 3.14c) and are significantly tilted offshore (Fig. 3.15c). In contrast, decreasing river discharge confines the plume water to near the river mouths (Fig. 3.14d), which can also be observed in the vertical section where the 24 isohaline is pushed toward the shore and is less tilted than in the baseline run (Fig. 3.15d).

The metrics reported in Table 3.4 further show that variations in river discharge markedly affect the average area of the surface river plume (salinity < 24), average shelf stratification, hypoxic area (Table 3.3) and the duration of persistent hypoxia.

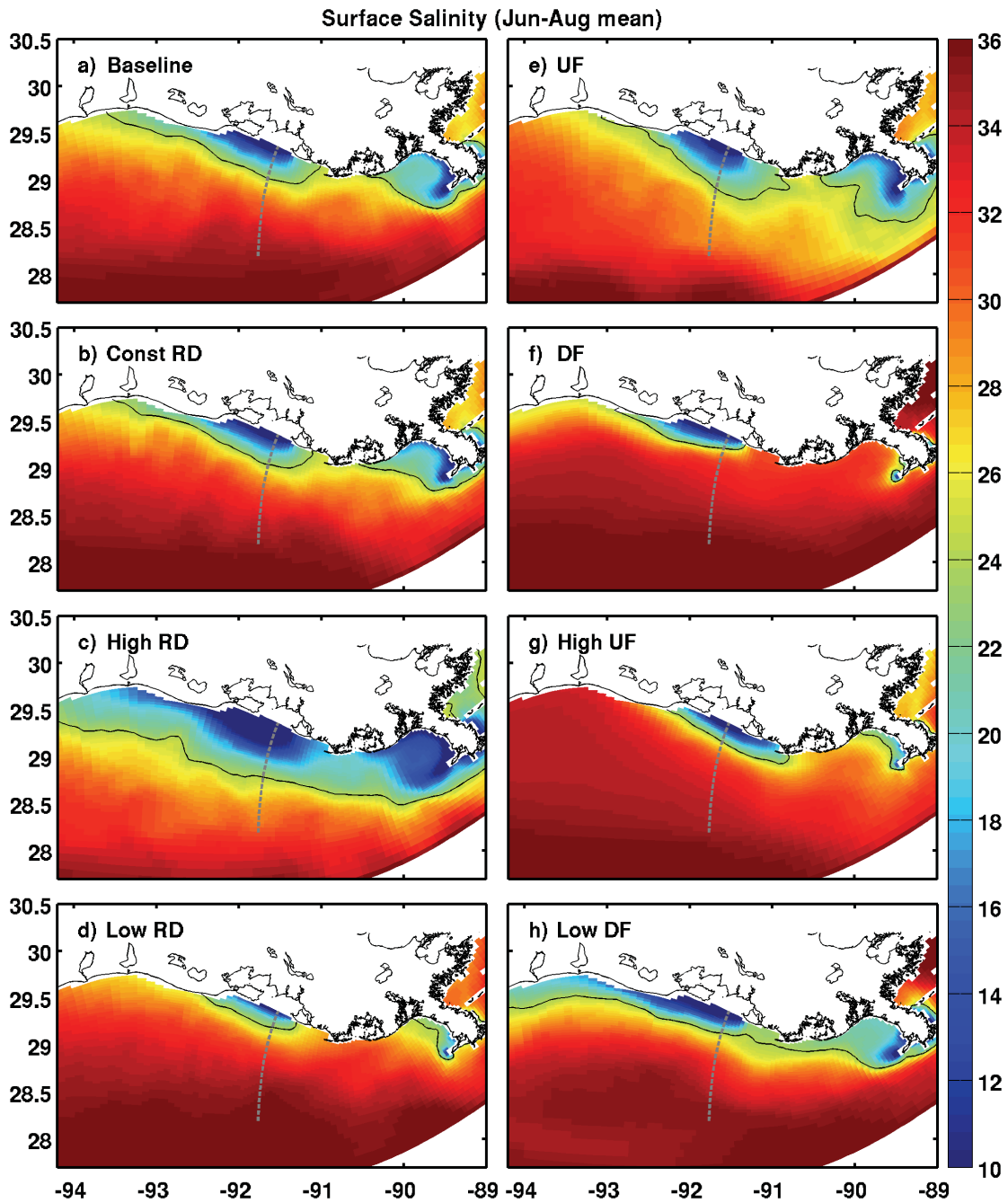


**Fig. 3.14.** Averaged surface salinity for all model runs. Values are averaged for the period June-August. The black line shows the 24 isohaline. The gray dashed line shows the position of cross-shore transect in Figure 3.15.

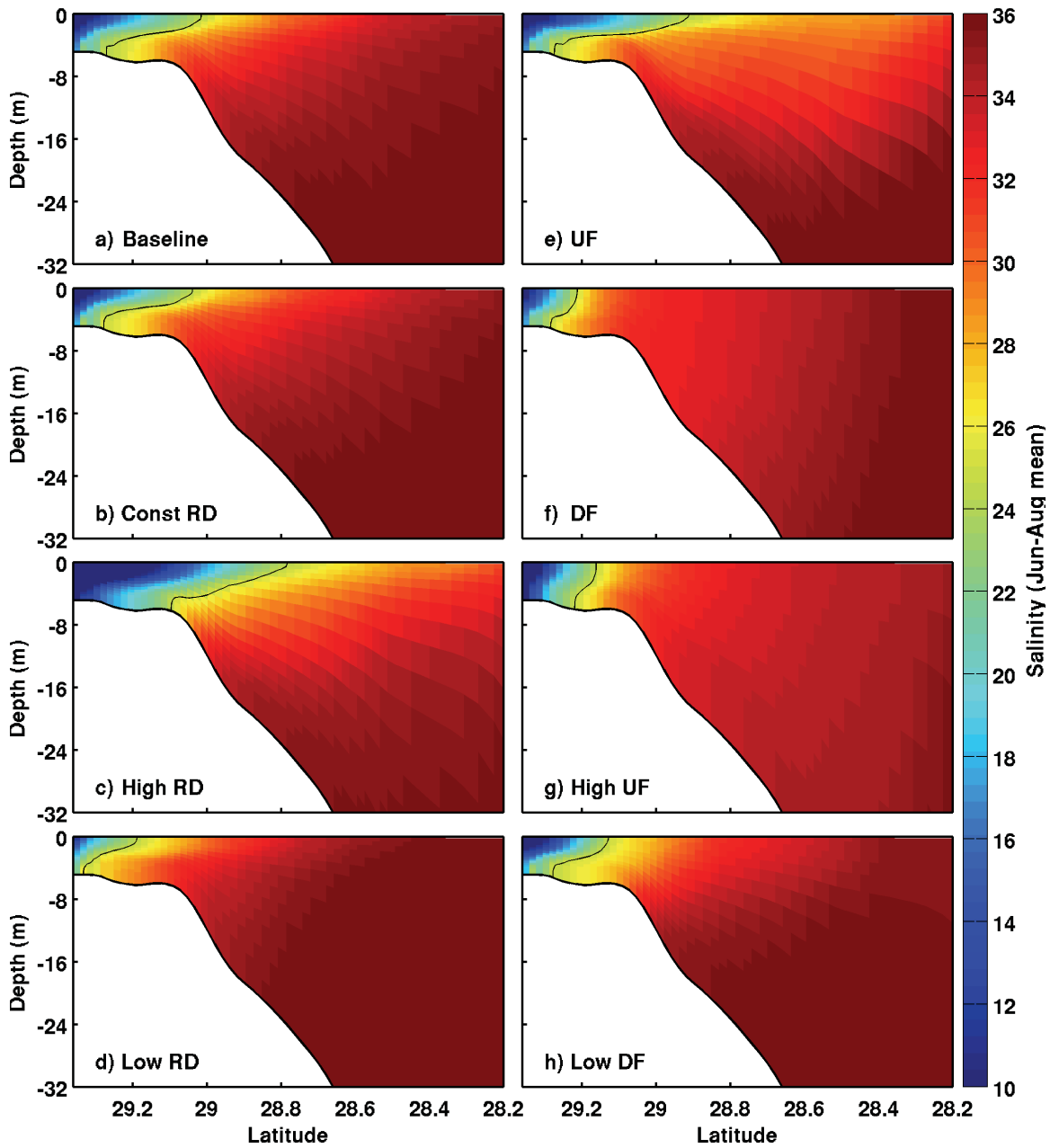


**Fig. 3.15.** Averaged salinity on a cross-shore transect for all model runs. Values are averaged for the period June-August. The black line shows the 24 isohaline. The position of the transect is shown in Figure 3.14.

### 3.3.2.2. Wind forcing

Seasonal changes in wind speed and direction strongly influence the seasonal cycle of the simulated hypoxic area (Fig. 3.10b). In the baseline run, hypoxia develops from June to September when wind direction switches to upwelling-favorable and wind speed is relatively low, and it shrinks and disappears for the rest of the year. In the UF wind run where light, upwelling-favorable wind conditions are imposed all year, extensive hypoxic conditions begin in January and persist through the year, and the integrated hypoxic area increases by roughly a factor of 2.6 to 5.8 compared to the baseline run (Table 3.3). In contrast, when strong, downwelling-favorable winds are imposed all year in the DF run, essentially no hypoxia is simulated.

Increasing the speed of upwelling-favorable wind in the High UF run essentially eradicates hypoxia, similar to the DF wind case (Fig. 3.10b). Decreasing the speed of downwelling-favorable wind in the Low DF run produces extensive hypoxia throughout the year, similar to the UF wind case; however, the simulated hypoxic area in the Low DF run is smaller than in the UF wind run (Fig. 3.10b).

The geographic distributions of hypoxia are also significantly different between the UF wind run and the Low DF wind run. As shown in Figure 3.11 (b, c) and Table 3.4, both runs result in an expansion of persistent hypoxic conditions over the shelf, with the area of persistent hypoxia respectively increased by 6.5 and 6.7 times than that in the baseline run. In the UF wind case a large area of extreme hypoxic conditions (>250 days within a year) is simulated along the eastern shelf. In the low DF wind case extreme hypoxic conditions are simulated closer to shore on the eastern shelf.

The shelf-averaged stratification is high for the whole year in the UF and the Low DF wind cases, but is relatively low throughout the year for the High UF and DF wind cases (Fig. 3.12b, c). The deviation in summer stratification from the baseline model run under the different wind forcing is shown in Figure 3.13 and the shelf-wide average values are summarized in Table 3.4. The persistent upwelling-favorable wind in UF wind case enhances stratification over the majority of the eastern shelf and in regions offshore, but reduces stratification on the western shelf and in near-shore regions (Fig. 3.14c). The

strong downwelling-favorable wind in the DF wind case (Fig. 3.13d) and the increased upwelling-favorable wind in High UF wind case (Fig. 3.13e) both reduce stratification throughout the shelf, except that the latter enhances stratification within a small area near shore around 91°W. Decreasing the downwelling-favorable wind in the Low DF case reduces stratification in river plumes while enhancing stratification on the western shelf and in the portion of the shelf (~91°W) between the Mississippi and Atchafalaya plumes (Fig. 3.13f).

The persistent upwelling-favorable wind in the UF wind case continuously drives freshwater eastward and offshore (Fig. 3.14e, Fig. 3.15e). The High UF wind case also drives freshwater eastward and offshore (Fig. 3.14g), but the increased wind speed in this scenario is able to mix the water column more thoroughly (Fig. 3.15g). Similarly, the strong downwelling-favorable wind in the DF wind case drives freshwater westward and onshore (Fig. 3.14f), and the wind speed is high enough to mix the water column thoroughly (Fig. 3.15f). Decreasing the downwelling-favorable wind in the Low DF wind case moves light plume water westward and onshore (Fig. 3.14h) but the wind speed is unable to mix the water completely (Fig. 3.15h).

### **3.4 Discussion**

#### **3.4.1 Model validation and roles of water column versus sediment processes**

The simple NWR+SOC model closely reproduces the observed temporal variations and spatial distributions of hypoxic extent and oxygen concentrations on the LA shelf when compared to the full biogeochemical model. The NWR+SOC model cannot capture the observed super-saturated oxygen concentrations at the surface due to the lack of biological oxygen production.

Comparison of the NWR+SOC, the SOC and the NWR simulations illustrates the relative importance of oxygen sinks in the water column versus the sediment. When turning off the water column oxygen sink, the SOC model simulates an only slightly smaller hypoxic area than the NWR+SOC model does; whereas when turning off the sediment oxygen consumption, the NWR model does not produce any hypoxia. This



supports the hypothesis that on the LA shelf, total oxygen consumption in the bottom layer is more associated with sediment oxygen consumption than water column respiration (Fennel et al., 2013), which is in contrast to the situation in Chesapeake Bay (Li et al., 2015). The difference in the dominant type of respiration responsible for producing hypoxia might be due to the differences in geometry and hypoxia structure between the LA shelf and Chesapeake Bay. The LA shelf is largely characterized by a broad and gently-sloping area where hypoxic conditions are restricted to a relatively thin layer above the sediment (Fennel et al., 2013); while the Chesapeake Bay has a relatively deep and narrow central channel isolated by sills and flanked by wide shallow areas, where the dense, low-oxygen waters can accumulate and form a thick hypoxic layer extending tens of meters above the bottom (Pierson et al., 2009). While the importance of local respiration of organic matter to seasonal oxygen decline has been well recognized in other upwelling coastal systems (Hales et al., 2006; Connolly et al., 2010; Bianucci et al., 2011; Adams et al., 2013; Siedlecki et al., 2014), the relative importance of sediment versus water column respiration to near-bottom hypoxia formation in these systems is still debated. An observational study by Connolly et al. (2010) found that biochemical oxygen consumption in the water column and sediments each contribute ~50% to the total oxygen consumption in near-bottom water over the Washington shelf. Using a coupled physical and biogeochemical model, Bianucci et al. (2011) demonstrated that remineralization within the sediments, representing ~75% of total oxygen sink, is the dominant process consuming oxygen within the bottom layers on the Vancouver Island shelf. A more recent modeling study by Siedlecki et al. (2014) found that sediment oxygen demand is more important in the Washington coast, which has a broad and shallow shelf (< 60 m), whereas water column respiration is more important in recirculation regions such as the Heceta Bank in Oregon coast.

In summary, the fact that the simple oxygen model with a constant oxygen utilization rate in the water column and an oxygen- and temperature-dependent sediment oxygen consumption rate can reproduce the observed variability in oxygen concentrations well indicates the important role of physical processes and sediment oxygen sink. The controlling role of sediment oxygen utilization in hypoxia generation on the LA shelf is

further demonstrated by the sensitivity experiments disabling oxygen utilization either in the water column or in the sediment. In addition, the ability of the simple oxygen model to closely reproduce the hypoxia evolution of the full biogeochemical model implies that full biogeochemical model may not be necessary for short-term hypoxia forecasting on the LA shelf. However, I would like to note that a full biogeochemical model is necessary to study the effects of varying river nutrient loads on hypoxia and to evaluate the effectiveness of nutrient management strategies (e.g., as in Laurent and Fennel, 2014). The simple model is appropriate for short-term hypoxia forecasting but not for scenario simulations with varying nutrient loads in this region.

### **3.4.2. Model response to river discharge and wind forcing: from stratification to hypoxia**

The importance of stratification for the generation of hypoxia has long been discussed (Wiseman et al., 1997) and revealed in previous numerical studies (Hetland and DiMarco, 2008; Fennel et al., 2013). Using the same circulation model as in this chapter, Fennel et al. (2013) demonstrated that stratification strongly correlates ( $r = -0.78$  in year 2007) with the bottom oxygen concentration on the LA shelf. It follows that stratification is an important indicator of oxygen concentration in bottom waters and hence hypoxic conditions. In this section, I discuss how stratification and hypoxia respond to variations in river discharge and wind forcing on the LA shelf.

#### **3.4.2.1. River discharge**

The simulated seasonal cycle of hypoxia and time-integrated hypoxic area vary significantly with the overall magnitude of river discharge. This can be explained by the significant changes in shelf-averaged stratification associated with the changes in buoyancy inputs. Increasing river discharge leads to an expansion of the lighter, fresher river plume water offshore and westward and an enhancement of shelf-wide stratification, which consequently results in an increase in hypoxic area and the duration of hypoxic conditions over the shelf; whereas decreasing river discharge shrinks the plume, reducing the shelf-wide stratification and thereby significantly decreases the hypoxic area and duration of hypoxia over the shelf. An exception is observed in the regions adjacent to

the river mouths where stratification goes down as river discharge increases. I attribute this to the fact that with increased river discharge the freshwater plume is bottom-attached rather than a surface plume and thus less stratified; this is demonstrated in Figure 3.15c for the High RD run.

The slight difference in simulated seasonal cycle of hypoxic area between the Const RD run and the Baseline run (Fig. 3.10a) suggests that the temporal evolution in river discharge is not an important factor controlling the seasonal cycle of hypoxic area. However, temporal variations in river discharge significantly influence stratification, as suggested by the strong negative correlation between the deviation in stratification for the Const RD run relative to the Baseline run (Fig. 3.12d) and river discharge (Fig. 3.3). A similar result was reported by Scully (2013) who used a simple oxygen parameterization with a three-dimensional circulation model in Chesapeake Bay. This is presumably because seasonal bottom oxygen drawdown is the combined result of stratification and oxygen consumption, the latter of which is more associated with the oxygen consumption in sediment than water column on the LA shelf as shown in the model experiments.

Hetland and DiMarco (2008) suggested that stratification sets a physical bound on the region where hypoxia might occur whereas respiratory oxygen consumption associated with organic matter inputs sets the biological bound on the extent and magnitude of hypoxia. In the selected year 2007, the river discharge was mostly above the annual average before June and then decreased to below the annual average for the rest of the year, except for a small rise from mid-July to August (Fig. 3.3). As a result, the most significant deviations in stratification associated with holding river discharge constant occurred in non-summer months when sediment oxygen consumption was relatively low to form hypoxia (Fig. 3.12d). In other words, while stratification responds quickly to the temporal variability in river discharge, the lack of sufficient oxygen consumption to fuel hypoxia during the same period moderates the impact of temporal variability in river discharge on hypoxia.

### 3.4.2.2. Wind forcing

Using the same realistic biogeochemical model that I used for validation in this chapter, Feng et al. (2013) illustrated how changes in wind associated with changes in the horizontal river plume position affect stratification, primary production, and thereby hypoxia on the shelf. They found that the switch of wind direction to upwelling-favorable directions facilitates hypoxia development, and that the duration of upwelling-favorable wind affects the evolution of hypoxic conditions and the dates when maximum hypoxic extent occurs (for example, an earlier start of upwelling-favorable wind leads to an earlier maximum extent of the hypoxic area). My results show that the seasonal changes in wind speed and direction significantly influence the shelf-wide stratification and hence the simulated hypoxia, which are consistent with the mechanism demonstrated by Feng et al. (2013), but eliminate the confounding effects of a full biogeochemical model. In my simulations the persistently weak upwelling-favorable wind continuously expands the lighter and fresher plume water eastward and offshore, which enhances shelf-wide stratification and promotes widespread hypoxia. In contrast, the persistently strong downwelling-favorable wind confines the fresher river plume to the near-shore and the high wind speed homogenizes the water column, reducing stratification and producing essentially no hypoxia throughout the year. Regardless of the wind direction, increasing wind speed destroys the water column stratification and hence decreases hypoxic area, whereas decreasing wind speed enhances water column stratification and hence hypoxic area. This result suggests that changes in wind speed can have a strong impact on stratification and the seasonal cycle of hypoxia.

Despite the similar wind magnitude in the UF wind and low DF wind cases, the stratification in the former is overall stronger than that in the latter case, implying that wind direction can also impact stratification significantly. Moreover, wind direction significantly influences the geographic distribution of the river plume and thereby the geographic distribution of hypoxia. For example, the UF wind case and low DF wind case have similar wind speed, but the UF wind expands the lower-salinity river plume eastward and to the offshore and hence mainly enhances stratification and hypoxic conditions over the eastern shelf and offshore regions; whereas the low DF wind

constrains the lower-salinity river plume near the shore and thereby enhances stratification and hypoxia more significantly in near-shore regions.

### **3.4.3 Consistency with observations of hypoxia**

The dominant role of SOC as an oxygen sink in driving hypoxia is consistent with observations by Quinones-Rivera et al. (2007), who estimated that SOC accounts for ~73% of the total DO loss within 1 m of the sediments during summer based on  $\delta^{18}\text{O}$  measurements and an isotope fractionation model. Using a different measurement method, Murrell and Lehrter (2011) estimated that the benthic respiration only contributes on average  $20\pm 4\%$  of total respiration below the pycnocline. The very large difference in the relative contributions of sediment and water column respiration in these two studies is due to the assumed depth of the bottom layer, as illustrated by Fennel et al. (2013) using the same full biogeochemical model as here.

Both Wiseman et al. (1997) and Bianchi et al. (2010) have demonstrated a strong correlation between the observed mid-summer hypoxic area and the Mississippi River flow. Bianchi et al. (2010) further showed that hypoxic area has a similar correlation with either river flow or nutrient loading due to the high correlation between river flow and nutrient loading. Consistent with these studies, my model simulations show that the hypoxic area is very sensitive to the magnitude of river discharge. In fact, doubling the river discharge increases the integrated anoxic area (oxygen  $< 0.5 \text{ mg l}^{-1}$ ) by 145% while halving the river discharge reduces the integrated anoxic area by 64%. This is also true for the integrated hypoxic area (oxygen  $< 2 \text{ mg l}^{-1}$ ) but the changes are smaller. Since my simulation results are based on a model independent of nutrient loading they are not obscured by the effects of nutrient discharge on hypoxic area and isolate the systems response to physical processes.

The impact of wind speed and direction on hypoxia on the LA shelf has already been discussed by Wiseman et al. (1997), who found that the low-speed, upwelling-favorable wind during summer drives the river plume eastward and offshore, intensifying stratification and inhibiting the re-oxygenation of the near-bottom waters from above. This mechanism described by Wiseman et al. (1997) is well reflected by the differences in

distribution of the river plume and stratification from my four wind simulations with different wind speeds and directions. Under persistently weak upwelling-favorable wind, the low salinity river plume extends eastward and offshore, enhancing shelf-wide stratification and promoting widespread hypoxia. Under persistently strong downwelling-favorable wind, however, the low salinity river plume is confined to the near-shore and the water column reaches near vertical homogenization, producing essentially no hypoxia. Despite the direction, increasing (decreasing) wind speed weakens (strengthens) water column stratification and hence decreases (increases) hypoxic area on the LA shelf. Wind direction influences the geographic distribution of the river plume and thereby the geographic distribution of hypoxia.

Using a statistical model, Forrest et al. (2011) found significant correlation between observed hypoxic area and east-west wind speed. Similarly, Feng et al. (2012) showed that the observed hypoxic area significantly correlates with the duration of east-west wind. With a more realistic biogeochemical model as I used for validation in this chapter, Feng et al. (2013) further elucidated the underlying mechanism, namely that wind influenced hypoxia by affecting the vertical and horizontal distribution of low salinity, high chlorophyll plume water on the shelf. Here I took an intermediate approach between the simple statistical model and the more complex biogeochemical model. The coupling of a relatively simple oxygen model to a high-resolution, three-dimensional circulation model in this chapter allowed me to separate and investigate the effects of wind forcing on the spatial and temporal variability in hypoxia on the LA shelf without the confounding effects of a full biogeochemical model. The model did not capture the observed super-saturated surface oxygen concentrations during spring and summer, which might reduce the vertical oxygen flux through the pycnocline as the oxygen gradient between the upper and lower layers was moderated. But given that I examined the difference between the baseline run and sensitivity runs with different river and wind forcing, the results should not be strongly affected by the slight discrepancy between model and observations.

It is also worth noting that the river discharge and wind forcing ranges used in my model scenarios are not all realistic. The river discharges in the High RD and Low RD

runs vary, respectively, around the upper and lower range of the long-term river discharge (1983 to 2010). The wind scenarios have preserved the event-scale variability but they do not represent realistic seasonal variations in wind forcing over the LA shelf. To assess the impacts of climate change on hypoxia, more realistic model scenarios based on climate projections of river discharge and wind field changes in this region are required.

### **3.5 Summary**

In this chapter I used a three-dimensional circulation model with a relatively simple parameterization of oxygen dynamics to isolate and investigate the effects of physical processes on the development of seasonal hypoxia on the LA shelf. Despite simply assuming a constant biological oxygen utilization rate in the water column and an oxygen- and temperature-dependent sediment oxygen consumption rate, the model reasonably reproduces the observed variability of oxygen and the hypoxic area on the LA shelf, highlighting the important role of physical processes. Further, the model sensitivity experiments disabling oxygen utilization either in water column or in the sediment show that hypoxia generation on the LA shelf is driven by oxygen utilization in the sediment.

Based on the model simulations, the temporal variability in river discharge influences stratification significantly but has less effect on the seasonal evolution of the hypoxic area because oxygen consumption moderates the impact of stratification changes associating with temporal changes in river discharge. The seasonal cycle of hypoxia and integrated hypoxic area are very sensitive to the overall magnitude of river discharge. The increase in total river discharge leads to an offshore and westward expansion of the lighter, fresher river plume and enhances shelf-wide stratification, and thereby greatly increases the hypoxic area over the shelf. In contrast, the decrease in total river discharge shrinks the plume, reducing the shelf-wide stratification and hence significantly decreases the hypoxic area.

Model simulations demonstrate that changes in wind speed have the greatest impact on the seasonal cycle of hypoxia and hypoxic duration. Persistently weak upwelling-favorable winds expand the low-salinity river plume eastward and offshore, enhancing shelf-wide stratification and promoting widespread hypoxia, whereas

persistently strong downwelling-favorable winds confine the low-salinity river plume to the near-shore and homogenize the water column, precluding the generation of hypoxia. Regardless of the wind direction, increasing wind speed weakens the water column stratification and hence decreases the hypoxic area, while decreasing wind speed does the opposite. Wind direction significantly influences the geographic distribution of the river plume and thereby the geographic distribution of hypoxia.

The facts that the simple oxygen model essentially reproduces the hypoxia evolution of the full biogeochemical model, and that physical dynamics are key for determining magnitude and distribution of hypoxia has implications for short-term hypoxia forecasting, namely that a full biogeochemical model may not be necessary for this purpose. It follows that prior to using a complex biogeochemical model, one could take an intermediate approach by developing a relatively simple model that parameterizes biological oxygen terms using empirical relationships derived from observations. This is especially the case for regions that have already developed skillful hydrodynamic models.



## CHAPTER 4

# INSIGHTS ON MULTIVARIATE UPDATES OF PHYSICAL AND BIOGEOCHEMICAL OCEAN VARIABLES USING AN ENSEMBLE KALMAN FILTER AND AN IDEALIZED MODEL OF UPWELLING<sup>3</sup>

### 4.1 Introduction

With the rapid expansion of ocean observing platforms, which now provide a wealth of observations, and growing numerical model capabilities, effective ways of combining observations and dynamic models through data assimilation (DA) are needed. While DA techniques and methodologies are well developed in meteorology and physical oceanography (e.g., Ghil and Malanotte-Rizzoli, 1991; Houtekamer and Mitchell, 1998, 2001; Kalnay, 2003), their applications in marine biogeochemical models are less mature, but actively developing (see reviews of biogeochemical state estimation in Gregg, 2008, Edwards et al., 2015, and state-parameter estimation in Gharamti et al., 2017a, b). Biogeochemical data assimilation falls into two general categories, the optimization of biogeochemical model parameters through minimization of a cost function (e.g., Fennel et al., 2001; Friedrichs et al., 2007; Kuhn et al., 2015) and updates to the biogeochemical model state by incorporating available observations sequentially (e.g., Eknes and Evensen, 2002; Natvik and Evensen, 2003; Ciavatta et al., 2011; Hu et al., 2012; Ford et al., 2012; Mattern et al., 2013; Ford and Barciela, 2017). Recent efforts have shown that model parameters can also be updated sequentially along with the model state variables (e.g., Simon et al., 2015; Gharamti et al., 2017a, b).

For biogeochemical state estimation, efforts have primarily been made in assimilating satellite ocean color observations, predominantly satellite-derived

---

<sup>3</sup>Based on: Yu, L., Fennel, K., Bertino, L., Gharamti, M.E., and Thompson, K. (2018) Insights on multivariate updates of physical and biogeochemical ocean variables using an Ensemble Kalman Filter and an idealized model of upwelling. *Ocean Modelling*, 126, 13-28

chlorophyll, into coupled physical-biogeochemical models (e.g., Natvik and Evensen, 2003; Gregg, 2008; Ciavatta et al., 2011; Hu et al., 2012; Ford et al., 2012; Fontana et al., 2013; Ford and Barciela, 2017). Assimilation of satellite ocean color products other than chlorophyll, such as phytoplankton absorption coefficients (Shulman et al., 2013), diffuse light attenuation coefficients (Ciavatta et al., 2014), and remote-sensing reflectance (Jones et al., 2016) are also being pursued. However, it has long been recognized that deficiencies in biogeochemical fields can arise from deficiencies in the physical state (e.g., Doney, 1999; Oschlies and Garcon, 1999; Doney et al., 2004) because the physics controls both horizontal and vertical transport of nutrients, oxygen, plankton and many other biogeochemical variables. Several studies have investigated the impact of assimilating physical data alone on coupled physical-biogeochemical systems (Berline et al., 2007; Samuelsen et al., 2009; While et al., 2010; El Moussaoui et al., 2011; Fiechter et al., 2011; Raghukumar et al., 2015). One important and perhaps surprising finding drawn from these studies is that, despite the clear improvement in physical model fields, the physical data assimilation alone does not generally improve, but often degrades, simulated biogeochemical fields. For example, While et al. (2010) and El Moussaoui et al. (2011) reported overestimated surface nutrients and chlorophyll concentrations, particularly in equatorial regions, associated with spurious increases in vertical velocities when assimilating physical data in global ocean models. Berline et al. (2007) found large increases in vertical nutrient fluxes in mid-latitudes and sub-tropics that were partly due to the misalignment between physical and biogeochemical fields resulting from updates of the physical fields. Raghukumar et al. (2015) also showed that assimilating physical data leads to elevated production, particularly in oligotrophic regions, and attributed the overestimation to a net upward nutrient flux resulting from high vertical velocity fluctuations due to the “initialization shocks” after updates to the density distribution, and increased nutrient variance on density surfaces due to the adjustment of physical variables in the assimilation step.

Collectively the above studies demonstrate that adjusting only physical or biogeochemical fields is not sufficient to improve the full three-dimensional (3D) biogeochemical model state. An obvious next step is the simultaneous updating of

physical and biogeochemical fields. Two approaches have emerged to address it. The simpler approach is applying a correction to the nutrient field alongside the physical data assimilation (Shulman et al., 2013, While et al. 2010). The second approach is to jointly assimilate physical and biogeochemical observations into the models. To date, few studies have explored this idea but with encouraging results (Anderson et al., 2000; Ourmières et al., 2009; Song et al., 2016a,b; Mattern et al., 2016). These studies show that assimilating both physical and biogeochemical data can maintain dynamical consistency between the physical and biogeochemical fields and provide better state estimates than only assimilating one or the other. However, one clear drawback of this approach is that the required physical and biogeochemical observations might not always be available concurrently.

Here I propose and test an alternative approach for updating both types of model fields even when only one data type (biogeochemical or physical) is available. The approach takes advantage of the inherently multivariate nature of the Ensemble Kalman Filter (EnKF) to generate multivariate increments that can be applied consistently to all model state variables. While the EnKF has been used to assimilate physical or biological ocean observations in the past, its ability to update biological model fields by assimilating physical observations and *vice versa* has not yet been tested in ocean applications. This paper aims to systematically assess whether, when and why multivariate EnKF updates of both physical and biogeochemical fields can outperform isolated updates of physical or biogeochemical fields by assimilating only one observation type, and compare these two DA strategies against the joint updates of both fields by assimilating both observation types. This is achieved by conducting a series of twin experiments in an idealized ocean channel that experiences wind-driven upwelling.

## **4.2 Model description and experimental setup**

### **4.2.1 The coupled physical-biogeochemical model**

I use the ROMS model configured in a computationally efficient idealized channel. ROMS is a free-surface, terrain-following, primitive equation ocean model that has been used extensively for coupled physical-biogeochemical modeling and data assimilation

(e.g., Hu et al., 2012; Raghukumar et al., 2015; Song et al., 2016a, 2016b). The idealized channel is 82 km wide, with the depth symmetrically increasing from 25 m at the two edges to 140 m in the middle (Fig. 4.1). The model grid is uniformly spaced with a horizontal resolution of 1 km, generating 84 cross-channel and 82 along-channel grid points, and has 16 terrain-following vertical layers with thickness ranging from 1.6 m at the surface near the channel edges to 22.6 m at the bottom of the mid-channel. Periodic lateral boundary conditions are applied to the southern and northern open boundaries; that is, any physical or biogeochemical tracer or flow that leaves the domain through one boundary will re-enter at the opposite side. Vertical mixing is parameterized using the Mellor and Yamada (1982) Level 2.5 turbulence closure scheme. Bottom friction is specified using a linear drag formulation.

The model is forced with a uniform along-channel wind that generates upwelling on one side of the channel and downwelling on the other. The wind forcing is prescribed by a clipped sine curve resulting in 30 days of non-zero wind stress followed by 30 days of relaxation without any wind forcing. Gaussian noise with a standard deviation of 0.002 Pa is added to generate a more realistic wind regime. One cycle with a peak wind stress of 0.07 Pa (high wind) and 0.06 Pa (low wind) is shown in Figure 4.1a.

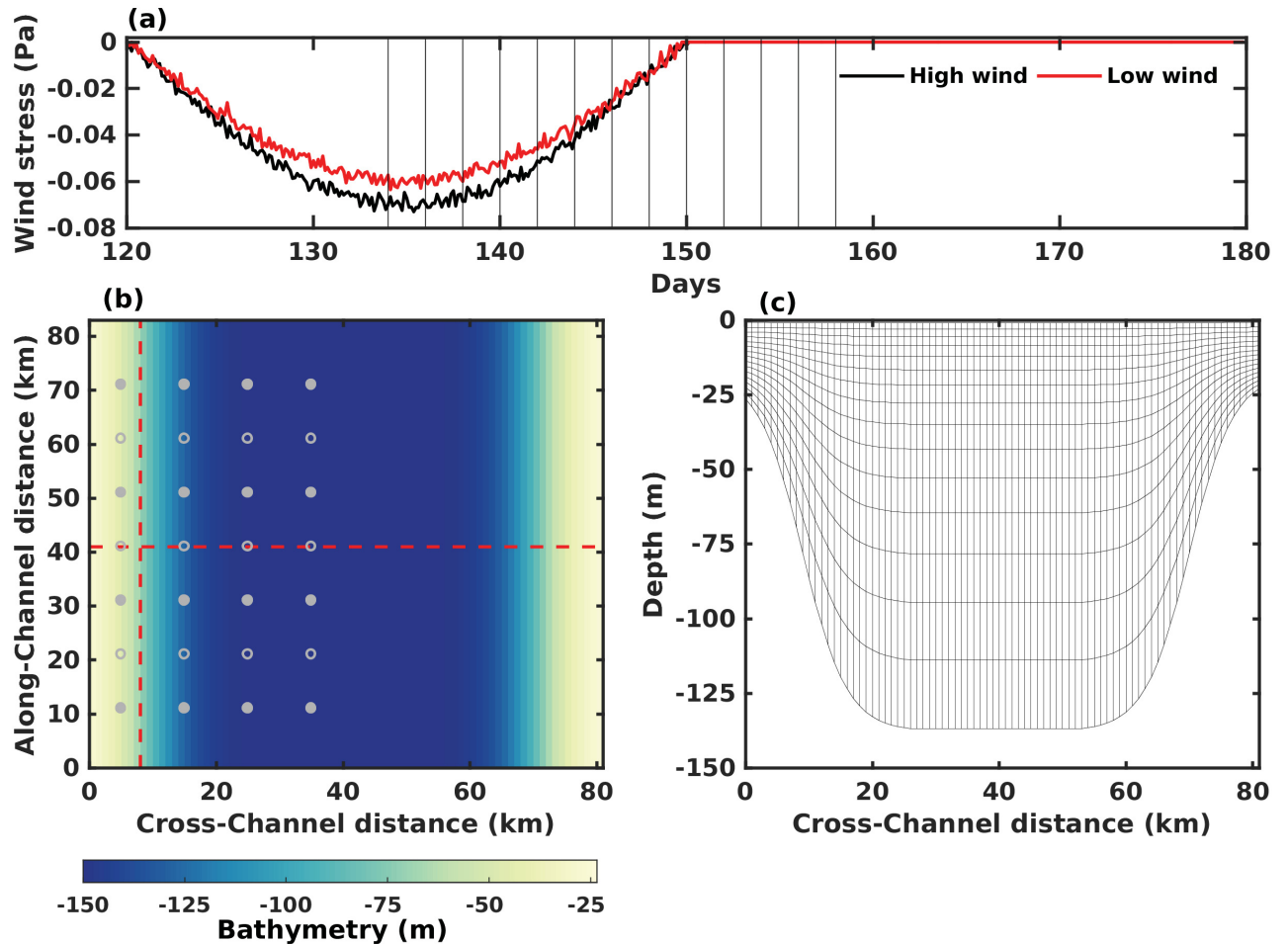


**Fig. 4.1.** (a) Wind stress for the high-wind and low-wind model runs. The vertical lines indicate the timing of assimilation steps. (b) Model bathymetry and (c) vertical grid of cross-channel transect. The red dashed lines in (b) show the position of the cross-channel transect and an along-channel section. The circles show the 28 stations where temperature profiles are sampled. The filled circles show the 16 stations where nitrate profiles are sampled.

The biogeochemical component of the coupled model uses the nitrogen cycle model of Fennel et al. (2006). The model is a relatively simple representation of the pelagic nitrogen (N) cycle, including two species of dissolved inorganic nitrogen, nitrate ( $\text{NO}_3$ ) and ammonium ( $\text{NH}_4$ ); one phytoplankton group (Phy); chlorophyll (Chl) as a separate state variable to allow for photoacclimation; one zooplankton group (Zoo); and two pools of detritus representing large, fast-sinking particles (LDet) and suspended, small particles (SDet). The model accounts for photoacclimation of phytoplankton based on the model of Geider et al. (1997), resulting in a variable ratio of chlorophyll to

phytoplankton biomass. In the model, the biogeochemical fields do not influence physical fields, i.e. there is no feedback from biology to physics. This coupled model has been a valuable tool for understanding interacting physical and biogeochemical processes within realistic configurations for both coastal (e.g., Fennel et al., 2006, 2008) and open ocean ecosystems (e.g., Xue et al., 2013), as well as for data assimilation experiments (e.g., Hu et al., 2011; Mattern et al. 2013).

The biogeochemical component of the coupled model was spun up for 1 year without any wind forcing, and no flow at the lateral boundaries. The initial temperature ranges from 14.5 °C at the mid-channel bottom to 22 °C at the surface, initial nitrate ranges from 13.5 mmol N m<sup>-3</sup> at depth to 0.5 mmol N m<sup>-3</sup> at the surface, and all other initial biogeochemical variables were homogeneous at a low positive value. Salinity was fixed at 35 PSU and surface heat flux was not included in this idealized setup. The biogeochemical variables reached a steady state after 1 year of spin-up. The spun-up biogeochemical fields were used as initial condition for all coupled simulations, which were forced with high or low wind shown (Fig. 4.1a) for 180 days (covering three wind cycles).

#### **4.2.2 Experimental framework**

The performance of different data assimilation strategies is evaluated in twin experiments that consist of a reference model run representing the ‘truth’ from which synthetic observations are generated, and a model with biased physics and biology that is subject to ensemble-based assimilation of the synthetic observations. I test two contrasting scenarios: Scenario 1, where the forecast model is forced with lower wind stress and a lower photosynthesis-irradiance (PI) parameter value than the truth leading to underestimation of the true upwelling and productivity; Scenario 2, where a higher wind stress and higher PI value lead to overestimation of upwelling and productivity. For the sake of brevity, I only detail the experimental setup of Scenario 1; Scenario 2 is identical except for the wind forcing and biological parameter set.

In Scenario 1, the reference (or ‘truth’) is generated by running the coupled model as described in section 4.2.1 and forced with higher wind (peak wind stress of 0.07 Pa,

denoted as high wind in Fig. 4.1a). The along-channel, northward wind leads to upwelling of nutrient-rich, cold water at the western edge of the channel stimulating phytoplankton growth (assuming Coriolis frequency  $f > 0$ ).

Synthetic observations are sampled from the reference run, including sea surface height (SSH), sea surface temperature (SST) and surface chlorophyll at all grid points (assuming no data missing due to cloud cover), and 28 temperature and 16 nitrate profiles from a regular sampling grid (see Fig. 4.1b). Typical Gaussian observation errors, i.e. variable (mean, standard deviation), of  $N(0, 0.3^\circ\text{C})$  for temperature (both SST and temperature profiles),  $N(0, 1 \text{ cm})$  for SSH,  $N(0, 35\% \cdot \text{true concentration})$  for surface chlorophyll, and  $N(0, 10\% \cdot \text{true concentration})$  for nitrate profiles are added to the synthetic data. In addition, smaller errors in the biological observations, i.e.  $N(0, 10\% \cdot \text{true concentration})$  for chlorophyll and  $N(0, 5\% \cdot \text{true concentration})$  for nitrate, are tested as described in section 4.2.2.3.

In the biased model, the peak wind stress is about 14% smaller. Gaussian noise with a standard deviation of 0.002 Pa was added to the wind stress to create an ensemble of wind forcing files (one realization is shown in Fig. 4.1a, denoted as low wind). In addition, the five biological parameters to which the system is most sensitive were perturbed. These parameters were identified in sensitivity experiments as follows. For each parameter the model was run twice, after doubling and halving the parameter value. The five parameters for which these perturbations resulted in the largest total Root Mean Square (RMS) difference of biogeochemical variables to the unperturbed simulation are referred to as the most sensitive ones. In the ensemble simulations, all five parameters are sampled from a uniform distribution around their nominal value with a variance of 75% of the nominal value. The nominal values of the top two most sensitive parameters, the photosynthesis-irradiance initial slope ( $0.015 \text{ mg C (mg chl W m}^{-2} \text{ d}^{-1})$ ) and zooplankton grazing rate ( $0.6 \text{ d}^{-1}$ ), are set to be 40% lower than those of the reference run to simulate model bias errors. The other three parameters, phytoplankton growth rate ( $1.0 \text{ d}^{-1}$ ), mortality rate ( $0.1 \text{ d}^{-1}$ ), and maximum chlorophyll to carbon ratio ( $0.0535 \text{ mg chl (mg C)}^{-1}$ ), are not biased.

### 4.2.2.1 DEnKF algorithm

I use the deterministic formulation of the EnKF (DEnKF), which was introduced by Sakov and Oke (2008) and has been used previously in biogeochemical data assimilation applications (e.g., Simon et al., 2015; Jones et al., 2016).

The central idea underlying the EnKF is that an ensemble of model simulations can be used to approximate the model's estimate of uncertainty, and that the model state can be updated using available observations as the ensemble is integrated forward in time (Evensen 1994). The EnKF algorithm consists of sequential forecast and analysis steps. During the forecast step, the model ensemble is propagated forward in time. During the analysis step, the model state is updated using the Kalman Filter (KF) analysis equation:

$$\mathbf{x}^a = \mathbf{x}^f + \mathbf{K}(\mathbf{d} - \mathbf{H}\mathbf{x}^f), \quad (4.1)$$

where  $\mathbf{x}$  is the  $n \times 1$  model state estimate vector ( $n$  is the number of model state variables at all grid points), the superscripts  $a$  and  $f$  represent the analysis and the forecast estimates, respectively,  $\mathbf{d}$  is the  $m \times 1$  vector of observations ( $m$  is the number of available observations),  $\mathbf{H}$  (linear in this form, dimension of  $m \times n$ ) is the measurement operator mapping the model state onto the observations, and  $\mathbf{K}$  is the  $n \times m$  Kalman gain matrix, given as

$$\mathbf{K} = \mathbf{P}^f \mathbf{H}^T (\mathbf{H} \mathbf{P}^f \mathbf{H}^T + \mathbf{R})^{-1} \quad (4.2)$$

where  $\mathbf{P}^f$  represents the  $n \times n$  prior sample error covariance matrix (approximated using the forecast ensemble),  $\mathbf{R}$  is the  $m \times m$  observation error covariance, and superscript  $T$  denotes matrix transpose.

In the original stochastic EnKF (Burgers et al. 1998), the forecast ensemble  $\mathbf{X}^f$  is updated via Kalman analysis Eq. 4.1 and requires perturbing observations  $\mathbf{d}$  in order to obtain an analysis error covariance consistent with that given by the (linear) Kalman Filter. In contrast, the DEnKF updates the ensemble mean and ensemble anomalies separately without perturbing observations, and is hence termed 'deterministic'. First, the



forecast ensemble mean  $\bar{X}^f$  is updated as in Eq. 4.1. Then, the forecast ensemble anomalies  $A^f$  are updated to obtain the analysis ensemble anomalies  $A^a$  by  $A^a = A^f - \frac{1}{2}KHA^f$ , which ensures that the resulting covariance matrix is slightly inflated compared to the theoretical value given by the Kalman Filter. Finally, the analysis ensemble is reconstructed as  $X^a = A^a + [\bar{X}^a, \dots, \bar{X}^a]$ . For more details on the DEnKF see Sakov and Oke (2008).

In principle, the DEnKF can update the entire model state based on the correlations in the ensemble covariance between the observations and model variables. However, computational constraints often prohibit inclusion of all 3D state variables in the assimilation state vector  $X_i^f$  (the  $i$ th ensemble member). Here I limit updates to the four biological variables (nitrate, chlorophyll, phytoplankton and zooplankton) and one physical variable (temperature) that are most relevant to the dynamics of the system.

#### 4.2.2.2 Assimilation settings

I chose an ensemble size of 20 for the data assimilation experiments. Relatively small ensembles like this can lead to spurious correlations between distant grid points. To prevent the potential negative effects of spurious correlations, I applied a distance-based localization method known as local analysis (Evensen, 2003; Hunt et al., 2007; Sakov and Bertino, 2011). In local analysis, the spatial domain of influence of each observation is artificially reduced by multiplying the ensemble anomalies and innovations with a distance-dependent localization function (Gaspari and Cohn 1999). I chose a localization radius of 20 km for SST, SSH, temperature profiles and nitrate profiles, and 10 km for surface chlorophyll. Additionally, to account for the underestimation of the forecast error covariance due to the small ensemble size, an inflation factor of 1.05 was applied to the ensemble anomalies inflating the ensemble around its mean at every update step (Anderson and Anderson 1999). The localization radius and inflation factor are based on initial tests that involve selecting the values that best reduce the model-data errors without causing ensemble collapse or generating discontinuities in the analyzed fields.

Additional practical implementation choices were made to make the DEnKF performance more robust as follows. Because chlorophyll and nitrate concentrations at some grid points can be as low as  $10^{-4}$  mg/m<sup>3</sup> (for chlorophyll) or mmol/m<sup>3</sup> (for nitrate), resulting in extremely low magnitudes of the observation error covariance  $\mathbf{R}$ , I set a lower limit of  $10^{-2}$  for the diagonal elements of  $\mathbf{R}$  corresponding to chlorophyll and nitrate observations. This is equivalent to artificially increasing the error of very low chlorophyll and nitrate observations. This can be thought of as applying inflation in the observation space, which has already been explored in Anderson (2009). I also inflate the assumed observation error covariance by a factor of 2 when updating the ensemble anomalies while using the original observation error variance for updating the ensemble mean as proposed in Sakov et al. (2012). This is done to produce a weaker update for the ensemble-based state error covariance without changing the ensemble analysis mean, and hence retain a larger ensemble spread. To prevent an initial shock to the system due to large initial updates, I increased the observation error by a factor of 8, 4 and 2 for the first three DA steps, respectively as in Sakov et al. (2012). Finally, a post-processing step was performed at the end of each update step resetting any negative values of temperature and biogeochemical variables to their corresponding forecast values (less than 0.2% of grid cells were affected by this throughout the assimilation period).

#### **4.2.2.3 Data assimilation experiments**

I carried out a series of assimilation experiments for Scenarios 1 and 2 (Table 4.1) using different strategies for assimilating a single (biogeochemical or physical) or both observational data types: Method 1 “Isolated updates”, where only one of the two data types is used, either physical observations to update physical model fields or biogeochemical observations to update biogeochemical model fields; Method 2 “Multivariate updates | single data type”, where only one data type is used to update both physical and biogeochemical model fields taking advantage of the multivariate covariance structure within the DEnKF; and Method 3 “Joint updates | both data types”, where both data types are assimilated in a two-step update, with physical observations being used first and biogeochemical observations used next. The acronyms for assimilation experiments introduced in Table 4.1 are in accord with the posterior probability of the model state

given the observations (e.g.,  $p(\text{model} \mid \text{observation})$ ). In all experiments, the DEnKF update is performed every two days during upwelling peaks of the second and third wind cycle (day 74 to 98 and 134 to 158, respectively) leading to 26 assimilation steps in total. Detailed analysis of the experiments focuses on the third wind cycle when the largest deviation between the biased ensemble runs and the true state has developed.

The assimilation impact is assessed by comparing the assimilative runs to an ensemble of model simulations with the same model configuration but without any data assimilation. This ensemble run is referred to as the ‘free run’. The model’s forecast skill, a metric of how long the model’s forecast from the analysis outperforms the free run, is also assessed. For this purpose, I perform 25-day ensemble runs, referred to as ‘forecast runs’, that are initialized from the updated states on day 140 (the 17<sup>th</sup> DA step) and forced with the same winds as the assimilation runs.

Model-data misfit is quantified by examining the deviations from the truth (model minus truth). For DA runs at assimilation times, when both forecast and analysis exist, the forecast ensemble mean is used for calculating the deviation. I first computed the daily deviations at each grid point during the analysis period (day 134 to 158), and then averaged the deviation or absolute deviation values over space and time to obtain the mean deviation (bias) and the mean absolute deviation (MAD). Symbols  $\text{bias}_{\text{surf}}$  and  $\text{MAD}_{\text{surf}}$  represent bias and MAD averaged over the surface layer only, whereas  $\text{MAD}_{\text{all}}$  represents averaging over the entire water column.

**Table 4.1.** Overview of assimilation experiments. Assimilated or updated fields are checked (✓) and marked by blue and green area to distinguish physical and biogeochemical fields. The numbers 1 and 2 in Method 3 experiments indicate the step where the corresponding field is assimilated or updated. The second column gives the code for each experiment. In accord with the posterior probability of the model state given the observations (e.g.,  $p(\text{model} \mid \text{observation})$ ) the capital letters that appear before the vertical line define the 3D fields to be updated. B, N and T correspond to the biogeochemical variables (chlorophyll, phytoplankton, zooplankton and nitrate), just nitrate, and temperature, respectively. The variables that appear after the vertical line define the observations that are assimilated, where *chl*, N,  $P_{\text{surf}}$  and  $P_{\text{all}}$  denote surface chlorophyll, nitrate profiles, physical variables at the surface (SSH and SST), and physical variables at both surface and depth (SSH, SST and T profiles), respectively. The subscript following *chl* (or N) denotes reductions in the observation error of surface chlorophyll (or nitrate profiles) to 10% (or 5%) instead of the default 35% (10%) used in the other experiments. The underscore in Method 3 codes indicates the separation of the two update steps.

	Experiment	Updated 3D Fields			Assimilated Observations			
		T	N	chl, phy, zoo	SSH, SST	T profiles	Surface chl	N profiles
<b>Method 1</b> “Isolated updates”	B <i>chl</i>		✓	✓			✓	
	B <i>chl</i> <sub>10%</sub>		✓	✓			✓	
	B <i>chl</i> N		✓	✓			✓	✓
	B <i>chl</i> N <sub>5%</sub>		✓	✓			✓	✓
	T <i>P</i> <sub>surf</sub>	✓			✓			
	T <i>P</i> <sub>all</sub>	✓			✓	✓		
<b>Method 2</b> “Multivariate updates   single data type”	TB <i>chl</i>	✓	✓	✓			✓	
	TB <i>chl</i> <sub>10%</sub>	✓	✓	✓			✓	
	TB <i>chl</i> N	✓	✓	✓			✓	✓
	TB <i>chl</i> N <sub>5%</sub>	✓	✓	✓			✓	✓
	TN <i>P</i> <sub>surf</sub>	✓	✓		✓			
	TN <i>P</i> <sub>all</sub>	✓	✓		✓	✓		
<b>Method 3</b> “Joint updates   both data types”	T <i>P</i> <sub>surf</sub> _B <i>chl</i>	✓1	✓2	✓2	✓1		✓2	
	T <i>P</i> <sub>all</sub> _B <i>chl</i> N	✓1	✓2	✓2	✓1	✓1	✓2	✓2
	TN <i>P</i> <sub>surf</sub> _B <i>chl</i>	✓1	✓1, 2	✓2	✓1		✓2	
	TN <i>P</i> <sub>all</sub> _B <i>chl</i> N	✓1	✓1, 2	✓2	✓1	✓1	✓2	✓2

## 4.3 Results

Below I provide a detailed analysis of Scenario 1 (the case underestimating upwelling and productivity). Results from Scenario 2 (the case overestimating upwelling and productivity) are presented in section 4.3.4.

### 4.3.1 Comparison between truth and free run

Time series of domain-averaged surface temperature, nitrate and phytoplankton from the truth, free run and different DA runs are shown in Figure 4.2. Compared to the truth, the free run is overall warmer and has lower surface nitrate and phytoplankton due to weaker upwelling. Figure 4.3 shows a snapshot of SSH, surface temperature, nitrate and phytoplankton on day 140. SSH anomalies on both upwelling and downwelling edges are smaller in the free run than the truth. In the free run, the band of cold, nutrient-rich water along the upwelling edge is much narrower than in the truth, and the band of elevated phytoplankton concentrations detached from the coast in the truth is not simulated by the free run. The corresponding vertical distributions of the same variables along a cross-channel transect are shown in Figure 4.4. The reference isotherm (represented by the 16 °C isotherm) and reference isopleth of nitrate (represented by the 5 mmol NO<sub>3</sub> m<sup>-3</sup> isoline) coincide and are deeper in the free run than the truth at the upwelling edge. Along-channel section-averaged temperature and nitrate profiles near the upwelling edge (Fig. 4.5a, e) show that in the free run temperature is warmer and nitrate concentration lower than the truth in the top 60 m. The differences between the truth and free run are also reflected by the positive bias<sub>surf</sub> in temperature, negative bias<sub>surf</sub> in nitrate and phytoplankton as well as the large MAD<sub>all</sub> in all variables (Fig. 4.6).

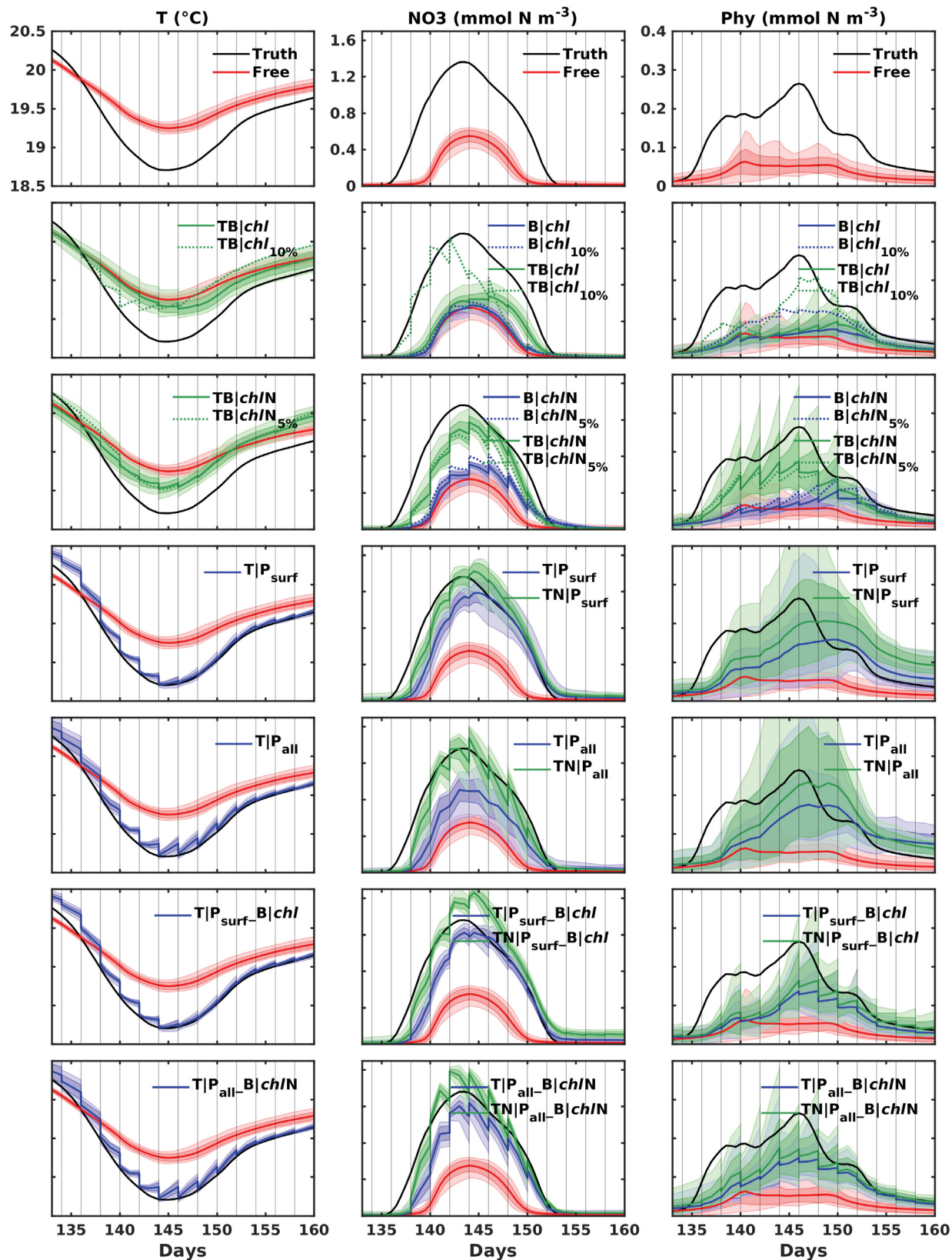


**Fig. 4.2.** Time series of the surface domain-averaged water temperature (T), concentrations of nitrate (NO<sub>3</sub>), and phytoplankton (Phy) for truth, free run and different



assimilation runs. For the free and assimilation runs, the ensemble means are shown as solid colored lines, the standard deviation of the ensemble as dark colored area, and the range between the minimum and maximum value of the ensemble as light colored area. Black vertical lines indicate the timing of assimilation steps.

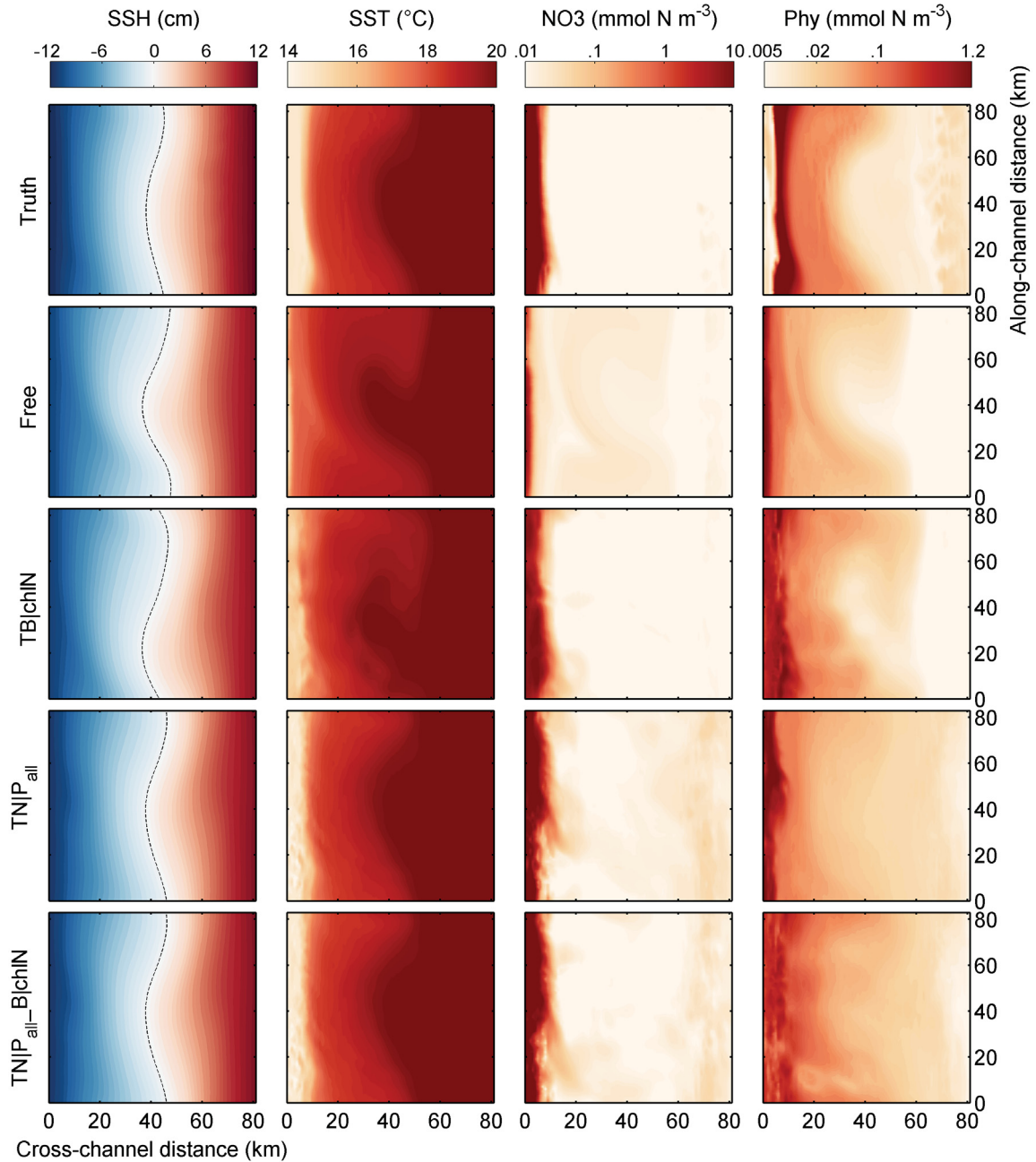


**Fig. 4.3.** Surface layer on day 140 (assimilation step 17) for different state variables from the truth, free run and different assimilation runs. The black dashed line shows the zero contour line.

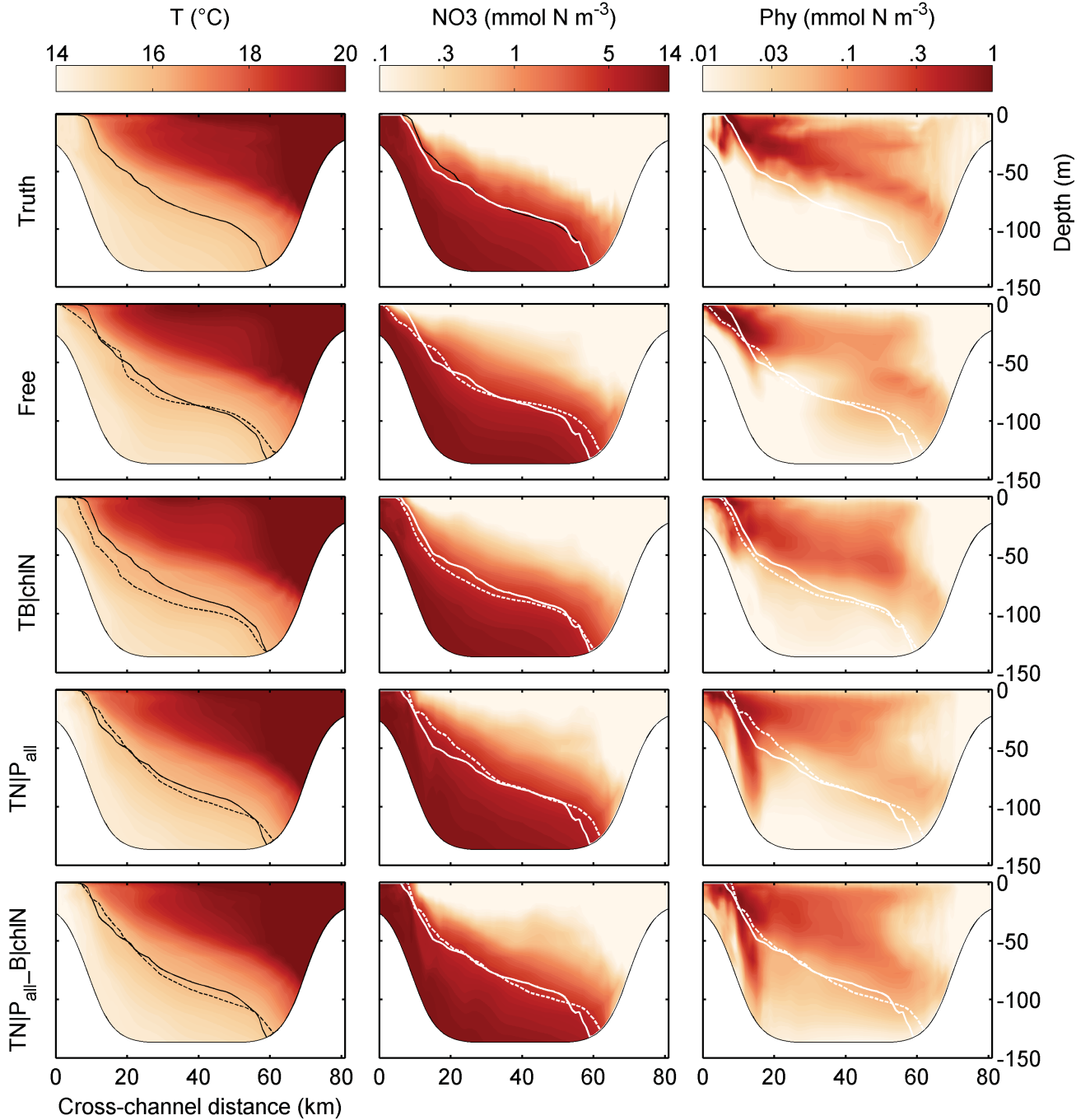


**Fig. 4.4.** Cross-channel transect (see Fig. 4.1 for its location) on day 140 (assimilation step 17) for different state variables from the truth, free run and different assimilation runs. The 16 °C isotherm and 5 mmol  $\text{NO}_3 \text{ m}^{-3}$  isopleth for the truth are marked as solid black and white lines, respectively. Dashed black and white lines mark the 16 °C isotherm and 5 mmol  $\text{NO}_3 \text{ m}^{-3}$  isopleth for the actual simulation in each panel.



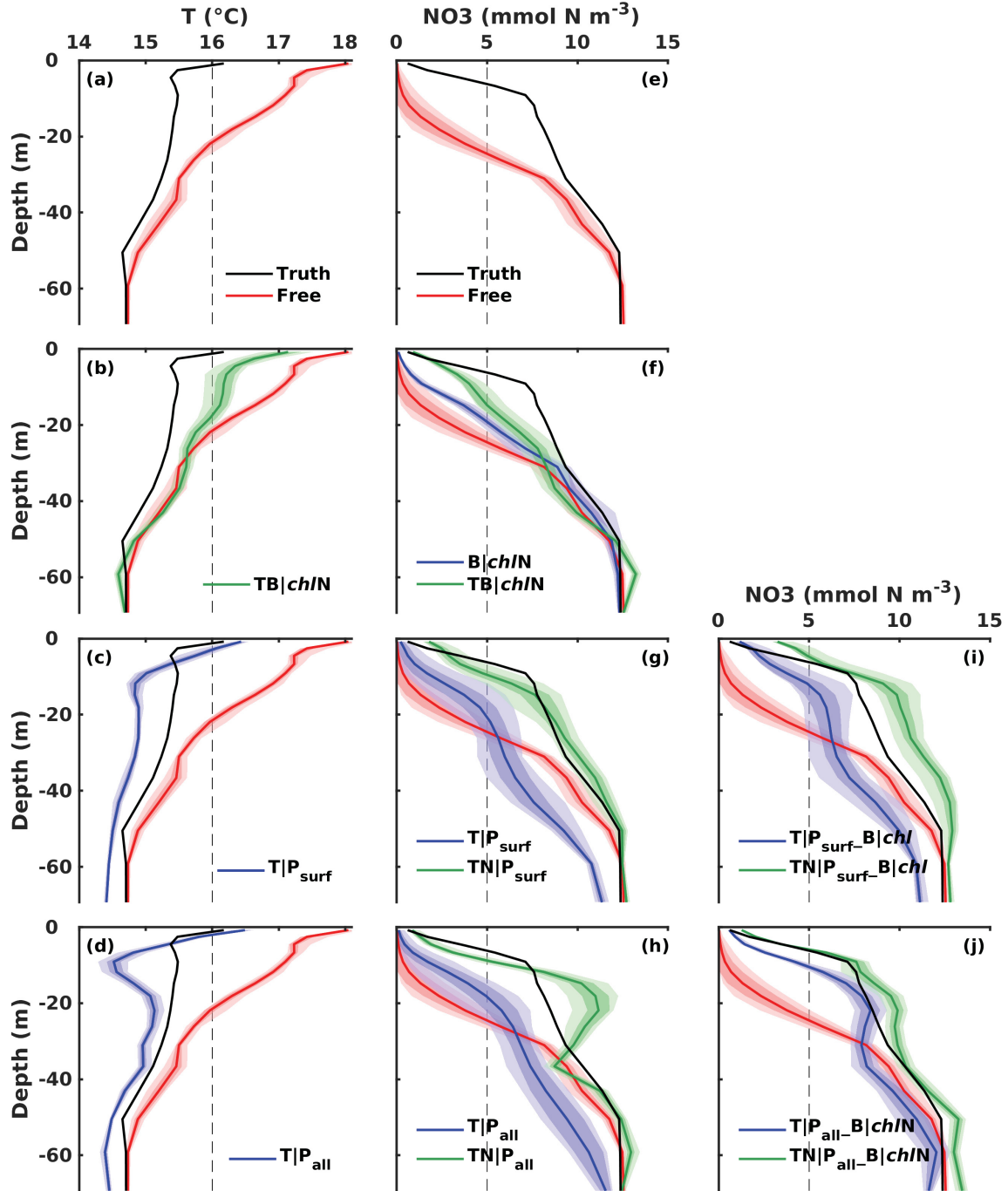


**Fig. 4.5.** Averaged (a-d) temperature ( $T$ ) and (e-j) nitrate ( $\text{NO}_3$ ) profiles over stations along the along-channel section (see Fig. 4.1 for their locations) on day 140 (assimilation step 17) for the truth, free run and different assimilation runs. For the free and assimilation runs, the solid colored lines represent ensemble means of the section-averaged profiles, the dark colored areas represent standard deviation of the ensemble, and the light colored areas represent range between the minimum and maximum value of the ensemble. The positions of  $16\text{ }^\circ\text{C}$  isotherm and  $5\text{ mmol NO}_3\text{ m}^{-3}$  isopleth are marked as dashed lines.

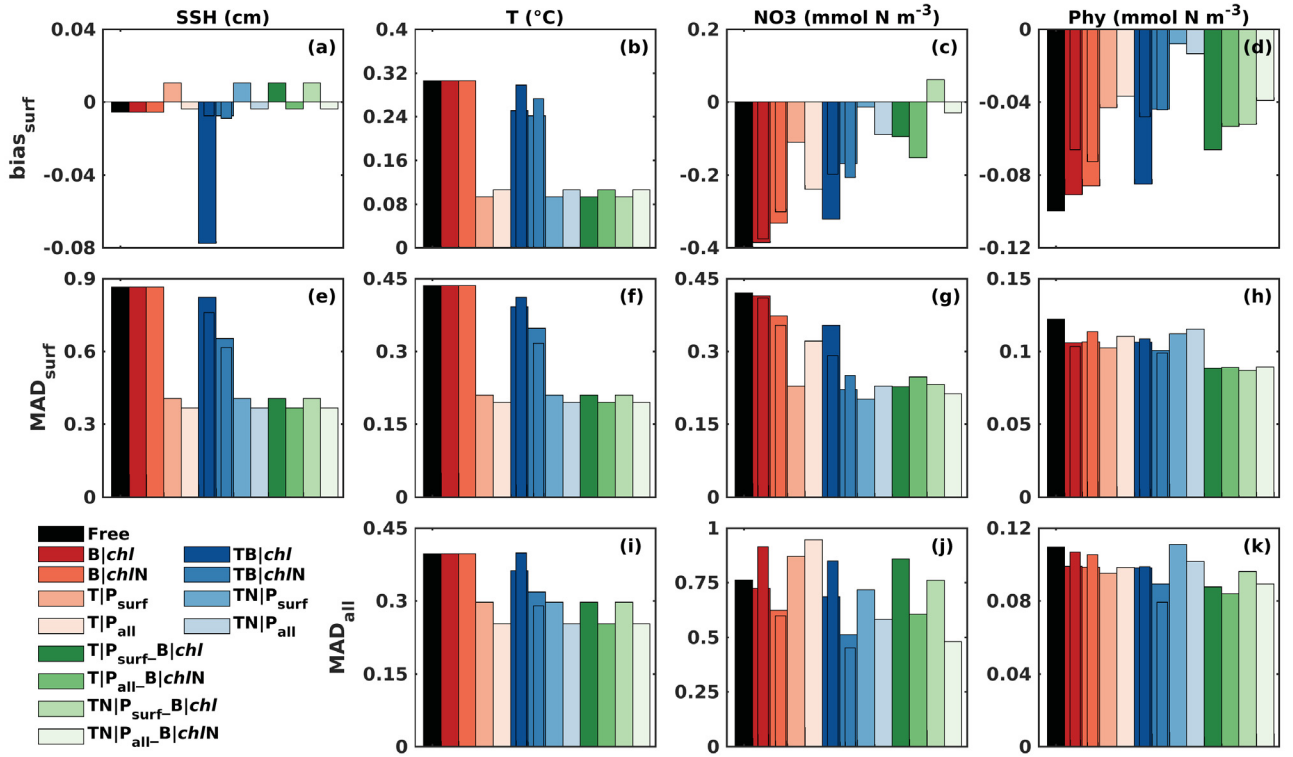


**Fig. 4.6.** The domain- and time-averaged (a-d)  $\text{bias}_{\text{surf}}$ , (e-h)  $\text{MAD}_{\text{surf}}$  and (i-k)  $\text{MAD}_{\text{all}}$  for different state variables from the free run and different assimilation runs. The narrower bars partially overlapping some assimilation runs represent the metrics for sensitivity runs with lower observation error of chlorophyll ( $\text{Blchl}_{10\%}$  in dark red and  $\text{TB|chl}_{10\%}$  in dark blue) and nitrate ( $\text{BlchlN}_{5\%}$  in 2<sup>nd</sup> red bar and  $\text{TB|chlN}_{5\%}$  in 2<sup>nd</sup> blue bar), respectively.

### 4.3.2 Impact of assimilation on physical and biogeochemical states

#### 4.3.2.1 Method 1 “Isolated updates”

First, I assess the assimilation impact when biogeochemical variables are used to update only biogeochemical variables, or physical variables to update only physical variables. Assimilating surface chlorophyll to correct the biogeochemical variables alone ( $\text{Blchl}$  and  $\text{Blchl}_{10\%}$ ) barely affects the time evolution of surface nitrate and improves surface phytoplankton only when the chlorophyll observation error is reduced to 10% (Fig. 4.2, second row). The point-to-point comparison metrics confirm that  $\text{Blchl}$  and  $\text{Blchl}_{10\%}$  slightly reduce  $\text{bias}_{\text{surf}}$  and  $\text{MAD}_{\text{surf}}$  for phytoplankton, but  $\text{Blchl}_{10\%}$  leads to

an increase in  $MAD_{all}$  for nitrate and phytoplankton (Fig. 4.6). In *BlchlN* and *BlchlN*<sub>5%</sub>, where nitrate profiles are assimilated in addition to surface chlorophyll, the updates in surface nitrate and phytoplankton are more noticeable than in *Blchl*, but the ensemble mean is still far from the truth (Fig. 4.2, third row), and the reference isopleth of nitrate in *BlchlN* is only slightly lifted up to the truth (Fig. 4.5f). The metrics in Figure 4.6 show that *BlchlN* improves nitrate with a smaller  $bias_{surf}$  and  $MAD_{all}$  than *Blchl*. Reducing the nitrate observation error (*BlchlN*<sub>5%</sub>) leads to little further improvement relative to *BlchlN*.

Assimilating SST and SSH ( $TIP_{surf}$ ) remarkably improves surface temperature and increases surface nitrate and phytoplankton concentrations toward the truth without directly updating them during analysis steps (Fig. 4.2, fourth row). However, the phytoplankton peak is delayed and concentrations are overestimated after the peak in upwelling.  $TIP_{surf}$  clearly lifts up the reference isotherm and isopleth of nitrate toward the truth (Fig. 4.5c, g), but degrades the nitrate profile at depths greater than 25 m (Fig. 4.5g). The comparison metrics show that  $TIP_{surf}$  improves SSH, temperature, surface nitrate, and phytoplankton with lower biases and MAD values, but degrades subsurface nitrate with higher  $MAD_{all}$  than the free run (Fig. 4.6). Compared to  $TIP_{surf}$ , assimilating additional temperature profiles ( $TIP_{all}$ ) improves the timing of the phytoplankton peak but overestimates phytoplankton more after peak upwelling (Fig. 4.2, fifth row). Comparison metrics in Figure 4.6 show that  $TIP_{all}$  further improves temperature with lower  $MAD_{all}$ , but degrades nitrate with higher MAD values than those in  $TIP_{surf}$  and the free run (Fig. 4.6).

None of the Method 1 “Isolated updates” approaches satisfactorily improves the biogeochemical ocean model state, although the physical model state is remarkably improved by assimilating the physical data.

#### 4.3.2.2. Method 2 “Multivariate updates | single data type”

Second, I assess the impact of multivariate updates, where a single data type (biogeochemical or physical observations) is used for multivariate updates of biogeochemical variables and temperature. Assimilating only surface chlorophyll (TBchl) slightly improves surface temperature and nitrate relative to Bchl (Fig. 4.2, second row) with slightly smaller  $\text{bias}_{\text{surf}}$  and  $\text{MAD}_{\text{all}}$  (Fig. 4.6). Reducing the chlorophyll observation error (TBchl<sub>10%</sub>) leads to larger increases in surface nitrate and phytoplankton (Fig. 4.2, second row) that further reduce their  $\text{bias}_{\text{surf}}$  and nitrate  $\text{MAD}_{\text{surf}}$ , but also substantially increases nitrate  $\text{MAD}_{\text{all}}$ . Assimilating additional nitrate profiles to update both physical and biogeochemical fields in TBchlN and TBchlN<sub>5%</sub>, remarkably improves the time evolution of surface temperature during the upwelling period, and nitrate and phytoplankton for the entire time period (Fig. 4.2, third row) compared to BchlN, BchlN<sub>5%</sub> and TBchl. Improvement in TBchlN is also obvious in the spatial distributions, with an extended area of cold and high-nutrient water along the upwelling edge (Fig. 4.3) and a clear lift of the reference isotherm near the surface and isopleth of nitrate toward the truth compared to the free run and BchlN (Figs. 4.4 and 4.5). TBchlN and TBchlN<sub>5%</sub> yield the smallest  $\text{MAD}_{\text{all}}$  for all variables among DA runs that only assimilate biogeochemical observations (Fig. 4.6).

Then I used physical observations (SSH and SST in TNIP<sub>surf</sub>; SSH, SST and temperature profiles in TNIP<sub>all</sub>) for multivariate updates of physical variables and the nitrate field. I only update the nitrate field instead of all biogeochemical variables because of the high correlation between physical fields and nitrate in contrast to the relatively low correlation between physical fields and other biogeochemical variables. Compared to TIP<sub>surf</sub> and TIP<sub>all</sub> (Method 1), TNIP<sub>surf</sub> and TNIP<sub>all</sub> lead to larger increases in surface nitrate and phytoplankton and overall agree better with the truth except that surface phytoplankton is overestimated after peak upwelling (Fig. 4.2, fourth and fifth rows). TNIP<sub>all</sub> also remarkably improves the spatial distribution of surface and subsurface temperature and nitrate, but fails to improve that for phytoplankton (Figs. 4.3 and 4.4). Vertically viewed, both TNIP<sub>surf</sub> and TNIP<sub>all</sub> effectively lift the depths of reference

isotherm and isopleth of nitrate approaching the truth (Fig. 4.5). Overall  $TNIP_{all}$  yields lower  $MAD_{all}$  for temperature and nitrate than  $TNIP_{surf}$  (Fig. 4.6).

Method 2 “Multivariate updates | single data type” improves the physical and biogeochemical ocean model states more satisfactorily than Method 1 “Isolated updates” does.

#### **4.3.2.3. Method 3 “Joint updates | both data types”**

The last set of assimilation experiments used both data types (physical and biogeochemical observations) to provide a two-step update, where physical observations are assimilated first to update physical fields or both types of fields and biogeochemical observations are assimilated next to update biogeochemical fields only. I have also performed tests where in the second step biogeochemical observations are used to update both types of variables but found this slightly degraded the updated physical fields from step one, probably because in the first step physical observations already provide sufficient improvement to physical fields. Here I used a two-step update approach for two practical reasons: (i) its relatively lower computation cost, and (ii) ease of selecting subsets of variables to be updated. Theoretical considerations do provide some support for the two-step update. Specifically in a Bayesian formulation, if the observations have non-correlated errors, one and two-step updates should produce the same results (e.g., Bierman 1977). I note however, this exact equivalence is broken by the presence of localization, inflation, and the linearity assumption underlying the EnKF.

Compared with the physical DA runs ( $TIP_{surf}$ ,  $TIP_{all}$ ,  $TNIP_{surf}$  and  $TNIP_{all}$ ), Method 3 runs ( $TIP_{surf\_Blchl}$ ,  $TIP_{all\_Blchl/N}$ ,  $TNIP_{surf\_Blchl}$  and  $TNIP_{all\_Blchl/N}$ ) are as effective in increasing the surface nitrate, but underestimate surface phytoplankton slightly more during peak upwelling while agreeing better with the truth afterwards (Fig. 4.2, sixth and seventh row). Similar to  $TBlchl/N$  and physical DA runs, Method 3 effectively raises the reference isopleth of nitrate to the truth (Figs. 4.4 and 4.5). However,  $TIP_{surf\_Blchl}$  and  $TNIP_{surf\_Blchl}$  lead to relatively high  $MAD_{all}$  for nitrate, similar to that in  $TIP_{surf}$  and  $TNIP_{surf}$ , suggesting that the assimilation of additional surface chlorophyll has little information to constrain subsurface nitrate. With additional profile observations,

TIP<sub>all</sub>\_BlchlN and TNIP<sub>all</sub>\_BlchlN simulate nitrate profiles that better delineate the true pattern throughout the water column (Fig. 4.5i, j) and substantially reduce MAD<sub>all</sub> for nitrate than TIP<sub>surf</sub>\_Blchl and TNIP<sub>surf</sub>\_Blchl (Fig. 4.6).

**Table 4.2.** Overview of assimilation effect on physical and biogeochemical model state variables in Scenario 1. The assimilation effect for each variable is quantified by the percentage change of MAD<sub>all</sub> in each assimilation experiment relative to the Free run MAD<sub>all</sub>. A decrease larger than or equal to 10% is considered a “beneficial” effect (marked by green), an increase larger than or equal to 10% is considered “detrimental” (marked by blue), while less than 10% change is considered “neutral”. Variables that are not affected by assimilation in a specific experiment are left blank.

Unit: %	Experiment	SSH	T	NO3	Chl	Phy	Zoo	SDet	LDet	NH4
<b>Method 1</b>	Blchl			-4.9	-3.3	-9.7	-2.4	-7.0	-4.2	-3.8
	Blchl <sub>10%</sub>			+20	+13	-2.6	+14	+1.4	+15	+4.6
	BlchlN			-18	-2.1	-10	-4.2	-13	-8.7	-8.3
	BlchlN <sub>5%</sub>			-22	+3.7	-3.9	-6.8	-14	-9.0	-9.9
	TIP <sub>surf</sub>	-53	-25	+14	+5.0	-13	-4.9	-32	-20	+4.3
	TIP <sub>all</sub>	-58	-36	+24	+8.6	-10	-3.9	-29	-20	+5.7
<b>Method 2</b>	TBlchl	-4.9	-9.0	-10	-6.3	-10	-4.2	-8.1	-6.2	-5.1
	TBlchl <sub>10%</sub>	-12	+0.3	+11	-0.4	-9.8	-1.7	-8.5	-11	-5.8
	TBlchlN	-25	-20	-33	-15	-19	-4.8	-23	-15	-5.4
	TBlchlN <sub>5%</sub>	-29	-27	-41	-23	-28	-17	-32	-26	-11
	TNIP <sub>surf</sub>	-53	-25	-5.8	+18	+1.2	-4.9	-32	-19	+4.0
	TNIP <sub>all</sub>	-58	-36	-24	+9.1	-7.2	-2.9	-28	-22	+5.7
<b>Method 3</b>	TIP <sub>surf</sub> _Blchl	-53	-25	+13	-6.3	-20	-4.9	-32	-20	+4.2
	TIP <sub>all</sub> _BlchlN	-58	-36	-21	-16	-23	-6.6	-33	-23	+4.4
	TNIP <sub>surf</sub> _Blchl	-53	-25	-0.2	-1.0	-12	-3.0	-31	-20	+4.5
	TNIP <sub>all</sub> _BlchlN	-58	-36	-37	-13	-18	-11	-34	-31	+2.9

Among all DA runs across different methods (with the same observation error applied), TNIP<sub>all</sub>\_BlchlN generally yields the lowest MAD<sub>surf</sub> or MAD<sub>all</sub> for all variables presented in Fig. 4.6 as well as zooplankton, small and large detritus listed in Table 4.2. Based on Table 4.2, the Method 2 and Method 3 generally yield beneficial effects on more biogeochemical variables than Method 1. Interestingly, despite the beneficial effects on phytoplankton in many assimilation runs, zooplankton is barely improved except in

TN|P<sub>all</sub>\_BlchlN and TBlchlN<sub>5%</sub>. I found that surface zooplankton is persistently underestimated in all assimilation runs (not shown), consistent with the lower grazing rate used in the biased model in Scenario 1. Also noticeable from Table 4.2 is that small and large detritus are improved in all assimilation runs except those only assimilating surface chlorophyll, while ammonium is least improved by assimilation among all variables.

#### 4.3.2.4 Nitrate and temperature correlation

To investigate whether and to what degree the assimilation affects the correlation between temperature and nutrients, I present scatterplots of nitrate and temperature from the 28 stations shown in Fig. 4.1b at all assimilation dates (Fig. 4.7). In the free run (Fig. 4.7a), there is a tight correlation between temperature and nitrate in nitrate-rich subsurface water, the variance of the nitrate concentration around the best fit between nitrate and temperature is small and its PDF (probability density function) peaks sharply near 0 (Fig. 4.7h). Compared to the free run, Method 1 runs that adjust only the nitrate or temperature fields (BlchlN in Fig. 4.7b and T|P<sub>all</sub> in Fig. 4.7c) and a Method 3 run that has weak effect on nitrate with assimilation of surface chlorophyll (T|P<sub>surf</sub>\_Blchl in Fig. 4.7d) degrade the temperature-nitrate relationship. In these cases the nitrate variance on temperature surfaces increases by more than 4 times and flatter, more skewed PDFs of nitrate result (Fig. 4.7h, i, j) compared to the free run. In contrast, assimilation runs in which temperature and nitrate are adjusted simultaneously either based on multivariate updates (Method 2 runs TBlchlN in Fig. 4.7e and TN|P<sub>all</sub> in Fig. 4.7f, and Method 3 run TN|P<sub>surf</sub>\_Blchl in Fig. 4.7g) or by assimilating both fields (Method 3 runs T|P<sub>all</sub>\_BlchlN and TN|P<sub>all</sub>\_BlchlN, not shown) better preserve the temperature-nitrate relationship. In these multivariate update runs the nitrate variance increases much less (compared Fig. 4.7e, f, g with Fig. 4.7b, c, d) and the PDF of nitrate is much sharper than in isolated update runs (Fig. 4.7h, i, j).



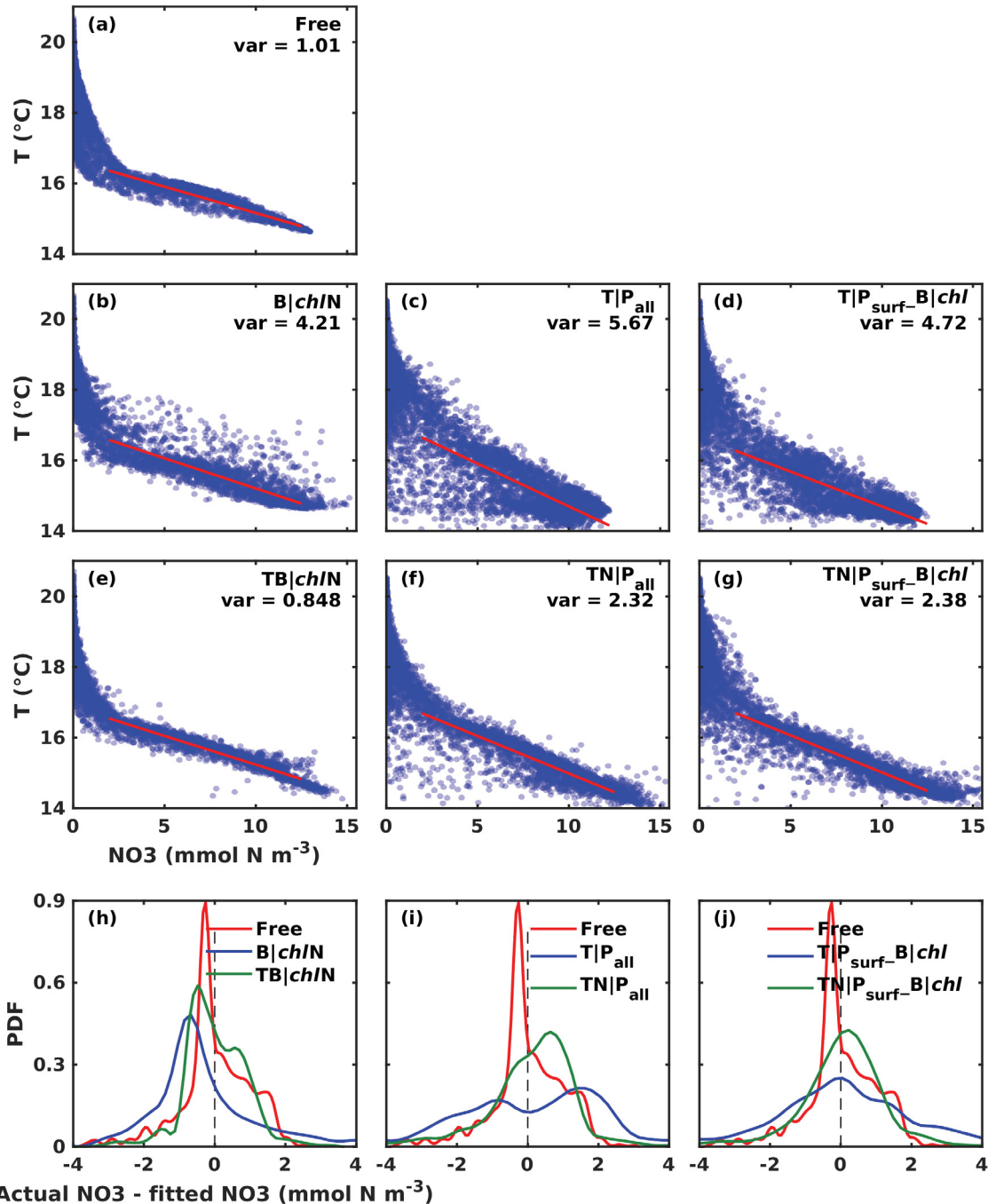


**Fig. 4.7.** (a-g) Scatterplots of nitrate ( $\text{NO}_3$ ) and temperature ( $T$ ) collected from 28 stations shown in Fig. 4.1b at all depths and at all analysis dates for the free run and different assimilation runs. The red line indicates the linear fit between nitrate and temperature for nitrate concentration between 2 and  $12.5 \text{ mmol m}^{-3}$ . Variance ( $\text{var}$ ) is calculated as the squared deviation of actual nitrate values from the linear fitted nitrate values at corresponding temperatures. (h-j) Probability density function (PDF) of the deviation of actual nitrate values from fitted nitrate values for each run.



### 4.3.3. Impact of assimilation on the forecast skill

The comparisons of assimilation experiments in previous sections show that Method 2 “Multivariate updates | single data type” and Method 3 “Joint updates | both data types” improve ocean model fields more significantly and better preserve the temperature-nitrate correlation than Method 1 “Isolated updates”. Here I examine whether the different assimilation methods improve model forecast skill and how they differ.

Figure 4.8 shows the difference of domain-averaged  $MAD_{surf}$  and  $MAD_{all}$  between the free and forecast runs for SSH, temperature, nitrate and phytoplankton, where a positive value indicates improvement by assimilation. It is evident that all assimilation methods improve model forecast skill in all or at least some model fields and display positive MAD differences for 10 to 25 days depending on the method and model field. Specifically for physical fields, Method 2 run *TBlchlN* improves forecast skill of SSH for 24 days and temperature fields for 15 days, which is as good as the physical DA runs ( $TIP_{all}$  and  $TNIP_{all}$ ) and Method 3 runs (Fig. 4.8a, b, e). Assimilating additional temperature profiles slightly improves forecast skill for physical fields with overall higher MAD differences (e.g., compare  $TIP_{all\_BlchlN}$  and  $TIP_{surf\_Blchl}$  in Fig. 4.8a, b, e). With respect to nitrate, Method 2 (*TBlchlN*,  $TNIP_{all}$ ) and Method 3 (all except  $TIP_{surf\_Blchl}$ , which has little improvement on nitrate  $MAD_{all}$ ) strongly improve forecast skill for 10 days in surface waters and 12 days in the entire water column. By comparison, Method 1 leads to smaller and shorter-lasting improvements (*BlchlN*) or even has a deleterious impact ( $TIP_{all}$  in nitrate). Assimilating additional profiles brings extra improvement in forecast skill for nitrate (e.g., compare  $TNIP_{all\_BlchlN}$  and  $TNIP_{surf\_Blchl}$  in Fig. 4.8f). For the phytoplankton field, the improvement in forecast skill from assimilation is sustained for longer, with positive  $MAD_{surf}$  and  $MAD_{all}$  difference for 25 days in all forecast runs except for surface phytoplankton in  $TNIP_{all}$ , and overall larger MAD difference in Method 3 runs than Method 2 or Method 1 runs (Fig. 4.8d, g).

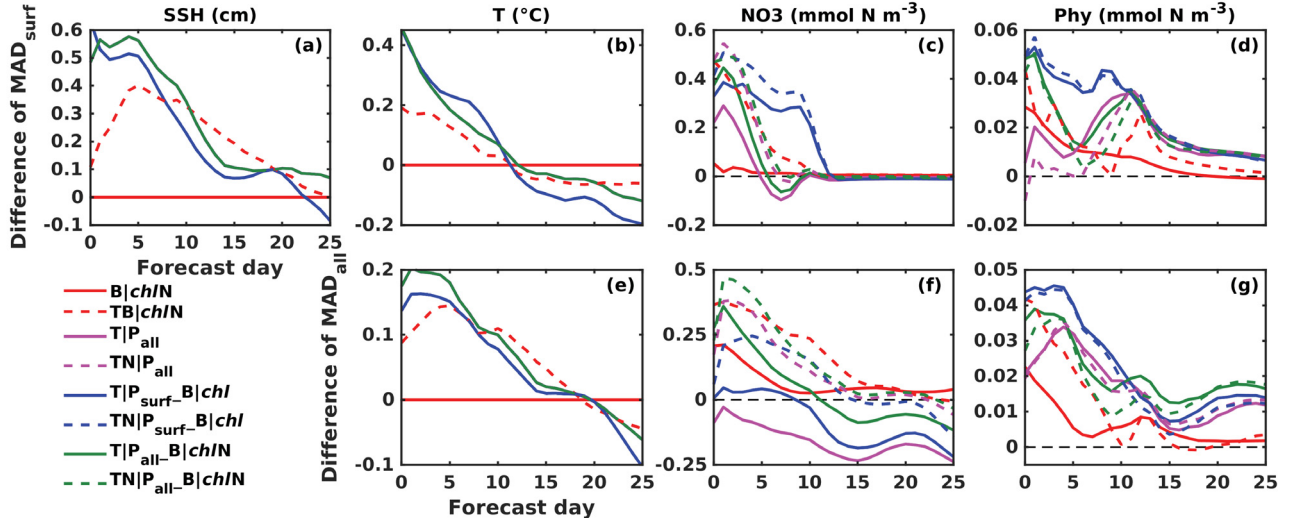


**Fig. 4.8.** Difference of domain-averaged (a-d)  $MAD_{surf}$  and (e-g)  $MAD_{all}$  between the free run and forecast runs initialized from the ensemble analysis on day 140 (assimilation step 17).

#### 4.3.4. Sensitivity of the assimilation methods to twin experimental design

I have shown in the above sections that assimilation corrects the “underestimating upwelling and productivity” Scenario 1 by increasing the upwelling and/or concentrations of biogeochemical variables, with the improvements varying among different assimilation methods. The conclusions drawn in Scenario 1 hold in the contrasting Scenario 2 where upwelling and productivity are overestimated. Consistent with Scenario 1, Figure 4.9 shows that when only assimilating surface chlorophyll, Method 2 run *TBchl* only slightly outperforms Method 1 run *Bchl* with slightly reduced upwelling of cold water and nitrate to the surface. However, when additional nitrate profiles are assimilated, the improvement by Method 2 run *TBchlN* over Method 1 run *BchlN* is clear with both, surface temperature and nitrate, substantially improved. Assimilating physical observations satisfactorily improves surface temperature and results in a better representation of surface nitrate when nitrate is updated along with temperature (*TN|P<sub>all</sub>* compared with *T|P<sub>all</sub>*). However, both runs, particularly *T|P<sub>all</sub>*, substantially increase surface phytoplankton, leading to even larger overestimation of surface phytoplankton than in the free run (Fig. 4.9). The elevated production at the surface is partially associated with spurious fluctuations in vertical velocity when physical fields are significantly adjusted

(e.g., see higher Root Mean Square (RMS) vertical velocity in  $TB|chlN$ ,  $TN|P_{surf}$  and  $TN|P_{all}$  in Fig. D1 in the Appendix D). As a result, more nutrients are brought from the subsurface to the surface. The problem of overestimating surface phytoplankton is substantially mitigated when surface chlorophyll and nitrate profiles are assimilated in addition to physical observations in  $TN|P_{all}-B|chlN$  (Fig. 4.9).

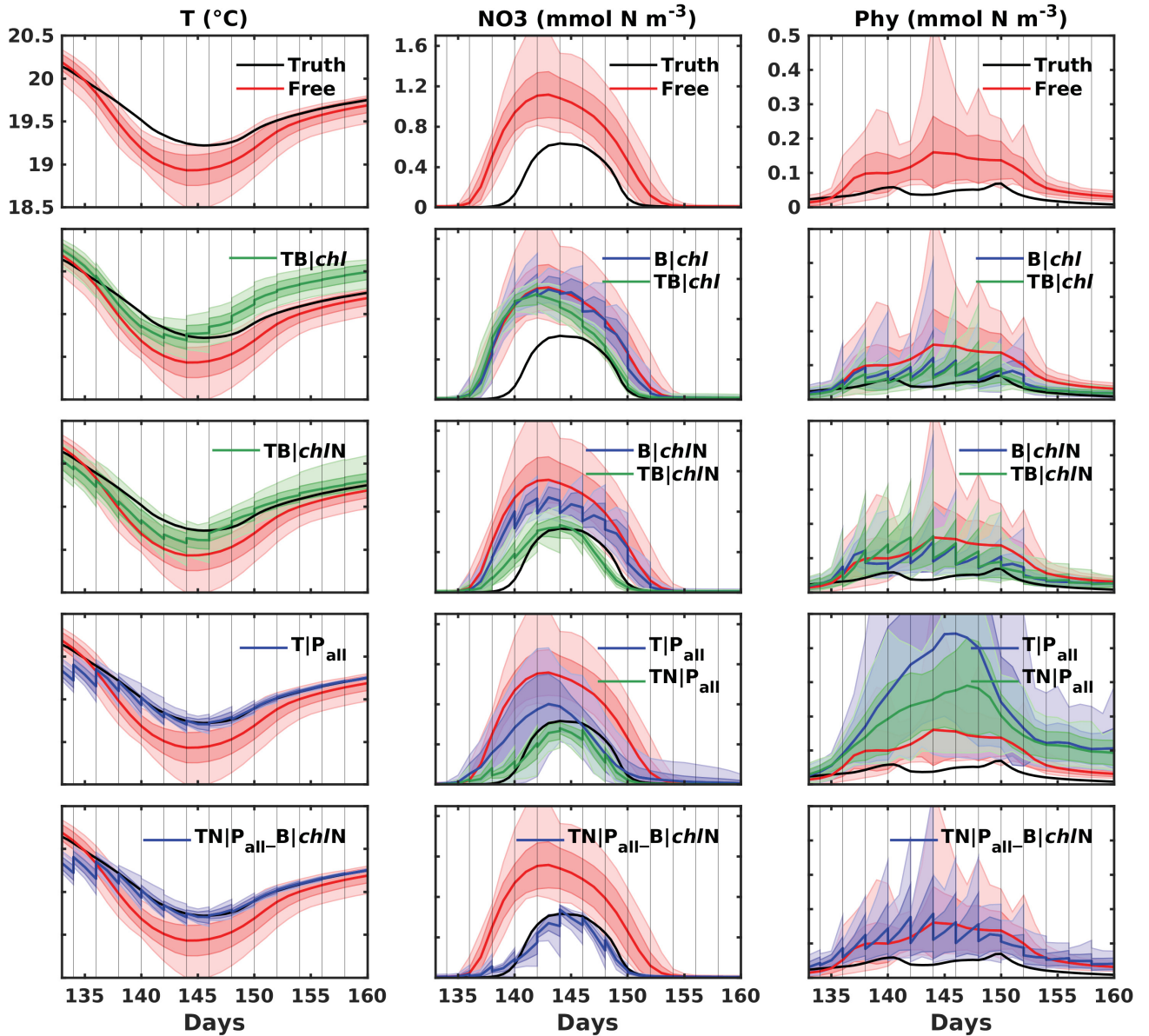


**Fig. 4.9.** Same as Figure 4.2 but for the “overestimating upwelling and productivity” Scenario 2 twin experiments.

The quantitative effects are summarized in Table D1 in the Appendix D. Compared to Scenario 1, the beneficial effects on biogeochemical variables in Scenario 2, in terms of  $MAD_{all}$  reduction, are weaker, but the degradation of biogeochemical fields (except surface nitrate) when assimilating physical observations to update physical fields alone ( $TIP_{all}$ ) is clearer. Consistent with Scenario 1, Table D1 shows that Method 2 outperforms Method 1 also in Scenario 2 with lower  $MAD_{surf}$  and  $MAD_{all}$  for all biogeochemical variables. Overall, Method 3 yields the lowest  $MAD_{surf}$  or  $MAD_{all}$  for physical and biogeochemical variables.

#### 4.4 Discussion

I have performed a series of twin experiments comparing different assimilation strategies in an idealized upwelling channel that is subject to biased physics, i.e. with weaker or stronger upwelling than the truth, and biased biology, i.e. with perturbed biogeochemical parameters. The results show that updating the biogeochemical or physical model state alone (Method 1 “Isolated updates”) is not sufficient for improving the biogeochemical ocean state and forecasts. Without addressing the issue of biased upwelling, which is at the root of the inaccurate simulation of biogeochemical fields, any corrections to the biogeochemical fields during assimilation updates dissipate quickly and do not lead to sustained improvements. When adjusting the physical model state alone, subsurface nitrate distributions are degraded and surface productivity is overestimated despite substantial improvements in physical fields. The degradation in biogeochemical fields is primarily due to two issues: the increased nutrient variance on temperature iso-surfaces when only adjusting the temperature or nutrient field, and the spurious, high vertical velocities when physical fields are substantially adjusted. Both issues can result in unreasonable nutrient inputs to the euphotic zone as has been reported in Raghukumar et al. (2015).

My experiments show that simultaneously adjusting physical and biogeochemical fields is key to avoid breaking the temperature-nutrient relationship, and to improve the biogeochemical ocean model state estimation. The simultaneous update can be achieved by Method 2 “Multivariate updates | single data type”, which takes advantage of the

correlation between physical and biogeochemical fields and the multivariate nature of the Kalman filter, or by Method 3 “Joint updates | both data types”, which assimilates physical and biogeochemical observations sequentially. In realistic applications, Method 3 is more cumbersome because physical and biogeochemical observations may not be available concurrently. This makes the remarkable improvement obtained by Method 2 very attractive when only one type of observations is available. In my case, the extra benefit of Method 2 over Method 1 results from a strong correlation between the biogeochemical (or physical) observations and the unobserved physical (or biogeochemical) model fields to be updated, specifically temperature and nitrate. For example, assimilating surface chlorophyll alone leads to limited improvement on the 3D biogeochemical state estimation even when correcting both physical and biogeochemical fields, because the correlation between surface chlorophyll and interior temperature and nitrate fields is weak. This is also confirmed by the sensitivity tests which show that assimilating surface chlorophyll with lower observation error increases the  $MAD_{all}$  for temperature and nitrate despite the improvement in surface phytoplankton. In contrast, when additional nitrate profiles are assimilated, the biogeochemical state is much improved and the superiority of Method 2 over Method 1 is much clearer. Reducing the observation error of nitrate profiles further reduces  $MAD_{all}$  for all physical and biogeochemical model fields (compare  $TB_{chl/N}$  and  $TB_{chl/N_{5\%}}$  in Table 4.2).

Other studies have reported similar success in taking advantage of the relationship between temperature (or density) and nutrients using methods other than EnKF. While et al. (2010) showed that applying an increment to the nutrient field based on the nutrient-potential density relationship during the physical data assimilation improves nutrient distribution. Shulman et al. (2013) found that instantaneously updating nitrate based on observation-derived statistical relations between temperature and nitrate improves model nitrate fields.

Coupled physical-biogeochemical data assimilation as in Method 3 “Joint updates | both data types” has demonstrated success in a few studies using methods other than EnKF (Anderson et al., 2000; Ourmières et al., 2009; Song et al., 2016a, b, Mattern et al., 2016). Here I demonstrate the advantages of Method 3 for the EnKF. My results add that

even when physical and biogeochemical observations are assimilated using Method 3, updating physical and biogeochemical fields simultaneously with physical observations can result in a bigger improvement in the biogeochemical model state (e.g., see higher forecast skills in  $TNIP_{surf\_Blchl}$  and  $TNIP_{all\_BlchlN}$  in relative to  $TIP_{surf\_Blchl}$  and  $TIP_{all\_BlchlN}$  in Fig. 4.8c, f). This is especially true when the available biogeochemical observations are not able to effectively constrain the biased biogeochemical fields, i.e.  $TIP_{surf\_Blchl}$  (where only surface chlorophyll is assimilated to update the biology) fails to reduce the increased nitrate variance on temperature surfaces following assimilation of physical data.

I notice that despite the remarkable improvement in nitrate in Method 2 and 3 runs which assimilate nitrate profiles ( $TBlchlN$  and  $TIP_{all\_BlchlN}$ ), discrepancies between the domain-averaged surface phytoplankton (Figs. 4.2 and 4.9) in the DA runs and the truth remain. I attribute these discrepancies to a combination of two factors. First, the relatively high observation error of 35% for chlorophyll results in more modest DEnKF updates than a smaller observation error would. An uncertainty of 35% is typically used for satellite chlorophyll and has been adopted in several prior assimilation studies (e.g., Ciavatta et al., 2011; Hu et al., 2012). The sensitivity experiments show that reducing the chlorophyll observation error could drive surface phytoplankton closer to the truth (e.g., compared  $Blchl_{10\%}$  with  $Blchl$ , and  $TBlchl_{10\%}$  with  $TBlchl$  in Fig. 4.2). Second, I forced the ensemble of free and DA runs with phytoplankton initial slopes and zooplankton grazing rate values that are 40% lower than those for the truth in Scenario 1 and 40% higher in Scenario 2, which act to exacerbate the underestimation or overestimation of productivity. The two factors contributing to the bias in phytoplankton estimation, in addition to the biased physical fields, can also explain the inaccurate zooplankton which is consistently underestimated in Scenario 1 and overestimated in Scenario 2. Improvements could be achieved by applying bias correction methods such as state augmentation to simultaneously estimate and correct biased parameters with the model state variables (e.g., see review in Dee 2005, and more recent biogeochemical ocean model applications in Simon et al., 2015 and Gharamti et al., 2017a, b) and will be the focus of future work.

I would also like to note that in my experiments, assimilating SSH and SST alone (e.g.,  $TNIP_{surf}$ ) is almost as effective as assimilating additional temperature profiles (e.g.,  $TNIP_{all}$ ) in lifting the depths of the reference isotherm and isopleth of nitrate toward the truth, primarily due to the tight correlation between SSH and model interior density and nutrient structures (Wilson and Adamec, 2002). It should be noted, however, that surface heat flux was not included in my model simulations. I expect that the performance of assimilating SST to update the thermocline will diminish as surface heat fluxes modify upper water temperatures. Nevertheless,  $TNIP_{all}$  outperforms  $TNIP_{surf}$  with clearly lower  $MAD_{all}$  for temperature, nitrate and phytoplankton, demonstrating the importance of assimilating additional subsurface observations in improving the accuracy of estimated 3D fields beyond the position of the thermocline and nutricline.

To date, satellite chlorophyll, SST and SSH observations are the main observation streams for data assimilation due to their excellent spatial and temporal resolution and almost real-time accessibility for most regions of the world's oceans. Fortunately with the rapid expansion of ocean observing platforms, profiles of physical and biogeochemical variables from floats and gliders will become more abundant and available for data assimilation to further improve model estimation and prediction.

#### **4.5 Summary**

In this chapter I have assessed the impacts of updating physical and biogeochemical model fields individually versus simultaneously via different DA strategies on ocean ecosystem estimation and prediction. I found that adjusting the physical or biogeochemical model state alone (Method 1 “Isolated updates”) degrades the tight correlation between temperature and nitrate and is insufficient to improve biogeochemical ocean state and prediction. Simultaneous multivariate or sequential updates to physical and biogeochemical fields are required to avoid degrading the temperature and nitrate relationship and to strongly improve the biogeochemical model state. Simultaneous updates can be realized through Method 2 “Multivariate updates | single data type” by assimilating either physical or biogeochemical observations to update both model fields or Method 3 “Joint updates | both data types” that sequentially



assimilates physical and biogeochemical observations. Surface chlorophyll is of limited use for improving the 3D model state in my idealized upwelling system even when correcting physical and biogeochemical fields because the correlation between surface chlorophyll and interior nitrate and density structures is weak. This highlights the importance of collecting subsurface information for improving biogeochemical ocean model state. Overall, Method 3 “Joint updates | both data types” outperforms Method 2 “Multivariate updates | single data type” in terms of skill metrics, while Method 2 represents a capable alternative when only physical or biogeochemical observations are available.



## CHAPTER 5

# ENSEMBLE DATA ASSIMILATION FOR IMPROVING THE SIMULATION OF CIRCULATION AND MOVEMENT OF A DEEP-WATER HYDROCARBON PLUME IN THE GULF OF MEXICO

### 5.1 Introduction

Accurate estimates of ocean circulation are essential for predicting transport of ocean biogeochemical constituents and pollutants, assessing environmental impacts, and managing accident response efforts. This is particularly true for the Gulf of Mexico (GOM), which has rich fisheries, diverse ecosystems, and marine protected areas but also experiences significant anthropogenic pressures from oil and gas extraction, including deep-sea oil drilling, and river discharge of excess nutrients to the northern shelf leading to widespread seasonal hypoxia there (Sturges and Lugo-Fernández, 2005). The explosion of the offshore drilling rig Deepwater Horizon (DwH) in April 2010 delivered an unprecedented quantity of crude oil (4.9 million barrels) into the GOM (Camilli et al., 2010) and served as a clear demonstration of the need for reliable circulation forecasts to aid in response and mitigation actions after the incident.

Circulation in the deep basin of the GOM is dominated by the intrusion of the Loop Current (LC) which aperiodically sheds large anticyclone eddies (known as Loop Current eddies, LCEs) (Sturges and Leben, 2000). The LC is a warm ocean current, originating in the Caribbean Sea, which flows northward into the GOM via the Yucatan Strait, and then loops east and south before exiting through the Florida Straits and feeding the Gulf Stream. Circulation on the continental shelves of the GOM is largely driven by wind and freshwater discharge from rivers with distinct seasonal variability (Morey et al., 2005). Interactions between the shelf and the deep ocean circulation occur through onshore/offshore transports, though constrained by the conservation of potential vorticity (Schmitz et al., 2005; Zavala-Hidalgo et al., 2014).

Numerous observational and modeling studies have advanced our understanding of the ocean circulation in the GOM (see, e.g., contributions in Sturges and Lugo-Fernández 2005, Lugo-Fernández 2016). These studies demonstrate that observations (either from satellites or *in situ*) and numerical models are complementary and indispensable resources to increase knowledge of the GOM circulation, and that combining the two via data assimilation (DA) is necessary to accurately hindcast/forecast the circulation given its complexity and broad range of spatial and temporal scales.

Earlier data assimilation efforts in the GOM have assimilated satellite sea surface height (SSH) with or without sea surface temperature (SST) and/or *in situ* data using simple techniques such as optimal interpolation (OI) (e.g., Wang et al., 2003; Kantha et al., 2005; Oey et al., 2005b; Chassignet et al., 2007) or a combination of OI and nudging (Fan et al., 2004; Lin et al., 2007). Despite their simplicity, the assimilation methods demonstrated that assimilation of satellite altimetry data improves model skill in reproducing mesoscale (10-100 km) circulation variability, primarily associated with dynamics of the LC and LCEs. However, some studies found that smaller-scale eddies in the shelf break and slope regions of the GOM are not reproduced by assimilating SSH data alone (Wang et al., 2003) but require inclusion of higher-resolution localized data such as drifters (Lin et al., 2007). This is primarily because satellite altimetry currently is capable of resolving large-scale to mesoscale structures but not submesoscale processes (100 m - 10 km) (Jacobs et al., 2014; Berta et al., 2015). Other *in situ* datasets, such as temperature and salinity profiles and surface drifter observations of velocity, have been reported as valuable complementary datasets in further improving model-simulated temperature fields (Shay et al., 2011), and velocity and trajectory estimates (Carrier et al., 2014; Muscarella et al., 2015) in the upper ocean of the GOM.

Advances in computing power in the past decades have spurred the application of more advanced ensemble DA techniques for the GOM with two benefits. First, ensemble mean forecasts can outperform the conventional single forecast of flow fields in the GOM, as shown by both Yin and Oey (2007) and Khade et al. (2017) who performed ensemble forecasts with perturbed initial fields obtained by the breeding method introduced in Toth and Kalnay (1993). Second, ensemble spread can provide confidence indices for the

ensemble mean forecast, as demonstrated in Counillon and Bertino (2009a, b) who used the Ensemble Optimal Interpolation (EnOI) method to assimilate altimetry data and show success in forecasting LC eddy shedding.

The Ensemble Kalman Filter (EnKF) is an alternative ensemble DA technique with the advantage that a flow-dependent background error covariance is used in contrast to the time-invariant covariance in OI- or variational-based DA systems. When assimilating SSH, the multivariate EnKF propagates SSH information into temperature and salinity profiles based on the correlations between SSH and temperature and salinity fields contained in the ensemble covariance. Hoteit et al. (2013) applied the EnKF to an ocean circulation model of the GOM with a horizontal resolution of  $1/10^\circ$ , and showed that the DA system realistically reproduced the evolution of the LC when assimilating weekly satellite SSH and SST data. Xu et al. (2013) implemented a variant of the EnKF method into a GOM model and found that it reproduced the position of LCEs and the strength of the LC more accurately in hindcast and forecast mode than OI due to the EnKF's time-evolving error covariance.

A practical limitation of the GOM assimilation efforts described above is that the skill assessments of the hindcasts or forecasts were mostly relying on comparisons against surface or near-surface observations (e.g., SSH, SST, surface velocities) largely due to a lack of observations at depth. Necessarily, these previous assimilation studies focussed on the improvements of the dynamics of the LC and associated eddies and/or surface current fields observable from satellite or drifters without direct examination of the impact of assimilation on subsurface flow fields. As the deep-water oil spill at the DWH rig has shown, knowledge of an assimilation system's skill in simulating the subsurface circulation is important for prediction of deep hydrocarbon plume transport and design of effective response efforts.

One approach for skill assessment of a DA system is to conduct twin experiments (e.g., Anderson 1996; Halliwell et al., 2014). The essential idea is to predefine a simulation as the "truth," sample synthetic observations from this "truth," assimilate these into a different simulation referred to as the forecast run, and assess the skill against

independent observations sampled from the “truth.” If the chosen truth and forecast runs are from different model types or significantly different configurations of the same model type (e.g., using different physical parameterizations or spatial resolution) the method is referred to as the ‘fraternal twin’ approach; otherwise, if the same model but with perturbed initial, forcing or boundary conditions is used, the method is referred to as the ‘identical twin’ approach (Halliwell et al., 2014). The identical twin approach can provide biased impact assessments when the error growth rate between the truth and forecast runs is insufficient. To avoid this potential bias in impact assessments, Halliwell et al. (2014) suggested that the model for the forecast run should be configured differently enough from that for the truth run so that error growth between them has the same magnitude as the error growth between state-of-the-art ocean models and the true ocean. In practice this is difficult to assess. Halliwell et al. (2014) showed that alternatively one can compare the assimilation impact in the fraternal twin framework with that in a realistic configuration; if similar impact is obtained in both twin and realistic configurations, the fraternal twin DA framework can be considered rigorous for assessing assimilation impact and conducting Observing System Simulation Experiments (OSSEs). OSSEs are useful for evaluating the impact of an ocean observing systems prior to deployment and/or the impact of alternate designs of existing systems (e.g., Halliwell et al. 2015).

Collectively previous assimilation studies in the GOM demonstrate the high potential of applying DA to improve model hindcasts/forecasts of circulation features in the GOM, but assessments of DA systems are limited and especially rare for subsurface waters. The objectives of this chapter are to develop an EnKF-based assimilative model to rigorously assess the model’s skill and different observing system configurations through fraternal twin experiments and in realistic assimilation mode, and to assess the impact of the data assimilation system on the distribution of a simulated deep-water hydrocarbon plume through identical twin experiments. Specifically, the following questions are addressed: i) What are the relative benefits of assimilating temperature and salinity profiles versus satellite data in improving the skill of different physical variables in the model? ii) Can the identical twin approach yield impact assessments consistent with those using the fraternal twin approach? iii) Does the assimilation system’s skill in

reproducing the satellite-observed dynamics of the LC and associated eddies in the GOM translate into skill in simulating the subsurface circulation? And iv), does an improved simulation of circulation of the deep GOM lead to improvements near the DwH spill site and more accurate simulation of the deep-water hydrocarbon plume?

Toward the objectives the following steps are taken. First, I implement the EnKF technique in a high-resolution ROMS model configured for the GOM. The physical model is coupled with a simple hydrocarbon model that includes two hydrocarbon tracers to mimic the neutrally buoyant fractions (i.e., insoluble and soluble) of the deep-water oil plume emanating from the DwH spill site. I then conduct a rigorous skill assessment of the assimilation system using fraternal twin experiments where the “truth” is a data-assimilative global Hybrid Coordinate Ocean Model (HYCOM) simulation (Chassignet et al., 2009). Motivated by the practical interest of tracking the deep-water hydrocarbon plume from the DwH spill, the assimilation impact on the subsurface circulation (between 200 m and 1000 m) is emphasized, and the degree of improvement in the open GOM (where mesoscale processes like LC and LCEs dominate) and in the shelf-break region near the DwH site (where submesoscale processes are important and impacts of open ocean, bathymetry and local wind and river forcing coexist) is compared. The assimilation system is then applied in a realistic configuration by assimilating real satellite SSH and SST data and profile observations. Lastly, a series of identical twin experiments is conducted with the ROMS physical-hydrocarbon model to investigate the assimilation impacts on the movement of the deep-water hydrocarbon plume.

## **5.2 Model description and experimental setup**

### **5.2.1 The coupled physical-hydrocarbon model**

The circulation model is a configuration of ROMS for the entire GOM (Fig. 5.1). The model has a horizontal resolution of 5 km and 36 terrain-following vertical layers with higher resolution near the surface and bottom layers. Vertical turbulent mixing is parameterized using the Mellor and Yamada (1982) Level 2.5 closure scheme, and bottom friction is specified using a quadratic drag formulation. The model utilizes a third-order accurate, non-oscillatory HSIMT (High-order Spatial Interpolation at the Middle

Temporal level) (Wu and Zhu, 2010) advection scheme for tracers, which is mass-conservative and positive-definite with low dissipation and no overshooting. The model is forced with 6-hourly atmospheric surface forcing from the European Centre for Medium-Range Weather Forecasts (ECMWF) global atmospheric reanalysis (Dee et al., 2011). River input is included using daily runoff data from US Geological Survey river gauges along the coast. For open-boundary conditions, the model is one-way nested inside the  $1/12^\circ$  data-assimilative global HYCOM (Chassignet et al., 2009). Tidal forcing is neglected because tides are small in the GOM.

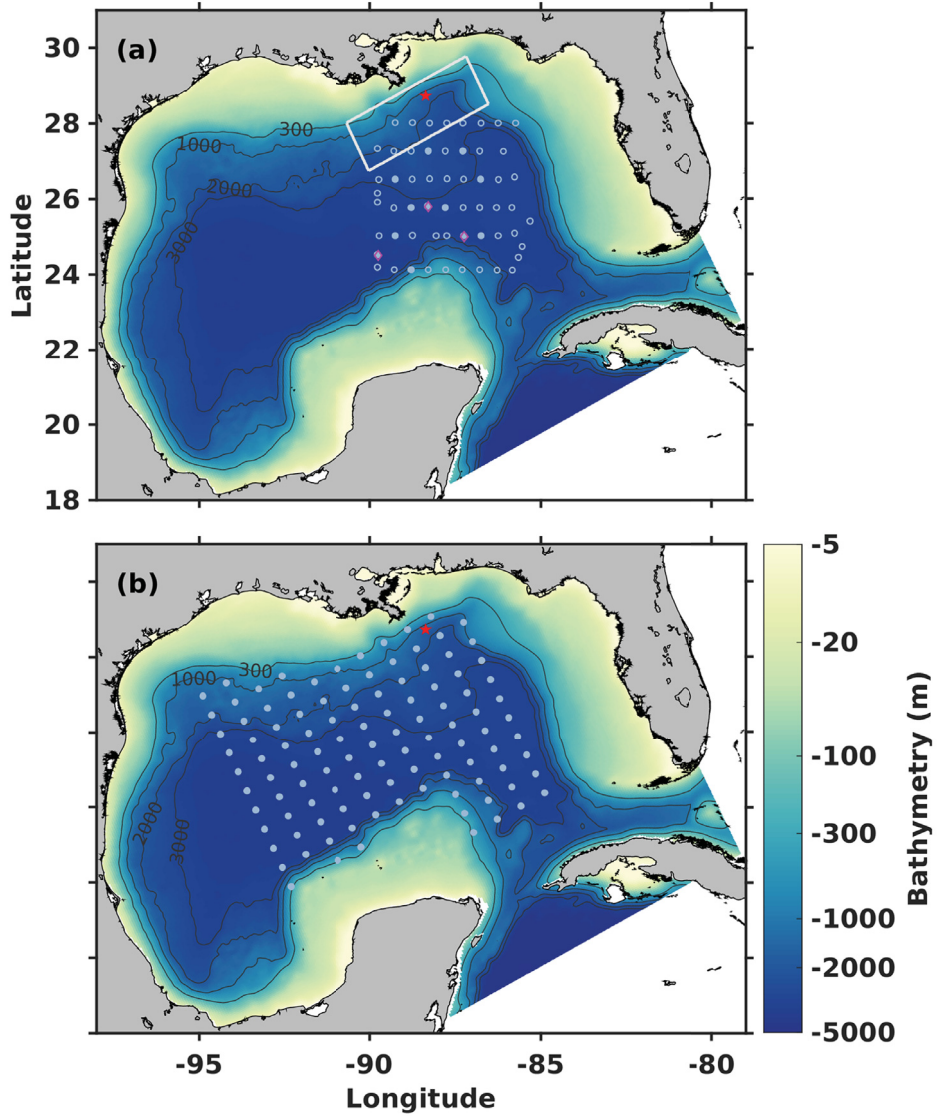


**Fig. 5.1.** Model domain and bathymetry. The red star denotes the location of the Deepwater Horizon oil rig. (a) The symbols represent stations where temperature (circles) and salinity (magenta diamonds) profiles were collected by Shay et al. (2011), with deep temperature or salinity profiles (down to 1000 m) marked as filled circles or magenta diamonds and shallow temperature profiles (down to 400 m) as open circles. This sampling scheme was used for twin experiments F2 and I2. The white rectangle indicates a subregion used for averaging. (b) Sampling scheme for twin experiments F3 and I3. The dots represent stations where temperature and salinity profiles extending to 1000 m depth were sampled from the truth run.

The model includes two hydrocarbon tracers, HydroC1 and HydroC2, to represent the insoluble and soluble fractions of the deep-water oil plume, respectively. Hydrocarbon weathering and removal in the water column are prescribed by a constant decay rate ( $r$ ). The equation for the evolution of hydrocarbon tracers, denoted as  $C$ , can be written as:

$$\frac{\partial C}{\partial t} = -\left(u \frac{\partial C}{\partial x} + v \frac{\partial C}{\partial y} + w \frac{\partial C}{\partial z}\right) + \frac{\partial}{\partial z} \left(K_v \frac{\partial C}{\partial z}\right) + S - r C \quad (5.1)$$

where the four terms on the right-hand side represent horizontal and vertical advection, vertical diffusion, hydrocarbon source term and decay of hydrocarbon, respectively. Specifically,  $x$  and  $y$  represent the two horizontal coordinates and  $z$  the vertical coordinate,  $u$ ,  $v$ , and  $w$  ( $\text{m s}^{-1}$ ) are velocity components in  $x$ -,  $y$ -, and  $z$ -coordinates, respectively,  $K_v$  is the vertical diffusivity ( $\text{m}^2 \text{s}^{-1}$ ),  $S$  represents the hydrocarbon source ( $\text{kg m}^{-3} \text{d}^{-1}$ ), and  $r$  represents hydrocarbon decay rate ( $\text{d}^{-1}$ ). Horizontal diffusion of hydrocarbons is considered very small compared to other terms and neglected in equation (5.1) but is non-zero for temperature and salinity. The hydrocarbon sources  $S$  for the two tracers are based on the measurements of hydrocarbon flow rate and compositions of hydrocarbon in Ryerson et al. (2012). According to Ryerson et al. (2012), the hydrocarbon mass flux into the deep plume was around  $3.4 \times 10^6 \text{ kg d}^{-1}$  averaged over the 87-day spill period (20 April to 15 July 2010), with the insoluble and soluble fractions contributing to 31% and 69% of the deep plume mass, respectively. Therefore, I assumed spill rates of  $1.05 \times 10^6 \text{ kg d}^{-1}$  and  $2.35 \times 10^6 \text{ kg d}^{-1}$  for HydroC1 and HydroC2, respectively during the oil spill period, and  $0 \text{ kg d}^{-1}$  before or after. In the model, the hydrocarbons were released only into the grid cell closest to the DwH location centered at 1100 m. Dividing the spill rates by the volume of this grid cell yields the oil source term values  $S$  for the two hydrocarbon tracers  $4.3 \times 10^{-4}$  and  $1.4 \times 10^{-3} \text{ kg m}^{-3} \text{d}^{-1}$ , respectively. At all other grid cells in the domain, the hydrocarbon sources are set to 0. The hydrocarbon decay rates are uncertain. A half-life of 3.05 day (corresponding to a decay rate of  $0.23 \text{ d}^{-1}$ ) is adopted for the soluble fraction HydroC2 following North et al. (2015) and a half-life of 13.86 day (decay rate of  $0.05 \text{ d}^{-1}$ ) for the slower-decaying insoluble fraction HydroC1. The latter is based on sensitivity tests using different decay rates for HydroC1; the one that led to the simulated hydrocarbon concentrations closest to the available



measurements in August 2010 was chosen. Model simulations were run from 1 April to 1 October 2010.

The skill of the model without data assimilation is very important in a DA system, because the model controls the propagation and growth of errors. Previous studies in the GOM have highlighted two important aspects for model skill, namely a sufficiently high horizontal resolution to represent mesoscale dynamics (e.g., Chassignet et al., 2005) and accurate representation of the LC inflow through the Yucatan Straits (e.g., Oey, 2003). My ROMS model generally meets the two requirements in that its 5-km horizontal resolution is sufficient to resolve mesoscale processes (the baroclinic Rossby radius is 30 to 40 km in the central GOM, see, e.g., Oey et al., 2005); and that the ROMS model is nested in a data-assimilative HYCOM model that simulates an accurate structure of the LC and its eddies through assimilation. Initial model-data comparisons to assess the model's skill showed that it has skill in simulating the dominant features of the LC intrusion although it tends to overestimate the northward extension of LC. The model simulation also shows reasonably good agreement when compared with Argo temperature and salinity profiles. With respect to hydrocarbons, the model is able to simulate the observed westward extension of the deep-water oil plume.

### **5.2.2 Experimental framework**

The DEnKF technique described in Chapter 4 was implemented in the GOM model. The robustness of the assimilation system as well as the impact of assimilation on physical variables are assessed through fraternal twin experiments, and in an assimilation experiment with real observations. Also, the impact of assimilation on hydrocarbon plume movement is assessed through identical twin experiments. The three groups of experiments (i.e., fraternal twin, realistic assimilation, and identical twin) share the same ROMS model and utilize the similar assimilation configurations as described in more detail below.

### 5.2.2.1 Fraternal twin experiments

In the fraternal twin experiments, the “truth” is generated by interpolating the daily outputs of the  $1/12^\circ$  data-assimilative global HYCOM (Chassignet et al., 2009) onto the ROMS model grid. Synthetic observations are sampled from the truth, including SSH, SST, and temperature and salinity profiles. Typical Gaussian observation errors of  $N(0, 2 \text{ cm})$  for SSH,  $N(0, 0.3 \text{ }^\circ\text{C})$  for temperature (both SST and temperature profiles), and  $N(0, 0.01)$  for salinity are added to the sampled data. SSH and SST are sampled weekly at every fifth horizontal grid point to yield a spatial resolution similar to that of the real satellite SSH and SST observations (both at  $1/4^\circ$  resolution) assimilated in the realistic configuration. In addition, SSH in regions shallower than 300 m is not used for assimilation because satellite altimetry data is less accurate in coastal areas. For SST, only those in regions shallower than 10 m are excluded. Importantly when preparing the synthetic SSH observations, the mean dynamic topography (MDT) of the HYCOM truth run had to be removed from the sampled SSH data and the MDT of the ROMS model had to be added. The MDTs of the HYCOM and ROMS models were obtained by averaging their respective daily SSH outputs from 2010 to 2016. Temperature and salinity profiles were sampled with two different sampling schemes (see locations in Fig. 5.1). The first scheme adopts the sampling dates and locations used in the survey described in Shay et al. (2011). The key features of this scheme are: i) the sampling is centered on the LC region; ii) the majority of the temperature profiles are limited to the upper 400 m; and iii) very few salinity profiles were collected. The second scheme represents an extended coverage, where temperature and salinity profiles are simultaneously sampled at a horizontal resolution similar to the first scheme but covering the central GOM, extending vertically to 1000 m depth, and sampled on 23 instead of 9 dates.

A non-assimilative run, subsequently referred to as the free run, is initialized on 1 April 2010 from the global HYCOM. This ROMS simulation is used to evaluate the impact of the assimilation by comparisons with data-assimilative runs. SSH and temperature and salinity transects of the truth and free runs on 28 May (58 days after initialization) are shown in Figure 5.2. In the truth, an anticyclonic eddy has already shed from the LC (Fig. 5.2a), while in the free run the eddy is forming but has not yet detached

from the LC (Fig. 5.2a). In the vertical view, the differences in temperature and salinity between the truth and free runs are most significant within the LC's vertical extent (top ~800 m). This comparison illustrates that the free run approximately satisfies the requirements of a credible twin experiment suggested in Halliwell et al (2014). It is able to reproduce the key feature of the ocean phenomenon (i.e. the LC intrusion) with some realism, and there are sufficient differences (errors) between the free and truth runs for the assimilation method to correct.

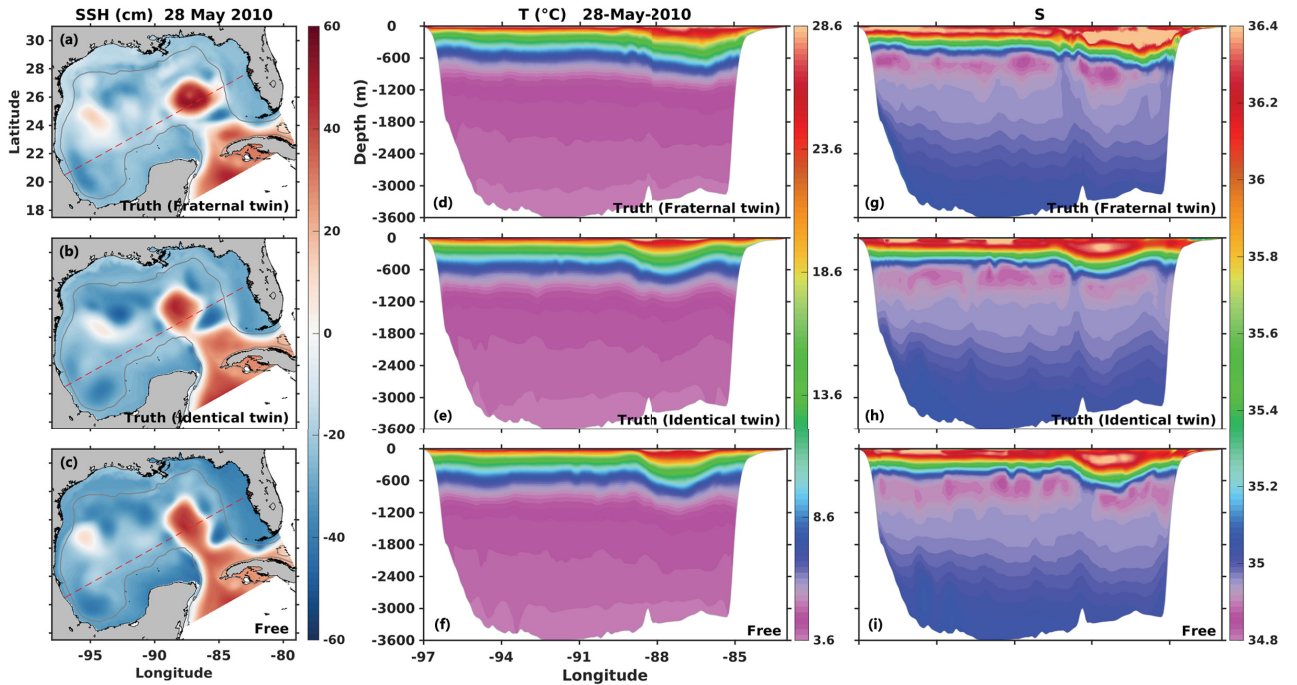


**Fig. 5.2.** Sea surface height (SSH, cm), and transects of temperature (T, °C) and salinity (S) on 28 May 2010. Panels a, d, and g are from HYCOM and used as the truth in the fraternal twin experiments. Panels b, e, and h are from ROMS and used as truth in identical twin experiments. Panels c, f, and i are from the free ROMS run. The gray contour in the SSH maps marks the bathymetric depth of 300 m, and the red dashed line shows the position of the transect in panels d to i.

In the DA experiments, 20-member ensembles of model integrations are started from different initial conditions and forced by perturbed boundary conditions and wind fields. The initial conditions were created by using three-dimensional (3D) fields from daily HYCOM outputs within a 20-day window centered on the initialization date 1 April 2010. The boundary conditions were generated by applying a time lag of up to +/-10 days to the boundary condition (i.e., the first member's boundary conditions are 10 days ahead

while the 20<sup>th</sup> member's are 10 days behind the actual date) following Counillon and Bertino (2009). The perturbed wind fields were created by first conducting an empirical orthogonal function (EOF) decomposition of the wind field and then adding perturbations from the mixture of first 4 EOF modes to the wind field, where the four perturbation modes were multiplied with zero-mean unit-variance random numbers and a scale factor of 0.5 similar to Thacker et al. (2012) and Li et al. (2016).

The ensemble size of 20 was chosen largely due to the limitations on the computing resources available. However, this small size works reasonably well in my application and has been successfully applied in previous ensemble-based assimilation studies (e.g., Hu et al., 2012; Mattern et al., 2013). Distance-based localization with an influence radius of 50 km was applied as described in Evensen (2003) to prevent the potential negative effects of spurious correlations between distant grid points that can result from relatively small ensembles. Furthermore, an inflation factor of 1.05 was applied to the ensemble anomalies inflating the ensemble around its mean at every assimilation step (Anderson and Anderson, 1999) to account for the underestimation of the forecast error covariance due to the small ensemble size. The localization radius and inflation factor are both based on initial tests and were selected to best reduce the model-data misfit without losing ensemble spread or generating discontinuities in the analysis fields. Finally, a post-processing procedure was performed after each assimilation step, which reset any negative values of temperature or salinity analysis to their corresponding forecast values (less than 0.1% of grid cells were affected by this throughout the assimilation period).

Observations are assimilated weekly from 2 April to 3 September 2010 updating the 3D temperature and salinity fields by taking advantage of the multivariate nature of the EnKF. After the last assimilation step on 3 September 2010, the ensemble of simulations is run without any data assimilation for 4 more weeks. An overview of the three assimilation experiments (referred to as F1, F2 and F3) is presented in Table 5.1. Model-data misfit is quantified by computing the Mean Absolute Deviations (MAD) of model simulations and the truth or real observations. For ensemble assimilation runs the forecast ensemble mean at assimilation steps is used for calculating the MAD.

**Table 5.1.** Overview of data assimilation twin experiments. Capital letters F and I refer to fraternal twin and identical twin experiments, respectively. Sampling scheme for twin experiments F2 and I2 is based on the actual sampling locations and dates for temperature and salinity profiles in Shay et al. (2011).

<b>Experiment</b>	<b>Synthetic observations assimilated</b>
F1 & I1	Weekly SSH and SST within regions deeper than 300 m and 10 m, respectively.
F2 & I2	Weekly SSH and SST as in F1 and I1, and temperature and salinity profiles at 9 sampling dates from 8 May to 9 July 2010 and at locations shown in Fig. 5.1a - 472 temperature and 34 salinity profiles - 363 of the temperature profiles are sampled to depth < 400 m
F3 & I3	Weekly SSH, SST as in F2 and I2, and weekly 108 temperature and salinity profiles that extend to 1000 m at locations shown in Fig. 5.1b.

### **5.2.2.2 Data assimilation experiment assimilating real observations**

The DA experiment assimilating real observations is similar to the fraternal twin experiment F2 except that Sea Level Anomaly (SLA) from AVISO (Archiving Validation and Interpretation of Satellite Oceanographic Data, <http://www.aviso.oceanobs.com/>), 1/4 ° SST from the AVHRR (Advanced Very High Resolution Radiometer, <http://marine.copernicus.eu/>), and temperature and salinity profiles from Shay et al. (2011) are assimilated. Similar to the procedure in the fraternal twin, an MDT obtained from the 7-year averaged SSH of the free-running ROMS model was added to the satellite SLA. Argo temperature and salinity profiles (<http://www.usgodae.org/>) available during the simulation time were not assimilated but retained for an independent skill assessment.

### **5.2.2.3 Identical twin experiments**

The identical twin experiments have similar setup as the fraternal twin experiments except the “truth” is generated from a ROMS simulation that differs from the free run only in its initial conditions, boundary conditions and wind forcing. More specifically, the truth run is started from an initial state on 1 April 2010 sampled from an earlier spinup ROMS simulation, and forced with boundary conditions that are lagging behind those of the free run by 14 days and wind fields reconstructed from the first 10

EOFs of the realistic ECMWF wind. Since the same model architecture is used in free and reference runs, there is no need to correct MDT when sampling SSH observations. A comparison of the truth and free runs in the identical twin setup is shown in Fig. 5.2, where differences between the truth and free runs in SSH and subsurface temperature and salinity fields are obvious and qualitatively comparable to the difference between the truth and free runs from the fraternal twin setup.

Similar to the fraternal twin setup, three data assimilation experiments (I1, I2 and I3) are conducted in the identical twin framework assimilating only SSH and SST weekly or with additional temperature and salinity profiles using the two different sampling schemes described earlier (Table 5.1).

## **5.3 Results**

### **5.3.1 Impact of assimilation on physical variables: fraternal twin experiments**

First, the impact of the assimilation system on physical variables in the fraternal twin experiments (F1, F2 and F3) is described. The overall improvement of physical variables throughout the open Gulf (defined as regions deeper than 300 m) is assessed by quantifying the reductions in MAD between the assimilation run and the free run.

Figure 5.3 shows the temporal evolution of domain-averaged MAD. Temporally and spatially averaged MAD are summarized in Table 5.2. Assimilating SSH and SST in F1 significantly reduces the MAD of SSH (reduction of 51%), temperature (29%) and velocity fields (25%), and slightly reduces MAD in salinity (11%). After the last assimilation step, MAD remain reduced for 4 weeks. Assimilating additional temperature and salinity profiles (in F2 and F3) further benefits the simulation of temperature and especially salinity fields, in particular in F3, where MAD in salinity are reduced by 23%. However, there is almost no effect on MAD of SSH and velocity fields from assimilating additional profiles (comparing F2 and F3 to F1).

**Table 5.2.** Mean Absolute Deviations (MAD) from the “truth” of physical variables for free and data assimilation runs in fraternal twin and identical experiments. The MAD were averaged over all grid cells excluding the shelves (defined by water depths < 300 m) and daily snapshots from 1 April to 1 October 2010. At assimilation steps the forecast ensemble mean was used for the calculation. The percentage change relative to the free run is presented in parentheses. The location of the subregion used for averaging velocities in the last two columns is shown as a white rectangle in Fig. 5.1a.

	SSH (cm)	T (°C)	S	u (m/s)	v (m/s)	u (m/s) in subregion	v (m/s) in subregion
<b><i>Fraternal twin</i></b>							
Free	11	0.72	0.15	0.11	0.11	0.13	0.084
F1	5.3 (-51%)	0.51 (-29%)	0.13 (-11%)	0.079 (-25%)	0.079 (-25%)	0.090 (-28%)	0.067 (-20%)
F2	5.3 (-52%)	0.50 (-30%)	0.13 (-13%)	0.079 (-26%)	0.080 (-24%)	0.088 (-30%)	0.065 (-23%)
F3	5.4 (-51%)	0.48 (-33%)	0.11 (-23%)	0.078 (-27%)	0.079 (-26%)	0.089 (-29%)	0.064 (-24%)
<b><i>Identical twin</i></b>							
Free	10	0.58	0.093	0.10	0.10	0.11	0.087
I1	4.2 (-59%)	0.32 (-45%)	0.073 (-21%)	0.055 (-47%)	0.055 (-46%)	0.065 (-41%)	0.052 (-40%)
I2	4.1 (-60%)	0.31 (-47%)	0.072 (-23%)	0.055 (-47%)	0.054 (-47%)	0.064 (-42%)	0.051 (-41%)
I3	4.4 (-57%)	0.29 (-50%)	0.068 (-27%)	0.056 (-46%)	0.055 (-46%)	0.064 (-42%)	0.050 (-42%)

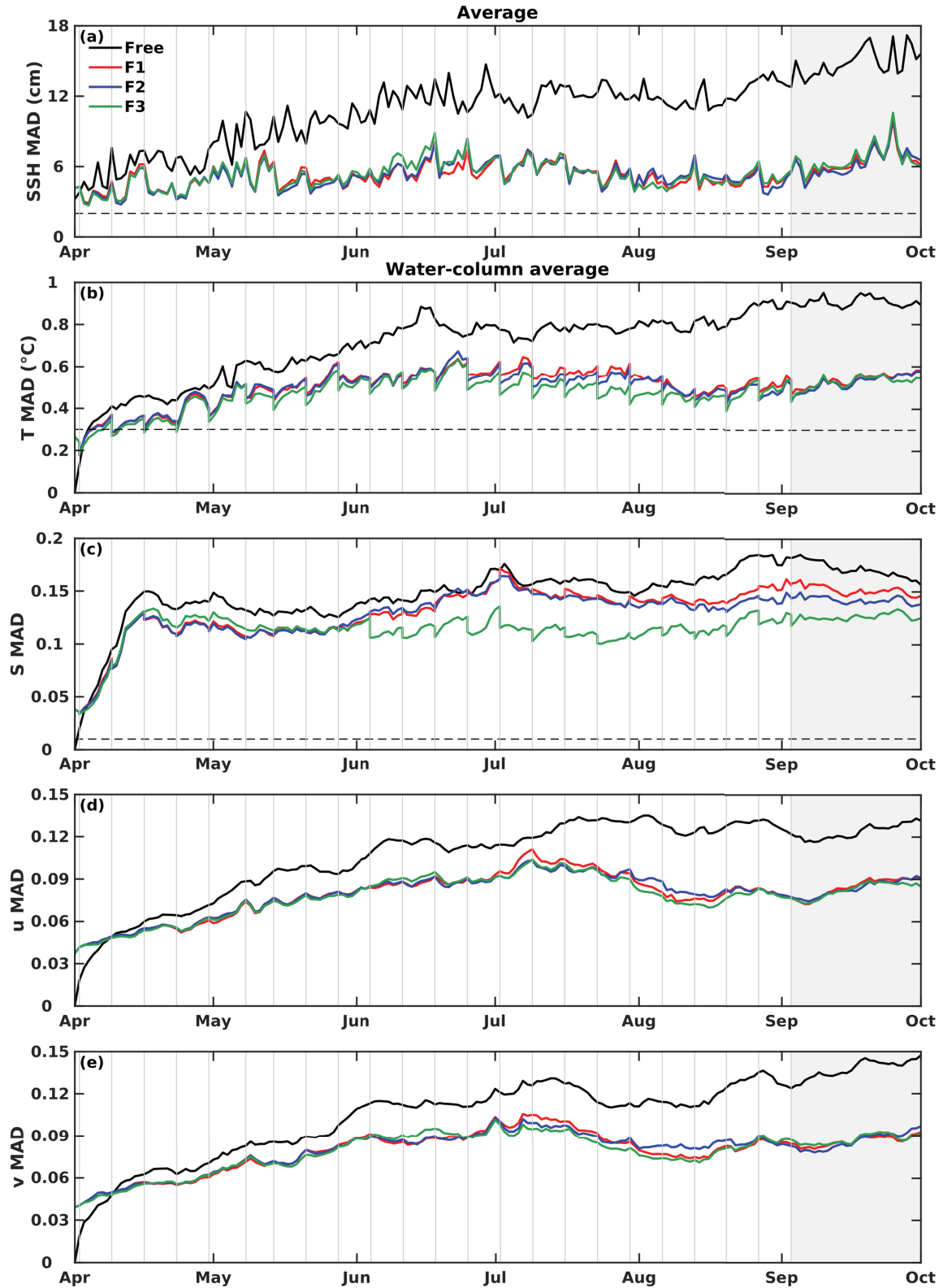


**Fig. 5.3.** Time series of MAD averaged over the open Gulf (excluding shelf regions shallower than 300 m) for (a) SSH (cm), (b) temperature (T, °C), (c) salinity (S), (d)  $u$  (m/s), and (e)  $v$  (m/s) from the free run and fraternal twin runs. MAD of all physical



variables except SSH were averaged over the entire water column. Black dashed lines in (a, b) denote the values of observation errors. Gray vertical lines indicate the assimilation steps. The gray area marks the 4-week time period without data assimilation.

Figures 5.4 and 5.5 illustrate where the MAD reductions occur horizontally. Compared to the free run, F1 reduces the MAD in SSH, temperature, and velocity components for almost entire domain, with the most significant reductions within the LC region (Fig. 5.4). The reduction in salinity MAD is relatively small in F1 but larger in F3 where additional temperature and salinity profiles are assimilated (Fig. 5.5). In contrast to the other physical variables (i.e., SSH, T, u and v), the biggest impact of assimilation on the salinity field is on the shelf where variability in salinity is larger than in the open Gulf because of river inputs. Also, in the fraternal twin the difference in salinity between truth and free run is largest on the shelf because of the differences in river inputs between the HYCOM and ROMS model configurations.

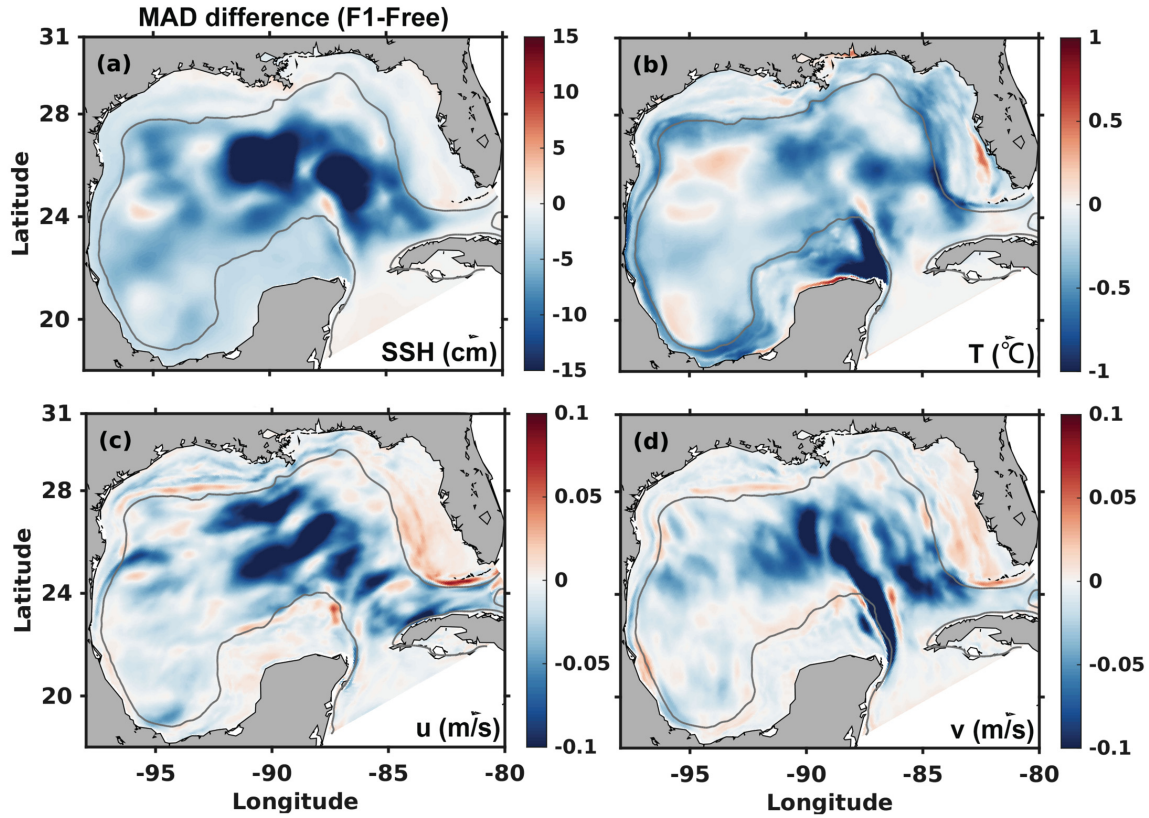


**Fig. 5.4.** The difference of physical variables' time-averaged (daily snapshots from 1 April to 1 October) MAD between fraternal twin F1 and the free run. MAD of temperature and velocities were averaged over the entire water column. Negative values (cold colors) correspond to a decrease in MAD compared to free run, whereas positive values (warm colors) correspond to an increase. The gray contour marks the bathymetric depth of 300 m.

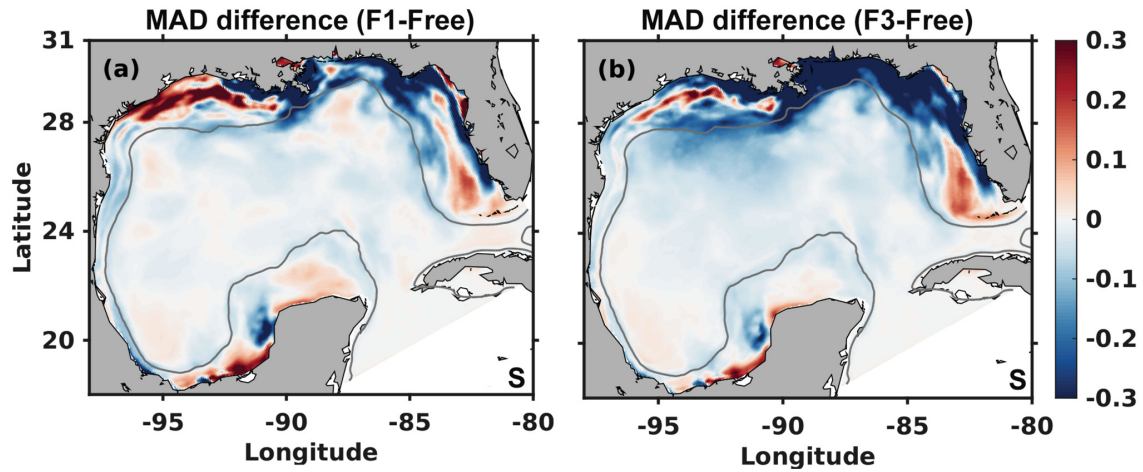


**Fig. 5.5.** Same as Figure 5.4 but for salinity comparing the fraternal twins F1 and F3. MAD of salinity were averaged over the entire water column.

Vertically, the reductions of spatially and temporally averaged MAD extend to nearly 900 m depth for temperature and velocities and 500 m depth for salinity (Fig. 5.6). The maximum reductions in MAD are on the order of 0.6 °C for temperature at around 200 m, of 0.12 for surface salinity and of 0.07 m/s for surface velocities. Compared to F1, assimilating temperature and salinity profiles in F3 leads to a greater reduction of MAD for temperature and salinity primarily in the upper 300 m, but no further impacts on MAD for velocities.

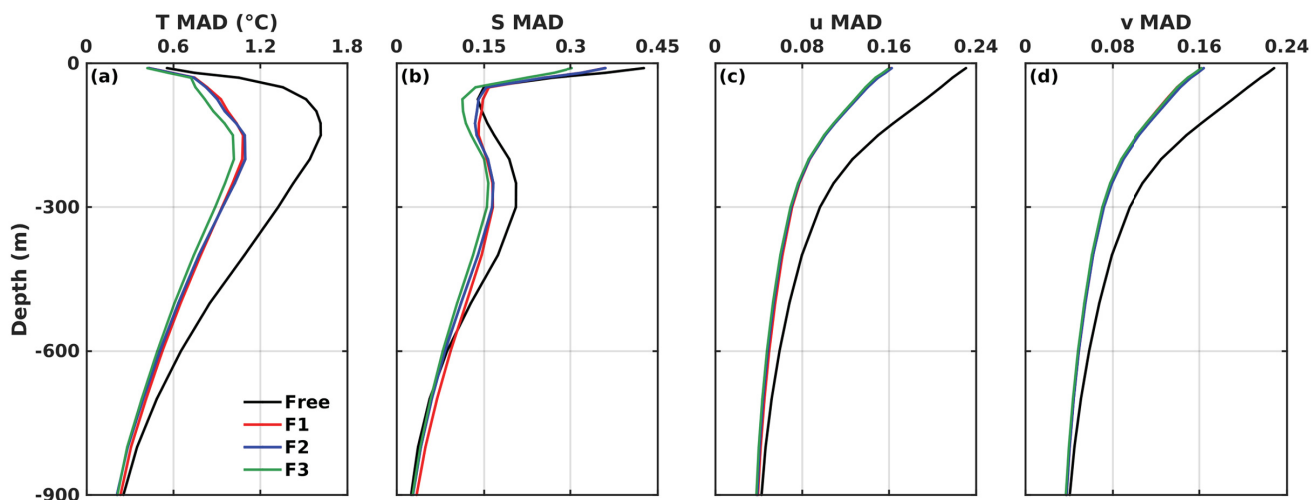


**Fig. 5.6.** Profiles of MAD averaged over the open Gulf (excluding shelf regions shallower than 300 m) and daily snapshots from 1 April to 1 October 2010 for (a) temperature (T, °C), (b) salinity (S), (c) u (m/s), and (d) v (m/s) from the free run and the fraternal twin runs.

Next, I assess the impact of assimilation on subsurface temperature and salinity fields. Temperature and salinity from the free run and the F1 and F3 runs are compared point-by-point against the “truth” in Fig. 5.7. Even without assimilation, the linear correlation between free and truth run for temperature is very close to the 1:1 line (with a slope of 0.97 and coefficient of determination  $R^2$  of 0.98). Large variances only occur in the thermocline region ranging in temperature from 8 to 26 °C (Fig. 5.7a). Assimilation further improves the linear correlation between the model and “truth” with increased slopes and  $R^2$ , significantly reduced variance in subsurface temperature, and reduced bias

and MAD (Fig. 5.7b, c). Compared to temperature, the linear correlation in salinity between the free run and “truth” is weaker and has larger variances (Fig. 5.7d). Again, assimilation improves the linear correlation between the model and “truth” with increased slope and  $R^2$ , and reduced MAD especially when extra temperature and salinity profiles are assimilated in F3 (Fig. 5.7e, f).

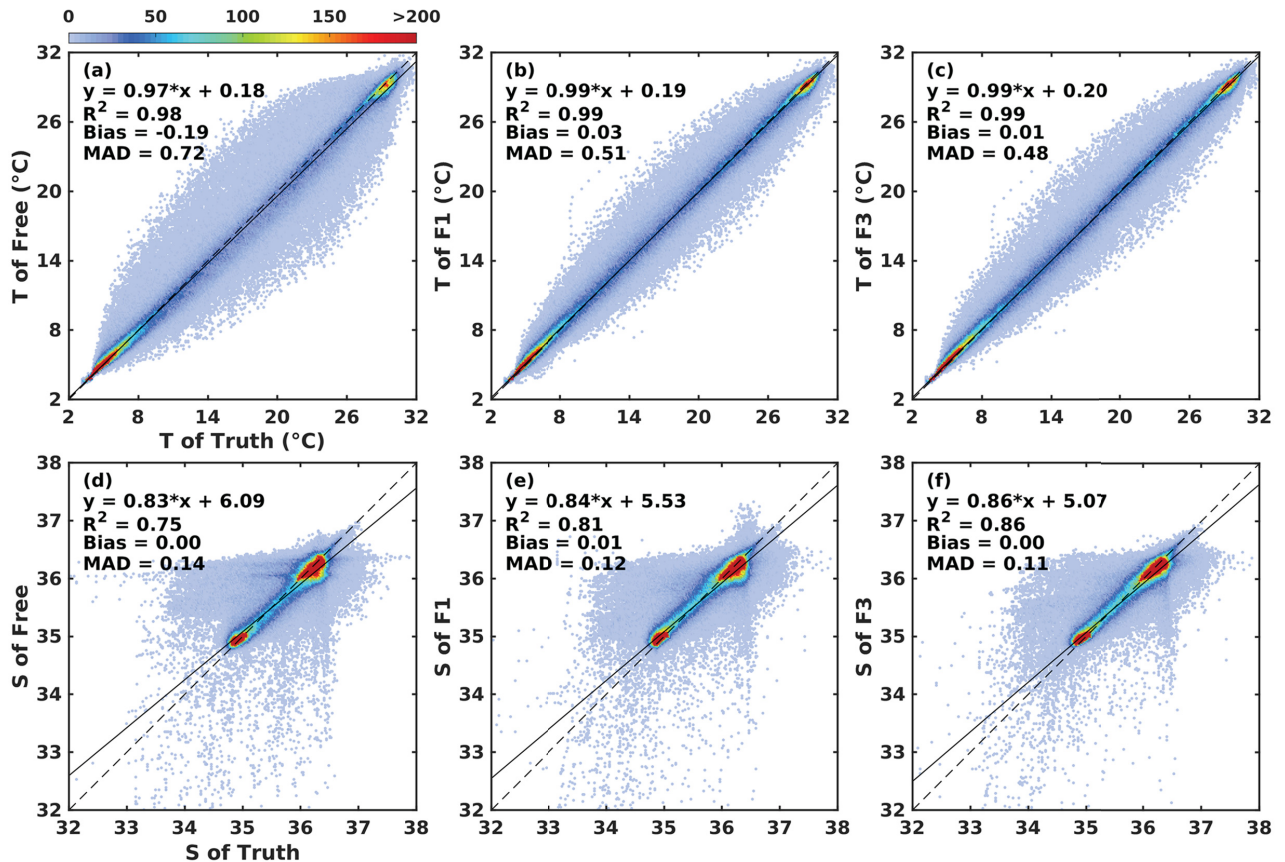


**Fig. 5.7.** Point-by-point comparison of (a, b, c) temperature (T, °C) and (d, e, f) salinity (S) from the “truth” versus those from free, F1 and F3 runs. Data values are shown as a two-dimensional histogram, with the color scale denoting the number of data. T and S data were sampled at every 10 grid cells within the open Gulf (excluding shelf regions shallower than 300 m) and every 5 days during the simulation period. T and S in top layer were excluded to ensure independent assessment. The total number of data is 401940. The black line is the linear regression between variable from the truth and other run. The dashed line is the 1:1 ratio line.

The “true” spatial distribution of mean temperature and salinity at 400 m depth in August shows only a weak northward intrusion of warm and salty LC water into the Gulf and a detached anticyclonic eddy that propagates northwestward (Fig. 5.8a, e). Compared to the “truth”, the free run overestimates the northward extension of the LC (depicted by the 12 °C isotherm and 35.5 isohaline), and the detached eddy is misaligned (Fig. 5.8 b, f). Assimilation corrects the extension and angle of the LC intrusion and the position of the eddy, significantly reducing the averaged MAD error by 47% (52%) and 31% (46%) for temperature and salinity, respectively in the F1 (F3) run (Fig. 5.8c, d, g, h).

Lastly the impact of the assimilation scheme on circulation near the spill site is examined. The temporal evolution of velocity MAD averaged over the water column and subregion defined in Fig. 5.1a is shown in Fig. 5.9. In contrast to the noticeable MAD reductions in the domain-averaged velocity MAD (Fig. 5.3d, e), reductions in velocity MAD in the subregion are negligible from April to mid-June but are obvious from mid-June to the end of September (Fig. 5.9). Overall the time-averaged MAD reduction in the subregion is of similar magnitude as in the open GOM (Table 5.2).



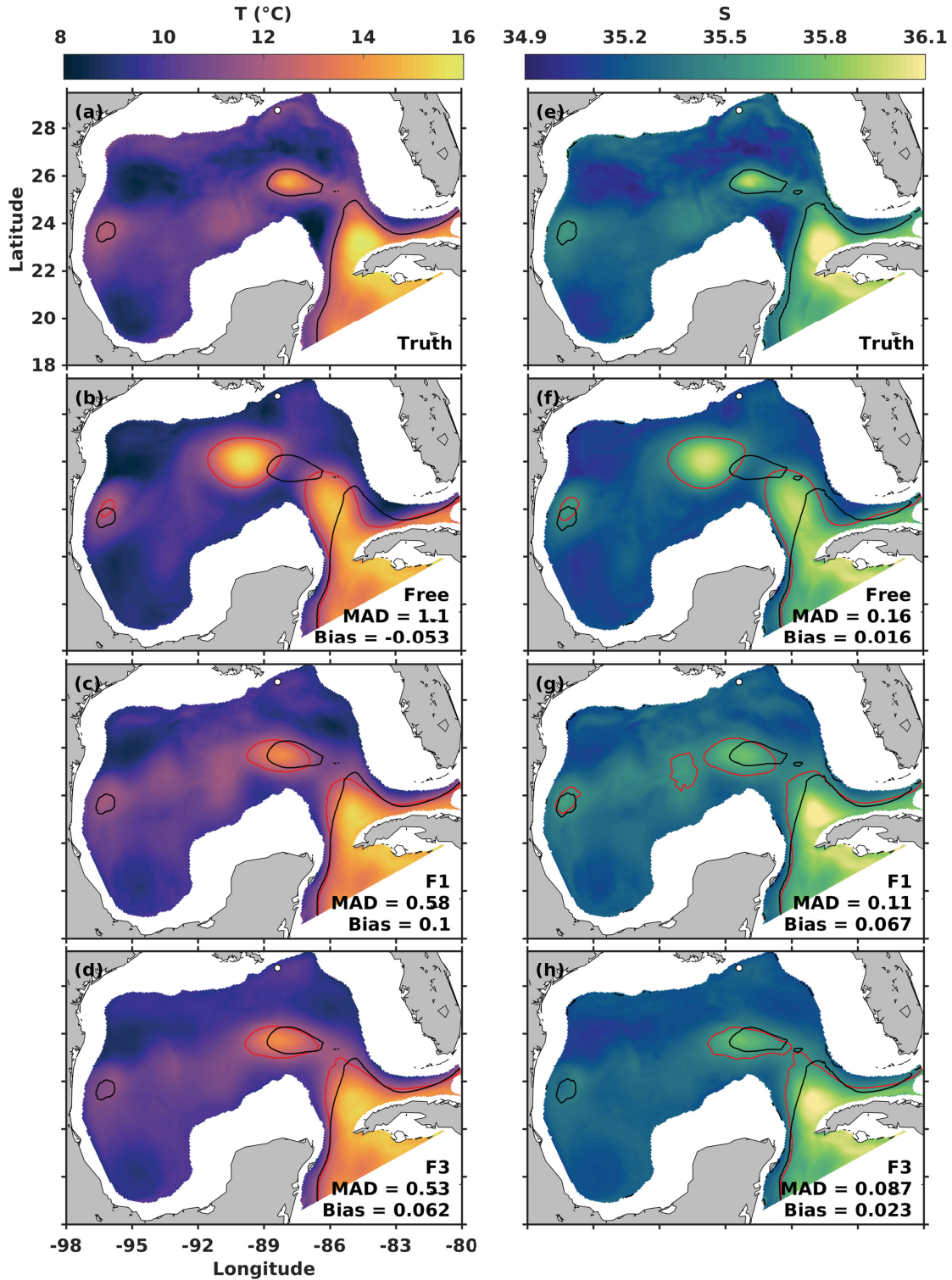


**Fig. 5.8.** August-mean (a, b, c, d) temperature (T, °C) and (e, f, g, h) salinity (S) at 400 m from the “truth”, free, F1 and F3 run in fraternal twin experiments. The white dot denotes the location of the Deepwater Horizon oil rig. The contours mark the 12 °C isotherm and 35.5 isohaline, respectively, where the black contours denote the isotherm or isohaline for the truth while red contours denote those for the actual simulation in each panel.

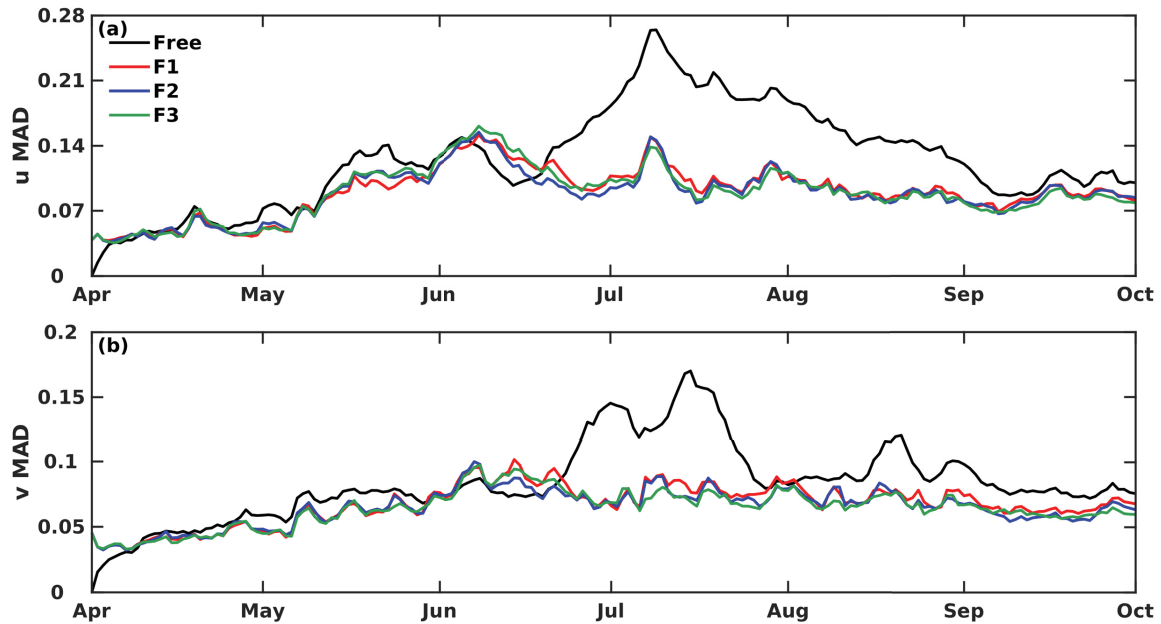


**Fig. 5.9.** Time series of subregion- and water column-averaged MAD for velocity components (a)  $u$  (m/s) and (b)  $v$  (m/s) from the free and fraternal twin runs. The location of the subregion for averaging is shown in Fig. 5.1a.

A comparison of subsurface mean circulation in August is shown in Fig. 5.10 to provide some context for the velocity MAD. The “truth” shows a limited northeastward intrusion of the LC into the GOM and two eddies shedding from the LC (Fig. 5.10a). As indicated by the water properties in Fig. 5.8, the free run overestimates the northward extension of the LC and simulates a more energetic detached anticyclonic eddy that has propagated further west (Fig. 5.10b). Assimilation in F1 brings the overall circulation pattern in the open GOM close to the “truth”, with a simulated shape, strength and location of the LC and LC eddies closer to the truth (Fig. 5.10c). However, the smaller-scale currents surrounding the spill site observed in the truth (i.e., the strong anticyclonic eddy on the east of the spill site and cyclonic eddy on the southwest of the site) are not satisfactorily represented in either free run or F1 run (Fig. 5.10d, e, f).

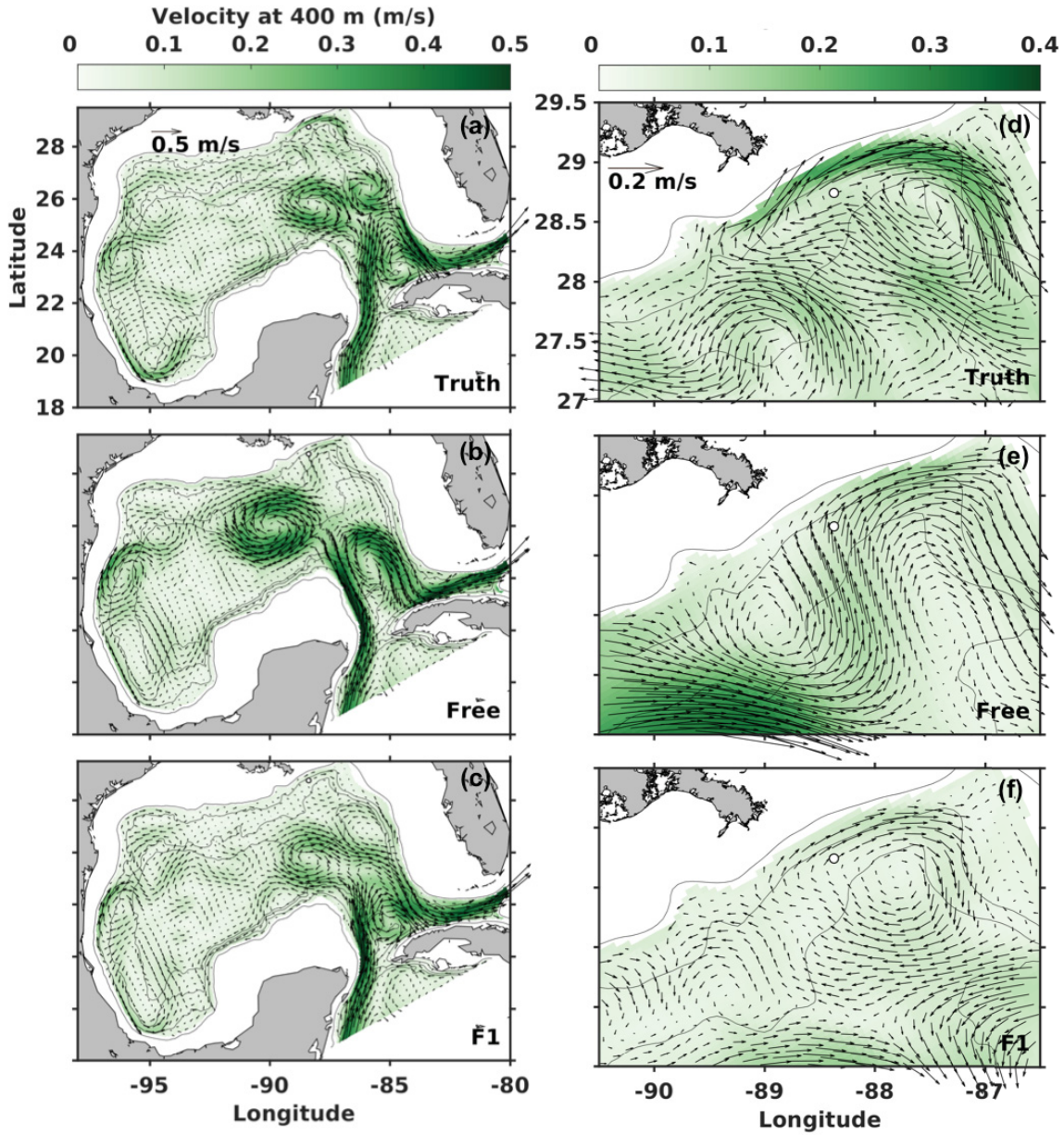


**Fig. 5.10.** August-mean velocity at 400 m in the “truth” (a, d), free (b, e) and F1 run (c, f) in fraternal twin experiments. Panels in the right column are zoomed into the region near the oil spill location. The white dot denotes the location of the Deepwater Horizon oil rig, and gray contours mark the bathymetric depths of 300, 1000, 2000 and 3000 m, respectively.



### 5.3.2 Impact of assimilation on physical variables: assimilating real observations

The previous section has shown the positive impact of assimilation on physical variables in the mesoscale through fraternal twin experiments. Now the impact of assimilation in a realistic configuration is assessed using satellite and *in situ* observations.

Consistent with the results from the fraternal twin experiments, assimilating SSH and SST significantly reduces the MAD for SSH (43%) and SST (27%), and the improvement remains for 4 weeks after the last assimilation step (Fig. 5.11, Table 5.3). The MAD for SSH and SST are reduced in most of the domain. The most significant reduction in MAD for SSH is in the LC region and westward pathway of LC eddies (Fig. 5.12).

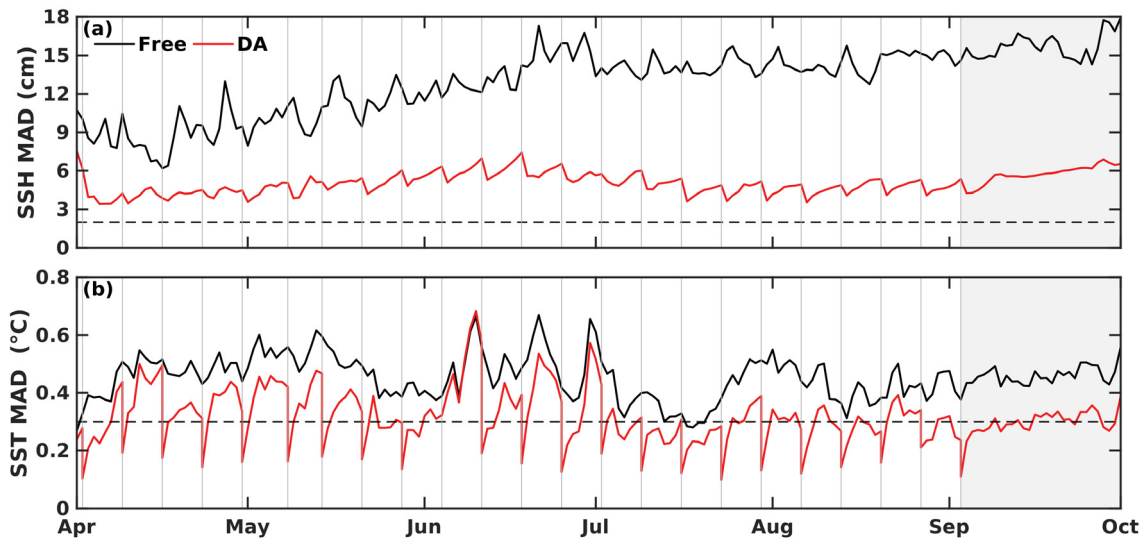


**Fig. 5.11.** Time series of MAD averaged over the open Gulf (excluding shelf regions shallower than 300 m) for (a) SSH (cm) and (b) SST ( $^{\circ}\text{C}$ ) from the free run and data assimilation run with real observations. Black dashed lines denote the values of observation errors. Gray vertical lines indicate assimilation steps. The gray area marks the 4-week time period without data assimilation.

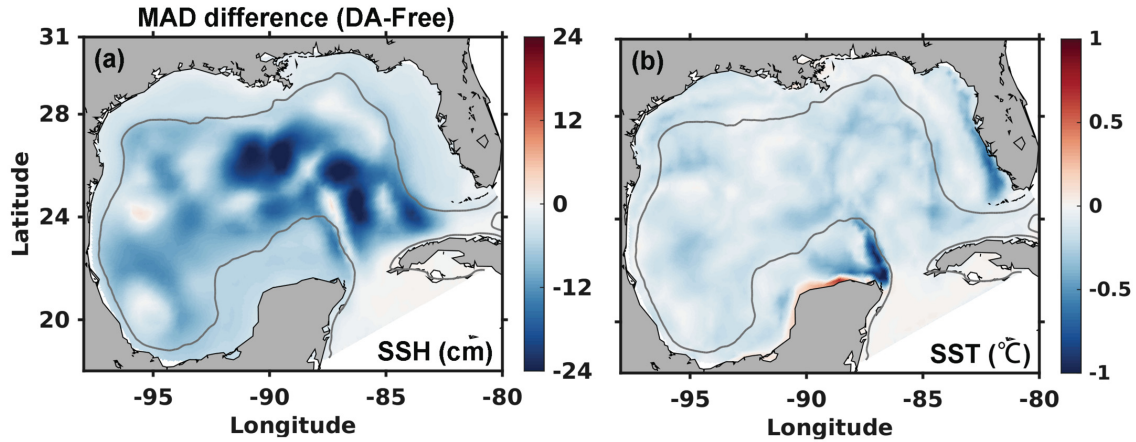


**Fig. 5.12.** Temporally averaged (daily snapshots from 1 April to 1 October) difference in MAD between the DA run and the free run for SSH and SST. Negative values (cold colors) correspond to a decrease of MAD compared to the free run, whereas positive values (warm colors) correspond to an increase in MAD. The gray contour marks the bathymetric depth of 300 m.

To evaluate the impact of assimilation on the temporal and spatial evolution of the LC and its eddies, the altimeter-derived and model-simulated LC fronts and eddies (depicted by the 10-cm SSH isoline following Counillon and Bertino 2009) are shown in Fig. 5.13. Compared to observations, the free run overestimates the northward extension of the LC (Fig. 5.13b), whereas the DA run better reproduces the observed shape and position of the time-evolving LC front (Fig. 5.13c).

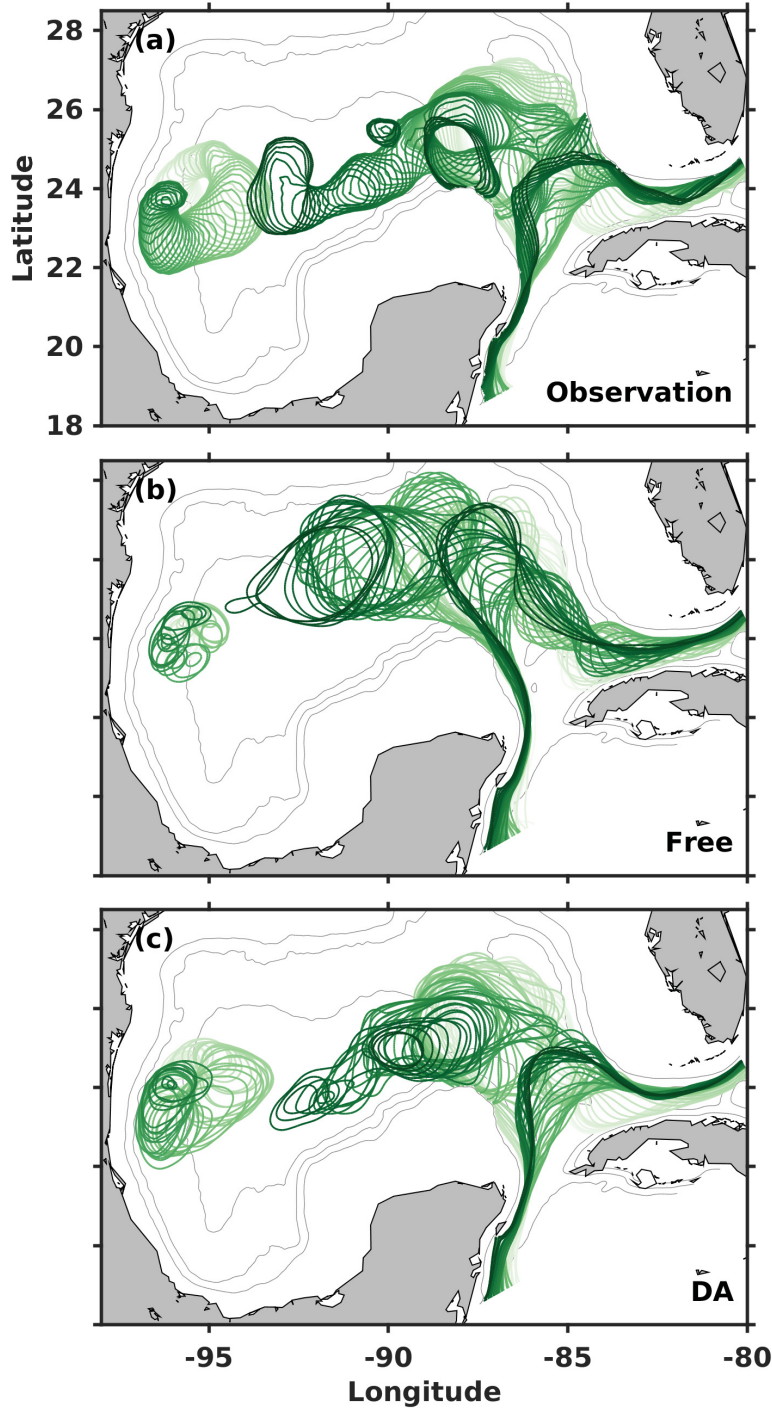


**Fig. 5.13.** Time-evolving Loop Current front depicted by the 10 cm SSH isoline from (a) altimeter observations, (b) free run and (c) DA run. Light to dark red green lines represent the 10 cm SSH isolines derived from observational or model data from 1 April to 1 October 2010 every 3 days. The gray contours mark the bathymetric depths of 300, 1000, and 3000 m, respectively.

**Table 5.3.** Mean Absolute Deviations (MAD) from the observations of physical variables for free and data assimilation runs in the assimilation system using real data. The MAD for SSH and SST were averaged over all grid cells excluding the shelves (defined by water depths < 300 m) and daily snapshots from 1 April to 1 October 2010. At assimilation steps the forecast ensemble mean was used for the calculation. The percentage change relative to the free run is presented in parentheses.

	SSH (cm)	SST (°C)	Argo T (°C)	Argo S
Free	13	0.82	1.31	0.26
DA	7.4 (-43%)	0.60 (-27%)	0.65 (-50%)	0.22 (-15%)

The observed temperature and salinity profiles from Argo provide a completely independent source of model validation. Figure 5.14 shows the point-by-point comparison of model-simulated versus observed Argo temperature and salinity. The linear fit line between the simulated and observed temperature for the free run (with a slope of 0.97 and  $R^2$  of 0.95) is very close to the 1:1 ratio line but shows large variances at temperatures ranging between 8 and 28 °C (Fig. 5.14a). The assimilation further improves the linear correlation between the simulated and observed temperature with an increased slope and  $R^2$ , significantly reduced variances, and reduced bias and MAD (Fig. 5.14b). Compared with temperature, the linear correlation between the simulated and observed salinity is weaker and has larger variances (Fig. 5.14c). Again, assimilation improves the linear correlation between the simulated and observed salinity with increased slope and  $R^2$ , and reduced bias and MAD (Fig. 5.14d).

To illustrate at what depths the assimilation has the strongest impact, Figure 5.15 shows temporally and horizontally averaged profiles of MAD and bias between the model and the independent Argo observations. The temperature MAD for the free run is largest (> 0.8 °C) at depths between 50 and 600 m; this is where the MAD reduction by assimilation has the strongest impact (Fig. 5.15a). In the free run, Argo temperatures are underestimated at all depths; DA notably reduces the underestimation throughout the top 600 m except for a layer around 100 m depth where a positive bias is created (Fig. 5.15b). The salinity MAD for the free run are largest at the surface and gradually decrease with depth (Fig. 5.15c). DA reduces the salinity MAD in the upper 400 m (Fig. 5.15c). The

free run also underestimates the Argo salinity in the top 400 m and, while DA reduces the underestimation in the upper 400 m it creates positive biases below (Fig. 5.15d).

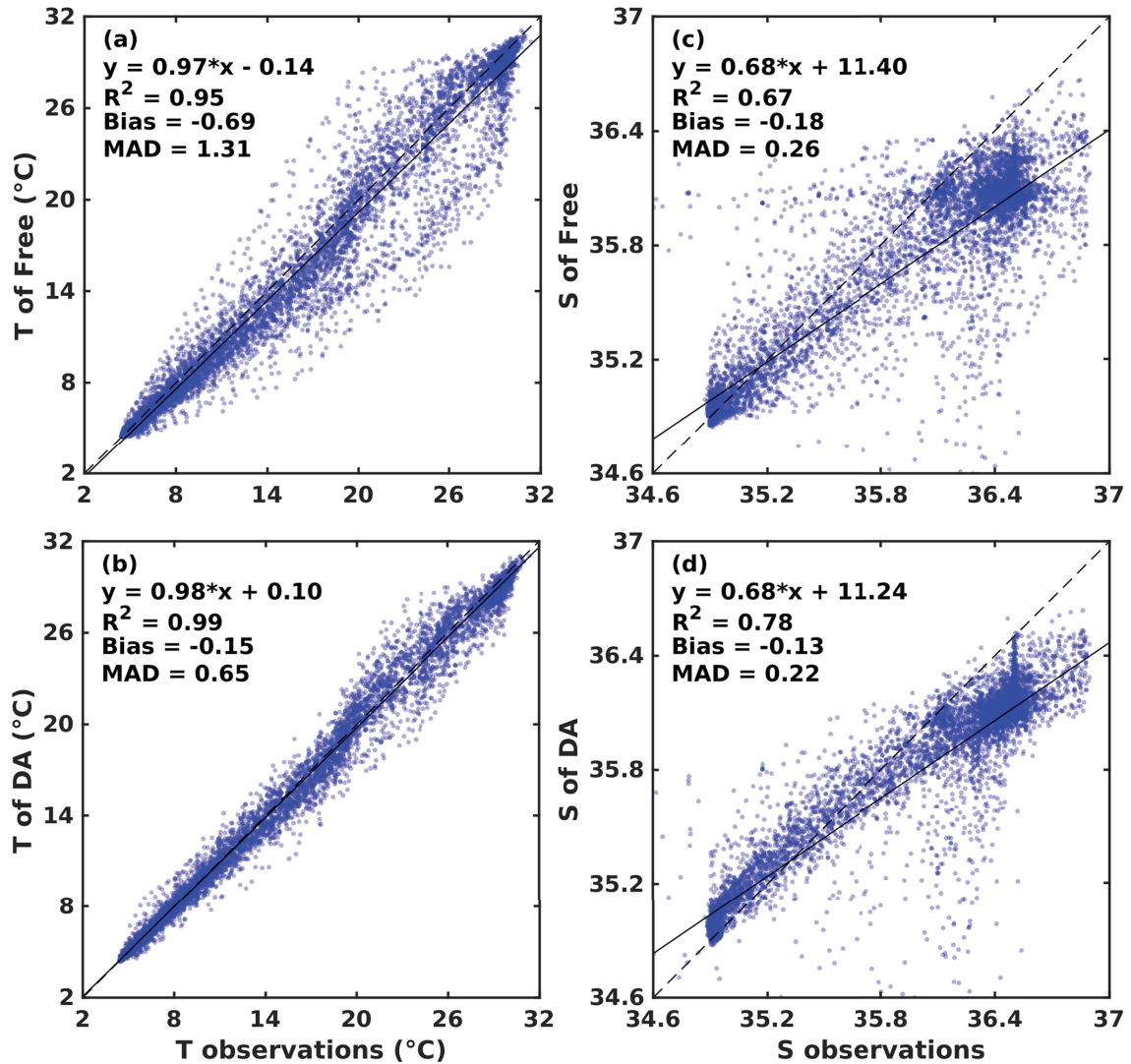


**Fig. 5.14.** Point-by-point comparison of (a, b) temperature (T, °C) and (c, d) salinity (S) from Argo observations versus those from free and DA run. The total number of data is 7018. The black line is the linear regression between variable from the truth and other run. The dashed line is the 1:1 ratio line.

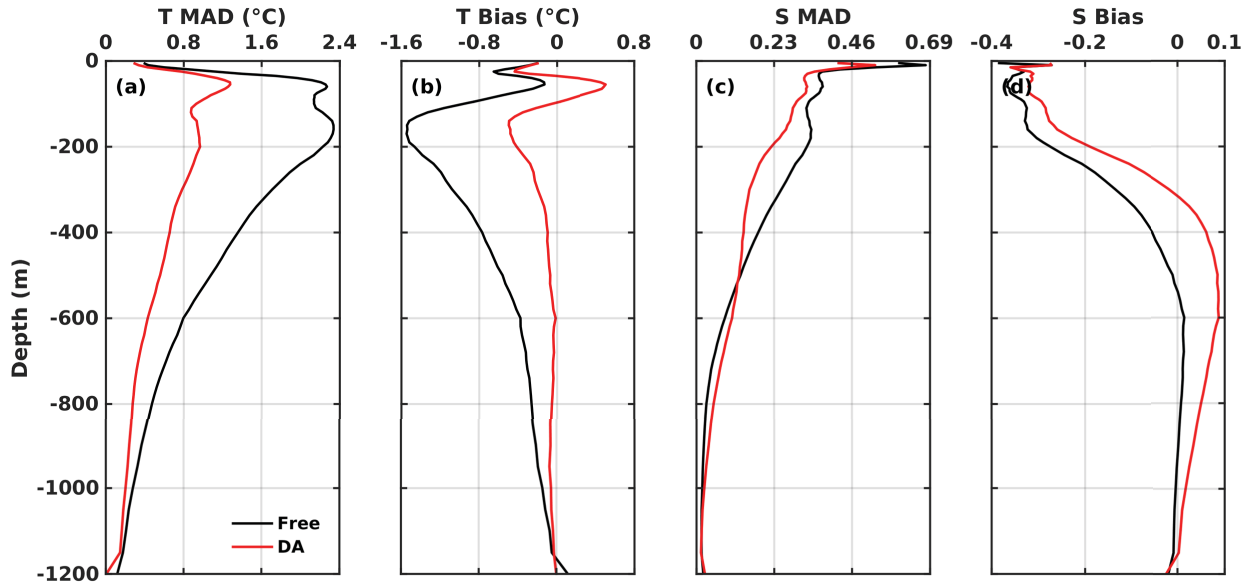


**Fig. 5.15.** Profiles of averaged MAD and bias for (a, b) temperature ( $T$ ,  $^{\circ}\text{C}$ ) and (c, d) salinity ( $S$ ) from the free and the DA run in relative to Argo observations.

Lastly, Figure 5.16 illustrates where and how the deviations between model and observations and the corrections by DA are distributed horizontally. The spatial distribution of the Argo temperature and salinity observations at 200 m clearly show the distinction between warmer and more saline LC waters from the colder and fresher rest of the Gulf (Fig. 5.16 a, d). The free run underestimates the observed temperature and salinity primarily in two regions: east of the LC and near the Mississippi delta; the former is associated with the exaggerated westward LC intrusion in the free run, while the latter might be more associated with river plume dynamics. Compared to the free run, the assimilation significantly reduces the deviations between model and observations, especially in the LC region, with significantly reduced bias and MAD reductions of 56% for temperature and 33% for salinity (Fig. 5.16c, f).



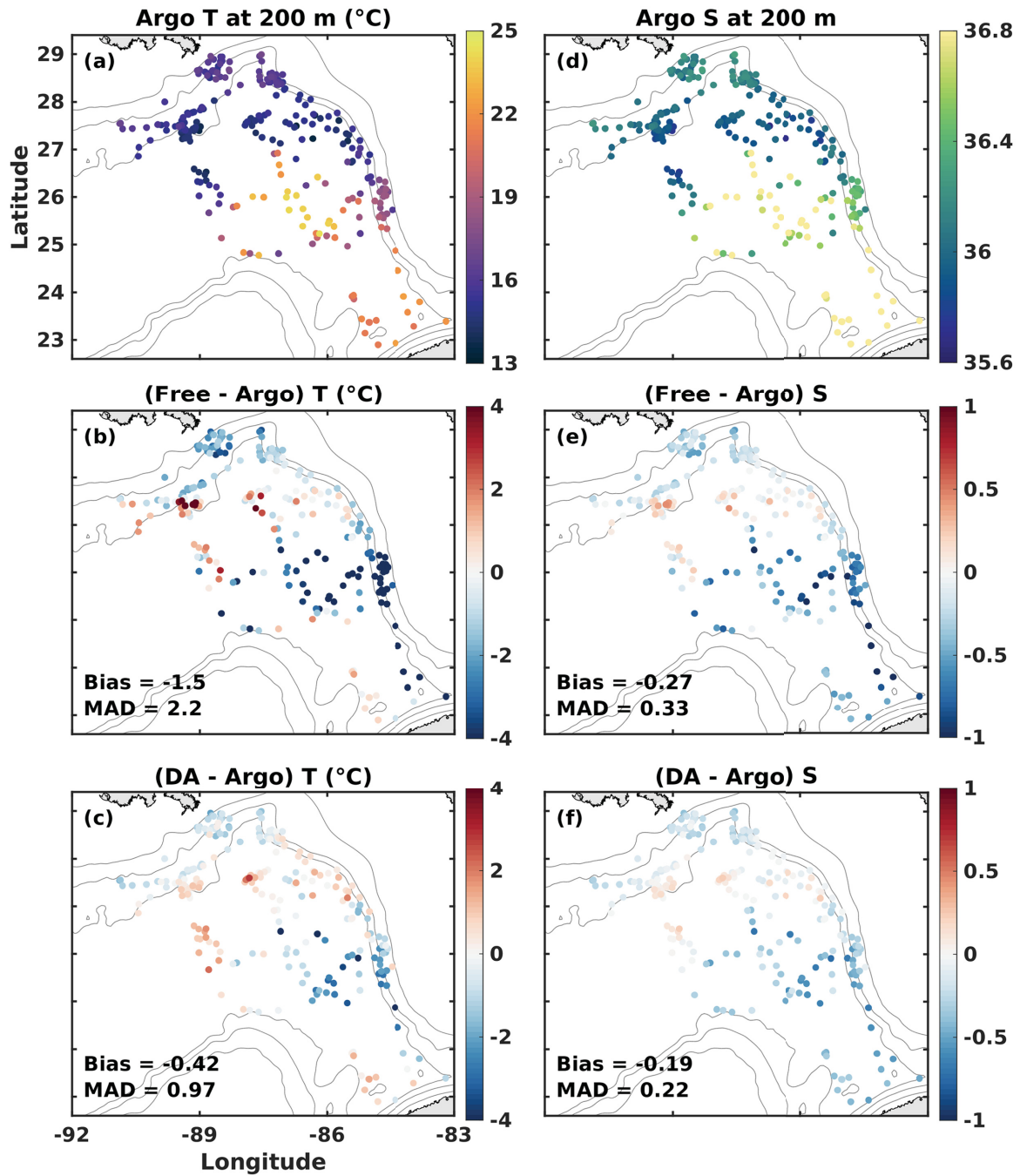


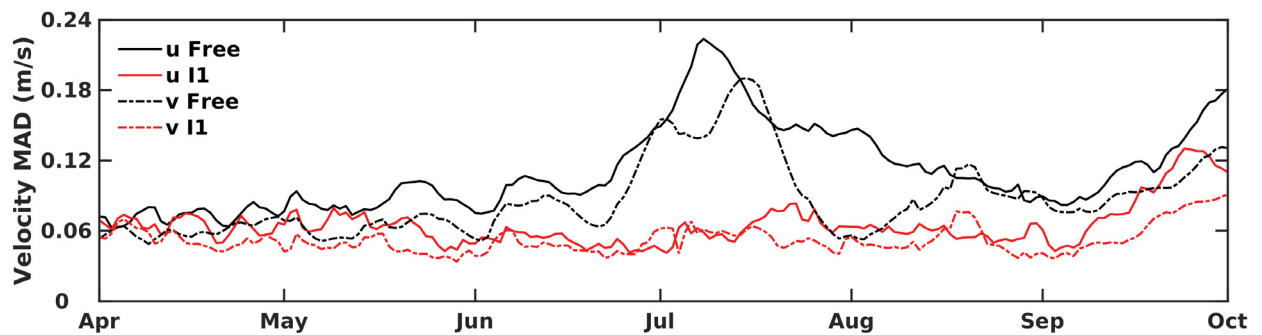
**Fig. 5.16.** Argo observations of (a) temperature (T, °C) and (d) salinity (S) at 200 m. (b, c, e, f) Difference between simulated and observed T and S at 200 m in (b, e) the free run and (c, f) DA run. The gray contours mark the bathymetric depths of 300, 1000, and 2000 m, respectively.

### 5.3.3 Impact of assimilation on physical variables and hydrocarbon fields: identical twin experiments

This section focuses on the impact of assimilation on circulation near the DwH spill site and the hydrocarbon plume distribution. First, the impact of assimilation on physical variables is briefly described in comparison to the corresponding results from the fraternal twin experiments. Then the impact of the assimilation on the hydrocarbon plume distribution is presented in more detail.

#### 5.3.3.1 Physical variables

Compared with fraternal twin experiment F1, assimilating SSH and SST in identical twin experiment I1 leads to even larger reductions in domain-averaged MAD of temperature, salinity and velocity fields. However, the benefit of assimilating additional temperature and salinity profiles is smaller than in the fraternal twin experiments (Table 5.2). Assimilating SSH and SST in I1 also reduces the subregion-averaged MAD for both  $u$  and  $v$  near the spill site with largest reductions in July (Fig. 5.17). The temporally averaged MAD reduction in the subregion is of a similar magnitude as the domain-averaged MAD for  $u$  and  $v$  (Table 5.2).



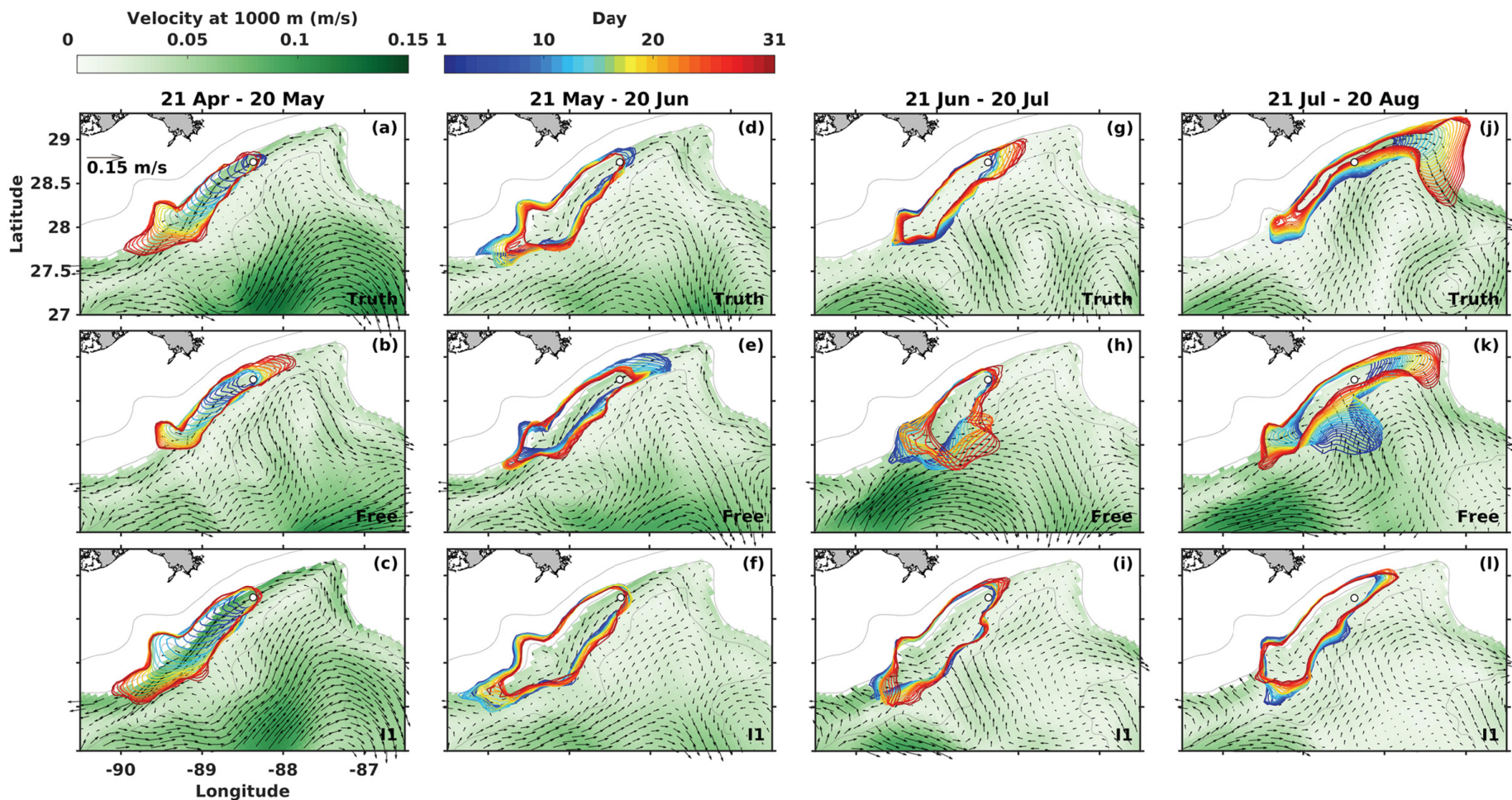
**Fig. 5.17.** Time series of subregion- and water column-averaged MAD for velocity components  $u$  and  $v$  (m/s) from the free run and I1. The location of the subregion for averaging is shown in Fig. 5.1a.



Figure 5.18 shows the time-averaged circulation at 1000 m during the first 4 months of the spill. The “truth” has three major circulation features near the DwH spill site: i) a southwestward current flows along the slope near the spill site for the first 2 months of the spill and then reverses direction for the following 2 months; ii) a strong anticyclonic eddy is present south of the spill site in the 1<sup>st</sup> month of the spill and then gradually propagates westward away, and iii) a weaker anticyclonic eddy is directly affecting the spill site in the 4<sup>th</sup> month (Fig. 5.18 a, d, g, j).

The free run reproduces the southwestward current along the spill site in the two months, but overestimates its magnitude on the western side and underestimates it on the eastern side of the spill site compared to the “truth” (Fig. 5.18b, e). Compared to the “truth”, the free run does not correctly simulate the reversal in current direction from southwestward to northeastward in the 3<sup>rd</sup> month (Fig. 5.18h). In the 4<sup>th</sup> month, the free run reproduces an anticyclonic flow field near the spill site, but its shape differs from that in the “truth” (Fig. 5.18k). The strong anticyclonic eddy in the free run is located further south than in the “truth” in the 1<sup>st</sup> month but then propagates closer to the spill site in the 3<sup>rd</sup> and 4<sup>th</sup> months (Fig. 5.18 b, e, h, k).

By assimilating SSH and SST, the major circulation features of the “truth” are reproduced better in assimilation run I1, but current velocities tend to be smaller especially for the anticyclonic circulation near the spill site in the truth during the 4<sup>th</sup> month (Fig. 5.18 c, f, i, l).



**Fig. 5.18.** Overlay of time-evolving  $0.1 \text{ g m}^{-2}$  HydroC contours (red lines) with the time-averaged velocity (m/s) at 1000 m (color map) during selected time interval in the truth (a, d, g, j), free (b, e, h, k) and DA1 run (c, f, i, l) in identical twin experiment. Blue to red color lines represent the  $0.1 \text{ g m}^{-2}$  HydroC contours from the first to last day of each averaging interval. The white dot denotes the location of the Deepwater Horizon oil rig, and gray contours mark the bathymetric depths of 300, 1000 and 2000 m, respectively.

### 5.3.3.2 Hydrocarbon fields

Circulation near the spill site strongly impacts the hydrocarbon plume distribution. In the “truth”, the hydrocarbon plume (represented by  $0.1 \text{ g m}^{-2}$  HydroC contours, where HydroC is the sum of HydroC1 and HydroC2) is mostly confined along the 1000 and 2000 m bathymetric contours (Fig. 5.18 a, d, g, j). It propagates southwestward along the slope during the first 2 months of the spill, before moving northeastward in the 3<sup>rd</sup> month and then southeastward in the 4<sup>th</sup> month. This plume movement clearly reflects the evolution of current direction around the spill site.

Consistent with the observed mismatch in current direction between the free run and the “truth”, the free run wrongly simulates a northeastward movement of the hydrocarbon plume in the 2<sup>nd</sup> half of 1<sup>st</sup> month and first half of the 2<sup>nd</sup> month (Fig. 5.18 b, e). In the 3<sup>rd</sup> month, the strong anticyclonic eddy impinges on the spill site in the free run but is more distant in the “truth” and directly affects the hydrocarbon plume (Fig. 5.18h). The resulting southward transport of plume water across the 2000 m bathymetric contour does not reflect the “truth”. In the 4<sup>th</sup> month, the free run reproduces the northeastward propagation of the hydrocarbon plume on the eastern side of the spill site but slightly overestimates the southwestward extension of the plume on the western side (Fig. 5.18k).

With assimilation in the I1 run, several of the discrepancies between the free run and “truth” are improved, especially in the first 3 months but the eastward propagation in the 4<sup>th</sup> month is missed almost entirely (Fig. 5.18 c, f, i, l). Also, the plume in the I1 run is less dynamic in the 4<sup>th</sup> month than that in the free run and “truth”, consistent with the smaller current velocities.

The temporal evolution of the hydrocarbon MAD in the free run peaks in mid May when it underestimates the magnitude of southwestward current along the spill site and mid July when it wrongly simulates a strong anticyclonic eddy that impinges on the spill site (Fig. 5.19). Assimilation in the I1 run leads to significantly reduced MAD in only May, otherwise the MAD is similar or higher than in the free run. The overall MAD reduction is 8% in I1 relative to the free run.

Also shown in Fig. 5.19 is the MAD from an extreme ‘zero-HydroC prediction’, which simply assumes no hydrocarbon in any grid cell at any time. In this case the MAD gradually increase during the spill period (20 April to 15 July) and then dramatically decreases after 15 July when the spill stops while hydrocarbons are continuously decaying. The free and I1 runs generally have lower MAD than the extreme prediction during the spill period, with exceptions in mid-May for the free run and mid-July for both free and I1 runs.

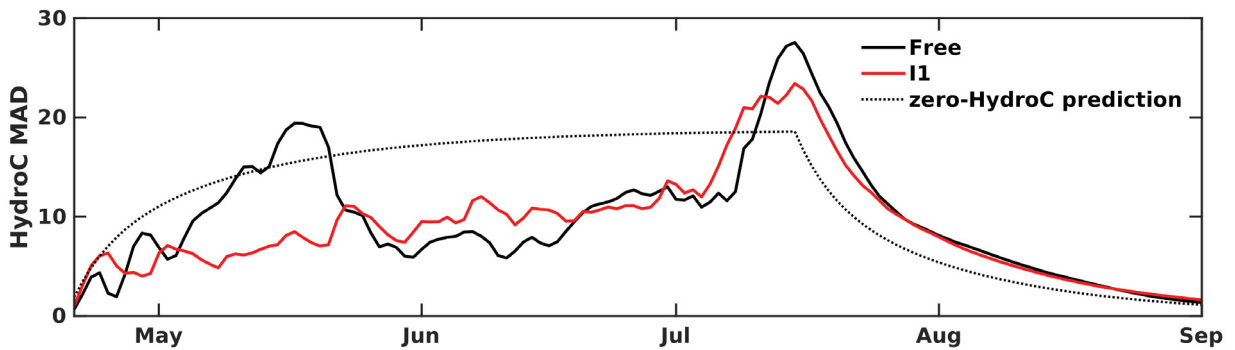


**Fig. 5.19.** Time series of domain-averaged MAD ( $\text{mg}/\text{m}^2$ ) for water column integrated HydroC from free run and I1 run in the identical twin experiments.

## 5.4 Discussion

I implemented the EnKF technique in a high-resolution regional model for the GOM. The skill of this data-assimilative system was rigorously assessed through a series of fraternal and identical twin experiments as well as a realistic assimilation experiment using satellite and *in situ* profile observations. The combination of twin and realistic assimilation experiments has demonstrated that the data-assimilation system is robust and effective in improving the 3D temperature/salinity fields and the dominant circulation features (i.e., the intrusion of LC and shed eddies) in the open GOM. Here I address each of the questions raised in the Introduction.

*Assimilating profiles versus satellite data:* Tests of different observing system configurations in fraternal twin experiments have illustrated the relative benefits of temperature and salinity profiles versus satellite SSH and SST in improving the skill of different physical state variables in the model. Consistent with previous assimilation

studies in the GOM (e.g., Wang et al., 2003; Counillon and Bertino 2009; Hoteit et al., 2013), my results show that assimilation of altimetry data can sufficiently constrain a range of large-scale to mesoscale features such as the LC and associated eddies. The warmer and more saline LC and its eddies have a temperature and salinity signature that is distinct from the so-called Gulf Common Water and have a clear signal of elevated SSH. Assimilation of SSH using the multivariate EnKF therefore can adjust temperature and salinity profiles based on the SSH information. This is shown in my fraternal twin and realistic assimilation experiments, where the assimilation of SSH and SST substantially corrects the subsurface temperature and salinity fields, with clear improvements in location and intensity of the LC and LC eddies. Salinity is less constrained than temperature when assimilating only SSH and SST. Assimilation of additional temperature profiles (experiment F2) slightly improves salinity but inclusion of salinity profiles (experiment F3) is more effective in improving salinity. This highlights the value of collecting *in situ* salinity profiles. A similar conclusion about the role of salinity measurements has been reached by Halliwell et al. (2015).

*Fraternal twin versus identical twin experiments:* Twin experiments have been widely used for assessing the performance of data assimilation schemes (e.g., Anderson et al., 1996; Srinivasan et al., 2011; Song et al., 2016; Yu et al., 2018) and for OSSE impact analyses (Halliwell et al., 2014, 2015). Halliwell et al. (2014) developed a complete set of design criteria and rigorous evaluation procedures for ocean OSSEs, which also serves as guidance on designing twin experiments for assessing the skill of a data-assimilative system. My fraternal twin experiments satisfied the requirements articulated by Halliwell et al. (2014) and thus enable a credible skill assessment. Additionally, the impact of assimilation in the fraternal twin experiment is very similar to that with realistic assimilation configuration, which further confirms the validity of the impact analysis by fraternal twin experiments. The identical twin experiments, however, are prone to biased skill assessments as the differences between the “truth” and free runs are often insufficient to represent the actual error growth between the ocean model and the true ocean. In identical twin experiment I1, the MAD reductions in physical fields are larger than in fraternal twin experiment F1; however, little further improvement is found



in the identical twin experiments when assimilating additional temperature and salinity profiles. The identical twin approach likely underestimates the value of the additional information from the profiles while overestimating the improvement resulting from assimilating SSH and SST. This issue is well known for identical twins in atmospheric OSSEs but not yet sufficiently recognized in ocean OSSEs and skill assessments of oceanic data-assimilative systems (Halliwell et al., 2014). A direct comparison of fraternal and identical twin experiments has, to the best of my knowledge, not been conducted previously for an ocean data assimilation system. The results of this chapter emphasize that caution is warranted when interpreting skill assessments and OSSEs from identical twin experiments.

*Subsurface circulation:* Based on my fraternal twin experiments, the improvement in temperature and velocity fields through assimilation of SSH and SST with or without temperature and salinity profiles extends as deep as 900 m. This is primarily because the deep basin of GOM is dominated by the energetic LC and associated eddies which extend from the surface to depths of 500 to 1000 m (Oey, 2008). The system's ability to accurately capture the dynamics of the LC and its eddies thus transfers into skill in reproducing the dominant features of the mesoscale subsurface circulation.

*Circulation near the DwH spill site:* While my assimilation experiments indicate that assimilating satellite altimetry satisfactorily constrains the large- to mesoscale structures on the order of 100 km that dominate the deep GOM, improvement in the circulation near the spill site is modest because submesoscale processes (100 m – 10 km) prevail in this region. The DwH spill site is located in the DeSoto Canyon region, a transition zone between the open Gulf where the circulation is dominated by the mesoscale LC and its eddies and the shelf where currents are largely driven by wind and density forcing. Therefore, the assimilation of SSH, SST and additional temperature and salinity profiles (at a resolution of ~70 km) in my twin experiments have relatively limited constrains on the smaller-scale circulation features near the spill site. This is consistent with Wang et al. (2003) who found that assimilating SSH and SST could not accurately resolve the smaller-scale eddies in the DeSoto Canyon. It has been suggested previously that higher-resolution localized observations would help to constrain

submesoscale processes in models (Lin et al., 2007; Jacobs et al., 2014; Carrier et al., 2014; Berta et al., 2015; Muscarella et al., 2015). Nevertheless, the substantial improvement in reproducing the mesoscale circulation features obtained through assimilation of SSH and SST does benefit the circulation near the spill site by more accurately simulating the impingement of LC eddies in the shelf break and slope regions.

The horizontal resolution of the model may also contribute to the misrepresentation of the submesoscale circulation. With a horizontal resolution of 5 km, the GOM model used here is not capable of fully resolving the submesoscale features. Ledwell et al., (2016) suggested that a horizontal resolution finer than 5 km is required in this region. Considering the computational costs of running an ensemble of finer-resolution model simulations for the GOM, a two-way nested approach with higher resolution near the oil spill site might be most affordable. Such a two-way nested modeling system could be based on the data-assimilative model developed here.

*Distribution of the deep-water hydrocarbon plume:* Similar to the fraternal twin experiments, in identical twin experiments the small-scale circulation near the spill site is improved only modestly despite of the significant improvement in circulation throughout the open GOM. While the movement of the hydrocarbon plume center is clearly determined by the currents near the spill site, the reduction in hydrocarbon MAD is much smaller than the reduction of MAD in the velocity fields, even during the time period when small-scale circulation patterns appear to be well captured by the DA run (21 Apr – 20 Jun). It is possible that a better representation of the submesoscale features (as discussed above) would significantly improve the simulation of hydrocarbon plume movement or else that observations of hydrocarbon concentrations itself need to be assimilated. Efforts to use information on surface oil distributions from satellite have been made by Liu and Weisberg (2011) to track surface oil slicks after the DwH spill and proved useful, but observation of deep plumes is more challenging. I would also like to note that, although the identical twin approach comes with a risk of overestimating the improvement on physical fields by assimilating SSH and SST, it does not affect the conclusion in this case because the focus is on the impact of improved circulation on hydrocarbon distributions.

## 5.5 Summary

An assimilation system that applies the EnKF to a high-resolution regional model of the Gulf of Mexico has been developed. The system was rigorously validated through fraternal twin experiments and tested in a realistic configuration assimilating satellite and *in situ* profile observations. In both, a fraternal twin framework and a realistic configuration, the data-assimilative system leads to robust improvements in temperature and salinity (both at the surface and in the subsurface). In particular, the location and strength of the LC and its eddies are improved by assimilating SSH, SST and profile observations.

In fraternal twin experiments, it is shown that despite the system's skill in reproducing the LC and mesoscale eddy dynamics, submesoscale features near the DWH spill site are not sufficiently improved, at least in part because no nearfield observations resolving submesoscale features were assimilated into the model. It is also possible that the horizontal resolution of 5 km is not fine enough to adequately resolve the submesoscale features. A two-way nested model with higher resolution in the region surrounding the oil spill site may be needed. The data-assimilative model developed here could serve as the coarser parent in such a two-way nested system.

In a series of identical twin experiments the impact of assimilation on the distribution of a deep-water hydrocarbon plume was investigated. While the movement of the hydrocarbon plume is clearly determined by the circulation near the spill site, the improvements in near-field circulation due to assimilation did not yield noticeable improvements in the representation of the plume. An accurate representation of the hydrocarbon plume distribution will likely require an assimilation system capable of resolving the submesoscale features near the spill site and may even require incorporation of observations of the evolving hydrocarbon distribution.



# CHAPTER 6

## CONCLUSIONS

The Gulf of Mexico, like many other marine systems in the world, is increasingly stressed by anthropogenic pressures, including excessive nutrient inputs from the Mississippi and Atchafalaya Rivers that promote widespread seasonal hypoxia on the shelf in the northern GOM, and the intensive oil exploration and extraction activities extending to the deep sea that lead to elevated risk of oil pollution. Capabilities that combine observations and numerical models for predicting the effects of these anthropogenic stressors are urgently needed. Neither observations nor numerical models alone are sufficient for providing a complete view of the true ocean state due to inherent errors, uncertainties and limitations in each; combining the two through data assimilation is crucial for achieving the best possible representation of the ocean state.

This situation has motivated me to apply regional-scale numerical ecosystem modelling (supplemented by comprehensive model-data comparisons) and the EnKF data assimilation technique in my thesis with the goal of improving our understanding and predictive capabilities for shelf water hypoxia and deep-sea oil spill pollution in the GOM. Specifically, in Chapter 2 I applied a physical-biogeochemical model that explicitly simulates oxygen sources and sinks in the northern GOM to identify the key mechanisms controlling hypoxia development. Using the same physical model but coupled to a simpler oxygen model that parameterizes biological oxygen terms using empirical relationships derived from observations, I examined the role of physical forcing factors in hypoxia generation in Chapter 3. In Chapter 4, I implemented and tested the EnKF method in an idealized upwelling model, where I demonstrated the benefits of multivariate EnKF updates to physical and biogeochemical model states through a series of twin experiments. Lastly in Chapter 5, the EnKF method is applied to a realistic physical-hydrocarbon model for the GOM to improve the simulated mesoscale circulation features and the movement of deep-water hydrocarbon plumes in the GOM.

## 6.1 Major findings

The major findings of the thesis and their significance are summarized below corresponding to the scientific questions and primary objectives listed in Chapter 1.

*1. Identify the primary processes controlling oxygen dynamics and hypoxia in the northern GOM. (Chapter 2)*

A comprehensive model-data comparison was first conducted, which demonstrates that the model can reasonably simulate the evolution of oxygen and associated key oxygen source and sink terms. The model simulation shows that in summer, stratification isolates oxygen-rich surface waters from hypoxic bottom waters; at the surface oxygen outgasses to the atmosphere at this time. The summer oxygen balance suggests that the combination of physical processes (advection and vertical diffusion) and sediment oxygen consumption largely determine the spatial extent and temporal dynamics of hypoxia on the shelf of northern GOM. Specifically, sediment oxygen consumption is the dominant oxygen sink within the bottom water volume that becomes hypoxic (within 5 m above the sediment). A large fraction of primary production occurs below the pycnocline in summer, but this primary production reduces the spatial extent of hypoxic bottom waters only slightly.

*2. Develop a relatively simple oxygen model to examine the physical controls on hypoxia generation in the northern GOM. (Chapter 3)*

The simple oxygen model assumes a constant oxygen utilization rate in the water column and a sediment oxygen consumption rate that depends on bottom water oxygen concentration and temperature. Despite its simplicity, the model reproduces the observed variability of dissolved oxygen and hypoxia in the northern GOM, highlighting the importance of physical processes. Model simulations further demonstrate that both river discharge and wind forcing have a strong effect on the distribution of the river plume and stratification, and thereby on bottom dissolved oxygen concentrations and hypoxia formation in the northern GOM. The seasonal cycle of hypoxia is relatively insensitive to the seasonal variability in river discharge,

but the time-integrated hypoxic area is very sensitive to the overall magnitude of river discharge. Changes in wind speed have the greatest effect on the simulated seasonal cycle of hypoxia and hypoxic duration, while changes in wind direction strongly influence the geographic distribution of hypoxia.

*3. Investigate the potential benefits of multivariate EnKF updates of physical and biogeochemical ocean state variables. (Chapter 4)*

Through a series of twin experiments conducted in an idealized upwelling model, I show that when biogeochemical and physical properties are highly correlated (e.g., thermocline and nutricline), multivariate updates of both are essential for improving model skill. This can be accomplished by assimilating either physical (e.g., temperature profiles) or biogeochemical (e.g., nutrient profiles) observations, taking advantage of the inherently multivariate nature of the EnKF. In the idealized upwelling system, the improvement of multivariate updates is largely due to a better representation of nutrient upwelling, which results in a more accurate nutrient input into the euphotic zone. In contrast, assimilating surface chlorophyll improves the model state only slightly, because surface chlorophyll contains little information about the vertical density structure. It is also shown that a degradation of the correlation between observed subsurface temperature and nutrient fields, which has been an issue in several previous assimilation studies, can be reduced by multivariate updates of physical and biogeochemical field.

*4. Apply EnKF to improve the simulation of circulation and movement of a deep-water hydrocarbon plume in the Gulf of Mexico. (Chapter 5)*

The EnKF method examined in Chapter 4 was implemented in a physical-hydrocarbon model for the GOM. In both, a twin and a realistic configuration, the data-assimilative system is demonstrated to be robust and effective in improving 3D temperature/salinity fields and dominant circulation features (i.e., the intrusion of the LC and shedding of eddies) in the open GOM. Fraternal twin experiments testing different observing systems show that: i) while the assimilative model can satisfactorily reproduce the mesoscale circulation features in the GOM by assimilating satellite data (i.e., SSH and

SST) alone, *in situ* temperature and especially salinity profiles are required to effectively constrain salinity fields; ii) the model's capability of capturing the dynamics of the LC and its eddies is related to its skill in reproducing the dominant features of subsurface circulation; iii) despite the system's skill in reproducing the LC and mesoscale eddy dynamics, submesoscale features near the DWH spill site are not sufficiently improved, which might be partly because no nearfield observations resolving submesoscale features were assimilated into the model, and partly because the model's horizontal resolution of 5 km is not fine enough to adequately resolve the submesoscale features. Identical twin experiments further show that the movement of the deep-water hydrocarbon plumes are essentially determined by the direction and magnitude of the currents near the spill site. The improvements in circulation near the spill site due to assimilation only yield modest improvements in the distribution of the plume. This suggests that an accurate representation of the deep-water hydrocarbon plume distribution might require an assimilation system capable of resolving the submesoscale features near the spill site and possibly observations of the evolving hydrocarbon distribution.

## **6.2 Implications for model development and assimilation method implementation and assessment**

Throughout the thesis, I have applied two numerical models of dissolved oxygen with different ecological complexity for the northern GOM focusing on different aspects of the oxygen dynamics, and implemented the state-of-the-art EnKF technique in an idealized upwelling model and a realistic model configured for the GOM. Thus, in addition to the scientific achievements described in the previous section, some implications for hypoxia model development and assimilation implementation and assessment are also achieved.

### ***Implications for hypoxia forecasting and model development***

The facts that the simple oxygen model in Chapter 3 essentially reproduces the hypoxia evolution simulated by the full biogeochemical model in Chapter 2 and that physical processes largely determine the magnitude and distribution of hypoxia imply

that a full biogeochemical model might not be necessary for short-term hypoxia forecasting in the northern GOM. It further implies that prior to using a complex biogeochemical model, one could take an intermediate approach by developing a relatively simple model that parameterizes biological oxygen terms using empirical relationships derived from observations. This is particularly true for regions that have already developed skilful hydrodynamic models. Furthermore, since the simple oxygen model is free of the potentially confounding effects of a full biogeochemical model, it is well suited for conducting model intercomparisons to identify the major physical model aspects that affect a model's ability to accurately simulate or predict hypoxia (e.g., as in Fennel et al., 2016).

Nevertheless, the simple model developed here is appropriate for short-term hypoxia forecasting but not for scenario simulations to assess the effects of varying nutrient loads in this region because the model is independent of nutrient loading. Instead, a full biogeochemical model like the one in Chapter 2 is necessary to study the effects of varying river nutrient loads on hypoxia and to evaluate the effectiveness of nutrient-reduction strategies (e.g., as in Laurent and Fennel, 2014; Fennel and Laurent, 2018).

### ***Implications for EnKF implementation***

A few assimilation settings were identified to be important for the performance of the assimilation system, as listed below.

*Ensemble generation.* Perhaps not surprisingly I found that the sources of error used to perturb (or generate) the ensemble simulations are crucial, as they largely determine whether the ensemble spread is representative of the forecast error (sufficiently large). This is especially the case for the GOM, where the dominant forcing of the circulation is distinct in the open Gulf and the shelf region. The open Gulf is dominated by the LC and its mesoscale eddies while shelf circulation is heavily influenced by wind and density forcing. In order to properly represent the forecast error, initial conditions, lateral boundary conditions and wind forcing were perturbed to generate the ensemble simulations in my assimilation experiments. I found that perturbing initial and boundary conditions mainly influences the dynamics in LC region by changing the position and

orientation of the LC and the propagation of the cyclonic eddies shed from the LC, whereas perturbing the wind forcing has the strongest impact in the shelf areas. My initial sensitivity tests show that simultaneously perturbing the three error sources yields a more realistic ensemble spread in the entire GOM domain than only perturbing one or two of them.

*Ensemble size, localization and inflation.* The biggest limitation for most ensemble-based data assimilation systems is probably the small ensemble size dictated by the availability of computing resources. This limitation requires the use of localization, which artificially reduces the spatial domain of the influence of observations at the update step, and hence prevents the potential negative effects of spurious correlations between distant grid points resulting from relatively small ensembles. In addition, to accounting for the underestimation of the forecast error covariance due to the small ensemble size, inflation of the ensemble spread is often applied. In practice, localization radius and inflation factor are selected by finding the values that best reduce the model-data errors without causing ensemble collapse or generating discontinuities in the analyzed fields. My initial tests of seeking the optimal values for localization radius and inflation factor show that the upwelling and GOM systems are more sensitive to the localization radius than the choice of inflation factor. The optimal value of the localization radius is also strongly impacted by the spatial resolution and type of the observations (e.g., a larger radius is required for assimilating nitrate profiles at coarser-resolution while a smaller radius is needed for assimilating surface chlorophyll at higher-resolution in Chapter 4).

### ***Implications for designing twin experiment framework***

Twin experiments are very useful for assessing the performance of an assimilation scheme and evaluating the impact of different observation sampling strategies, as demonstrated in Chapters 4 and 5. However, despite the carefully chosen error sources for ensemble generation and well-selected assimilation configuration parameters, the identical twin approach used in Chapter 5 was found to overestimate the positive impacts of assimilating satellite data while underestimating the impact of assimilating extra

profiles. This highlights the importance of designing credible fraternal twin experiments that allow a more rigorous assessment of the assimilation impact. Following Halliwell et al. (2014), Chapter 5 gives an example of setting up a fraternal twin experiment framework that meets the following requirements: i) the ‘truth’ run (a data-assimilative global HYCOM run) is able to reproduce the key feature of the ocean phenomenon (i.e. the LC intrusion) with sufficient realism; and ii) there are sufficient differences (errors) between the free and ‘truth’ runs for the assimilation method to correct.

### **6.3 Future work**

The two numerical models of dissolved oxygen for the northern GOM were applied to investigate hypoxia evolution under present forcing scenarios. They are also useful for conducting future scenario simulations to assess the impact of other anthropogenic stressors including global warming and rising atmospheric carbon dioxide level on the oxygen dynamics as well as other functions of the ecosystems in the GOM, as have been done in Laurent et al. (2018).

The benefits of multivariate EnKF updates of physical and biogeochemical ocean state variables have been thoroughly demonstrated in an idealized upwelling model in Chapter 4. These benefits need to be further tested and explored in a realistic model configured for the GOM or another region where sufficient observations for assimilating real physical and/or biogeochemical measurements are available.

Throughout the thesis, the EnKF method is only used to sequentially correct the model state by incorporating available observations. Nevertheless, even with perfect initial conditions obtained by state estimation, numerical models are expected to diverge from the true state due to the various sources of model errors, such as the inaccurate model forcing, boundary conditions, and other parameters associated with the physically or/and biologically mediated processes. It follows that, generating reliable forecasts requires good estimates of not only the current system state but also the model parameters (the “parameters” here is used in a broad sense to include forcing, boundary conditions, as well as parameter values used in physical and/or biogeochemical components of the model). One approach to achieve the simultaneous estimation of the model state variables

and biased parameters is the state augmentation method, which can be formulated either in a variational or sequential assimilation framework (e.g., see review in Dee, 2005). Successful applications of the EnKF method with state augmentation to jointly estimate the time-varying model state variables and biogeochemical model parameters have emerged and shown positive results (e.g., Simon et al., 2015; Gharamti et al., 2017a,b). Similar ideas could be applied to simultaneously correct the model forcing and boundary conditions along with the model state (e.g., by conducting an EOF analysis to obtain the spatial modes (or patterns) and corresponding time series of each mode's amplitude for the forcing fields or/and boundary conditions, and then introducing perturbation parameters to the time series that could be augmented to the model state vector and be updated simultaneously). Additionally, considering that the errors in model parameters (e.g., biogeochemical parameters, model forcing and boundary conditions) are likely correlated through time, an autoregressive (AR) model (e.g., AR(1) model) could be used to incorporate the time-dependence feature of the parameters when they are augmented with the state. Such ideas have not yet been explored in the EnKF assimilation framework and could be a focus of future work.

Impact analyses in fraternal twin OSSEs are needed to assess whether high-resolution *in situ* observations (e.g., measurements from drifters and/or current meters, and temperature and salinity profiles) that resolve the submesoscale features near the DwH spill site could improve the simulation of small-scale circulation features and hence the deep-water hydrocarbon plume distribution. Among the *in situ* observations, data collected by drifters might need to be handled differently as they are Lagrangian data that consist of position-time measurements instead of ocean velocity that could be directly assimilated into the model. Two common ways to assimilate drifter data are: i) derive velocity from the dataset by computing the change in drifter position within a time interval; ii) assimilate the drifter positions directly by simulating a series of tracers and then minimizing the distance between the observed and model simulated drifter trajectories via some assimilation schemes, or by state augmentation that augments the model with tracer advection equations and then tracks the correlations between the flow and tracers via Kalman Filter scheme (see, e.g., Carrier et al. (2013) and references



therein). In addition to the impact analysis on submesoscale circulation, identical twin OSSEs could be conducted to examine the impact of assimilating hydrocarbon information to further improve the simulated plume distribution.

As also suggested by the fraternal twin experiments, a two-way nested model with higher resolution near the DwH spill site may be needed to better resolve the submesoscale features of the circulation. The data-assimilative model developed in Chapter 5 could serve as the coarser parent in such a two-way nested system.

Last but not least, the impact of assimilation on hydrocarbon plume distribution in a realistic configuration assimilating satellite and *in situ* profile observations should be examined. The simulated deep-water hydrocarbon plume distribution could be validated against the observed oxygen drawdown in the deep water, a signal of hydrocarbon degradation, for independent skill assessment. Ultimately, the data-assimilative physical-hydrocarbon model will be built on to predict the movement and monitor the decay of hydrocarbon plumes in the water column in the event of a deep-water oil spill like the 2010 DwH disaster.

As a final remark, while in this thesis the regional-scale numerical modelling and data assimilation tools were applied to the Gulf of Mexico and focusing on the hypoxia and deep-water oil spill pollution only, these techniques are also applicable to other marine ecosystems and/or to improve our understanding and predictive capabilities of the effects of other anthropogenic perturbations.

# APPENDIX A

## COPYRIGHT PERMISSION

### Biogeosciences

An interactive open-access journal of the European Geosciences Union



[EGU.eu](#) | [EGU Publications](#) | [EGU Highlight Articles](#) | [Contact](#) | [Imprint](#) | [Data protection](#) |

#### Licence and copyright agreement

The following licence and copyright agreement is valid for any article submitted from **6 June 2017** onwards. For manuscripts submitted before, the [CC BY 3.0 License](#) was used.

#### Author's certification

By submitting a manuscript, the authors certify that they have read and agreed to the following terms:



- The authors are authorized by their co-authors to enter into these arrangements.
- The work is original and has not been formally published before (except in the form of an abstract, preprint, or as part of a published lecture, review, or thesis), that it is not under consideration for publication elsewhere, that its publication has been approved by all the author(s) and by the responsible authorities – tacitly or explicitly – of the institutes where the work has been carried out, and that the article does not infringe copyright or any other rights by third parties.
- The work does not contain content that is unlawful, abusive, or constitute a breach of contract or of confidence or of commitment given to secrecy.
- The authors warrant that they secure the right to reproduce any material that has already been published or copyrighted elsewhere.
- They agree to the following licence and copyright agreement:

#### Copyright


- Authors retain the copyright of the article. Regarding copyright transfers please see below.
- Authors grant Copernicus Publications an irrevocable non-exclusive licence to publish the article electronically and in print format and to identify itself as the original publisher.
- Authors grant Copernicus Publications commercial rights to produce hardcopy volumes of the journal for sale to libraries and individuals.
- Authors grant any third party the right to use the article freely as long as its original authors and citation details are identified.
- The article is distributed under the [Creative Commons Attribution 4.0 License](#). Unless otherwise stated, associated published material is distributed under the same licence:

#### Creative Commons Attribution 4.0 License

You are free to:

-  **Share** – copy and redistribute the material in any medium or format
-  **Adapt** – remix, transform, and build upon the material for any purpose, even commercially.

Under the following conditions:

-  **Attribution** – You must give appropriate credit, provide a link to the licence, and indicate if changes were made. You may do so in any reasonable manner, but not in any way that suggests the licensor endorses you or your use.

No additional restrictions – You may not apply legal terms or technological measures that legally restrict others from doing anything the licence permits.

#### Notices:

- The licensor cannot revoke these freedoms as long as you follow the licence terms.
- You do not have to comply with the licence for elements of the material in the public domain or where your use is permitted by an applicable exception or limitation.
- No warranties are given. The licence may not give you all of the permissions necessary for your intended use. For example, other rights such as publicity, privacy, or moral rights may limit how you use the material.
- The CC BY License, of which 4.0 is the recent version, was developed to facilitate open access – namely, free immediate access to, and unrestricted reuse of, original works of all types.
- Under this liberal licence, authors agree to make articles legally available for reuse, without permission or fees, for virtually any purpose. Anyone may copy, distribute, or reuse these articles, as long as the author and original source are properly cited. Thus, CC BY facilitates the dissemination, transfer, and growth of scientific knowledge.
- Please read the full [legal code](#) of this licence.

#### Copyright transfers

#### Crown copyright

#### Reproduction request

All articles published by Copernicus Publications have been licensed under the Creative Commons Attribution 4.0 License since 6 June 2017 (see details above) or under its former version 3.0 since 2007. Under these licences the authors retain the copyright. There is no need from the publisher's side to allow/confirm a reproduction. We suggest contacting the authors to inform them about the further usage of the material. In any case, the authors must be given credit.



**Title:** A modeling study of physical controls on hypoxia generation in the northern Gulf of Mexico

**Author:** Liuqian Yu, Katja Fennel, Arnaud Laurent

**Publication:** Journal of Geophysical Research: Oceans

**Publisher:** John Wiley and Sons

**Date:** Jul 18, 2015

Copyright © 2015, John Wiley and Sons

Logged in as:

Liuqian Yu

LOGOUT

### Order Completed

Thank you for your order.

This Agreement between Ms. Liuqian Yu ("You") and John Wiley and Sons ("John Wiley and Sons") consists of your license details and the terms and conditions provided by John Wiley and Sons and Copyright Clearance Center.

Your confirmation email will contain your order number for future reference.

#### [printable details](#)

License Number	4452111283143
License date	Oct 18, 2018
Licensed Content Publisher	John Wiley and Sons
Licensed Content Publication	Journal of Geophysical Research: Oceans
Licensed Content Title	A modeling study of physical controls on hypoxia generation in the northern Gulf of Mexico
Licensed Content Author	Liuqian Yu, Katja Fennel, Arnaud Laurent
Licensed Content Date	Jul 18, 2015
Licensed Content Volume	120
Licensed Content Issue	7
Licensed Content Pages	21
Type of use	Dissertation/Thesis
Requestor type	Author of this Wiley article
Format	Electronic
Portion	Full article
Will you be translating?	No
Title of your thesis / dissertation	IMPROVED PREDICTION OF THE EFFECTS OF ANTHROPOGENIC STRESSORS IN THE GULF OF MEXICO THROUGH REGIONAL-SCALE NUMERICAL MODELING AND DATA ASSIMILATION
Expected completion date	Nov 2018
Expected size (number of pages)	202
Requestor Location	Ms. Liuqian Yu Department of Oceanography, 1355 Oxford Street, Halifax, NS, B3H 4R2, Canada Halifax, NS B3H 4R2 Canada Attn: Ms. Liuqian Yu
Publisher Tax ID	EU826007151
Total	0.00 CAD



**Title:** Insights on multivariate updates of physical and biogeochemical ocean variables using an Ensemble Kalman Filter and an idealized model of upwelling

**Author:** Liuqian Yu, Katja Fennel, Laurent Bertino, Mohamad El Gharamti, Keith R. Thompson

**Publication:** Ocean Modelling

**Publisher:** Elsevier

**Date:** June 2018

© 2018 Elsevier Ltd. All rights reserved.

**LOGIN**

If you're a **copyright.com** user, you can login to RightsLink using your copyright.com credentials.

Already a **RightsLink** user or want to [learn more?](#)

Please note that, as the author of this Elsevier article, you retain the right to include it in a thesis or dissertation, provided it is not published commercially. Permission is not required, but please ensure that you reference the journal as the original source. For more information on this and on your other retained rights, please visit: <https://www.elsevier.com/about/our-business/policies/copyright#Author-rights>

**BACK****CLOSE WINDOW**

Copyright © 2018 [Copyright Clearance Center, Inc.](#) All Rights Reserved. [Privacy statement.](#) [Terms and Conditions.](#)  
Comments? We would like to hear from you. E-mail us at [customercare@copyright.com](mailto:customercare@copyright.com)

## APPENDIX B

**Table B1.** Parameters and parameter values of the biogeochemical model in Chapter 2.

Symbol	Description	Value	Unit
Nutrients			
$n_{max}$	Maximum nitrification rate	0.2	$d^{-1}$
$k_E$	Light intensity for half-saturated nitrification inhibition	0.1	$W m^{-2}$
$E_0$	Threshold for light-inhibition of nitrification	0.0095	$W m^{-2}$
Phytoplankton			
$\mu_0$	Phytoplankton growth rate at 0 °C	0.59	$d^{-1}$
$\alpha$	Initial slope of P-I curve	0.025	$mg C(mg Chl W m^{-2}d)^{-1}$
$k_{NO_3}$	Half saturation concentration for nitrate	0.5	$mmol N m^{-3}$
$k_{NH_4}$	Half saturation concentration for ammonium	0.5	$mmol N m^{-3}$
$k_{PO_4}$	Half saturation concentration for phosphate	0.03	$mmol P m^{-3}$
$m_P$	Phytoplankton mortality	0.15	$d^{-1}$
$\tau$	Phytoplankton and suspended detritus aggregation rate	0.01	$(mmol N m^{-3})^{-1}d^{-1}$
$\theta_{max}$	Maximum chlorophyll to phytoplankton ratio	0.0535	$mg Chl mg C^{-1}$
$w_{Phy}$	Sinking velocity of phytoplankton	0.1	$m d^{-1}$
Zooplankton			
$g_{max}$	Maximum grazing rate	0.6	$d^{-1}$
$k_P$	Phytoplankton ingestion half-saturation concentration	2	$(mmol N m^{-3})^2$
$\beta$	Assimilation efficiency	0.75	Dimensionless
$l_{BM}$	Excretion rate due to basal metabolism	0.1	$d^{-1}$
$l_E$	Maximum rate of assimilation related excretion	0.1	$d^{-1}$
$m_Z$	Zooplankton mortality	0.025	$(mmol N m^{-3})^{-1}d^{-1}$
Detritus			
$r_{SD}$	Remineralization rate of suspended detritus	0.3	$d^{-1}$
$r_{LD}$	Remineralization rate of large detritus	0.01	$d^{-1}$
$r_{RD}$	Remineralization rate of river detritus	0.03	$d^{-1}$
$w_{SDet}$	Sinking velocity of suspended detritus	0.1	$m d^{-1}$
$w_{LDet}$	Sinking velocity of large particles	5	$m d^{-1}$
$r_{ox}$	Yield of POM oxidation to ammonium in sediments	0.25	$mol N mol N^{-1}$

## I. Simulated oxygen budget and hypoxia by normal model simulation in Chapter 2

**Table B2.** Simulated 4-year (2004-2007) mean oxygen budget in summer for the four sub-regions. Oxygen source and sink terms are given for the surface layer above the pycnocline, for the mid layer and for the 5-m thick bottom layer.

Layers	O <sub>2</sub> flux	Mississippi Delta	Mississippi Intermediate	Atchafalaya Plume	Mid-shelf	All regions
Surface	Airsea	-21.2	-10.0	-12.2	-4.8	-11.3
	PP	85.1	68.9	94.8	79.3	79.7
	WR	56.9	55.7	59.6	67.1	60.2
	PP-WR	28.2	13.3	35.2	12.1	19.5
	H+Vadv	-7.8	-4.1	-12.0	-11.6	-8.5
	Vdiff	-5.5	-5.8	-21.1	-5.4	-7.8
	Net	-6.3	-6.6	-10.1	-9.7	-8.0
Mid	PP	65.4	55.3	44.4	61.8	58.1
	WR	61.3	45.6	38.7	55.9	51.5
	PP-WR	4.1	9.7	5.7	5.9	6.7
	H+Vadv	4.8	2.3	1.5	8.3	4.7
	Vdiff	-7.0	-11.5	-2.0	-14.7	-10.1
	Net	2.0	0.5	5.3	-0.4	1.2
Bottom	PP	13.6	19.6	23.9	8.7	15.4
	WR	14.1	19.2	35.3	11.1	17.8
	SOC	37.0	39.8	42.8	36.0	38.4
	PP-WR-SOC	-37.5	-39.4	-54.2	-38.5	-40.8
	H+Vadv	21.2	16.4	13.2	14.4	16.4
	Vdiff	12.4	17.3	23.1	20.1	17.9
	Net	-3.9	-5.7	-17.8	-4.0	-6.5

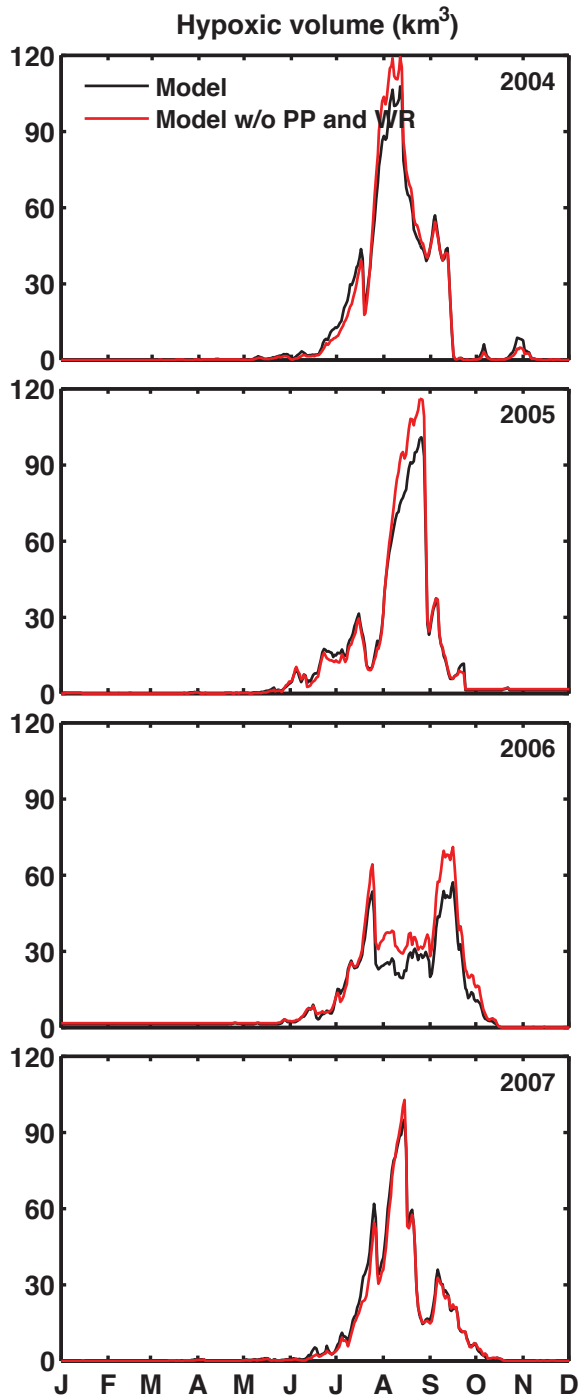


**Fig. B1.** Time series of simulated hypoxic volume for the full model (black line) and the model without biological processes in the water column (red line).

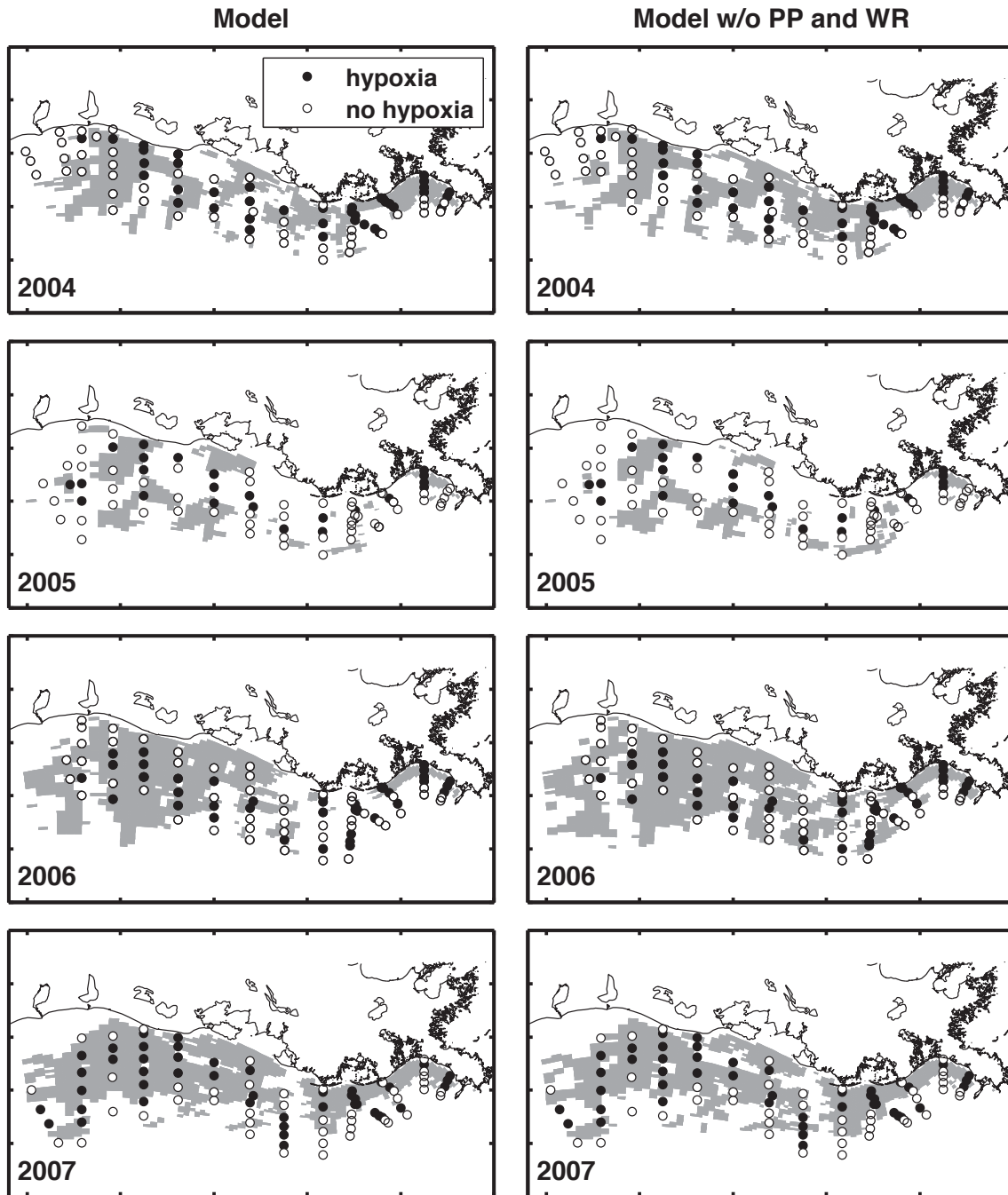


**Fig. B2.** Simulated (gray areas) and observed (dots) hypoxic conditions for the full model (left column) and the model without biological processes in water column (right column) for the years 2004 to 2007. The simulated hypoxic area includes all grid boxes where bottom water dissolved oxygen  $< 62.5$  mmol/m<sup>3</sup> during the July monitoring cruise. The stations where hypoxia was observed are shown as filled black dots, while stations without hypoxia are shown as white dots.



## II. Simulated oxygen budget and hypoxia by Model+CCR simulation in Chapter 2

**Table B3.** Simulated 4-year (2004-2007) mean oxygen budget in summer for the four sub-regions by Model+CCR simulation. Oxygen source and sink terms are given for the surface layer above the pycnocline, for the mid layer and for the 5-m thick bottom layer.

Layers	O <sub>2</sub> flux	Mississippi Delta	Mississippi Intermediate	Atchafalaya Plume	Mid-shelf	All regions
Surface	Airsea	-10.2	5.1	1.1	17.9	5.1
	PP	83.1	67.3	93.3	77.3	77.9
	WR	62.7	64.9	65.7	81.7	69.8
	PP-WR	20.4	2.4	27.5	-4.3	8.1
	H+Vadv	-6.7	-2.9	-12.8	-11.9	-8.1
	Vdiff	-9.8	-11.4	-26.4	-12.3	-13.5
	Net	-6.2	-6.8	-10.5	-10.7	-8.4
Mid	PP	64.7	54.6	44.0	61.1	57.4
	WR	83.7	64.3	45.1	81.2	71.4
	PP-WR	-19.0	-9.7	-1.1	-20.1	-13.9
	H+Vadv	24.2	17.3	4.1	27.4	20.2
	Vdiff	-3.7	-7.8	1.7	-8.7	-5.8
	Net	1.5	-0.3	4.8	-1.4	0.5
Bottom	PP	13.6	19.6	23.9	8.7	15.4
	WR	21.6	26.7	43.1	18.8	25.4
	SOC	32.4	36.7	38.4	30.9	34.1
	PP-WR-SOC	-40.4	-43.8	-57.6	-41.1	-44.1
	H+Vadv	22.6	17.8	12.2	14.8	17.2
	Vdiff	13.6	19.2	24.7	21.0	19.3
	Net	-4.2	-6.8	-20.7	-5.3	-7.7

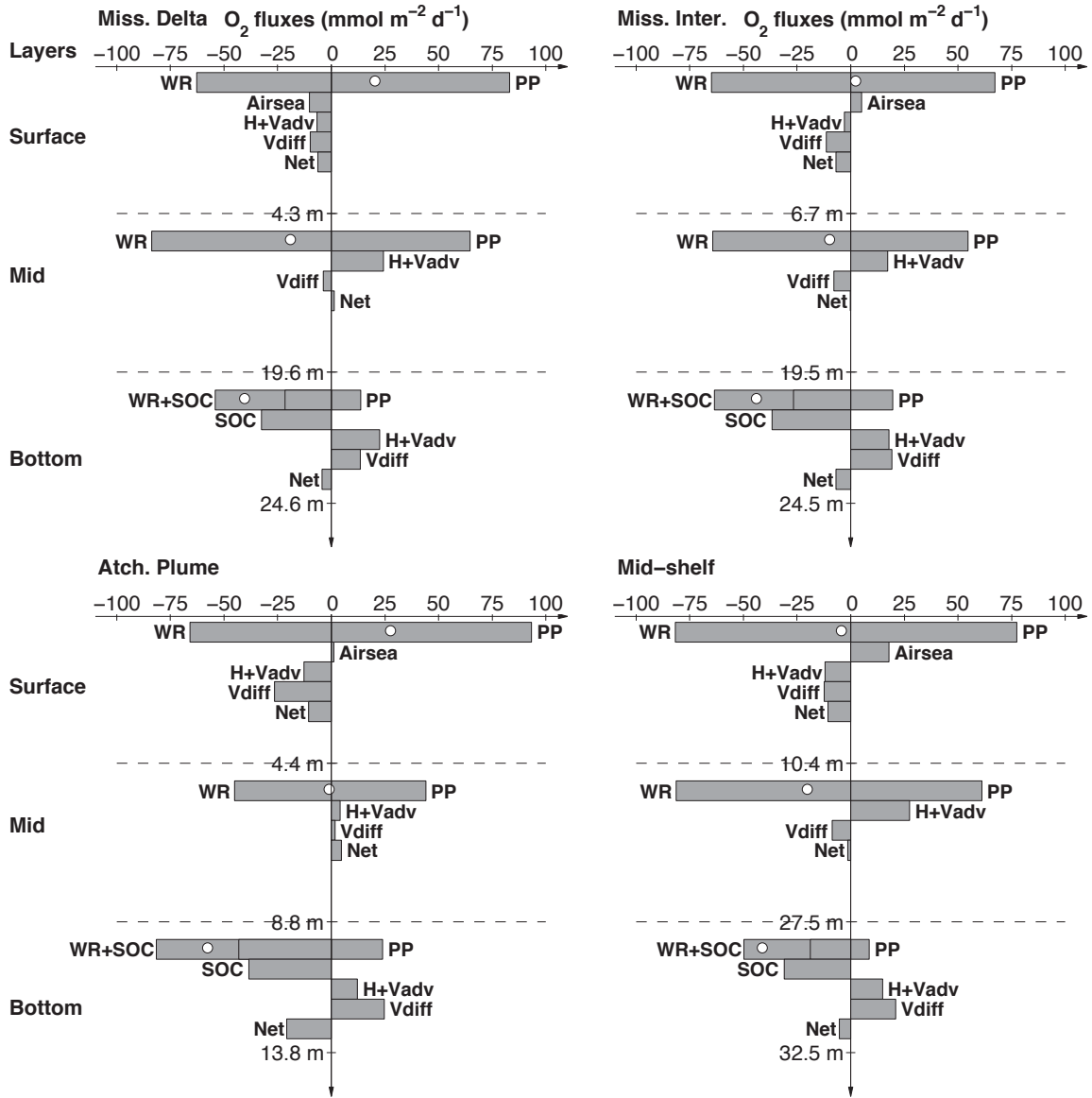


**Fig. B3.** Simulated 4-year (2004-2007) mean oxygen budget in summer for the 4 sub-regions by Model+CCR simulation. Oxygen source and sink terms are given for the surface layer above the pycnocline, for the mid layer and for the 5-m thick bottom layer. The average depth of the pycnocline, 5 m above bottom and the average water depth are indicated for each sub-region. The open circles indicate the balance of primary production and respiration in each layer. For the bottom layer, the bars for water column respiration (WR) and sediment oxygen consumption (SOC) are shown stacked and SOC is repeated separately.

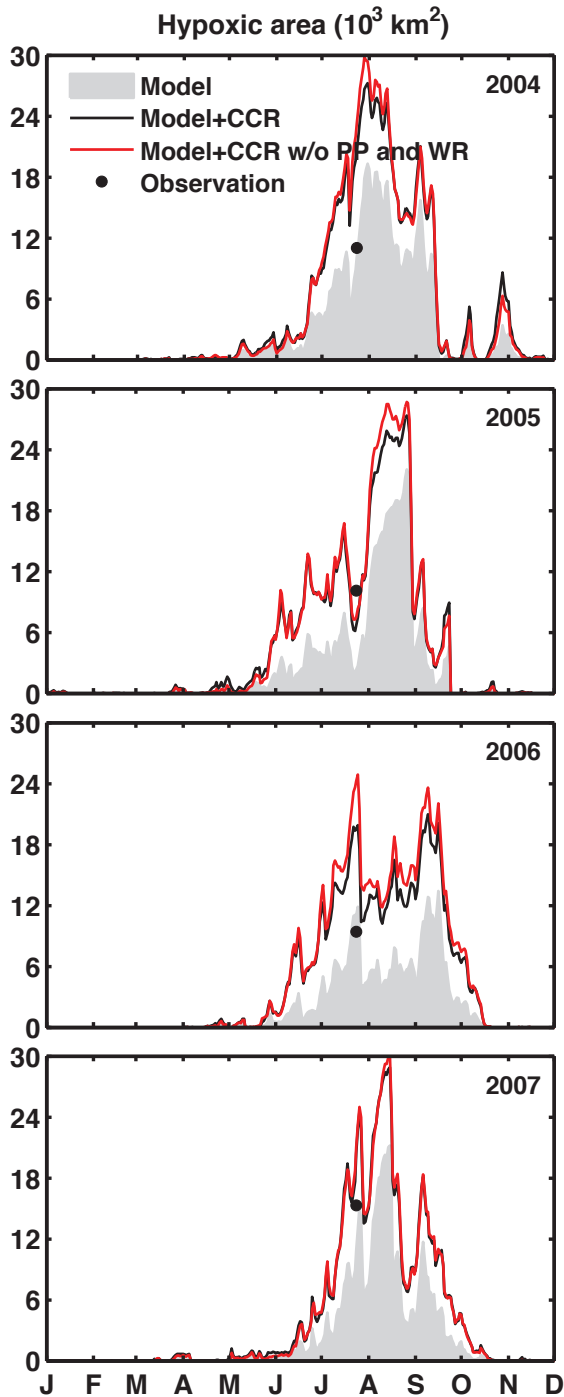


**Fig. B4.** Time series of simulated hypoxic extent for the normal model simulation (gray shadow), Model+CCR simulation (black line) and Model+CCR without biological processes in the water column (Model+CCR w/o PP and WR, red line). Also shown is the observed hypoxic extent in late July (black dots). The observed hypoxic extent was estimated by linearly interpolating the observed oxygen concentrations onto the model grid with Matlab's grid data function and then calculating the area with oxygen concentrations below the hypoxic threshold (Fennel et al., 2013).

## APPENDIX C

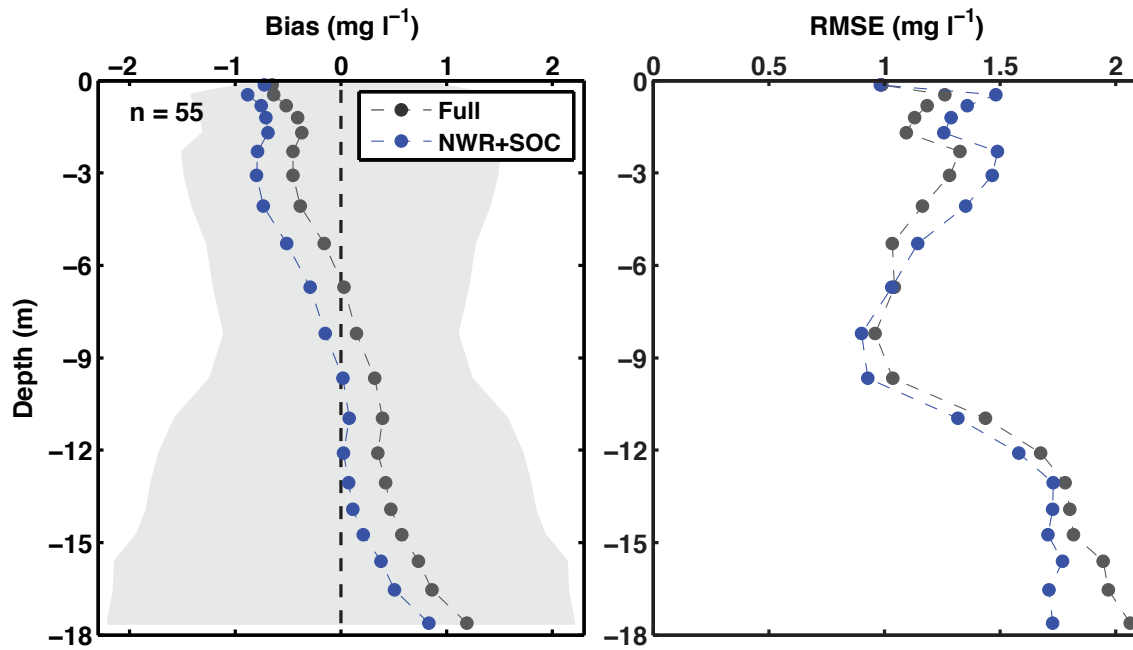


**Fig. C1.** Vertical profiles of model bias (model minus observations, mg O<sub>2</sub> l<sup>-1</sup>) and RMSE (root mean squared error, mg O<sub>2</sub> l<sup>-1</sup>) in dissolved oxygen (DO) in 2004-2007 at station C6. The light shadows represent the one standard deviation in the observations.

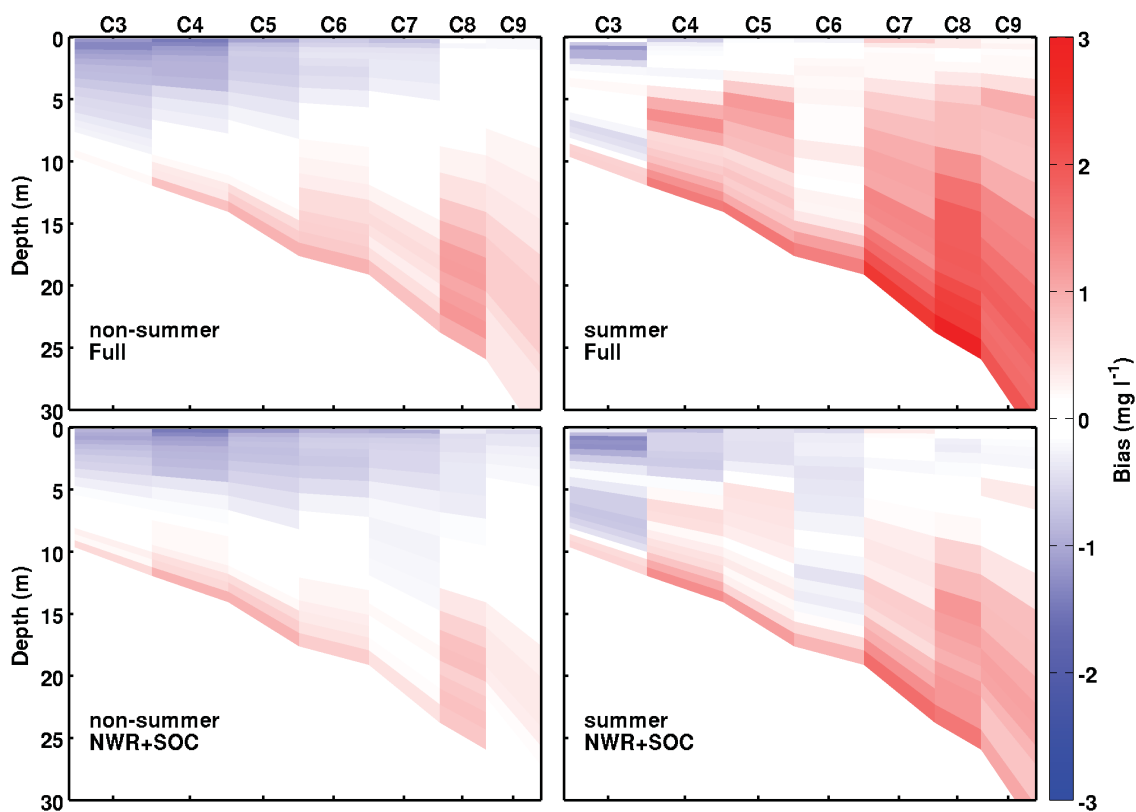


**Fig. C2.** The model bias (model minus observations, mg O<sub>2</sub> l<sup>-1</sup>) in non-summer and summer averaged dissolved oxygen (DO) in 2004-2007 at stations along C transect.

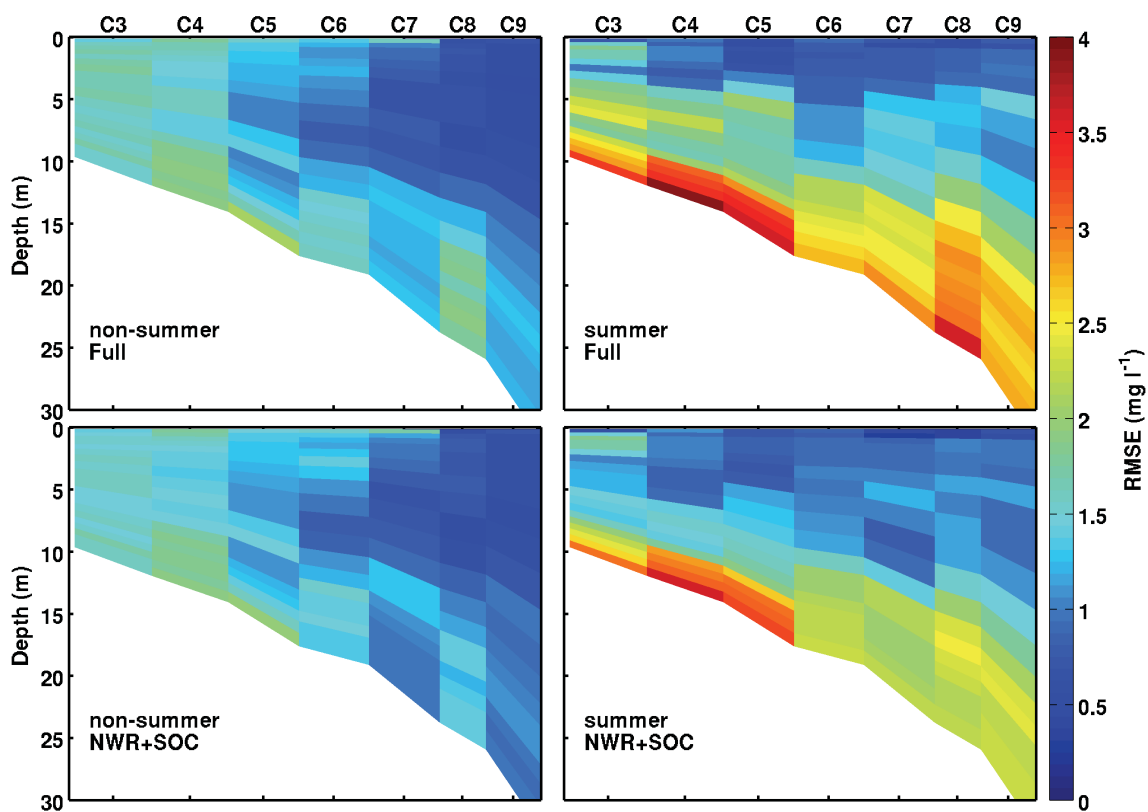


**Fig. C3.** The model RMSE (root mean squared error,  $\text{mg O}_2 \text{l}^{-1}$ ) in non-summer and summer averaged dissolved oxygen (DO) in 2004-2007 at stations along C transect.

## APPENDIX D

**Table D1.** Overview of assimilation effect on physical and biogeochemical model state variables in Scenario 2. The assimilation effect for each variable is quantified by the percentage change of MAD<sub>surf</sub> (MAD<sub>all</sub>) in each assimilation experiment relative to the Free run MAD<sub>surf</sub> (MAD<sub>all</sub>). A decrease larger than or equal to 10% is considered a “beneficial” effect (highlighted in bold), an increase larger than or equal to 10% is considered “detrimental” (highlighted in bold and italic), while less than 10% change is considered “neutral”. Variables that are not affected by assimilation in a specific experiment are left blank.

Unit: %	Experiment	Percentage change of MAD <sub>surf</sub>					Percentage change of MAD <sub>all</sub>			
		SSH	T	NO3	Chl	Phy	T	NO3	Chl	Phy
<b>Method 1</b>	<i>B chl</i>			-2.8	<b>-39</b>	<b>-43</b>		-6.6	<b>-12</b>	<b>-10</b>
	<i>B chl N</i>			<b>-17</b>	<b>-34</b>	<b>-33</b>		<b>-10</b>	-4.6	-0.2
	<i>T P<sub>all</sub></i>	<b>-41</b>	<b>-57</b>	<b>-40</b>	<b>+204</b>	<b>+178</b>	<b>-24</b>	<b>+75</b>	<b>+76</b>	<b>+61</b>
<b>Method 2</b>	<i>TB chl</i>	+1.3	<b>+14</b>	<b>-29</b>	<b>-48</b>	<b>-55</b>	<b>+13</b>	-4.1	<b>-14</b>	<b>-12</b>
	<i>TB chl N</i>	+7.7	<b>-10</b>	<b>-61</b>	<b>-36</b>	<b>-25</b>	+6.2	<b>-23</b>	-6.4	+1.1
	<i>TN P<sub>all</sub></i>	<b>-41</b>	<b>-57</b>	<b>-62</b>	<b>+53</b>	<b>+92</b>	<b>-24</b>	<b>-10</b>	<b>+30</b>	<b>+40</b>
<b>Method 3</b>	<i>TN P<sub>all</sub>-B chl N</i>	<b>-41</b>	<b>-57</b>	<b>-61</b>	<b>-20</b>	-2.0	<b>-24</b>	<b>-16</b>	+4.8	<b>+18</b>

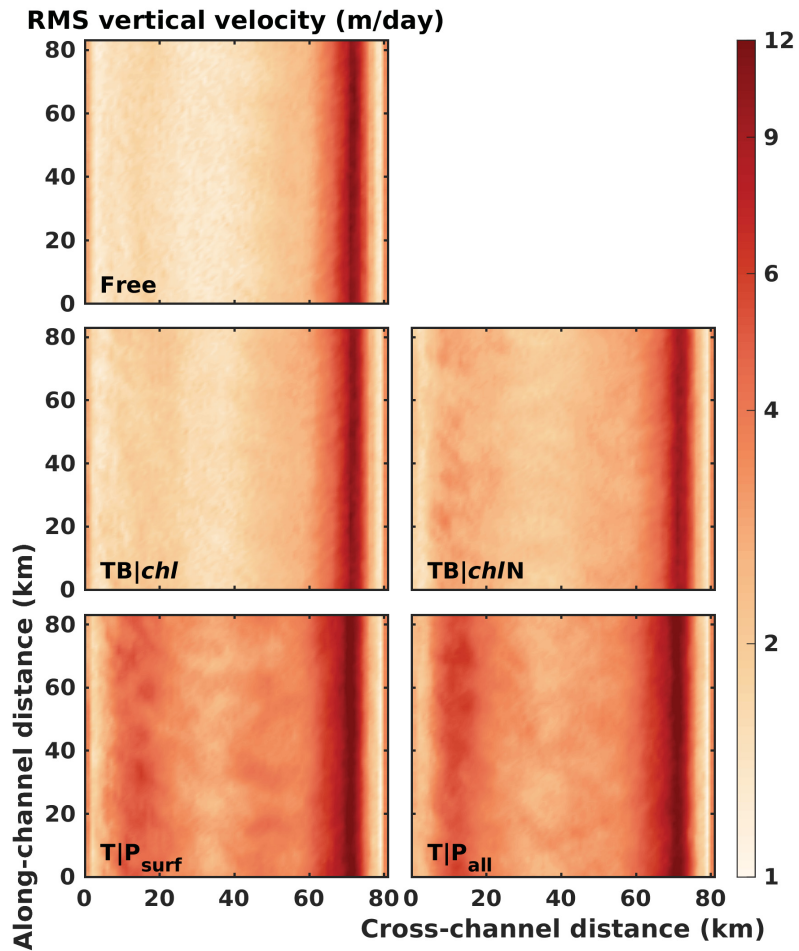


**Fig. D1.** Root mean square (RMS) vertical velocity at depths above 50 m, averaged at all analysis dates, for the truth, free run and different assimilation runs.



## BIBLIOGRAPHY

- Anderson, D.L.T., Sheinbaum, J., Haines, K., 1996. Data assimilation in ocean models. *Rep. Prog. Phys.* 59, 1209–1266.
- Anderson, J.L., 2009. Spatially and temporally varying adaptive covariance inflation for ensemble filters. *Tellus, Ser. A Dyn. Meteorol. Oceanogr.* 61 A, 72–83. <https://doi.org/10.1111/j.1600-0870.2008.00361.x>
- Anderson, J.L., Anderson, S.L., 1999. A Monte Carlo Implementation of the Nonlinear Filtering Problem to Produce Ensemble Assimilations and Forecasts. *Mon. Weather Rev.* 127, 2741–2758. [https://doi.org/10.1175/1520-0493\(1999\)127<2741:AMCIOT>2.0.CO;2](https://doi.org/10.1175/1520-0493(1999)127<2741:AMCIOT>2.0.CO;2)
- Anderson, L. a, Robinson, A.R., Lozano, C.J., 2000. Physical and biological modeling in the Gulf Stream region: I. Data assimilation methodology. *Deep Sea Res. Part I Oceanogr. Res. Pap.* 47, 1787–1827. [https://doi.org/10.1016/S0967-0637\(00\)00019-4](https://doi.org/10.1016/S0967-0637(00)00019-4)
- Berline, L., Brankart, J.-M., Brasseur, P., Ourmières, Y., Verron, J., 2007. Improving the physics of a coupled physical–biogeochemical model of the North Atlantic through data assimilation: Impact on the ecosystem. *J. Mar. Syst.* 64, 153–172. <https://doi.org/10.1016/j.jmarsys.2006.03.007>
- Berta, M., Griffa, A., Magaldi, M.G., Ozgokmen, T.M., Poje, A.C., Haza, A.C., Josefina Olascoaga, M., 2015. Improved surface velocity and trajectory estimates in the Gulf of Mexico from Blended satellite altimetry and drifter data. *J. Atmos. Ocean. Technol.* 32, 1880–1901. <https://doi.org/10.1175/JTECH-D-14-00226.1>
- Bianchi, T.S., DiMarco, S.F., Cowan, J.H., Hetland, R.D., Chapman, P., Day, J.W., Allison, M. a, 2010. The science of hypoxia in the Northern Gulf of Mexico: a review. *Sci. Total Environ.* 408, 1471–84. <https://doi.org/10.1016/j.scitotenv.2009.11.047>
- Bianucci, L., Fennel, K., Chabot, D., Shackell, N., Lavoie, D., 2015. Ocean biogeochemical models as management tools: a case study for Atlantic wolffish and declining oxygen 69, 380–388. <https://doi.org/10.1093/icesjms/fst048>
- Bierman Jr., V.J., Raesalais, N.N., Hinz, S.C., Dong-Wei, Z., Turner, E.R., Wiseman Jr., W.J., 1994. A Preliminary Mass Balance Model of Primary Productivity and Dissolved Oxygen in the Mississippi River Plume / Inner Gulf Shelf Region. *Estuaries* 17, 886–899.
- Boyer, T. P., J. I. Antonov, H. E. Garcia, D. R. Johnson, R. A. Locarnini, A. V. Mishonov, M. T. Pitcher, O. K. Baranova, and I. V. Smolyar, 2006. *World Ocean Database 2005*, edited by: Levitus, S., NOAA Atlas NESDIS 60, US Government Printing Office, Washington, DC, 190 pp., DVDs.

- Breed, G., Jackson, G., Richardson, T., 2004. Sedimentation, carbon export and food web structure in the Mississippi River plume described by inverse analysis. *Mar. Ecol. Prog. Ser.* 278, 35–51. <https://doi.org/10.3354/meps278035>
- Burgers, G., Jan van Leeuwen, P., Evensen, G., 1998. Analysis Scheme in the Ensemble Kalman Filter. *Mon. Weather Rev.* 126, 1719–1724. [https://doi.org/10.1175/1520-0493\(1998\)126<1719:ASITEK>2.0.CO;2](https://doi.org/10.1175/1520-0493(1998)126<1719:ASITEK>2.0.CO;2)
- Camilli, R., Reddy, C.M., Yoerger, D.R., Van Mooy, B. a S., Jakuba, M. V, Kinsey, J.C., McIntyre, C.P., Sylva, S.P., Maloney, J. V, 2010. Tracking hydrocarbon plume transport and biodegradation at Deepwater Horizon. *Science* 330, 201–204. <https://doi.org/10.1126/science.1195223>
- Carrier, M.J., Ngodock, H., Smith, S., Jacobs, G., Muscarella, P., Ozgokmen, T., Haus, B., Lipphardt, B., 2014. Impact of Assimilating Ocean Velocity Observations Inferred from Lagrangian Drifter Data Using the NCOM-4DVAR. *Mon. Weather Rev.* 142, 1509–1524. <https://doi.org/10.1175/MWR-D-13-00236.1>
- Cerco, C.F., 1995. Response of Chesapeake Bay to nutrient load reductions. *J. Environ. Eng.* 121, 549–557.
- Cerco, C.F., Cole, T., 1993. Three-Dimensional Eutrophication Model of Chesapeake Bay. *J. Environ. Eng.* 119, 1006–1025. [https://doi.org/10.1061/\(ASCE\)0733-9372\(1993\)119:6\(1006\)](https://doi.org/10.1061/(ASCE)0733-9372(1993)119:6(1006))
- Chassignet, E., Hurlburt, H., Metzger, E.J., Smedstad, O., Cummings, J., Halliwell, G., Bleck, R., Baraille, R., Wallcraft, A., Lozano, C., Tolman, H., Srinivasan, A., Hankin, S., Cornillon, P., Weisberg, R., Barth, A., He, R., Werner, F., Wilkin, J., 2009. US GODAE: Global Ocean Prediction with the HYbrid Coordinate Ocean Model (HYCOM). *Oceanography* 22, 64–75. <https://doi.org/10.5670/oceanog.2009.39>
- Chassignet, E.P., Hurlburt, H.E., Smedstad, O.M., Barron, C.N., Ko, D.S., Rhodes, R.C., Shriver, J.F., Wallcraft, A.J., Arnone, R.A., 2005. Assessment of Data Assimilative Ocean Models in the Gulf of Mexico Using Ocean Color 87–100. <https://doi.org/10.1029/161GM07>
- Chassignet, E.P., Hurlburt, H.E., Smedstad, O.M., Halliwell, G.R., Hogan, P.J., Wallcraft, A.J., Baraille, R., Bleck, R., 2007. The HYCOM (HYbrid Coordinate Ocean Model) data assimilative system. *J. Mar. Syst.* 65, 60–83. <https://doi.org/10.1016/j.jmarsys.2005.09.016>
- Chen, X., Lohrenz, S., Wiesenburg, D., 2000. Distribution and controlling mechanisms of primary production on the Louisiana–Texas continental shelf. *J. Mar. Syst.* 25, 179–207. [https://doi.org/10.1016/S0924-7963\(00\)00014-2](https://doi.org/10.1016/S0924-7963(00)00014-2)

- Cho, K., Reid, R.O., and Nowlin, W.D.: Objectively mapped stream function fields on the Texas–Louisiana shelf based on 32 months of moored current meter data, *J. Geophys. Res.*, 103 (C5), 10377–10390, 1998.
- Ciavatta, S., Torres, R., Martinez-Vicente, V., Smyth, T., Dall’Olmo, G., Polimene, L., Allen, J.I., 2014. Assimilation of remotely-sensed optical properties to improve marine biogeochemistry modelling. *Prog. Oceanogr.* 127, 74–95. <https://doi.org/10.1016/j.pocean.2014.06.002>
- Ciavatta, S., Torres, R., Saux-Picart, S., Allen, J.I., 2011. Can ocean color assimilation improve biogeochemical hindcasts in shelf seas? *J. Geophys. Res. Ocean.* 116, 1–19. <https://doi.org/10.1029/2011JC007219>
- Cochrane, J.D., Kelly, F.J., 1986. Low-frequency circulation on the Texas-Louisiana continental shelf. *J. Geophys. Res.* 91, 10645. <https://doi.org/10.1029/JC091iC09p10645>
- Counillon, F., Bertino, L., 2009a. High-resolution ensemble forecasting for the Gulf of Mexico eddies and fronts. *Ocean Dyn.* 59, 83–95. <https://doi.org/10.1007/s10236-008-0167-0>
- Counillon, F., Bertino, L., 2009b. Ensemble Optimal Interpolation: Multivariate properties in the Gulf of Mexico. *Tellus, Ser. A Dyn. Meteorol. Oceanogr.* 61, 296–308. <https://doi.org/10.1111/j.1600-0870.2008.00383.x>
- da Silva, A. M., C. C. Young-Molling, and S. Levitus (1994a), Atlas of Surface Marine Data 1994 Vol. 3, Anomalies of fluxes of heat and momentum. NOAA Atlas NESDIS 8, Natl. Oceanic and Atmos. Admin., Silver Spring, MD.
- da Silva, A. M., C. C. Young-Molling, and S. Levitus (1994b), Atlas of Surface Marine Data 1994 Vol. 4, Anomalies of fresh water fluxes, NOAA Atlas NESDIS 9, Natl. Oceanic and Atmos. Admin., Silver Spring, MD.
- Daley, R., 1991. Atmospheric data analysis, Cambridge Atmospheric and Space Science Series, Cambridge University Press, Cambridge, 1991
- Dee, D. P., 2005. Bias and data assimilation. *Quart. J. Roy. Meteor. Soc.*, 131, 3323–3343, doi:10.1256/qj.05.137.
- Doney, S.C., 1999. Major challenges confronting marine biogeochemical modeling. *Global Biogeochem. Cycles* 13, 705–714. <https://doi.org/10.1029/1999gb900039>

- Doney, S.C., Lindsay, K., Caldeira, K., Campin, J.-M., Drange, H., Dutay, J.-C., Follows, M., Gao, Y., Gnanadesikan, A., Gruber, N., Ishida, A., Joos, F., Madec, G., Maier-Reimer, E., Marshall, J.C., Matear, R.J., Monfray, P., Mouchet, A., Najjar, R., Orr, J.C., Plattner, G.-K., Sarmiento, J., Schlitzer, R., Slater, R., Totterdell, I.J., Weirig, M.-F., Yamanaka, Y., Yool, A., 2004. Evaluating global ocean carbon models: The importance of realistic physics. *Global Biogeochem. Cycles* 18, n/a-n/a. <https://doi.org/10.1029/2003GB002150>
- Doucet, A., Godsill, S., Andrieu, C., 2000. On sequential Monte Carlo sampling methods for Bayesian filtering. *Stat. Comput.* 10, 197–208. <https://doi.org/10.1023/A:1008935410038>
- Edwards, C. a., Moore, A.M., Hoteit, I., Cornuelle, B.D., 2015. Regional Ocean Data Assimilation. *Ann. Rev. Mar. Sci.* 7, 21–42. <https://doi.org/10.1146/annurev-marine-010814-015821>
- Eknes, M., Evensen, G., 2002. An Ensemble Kalman Filter with a 1-D marine ecosystem model. *J. Mar. Syst.* 36, 75–100.
- Eldridge, P.M., Morse, J.W., 2008. Origins and temporal scales of hypoxia on the Louisiana shelf: Importance of benthic and sub-pycnocline water metabolism. *Mar. Chem.* 108, 159–171. <https://doi.org/10.1016/j.marchem.2007.11.009>
- Eldridge, P.M., Roelke, D.L., 2010. Origins and scales of hypoxia on the Louisiana shelf: Importance of seasonal plankton dynamics and river nutrients and discharge. *Ecol. Modell.* 221, 1028–1042. <https://doi.org/10.1016/j.ecolmodel.2009.04.054>
- Evensen, G., 2003. The Ensemble Kalman Filter: Theoretical formulation and practical implementation. *Ocean Dyn.* 53, 343–367. <https://doi.org/10.1007/s10236-003-0036-9>
- Evensen, G., 1994. Sequential data assimilation with a nonlinear quasi-geostrophic model using Monte Carlo methods to forecast error statistics. *J. Geophys. Res.* 99, 10143. <https://doi.org/10.1029/94JC00572>
- Fan, S., Oey, L.Y., Hamilton, P., 2004. Assimilation of drifter and satellite data in a model of the Northeastern Gulf of Mexico. *Cont. Shelf Res.* 24, 1001–1013. <https://doi.org/10.1016/j.csr.2004.02.013>
- Feng, Y., DiMarco, S.F., Jackson, G. a., 2012. Relative role of wind forcing and riverine nutrient input on the extent of hypoxia in the northern Gulf of Mexico. *Geophys. Res. Lett.* 39, n/a-n/a. <https://doi.org/10.1029/2012GL051192>
- Feng, Y., Fennel, K., Jackson, G. a., DiMarco, S.F., Hetland, R.D., 2013. A model study of the response of hypoxia to upwelling-favorable wind on the northern Gulf of Mexico shelf. *J. Mar. Syst.* <https://doi.org/10.1016/j.jmarsys.2013.11.009>

- Fennel, K., Hetland, R., Feng, Y., DiMarco, S., 2011. A coupled physical-biological model of the Northern Gulf of Mexico shelf: model description, validation and analysis of phytoplankton variability. *Biogeosciences* 8, 1881–1899. <https://doi.org/10.5194/bg-8-1881-2011>
- Fennel, K., Hu, J., Laurent, A., Marta-Almeida, M., Hetland, R., 2013. Sensitivity of hypoxia predictions for the northern Gulf of Mexico to sediment oxygen consumption and model nesting. *J. Geophys. Res. Ocean.* 118, 990–1002. <https://doi.org/10.1002/jgrc.20077>
- Fennel, K., Losch, M., Schröter, J., Wenzel, M., 2001. Testing a marine ecosystem model: sensitivity analysis and parameter optimization. *J. Mar. Syst.* 28, 45–63. [https://doi.org/10.1016/S0924-7963\(00\)00083-X](https://doi.org/10.1016/S0924-7963(00)00083-X)
- Fennel, K., Wilkin, J., Levin, J., Moisan, J., O'Reilly, J., Haidvogel, D., 2006. Nitrogen cycling in the Middle Atlantic Bight: Results from a three-dimensional model and implications for the North Atlantic nitrogen budget. *Global Biogeochem. Cycles* 20, 1–14. <https://doi.org/10.1029/2005GB002456>
- Fennel, K., Wilkin, J., Previdi, M., Najjar, R., 2008. Denitrification effects on air-sea CO<sub>2</sub> flux in the coastal ocean: Simulations for the northwest North Atlantic. *Geophys. Res. Lett.* 35, 1–5. <https://doi.org/10.1029/2008GL036147>
- Fiechter, J., Broquet, G., Moore, A.M., Arango, H.G., 2011. A data assimilative, coupled physical-biological model for the Coastal Gulf of Alaska. *Dyn. Atmos. Ocean.* 52, 95–118. <https://doi.org/10.1016/j.dynatmoce.2011.01.002>
- Flather, R. A. (1976), A tidal model of the northwest European continental shelf, *Memoires de la Societe Royale de Sciences de Liege*, 141-164.
- Fontana, C., Brasseur, P., Brankart, J.M., 2013. Toward a multivariate reanalysis of the North Atlantic Ocean biogeochemistry during 1998–2006 based on the assimilation of SeaWiFS chlorophyll data. *Ocean Sci.* 9, 37–56. <https://doi.org/10.5194/os-9-37-2013>
- Ford, D., Barciela, R., 2016. Global marine biogeochemical reanalyses assimilating two different sets of merged ocean colour products. *Remote Sens. Environ.* <https://doi.org/10.1016/j.rse.2017.03.040>
- Ford, D.A., Edwards, K.P., Lea, D., Barciela, R.M., Martin, M.J., Demaria, J., 2012. Assimilating GlobColour ocean colour data into a pre-operational physical-biogeochemical model. *Ocean Sci.* 8, 751–771. <https://doi.org/10.5194/os-8-751-2012>
- Forrest, D.R., Hetland, R.D., DiMarco, S.F., 2011. Multivariable statistical regression models of the areal extent of hypoxia over the Texas–Louisiana continental shelf. *Environ. Res. Lett.* 6, 045002. <https://doi.org/10.1088/1748-9326/6/4/045002>

- Friedrichs, M.A.M., Dusenberry, J.A., Anderson, L.A., Armstrong, R.A., Chai, F., Christian, J.R., Doney, S.C., Dunne, J., Fujii, M., Hood, R., McGillicuddy, D.J., Moore, J.K., Schartau, M., Spitz, Y.H., Wiggert, J.D., 2007. Assessment of skill and portability in regional marine biogeochemical models: Role of multiple planktonic groups. *J. Geophys. Res.* 112, C08001. <https://doi.org/10.1029/2006JC003852>
- Fry, B., Justić, D., Riekenberg, P., Swenson, E.M., Turner, R.E., Wang, L., Pride, L., Rabalais, N.N., Kurtz, J.C., Lehrter, J.C., Murrell, M.C., Shadwick, E.H., Boyd, B., 2015. Carbon Dynamics on the Louisiana Continental Shelf and Cross-Shelf Feeding of Hypoxia. *Estuaries and Coasts* 38, 703–721. <https://doi.org/10.1007/s12237-014-9863-9>
- Gaspari, G., Cohn, S.E., 1999. Construction of correlation functions in two and three dimensions. *Q. J. R. Meteorol. Soc.* 125, 723–757. <https://doi.org/10.1002/qj.49712555417>
- Gehlen, M., Barciela, R., Bertino, L., Brasseur, P., Butenschön, M., Chai, F., Crise, A., Drillet, Y., Ford, D., Lavoie, D., Lehodey, P., Perruche, C., Samuelsen, A., Simon, E., 2015. Building the capacity for forecasting marine biogeochemistry and ecosystems: recent advances and future developments. *J. Oper. Oceanogr.* 8, s168–s187. <https://doi.org/10.1080/1755876X.2015.1022350>
- Gharamti, M.E., Samuelsen, A., Bertino, L., Simon, E., Korosov, A., Daewel, U., 2017a. Online tuning of ocean biogeochemical model parameters using ensemble estimation techniques: Application to a one-dimensional model in the North Atlantic. *J. Mar. Syst.* 168, 1–16. <https://doi.org/10.1016/j.jmarsys.2016.12.003>
- Gharamti, M.E., Tjiputra, J., Bethke, I., Samuelsen, A., Skjelvan, I., Bentsen, M., Bertino, L., 2017b. Ensemble data assimilation for ocean biogeochemical state and parameter estimation at different sites. *Ocean Model.* 112, 65–89. <https://doi.org/10.1016/j.ocemod.2017.02.006>
- Ghil, M., Malanotte-Rizzoli, P., 1991. Data Assimilation in Meteorology and Oceanography. *Adv. Geophys.* [https://doi.org/10.1016/S0065-2687\(08\)60442-2](https://doi.org/10.1016/S0065-2687(08)60442-2)
- Green, R.E., Breed, G. a., Dagg, M.J., Lohrenz, S.E., 2008. Modeling the response of primary production and sedimentation to variable nitrate loading in the Mississippi River plume. *Cont. Shelf Res.* 28, 1451–1465. <https://doi.org/10.1016/j.csr.2007.02.008>
- Greene, R.M., Lehrter, J.C., Hagy, J.D., 2009. Multiple regression models for hindcasting and forecasting midsummer hypoxia in the Gulf of Mexico. *Ecol. Appl.* 19, 1161–75.
- Gregg, W.W., 2008. Assimilation of SeaWiFS ocean chlorophyll data into a three-dimensional global ocean model. *J. Mar. Syst.* 69, 205–225. <https://doi.org/10.1016/j.jmarsys.2006.02.015>

- Haidvogel, D.B., Arango, H., Budgell, W.P., Cornuelle, B.D., Curchitser, E., Di Lorenzo, E., Fennel, K., Geyer, W.R., Hermann, A.J., Lanerolle, L., Levin, J., McWilliams, J.C., Miller, A.J., Moore, A.M., Powell, T.M., Shchepetkin, A.F., Sherwood, C.R., Signell, R.P., Warner, J.C., Wilkin, J., 2008. Ocean forecasting in terrain-following coordinates: Formulation and skill assessment of the Regional Ocean Modeling System. *J. Comput. Phys.* 227, 3595–3624. <https://doi.org/10.1016/j.jcp.2007.06.016>
- Halliwell, G.R., Kourafalou, V., Le Hénaff, M., Shay, L.K., Atlas, R., 2015. OSSE impact analysis of airborne ocean surveys for improving upper-ocean dynamical and thermodynamical forecasts in the Gulf of Mexico. *Prog. Oceanogr.* 130, 32–46. <https://doi.org/10.1016/j.pocean.2014.09.004>
- Halliwell, J.R., Srinivasan, A., Kourafalou, V., Yang, H., Willey, D., Le Hénaff, M., Atlas, R., 2014. Rigorous evaluation of a fraternal twin ocean OSSE system for the open Gulf of Mexico. *J. Atmos. Ocean. Technol.* 31, 105–130. <https://doi.org/10.1175/JTECH-D-13-00011.1>
- Hetland, R.D., DiMarco, S.F., 2012. Skill assessment of a hydrodynamic model of circulation over the Texas–Louisiana continental shelf. *Ocean Model.* 43–44, 64–76. <https://doi.org/10.1016/j.ocemod.2011.11.009>
- Hetland, R.D., DiMarco, S.F., 2008. How does the character of oxygen demand control the structure of hypoxia on the Texas–Louisiana continental shelf? *J. Mar. Syst.* 70, 49–62. <https://doi.org/10.1016/j.jmarsys.2007.03.002>
- Hoteit, I., Hoar, T., Gopalakrishnan, G., Collins, N., Anderson, J., Cornuelle, B., et al. (2013). A MITgcm/DART ensemble analysis and prediction system with application to the Gulf of Mexico. *Dynamics of Atmospheres and Oceans*, 63, 1–23. <https://doi.org/10.1016/j.dynatmoce.2013.03.002>
- Houtekamer, P.L., Mitchell, H.L., 2001. A Sequential Ensemble Kalman Filter for Atmospheric Data Assimilation. *Mon. Weather Rev.* 129, 123–137. [https://doi.org/10.1175/1520-0493\(2001\)129<0123:ASEKFF>2.0.CO;2](https://doi.org/10.1175/1520-0493(2001)129<0123:ASEKFF>2.0.CO;2)
- Houtekamer, P.L., Mitchell, H.L., 1998. Data assimilation using an ensemble Kalman filter technique. *Mon. Weather Rev.* 126, 796–811. [https://doi.org/10.1175/1520-0493\(1998\)126<0796:DAUAEK>2.0.CO;2](https://doi.org/10.1175/1520-0493(1998)126<0796:DAUAEK>2.0.CO;2)
- Houtekamer, P.L., Zhang, F., 2016. Review of the Ensemble Kalman Filter for Atmospheric Data Assimilation. *Mon. Weather Rev.* 144, 4489–4532. [doi:10.1175/MWR-D-15-0440.1](https://doi.org/10.1175/MWR-D-15-0440.1)
- Hu, J., Fennel, K., Mattern, J.P., Wilkin, J., 2012. Data assimilation with a local Ensemble Kalman Filter applied to a three-dimensional biological model of the Middle Atlantic Bight. *J. Mar. Syst.* 94, 145–156. <https://doi.org/10.1016/j.jmarsys.2011.11.016>



- Hunt, B.R., Kostelich, E.J., Szunyogh, I., 2007. Efficient data assimilation for spatiotemporal chaos: A local ensemble transform Kalman filter. *Phys. D Nonlinear Phenom.* 230, 112–126. <https://doi.org/10.1016/j.physd.2006.11.008>
- Jacobs, G.A., Bartels, B.P., Bogucki, D.J., Beron-Vera, F.J., Chen, S.S., Coelho, E.F., Curcic, M., Griffa, A., Gough, M., Haus, B.K., Haza, A.C., Helber, R.W., Hogan, P.J., Huntley, H.S., Iskandarani, M., Judt, F., Kirwan, A.D., Laxague, N., Valle-Levinson, A., Lipphardt, B.L., J. Mariano, A., Ngodock, H.E., Novelli, G., Olascoaga, M.J., Özgökmen, T.M., Poje, A.C., Reniers, A.J.H.M., Rowley, C.D., Ryan, E.H., Smith, S.R., Spence, P.L., Thoppil, P.G., Wei, M., 2014. Data assimilation considerations for improved ocean predictability during the Gulf of Mexico Grand Lagrangian Deployment (GLAD). *Ocean Model.* 83, 98–117. <https://doi.org/10.1016/j.ocemod.2014.09.003>
- Janjić, T., Bormann, N., Bocquet, M., Carton, J.A., Cohn, S.E., Dance, S.L., Losa, S.N., Nichols, N.K., Potthast, R., Waller, J.A., Weston, P., 2017. On the representation error in data assimilation. *Q. J. R. Meteorol. Soc.* 1257–1278. doi:10.1002/qj.3130
- Johnson, K., Berelson, W., Boss, E., Chase, Z., Claustre, H., Emerson, S., Gruber, N., Körtzinger, A., Perry, M.J., Riser, S., 2009. Observing Biogeochemical Cycles at Global Scales with Profiling Floats and Gliders: Prospects for a Global Array. *Oceanography* 22, 216–225. <https://doi.org/10.5670/oceanog.2009.81>
- Johnson, K.S., Coletti, L.J., Jannasch, H.W., Sakamoto, C.M., Swift, D.D., Riser, S.C., 2013. Long-term nitrate measurements in the ocean using the in situ ultraviolet spectrophotometer: Sensor integration into the APEX profiling float. *J. Atmos. Ocean. Technol.* 30, 1854–1866. <https://doi.org/10.1175/JTECH-D-12-00221.1>
- Jones, E.M., Baird, M.E., Mongin, M., Parslow, J., Skerratt, J., Margvelashvili, N., Matear, R.J., Wild-Allen, K., Robson, B., Rizwi, F., Oke, P., King, E., Schroeder, T., Steven, A., Taylor, J., 2016. Use of remote-sensing reflectance to constrain a data assimilating marine biogeochemical model of the Great Barrier Reef. *Biogeosciences* 1–35. <https://doi.org/10.5194/bg-2016-168>
- Justic, D., Rabalais, N.N., Turner, R.E., 2002. Modeling the impacts of decadal changes in riverine nutrient fluxes on coastal eutrophication near the Mississippi River Delta. *Ecol. Modell.* 152, 33–46.
- Justic, D., Rabalais, N.N., Turner, R.E., 1996. Effects of climate change on hypoxia in coastal waters : Effects of climate change on hypoxia doubled CO2 scenario for the northern Gulf of Mexico Dubravko. *Limnol. Oceanogr.* 41, 992–1003.
- Justić, D., and L. Wang (2014), Assessing temporal and spatial variability of hypoxia over the inner Louisiana–upper Texas shelf: Application of an unstructured-grid three-dimensional coupled hydrodynamic-water quality model, *Cont. Shelf Res.*, 72, 163-179.



- Kalnay, E., 2003. Atmospheric modeling, data assimilation, and predictability, *Annals of Physics*. <https://doi.org/10.1256/00359000360683511>
- Kantha, L., J-K. Choi, K. J. Schaudt, and C. K. Cooper, (this volume). A regional data-assimilative model for operational use in the Gulf of Mexico. In W. Sturges, A. Lugo-Fernández (Eds.), *Circulation in the Gulf of Mexico: Observations and Models, Geophysical Monograph Series* (Vol. 161, pp. 165-180). Washington, DC: American Geophysical Union.
- Kemp, W., Sampou, P.A., Garber, J., Tuttle, J., Boynton, W., 1992. Seasonal depletion of oxygen from bottom waters of Chesapeake Bay : roles of benthic and planktonic respiration and physical exchange processes. *Mar. Ecol. Prog. Ser.* 1992, 137–152.
- Khade, V., Kurian, J., Chang, P., Szunyogh, I., Thyng, K., Montuoro, R., 2017. Oceanic ensemble forecasting in the Gulf of Mexico: An application to the case of the Deep Water Horizon oil spill. *Ocean Model.* 113, 171–184. <https://doi.org/10.1016/j.ocemod.2017.04.004>
- Kitagawa, G., 1996. Monte Carlo Filter and Smoother for Non-Gaussian Nonlinear State Space Models. *J. Comput. Graph. Stat.*
- Kuhn, A.M., Fennel, K., Mattern, J.P., 2015. Model investigations of the North Atlantic spring bloom initiation. *Prog. Oceanogr.* 138, 176–193. <https://doi.org/10.1016/j.pocean.2015.07.004>
- Laurent, a., Fennel, K., Hu, J., Hetland, R., 2012. Simulating the effects of phosphorus limitation in the Mississippi and Atchafalaya River plumes. *Biogeosciences* 9, 4707–4723. <https://doi.org/10.5194/bg-9-4707-2012>
- Laurent, A., Fennel, K., 2013. Simulated reduction of hypoxia in the northern Gulf of Mexico due to phosphorus limitation. *Elem. Sci. Anthr.* 2, 000022. <https://doi.org/10.12952/journal.elementa.000022>
- Le Dimet, F., Talagrand, O., 1986. Variational algorithms for analysis and assimilation of meteorological observations: theoretical aspects. *Tellus A* 38 A, 97–110. <https://doi.org/10.1111/j.1600-0870.1986.tb00459.x>
- Ledwell, J.R., He, R., Xue, Z., DiMarco, S.F., Spencer, L.J., Chapman, P., 2016. Dispersion of a tracer in the deep Gulf of Mexico. *J. Geophys. Res. Ocean.* 1–12. <https://doi.org/10.1002/2015JC010952>.Received
- Lehrter, J.C., Murrell, M.C., and Kurtz, J.C.: Interactions between Mississippi River inputs, light, and phytoplankton biomass and phytoplankton production on the Louisiana continental shelf, *Cont. Shelf Res.*, 29, 1861-1872, 2009.
- Lehrter, J.C., Beddick, D.L., Devereux, R., Yates, D.F., and Murrell, M.C.: Sediment-water fluxes of dissolved inorganic carbon, O<sub>2</sub>, nutrients, and N<sub>2</sub> from the hypoxic region of the Louisiana continental shelf, *Biogeochemistry*, 109, 233-252, 2012.

- Lehrter, J.C., Ko, D.S., Murrell, M.C., Hagy, J.D., Schaeffer, B.A., Greene, R.M., Gould, R.W., and Penta, B.: Nutrient distributions, transports, and budgets on the inner margin of a river-dominated continental shelf, *J. Geophys. Res.- Oceans*, 118, 4822-4838, 2013.
- Lehrter, J.C., Fry, B., and Murrell, M.C.: Microphytobenthos production potential and contribution to bottom layer oxygen dynamics on the inner Louisiana continental shelf, *Bull. Mar. Sci.*, 90(3): 765-780, 2014.
- Li, Y., Li, M., Kemp, W.M., 2015. A Budget Analysis of Bottom-Water Dissolved Oxygen in Chesapeake Bay. *Estuaries and Coasts* 38, 2132–2148. <https://doi.org/10.1007/s12237-014-9928-9>
- Lin, X.H., Oey, L.Y., Wang, D.P., 2007. Altimetry and drifter data assimilations of loop current and eddies. *J. Geophys. Res. Ocean.* 112, 1–24. <https://doi.org/10.1029/2006JC003779>
- Liu, Y., Weisberg, R.H., 2011. Evaluation of trajectory modeling in different dynamic regions using normalized cumulative Lagrangian separation. *J. Geophys. Res. Ocean.* 116, 1–13. <https://doi.org/10.1029/2010JC006837>
- Liu, Y., Weisberg, R., Hu, C. H., & Zheng, L. (2011). Tracking the Deepwater Horizon Oil Spill: A modeling perspective. *Eos*, 92(6), 45–52.
- Lorenz, A.C., 1986. Analysis methods for numerical weather prediction. *R. Meteorol. Soc.* doi:10.1256/smsqj.47413
- Lugo-Fernández, A., 2016. The Loop Current Dynamics Experiment (2009–2011) in the Gulf of Mexico. *Dyn. Atmos. Ocean.* 76, 155. <https://doi.org/10.1016/j.dynatmoce.2016.11.001>
- Mattern, J.P., Dowd, M., Fennel, K., 2013. Particle filter-based data assimilation for a three-dimensional biological ocean model and satellite observations. *J. Geophys. Res. Ocean.* 118, 2746–2760. <https://doi.org/10.1002/jgrc.20213>
- Mattern, J.P., Song, H., Edwards, C.A., Moore, A.M., Fiechter, J., 2016. Data assimilation of physical and chlorophyll observations in the California Current System using two biogeochemical models
- McCarthy, M.J., Carini, S. a., Liu, Z., Ostrom, N.E., Gardner, W.S., 2013. Oxygen consumption in the water column and sediments of the northern Gulf of Mexico hypoxic zone. *Estuar. Coast. Shelf Sci.* 123, 46–53. <https://doi.org/10.1016/j.ecss.2013.02.019>
- Mellor, G.L. and Yamada, T., 1982. Development of a turbulence closure model for geophysical fluid problems. *Rev. Geophys. Space Phys.*, 20, 851-875

- Morey, S. L., Zavala-Hidalgo, J., & O'Brien, J. J., 2005. The seasonal variability of continental shelf circulation in the northern and western Gulf of Mexico from a high-resolution numerical model. In W. Sturges, A. Lugo-Fernández (Eds.), *Circulation in the Gulf of Mexico: Observations and Models, Geophysical Monograph Series* (Vol. 161, pp. 203–218). Washington, DC: American Geophysical Union.
- Murrell, M.C., Lehrter, J.C., 2010. Sediment and Lower Water Column Oxygen Consumption in the Seasonally Hypoxic Region of the Louisiana Continental Shelf. *Estuaries and Coasts* 34, 912–924. <https://doi.org/10.1007/s12237-010-9351-9>
- Murrell, M. C., D. L. Beddick, R. Devereux, R. M. Greene, J. D. Hagy, B. M. Jarvis, J. C. Kurtz, J. C. Lehrter, and D. F. Yates (2013a), Gulf of Mexico hypoxia research program data report: 2002-2007, p. 217, U. S. Environmental Protection Agency, Washington, DC, EPA/600/R-13/257, <http://tinyurl.com/ko9wj7j>.
- Murrell, M. C., R. S. Stanley, J. C. Lehrter, and J. D. Hagy (2013b), Plankton community respiration, net ecosystem metabolism, and oxygen dynamics on the Louisiana continental shelf: Implications for hypoxia, *Cont. Shelf Res.*, 52, 27–38, doi:10.1016/j.csr.2012.10.010.
- Muscarella, P., Carrier, M.J., Ngodock, H., Smith, S., Lipphardt, B.L., Kirwan, A.D., Huntley, H.S., 2015. Do Assimilated Drifter Velocities Improve Lagrangian Predictability in an Operational Ocean Model? *Mon. Weather Rev.* 143, 1822–1832. <https://doi.org/10.1175/MWR-D-14-00164.1>
- Natvik, L.J., Evensen, G., 2003. Assimilation of ocean colour data into a biochemical model of the North Atlantic: Part 1. Data assimilation experiments. *J. Mar. Syst.* 40–41, 127–153. [https://doi.org/10.1016/S0924-7963\(03\)00016-2](https://doi.org/10.1016/S0924-7963(03)00016-2)
- North, E.W., Adams, E.E., Thessen, A.E., Schlag, Z., He, R., Socolofsky, S.A., Masutani, S.M., Peckham, S.D., 2015. The influence of droplet size and biodegradation on the transport of subsurface oil droplets during the Deepwater Horizon spill: a model sensitivity study. *Environ. Res. Lett.* 10, 24016. <https://doi.org/10.1088/1748-9326/10/2/024016>
- Nunnally, C.C., Rowe, G.T., Thornton, D.C.O., Quigg, A., 2013. Sedimentary Oxygen Consumption and Nutrient Regeneration in the Northern Gulf of Mexico Hypoxic Zone. *J. Coast. Res.* 84–96. <https://doi.org/10.2112/SI63-008.1>
- Obenour, D.R., Michalak, A., Scavia, D., 2014. Assessing biophysical controls on Gulf of Mexico hypoxia through probabilistic modeling. *Ecol. Appl.* <https://doi.org/10.1890/13-2257.1>
- Obenour, D.R., Michalak, A.M., Zhou, Y., Scavia, D., 2012. Quantifying the impacts of stratification and nutrient loading on hypoxia in the northern Gulf of Mexico. *Environ. Sci. Technol.* 46, 5489–96. <https://doi.org/10.1021/es204481a>

- Obenour, D.R., Scavia, D., Rabalais, N.N., Turner, R.E., Michalak, A.M., 2013. Retrospective analysis of midsummer hypoxic area and volume in the northern gulf of Mexico, 1985-2011. *Environ. Sci. Technol.* 47, 9808–15. <https://doi.org/10.1021/es400983g>
- Oey, L.-Y., 2008. Loop Current and Deep Eddies. *J. Phys. Oceanogr.* 38, 1426–1449. <https://doi.org/10.1175/2007JPO3818.1>
- Oey, L.-Y., Lee, H.-C., 2003. Effects of winds and Caribbean eddies on the frequency of Loop Current eddy shedding: A numerical model study. *J. Geophys. Res.* 108, 3324. <https://doi.org/10.1029/2002JC001698>
- Oey, L.-Y., Ezer, T., Lee, H.-C., 2005a. Loop Current, rings and related circulation in the Gulf of Mexico: a review of numerical models and future challenges. In W. Sturges, A. Lugo-Fernández (Eds.), *Circulation in the Gulf of Mexico: Observations and Models, Geophysical Monograph Series* (Vol. 161, pp. 32–56). Washington, DC: American Geophysical Union.
- Oey, L.Y., Ezer, T., Forristall, G., Cooper, C., DiMarco, S., Fan, S., 2005b. An exercise in forecasting loop current and eddy frontal positions in the Gulf of Mexico. *Geophys. Res. Lett.* 32, 1–4. <https://doi.org/10.1029/2005GL023253>
- Oschlies, A., Garçon, V., 1999. An eddy-permitting coupled physical-biological model of the North Atlantic - 1. Sensitivity to advection numerics and mixed layer physics. *Global Biogeochem. Cycles* 13, 135–160. <https://doi.org/10.1029/98gb02811>
- Peña, M. a., Katsev, S., Oguz, T., Gilbert, D., 2010. Modeling dissolved oxygen dynamics and hypoxia. *Biogeosciences* 7, 933–957. <https://doi.org/10.5194/bg-7-933-2010>
- Pierson, J.J., Roman, M.R., Kimmel, D.G., Boicourt, W.C., Zhang, X., 2009. Quantifying changes in the vertical distribution of mesozooplankton in response to hypoxic bottom waters. *J. Exp. Mar. Bio. Ecol.* 381, S74–S79. <https://doi.org/10.1016/j.jembe.2009.07.013>
- Pond, S., and G. L. Pickard (1983), *Introductory dynamical oceanography*, 2nd edition Pergamon Press, Oxford.
- Quiñones-rivera, Z.J., Wissel, B., Justi, D., Fry, B., 2007. Partitioning oxygen sources and sinks in a stratified , eutrophic coastal ecosystem using stable oxygen isotopes 342, 69–83.
- Quiñones-Rivera, Z.J., Wissel, B., Rabalais, N.N., Justic, D., 2010. Effects of biological and physical factors on seasonal oxygen dynamics in a stratified, eutrophic coastal ecosystem. *Limnol. Oceanogr.* 55, 289–304. <https://doi.org/10.4319/lo.2010.55.1.0289>

- Rabalais, N.N., Turner, R.E., Dortch, Q., Justic, D., Jr, V.J.B., Jr, W.J.W., 2002. Nutrient-enhanced productivity in the northern Gulf of Mexico : past , present and future. *Hydrobiologia* 39–63.
- Rabalais, N.N., Turner, R.E., Sen Gupta, B.K., Boesch, D., Chapman, P., Murrell, M.C., 2007. Hypoxia in the Northern Gulf of Mexico : Does the Science Support the Plan to Reduce , Mitigate , and Control Hypoxia ? *Estuaries and Coasts* 30, 753–772.
- Rabalais, N.N., Turner, R.E., Sen Gupta, B.K., Boesch, D.F., Chapman, P., Murrell, M.C., 2007. Hypoxia in the northern Gulf of Mexico: does the science support the plan to reduce, mitigate, and control hypoxia? *Estuaries and Coasts* 30, 753–772. <https://doi.org/10.2307/27654714>
- Raghukumar, K., Edwards, C.A., Goebel, N.L., Broquet, G., Veneziani, M., Moore, A.M., Zehr, J.P., 2015. Impact of assimilating physical oceanographic data on modeled ecosystem dynamics in the California Current System. *Prog. Oceanogr.* 138, 546–558. <https://doi.org/10.1016/j.pocean.2015.01.004>
- Robinson, A.R., Lermusiaux, P.F.J., 2002. Data assimilation for modeling and predicting coupled physical-biological interactions in the sea, *The Sea*, Volume 12.
- Rowe, G.T., Chapman, P., 2002. Continental shelf hypoxia: Some nagging questions. *Gulf Mex. Sci.*
- Rowe, G.T., Kaegi, M.E.C., Morse, J.W., Boland, G.S., Briones, E.G.E., 2002. Sediment community metabolism associated with continental shelf hypoxia, Northern Gulf of Mexico. *Estuaries* 25, 1097–1106. <https://doi.org/10.1007/bf02692207>
- Ryerson, T.B., Camilli, R., Kessler, J.D., Kujawinski, E.B., Reddy, C.M., Valentine, D.L., Atlas, E., Blake, D.R., de Gouw, J., Meinardi, S., Parrish, D.D., Peischl, J., Seewald, J.S., Warneke, C., 2012. Chemical data quantify Deepwater Horizon hydrocarbon flow rate and environmental distribution. *Proc. Natl. Acad. Sci.* 109, 20246–20253. <https://doi.org/10.1073/pnas.1110564109>
- Sakov, P., Bertino, L., 2011. Relation between two common localisation methods for the EnKF. *Comput. Geosci.* 15, 225–237. <https://doi.org/10.1007/s10596-010-9202-6>
- Sakov, P., Counillon, F., Bertino, L., Lisæter, K.A., Oke, P.R., Korabely, A., 2012. TOPAZ4: an ocean-sea ice data assimilation system for the North Atlantic and Arctic. *Ocean Sci.* 8, 633–656. <https://doi.org/10.5194/os-8-633-2012>
- Sakov, P., Oke, P.R., 2008. A deterministic formulation of the ensemble Kalman filter: an alternative to ensemble square root filters. *Tellus A* 60, 361–371. <https://doi.org/10.1111/j.1600-0870.2007.00299.x>
- Samuelson, A., Bertino, L., Hansen, C., 2009. Impact of data assimilation of physical variables on the spring bloom from TOPAZ operational runs in the North Atlantic. *Ocean Sci.* 5, 635–647. <https://doi.org/doi:10.5194/os-5-635-2009>

- Schmitz, W. J., Jr., Biggs, D. C., Lugo-Fernandez, A., Oey, L.-Y., & Sturges, W., 2005. A synopsis of the circulation in the Gulf Of Mexico and on its continental Margins. In W. Sturges, A. Lugo-Fernández (Eds.), *Circulation in the Gulf of Mexico: Observations and Models, Geophysical Monograph Series* (Vol. 161, pp. 11-29). Washington, DC: American Geophysical Union.
- Schofield, O., Glenn, S.M., Moline, M.A., Oliver, M., Irwin, A., Chao, Y., Arrott, M., 2013. Encyclopedia of Sustainability Science and Technology. *Encycl. Sustain. Sci. Technol.* 81–100. <https://doi.org/10.1007/978-1-4419-0851-3>
- Scully, M.E., 2013. Physical controls on hypoxia in Chesapeake Bay: A numerical modeling study. *J. Geophys. Res. Ocean.* 118, 1239–1256. <https://doi.org/10.1002/jgrc.20138>
- Shay, L. K., Jaimes, B., Brewster, J. K., Meyers, P., McCaskill, E. C., Uhlhorn, E., Marks, F., Halliwell Jr., G. R., Smedstad, O. M., & Hogan, P., 2011, Airborne ocean surveys of the Loop Current complex from NOAA WP-3D in support of the Deepwater Horizon oil spill, In Y. Liu, A. Macfadyen, Z.-G. Ji, R. H. Weisberg (Eds.), *Monitoring and Modeling the Deepwater Horizon Oil Spill: A Record-Breaking Enterprise, Geophysical Monograph Series* (Vol. 195, pp. 131-152). Washington, DC: American Geophysical Union. doi:10.1029/2011GM001101
- Shen, Y., Fichot, C.G., Benner, R., 2012. Floodplain influence on dissolved organic matter composition and export from the Mississippi-Atchafalaya River system to the Gulf of Mexico. *Limnol. Oceanogr.* 57, 1149–1160. <https://doi.org/10.4319/lo.2012.57.4.1149>
- Shulman, I., Frolov, S., Anderson, S., Penta, B., Gould, R., Sakalaukus, P., Ladner, S., 2013. Impact of bio-optical data assimilation on short-term coupled physical, bio-optical model predictions. *J. Geophys. Res. Ocean.* 118, 2215–2230. <https://doi.org/10.1002/jgrc.20177>
- Simon, E., Samuelson, A., Bertino, L., Mouysset, S., 2015. Experiences in multiyear combined state-parameter estimation with an ecosystem model of the North Atlantic and Arctic Oceans using the Ensemble Kalman Filter. *J. Mar. Syst.* 152, 1–17. <https://doi.org/10.1016/j.jmarsys.2015.07.004>
- Song, H., Edwards, C.A., Moore, A.M., Fiechter, J., 2016a. Data assimilation in a coupled physical-biogeochemical model of the California Current System using an incremental lognormal 4-dimensional variational approach: Part 2-Joint physical and biological data assimilation twin experiments. *Ocean Model.* 106, 146–158. <https://doi.org/10.1016/j.ocemod.2016.04.001>



- Song, H., Edwards, C.A., Moore, A.M., Fiechter, J., 2016b. Data assimilation in a coupled physical-biogeochemical model of the California Current System using an incremental lognormal 4-dimensional variational approach: Part 3-Assimilation in a realistic context using satellite and in situ observations. *Ocean Model.* 106, 159–172. <https://doi.org/10.1016/j.ocemod.2016.04.001>
- Srinivasan, A., Chassignet, E.P., Bertino, L., Brankart, J.-M., Brasseur, P., Chin, T.M., Counillon, F., Cummings, J.A., Mariano, A.J., Smedstad, O.M., Thacker, W.C., 2011. A comparison of sequential assimilation schemes for ocean prediction with the HYbrid Coordinate Ocean Model (HYCOM): Twin experiments with static forecast error covariances. *Ocean Model.* 37, 85–111. <https://doi.org/10.1016/j.ocemod.2011.01.006>
- Sturges, W., Leben, R., 2000. Frequency of Ring Separations from the Loop Current in the Gulf of Mexico: A Revised Estimate. *J. Phys. Oceanogr.* 30, 1814–1819. [https://doi.org/10.1175/1520-0485\(2000\)030<1814:FORSFT>2.0.CO;2](https://doi.org/10.1175/1520-0485(2000)030<1814:FORSFT>2.0.CO;2)
- Sturges, W., & Lugo-Fernández, A. (Eds.) (2005). *Circulation in the Gulf of Mexico: Observations and Models. Geophysical Monograph Series* (Vol. 161), Washington, DC: American Geophysical Union.
- Testa, J.M., Kemp, W.M., 2012. Hypoxia-induced shifts in nitrogen and phosphorus cycling in Chesapeake Bay. *Limnol. Oceanogr.* 57, 835–850. <https://doi.org/10.4319/lo.2012.57.3.0835>
- Thacker, W.C., Long, R.B., 1988. Fitting dynamics to data. *J. Geophys. Res.* 93, 1227. <https://doi.org/10.1029/JC093iC02p01227>
- Thacker, W.C., Srinivasan, A., Iskandarani, M., Knio, O.M., Hénaff, M. Le, 2012. Propagating boundary uncertainties using polynomial expansions. *Ocean Model.* 43–44, 52–63. doi:10.1016/j.ocemod.2011.11.011
- Toth, Z. , Kalnay, E., 1993. Ensemble forecasting at NMC: the generation of perturbations. *Bull. Am. Meteorol. Soc.* 74, 2317–2330 .
- Turner, R.E., Rabalais, N.N., Justic, D., 2006. Predicting summer hypoxia in the northern Gulf of Mexico: riverine N, P, and Si loading. *Mar. Pollut. Bull.* 52, 139–48. <https://doi.org/10.1016/j.marpolbul.2005.08.012>
- Valentine, D.L., Fisher, G.B., Bagby, S.C., Nelson, R.K., Reddy, C.M., Sylva, S.P., Woo, M.A., 2014. Fallout plume of submerged oil from Deepwater Horizon. *Proc. Natl. Acad. Sci.* 111, 15906–15911. <https://doi.org/10.1073/pnas.1414873111>
- Valentine, D.L., Kessler, J.D., Redmond, M.C., Mendes, S.D., Heintz, M.B., Farwell, C., Hu, L., Kinnaman, F.S., Yvon-Lewis, S., Du, M.R., Chan, E.W., Tigreros, F.G., Villanueva, C.J., 2010. Propane Respiration Jump-Starts Microbial Response to a Deep Oil Spill. *Science* (80). 330, 208–211. <https://doi.org/10.1126/Science.1196830>

- Wang, D.-P., Oey, L.-Y., Ezer, T., Hamilton, P., 2003. Near-Surface Currents in DeSoto Canyon (1997–99): Comparison of Current Meters, Satellite Observation, and Model Simulation. *J. Phys. Oceanogr.* 33, 313–326. [https://doi.org/10.1175/1520-0485\(2003\)033<0313:NSCIDC>2.0.CO;2](https://doi.org/10.1175/1520-0485(2003)033<0313:NSCIDC>2.0.CO;2)
- Wanninkhof, R., 1992. Relationship between wind speed and gas exchange over the ocean. *J. Geophys. Res. Ocean.* 97, 7373–7382. <https://doi.org/10.1029/92JC00188>
- Wild-Allen, K., Herzfeld, M., Thompson, P.A., Rosebrock, U., Parslow, J., Volkman, J.K., 2010. Applied coastal biogeochemical modelling to quantify the environmental impact of fish farm nutrients and inform managers. *J. Mar. Syst.* 81, 134–147. <https://doi.org/10.1016/j.jmarsys.2009.12.013>
- Wikle, C.K., Berliner, L.M., 2007. A Bayesian tutorial for data assimilation. *Phys. D Nonlinear Phenom.* 230, 1–16. doi:10.1016/j.physd.2006.09.017
- Wilson, C., Adamec, D., 2002. A global view of bio-physical coupling from SeaWiFS and TOPEX satellite data, 1997–2001. *Geophys. Res. Lett.* 29, 1–4. <https://doi.org/10.1029/2001GL014063>
- Wiseman, W.J., Rabalais, N.N., Turner, R.E., Dinnel, S.P., MacNaughton, a., 1997. Seasonal and interannual variability within the Louisiana coastal current: stratification and hypoxia. *J. Mar. Syst.* 12, 237–248. [https://doi.org/10.1016/S0924-7963\(96\)00100-5](https://doi.org/10.1016/S0924-7963(96)00100-5)
- Wu, H., Zhu, J., 2010. Advection scheme with 3rd high-order spatial interpolation at the middle temporal level and its application to saltwater intrusion in the Changjiang Estuary. *Ocean Model.* 33, 33–51. <https://doi.org/10.1016/j.ocemod.2009.12.001>
- Xu, F. H., Oey, L. Y., Miyazawa, Y., & Hamilton, P. (2013). Hindcasts and forecasts of Loop Current and eddies in the Gulf of Mexico using local ensemble transform Kalman filter and optimum-interpolation assimilation schemes. *Ocean Modelling*, 69, 22–38. <https://doi.org/10.1016/j.ocemod.2013.05.002>
- Xue, Z., He, R., Fennel, K., Cai, W.J., Lohrenz, S., Hopkinson, C., 2013. Modeling ocean circulation and biogeochemical variability in the Gulf of Mexico. *Biogeosciences* 10, 7219–7234. <https://doi.org/10.5194/bg-10-7219-2013>
- Yin, X.Q., Oey, L.Y., 2007. Bred-ensemble ocean forecast of loop current and rings. *Ocean Model.* 17, 300–326. <https://doi.org/10.1016/j.ocemod.2007.02.005>
- Yu, L., Fennel, K., Bertino, L., El, M., Thompson, K.R., 2018. Insights on multivariate updates of physical and biogeochemical ocean variables using an Ensemble Kalman Filter and an idealized model of upwelling. *Ocean Model.* 126, 13–28. <https://doi.org/10.1016/j.ocemod.2018.04.005>



- Yu, L., Fennel, K., Laurent, A., Murrell, M.C., Lehrter, J.C., 2015a. Numerical analysis of the primary processes controlling oxygen dynamics on the Louisiana shelf. *Biogeosciences* 12, 2063–2076. <https://doi.org/10.5194/bg-12-2063-2015>
- Yu, L., Fennel, K., Laurent, A., 2015b. A modeling study of physical controls on hypoxia generation in the northern Gulf of Mexico. *J. Geophys. Res. Ocean.* 120, 5019–5039. <https://doi.org/10.1002/2014JC010634>
- Zavala-Hidalgo, J., Romero-Centeno, R., Mateos-Jasso, A., Morey, S.L., Martínez-López, B., 2014. The response of the Gulf of Mexico to wind and heat flux forcing: What has been learned in recent years? *Atmosfera* 27, 317–334. [https://doi.org/10.1016/S0187-6236\(14\)71119-1](https://doi.org/10.1016/S0187-6236(14)71119-1)